MEASUREMENT OF CARRIER FLUID VISCOSITIES OF OIL SAND SLURRIES

by

Ghassan Izhar Khan

A thesis submitted in partial fulfillment of the requirements for the degree of

Master of Science

in

Chemical Engineering

Department of Chemical Engineering
University of Alberta

© Ghassan Izhar Khan, 2019

Abstract

This study investigates the factors that contribute to the viscosity of the carrier fluid in oil sand slurries. The carrier fluid is defined as the fine particles and process water in a slurry. The carrier fluid viscosity is a crucial parameter in industry and is needed to accurately design pipelines and size vessels. In a pipeline, the slurry must be pumped at a velocity higher than the deposition velocity, which is a function of the carrier fluid viscosity. Failure to do so causes particle deposition and plugging of pipelines leading to shutdowns. The carrier fluid viscosity can also play a crucial role in the performance of separation vessels by hindering the flotation of bitumen during extraction. The goal of this project is to establish a correlation that can be used to calculate carrier fluid viscosities and minimize the need for the expensive and time-consuming viscosity measurements. The correlations that currently exist only account for overall fine solids concentrations to predict viscosities. However, the results of this study prove the contributing effect of clay activity and water chemistry factors on the viscosity of the carrier fluid. Therefore, it is necessary to account for such factors in order to accurately calculate viscosity. This study expands previous work to include clay activity and water chemistry when predicting viscosities. The types of clays present in a slurry can vary drastically based on the ore. The presence of highly active clays can cause increased ion exchange which leads to stronger aggregation and an increase in viscosity values. The copper-triethylenetetramine (Cu-Trien) method is used to calculate the activity levels of clays present. The effect of water chemistry on viscosity is also considered. Process water can vary greatly in terms of pH and dissolved ion concentrations. Water chemistry has been shown to affect the surface charge of clay particles and in turn the aggregation tendencies of the particles. Ion chromatography is used to determine water chemistry of the samples. Clay activity and water chemistry are incorporated with fine solids concentration in this study, to develop a model to predict carrier fluid viscosities with a high level of accuracy. This study also shows differences in viscosities measured by concentric cylinder (CCV) and double gap geometries. The CCV is shown to provide consistently higher viscosities than the double gap geometry for carrier fluid samples. This may be related to the effect of geometry on the equilibrium state of aggregation of

the clay flocs. The double gap viscometer measurements required the use of manufacturer-supplied conversion factors for shear stress and shear rate which are appropriate only for Newtonian fluids and so their applicability to these carrier fluids, which exhibited small yield stresses, may be limited. Consequently, the discrepancies between measurements made in different geometries require further investigation. Also, while the results of this study prove the potential for accurate viscosity predictions using CEC and water chemistry, further work is required prior to industrial application. Specifically, additional work must be carried out in the future with samples from different ores of varying clay activity to confirm the relationships found in this study. A wide array of CEC and water chemistry analyses should be conducted and correlated to carrier fluid viscosities to expand this work before it can be applied in industrial settings. The use of optical techniques in the future is also recommended to observe particle interactions directly in-situ and quantify the effects on viscosity.

Acknowledgements

I would like to thank my supervisor, Dr. Sean Sanders, for the opportunity to conduct research under his supervision and for his guidance throughout this project. He always challenged me to excel to the best of my abilities for which I am very grateful.

I would also like to thank my parents for being my source of inspiration and for teaching me the importance of hard work and dedication in life. Thank you also to Hamza for helping me see the lighthearted moments during the busiest of times.

I also would like to express my gratitude to all my fellow PTP group members, especially Angus Mathieson and Dr. David Breakey for their assistance during this project. I wish to thank Terry Runyon for her administrative expertise and help throughout this project.

I would like to thank Syncrude Canada Ltd. for sponsorship of this project. I am also especially thankful to Dr. Kevin Reid and the entire Syncrude R&D team for their support and assistance throughout this project.

Contents

List of Tables

List of Figures

List of Symbols

Symbol	Description	Units
$\dot{\gamma}$	Shear Rate	s^{-1}
ϵ	Rate of Energy Dissipated	W/kg
μ_f	Carrier Fluid Viscosity	Pa*s
μ_p	Plastic Viscosity	Pa*s
μ_r	Relative Viscosity	-
μ_w	Viscosity of Water of 25°C	Pa*s
ω	Spindle speed	rad/s
ρ_a	Density of Bitumen-Air aggregates	kg/m^3
ρ_f	Density of Carrier Fluid	kg/m^3
ρ_s	Density of Solids	kg/m^3
ρ_w	Density of Water at 25°C	kg/m^3
τ	Shear Stress	Pa
τ_y	Bingham Yield Stress	Pa
C	Overall Solids Volume Fraction	-
C_f	Final Concentration of Cu-Trien in solution	mol/L
C_i	Initial Concentration of Cu-Trien in solution	mol/L
c_i	Molar Concentration of Dissolved Ion	mol/L
C_s	Fine Solids Volume Fraction	-
C_{agg}	Concentration of Aggregates	-
C_{max}	Maximum Packing Concentration	-
d	Droplet Diameter	m

Symbol	Description	Units
T_{min}	Minimum Torque required for complete shear	N*m
v_∞	Terminal Rise Velocity	m/s
Z_i	Ionic Charge of Dissolved Ion	-
CEC	Cation Exchange Capacity	meq/100g
g	Acceleration due to Gravity	m/s^2
IS	Ionic Strength	mol/L
R	Geometry Radius	m
T	Torque	N*m
t	Time	s
W	Total Energy Input	J/kg

Chapter 1

Introduction

1.1 Background

Canada has the third largest oil reserves in the world [1]. Experts estimate that with the technology currently available, 164 billion barrels of oil can be recovered [2]. However, most of the oil present in Canada exists in the form of oil sands which present unique challenges during transportation and processing.

In surface mining operations, the oil sands are mixed with hot water and pumped through pipelines to processing plants. This process is called hydrotransport and serves two primary purposes. It promotes bitumen recovery by breaking down lumps and conditioning the slurry for separation vessels and it also provides an efficient method of transportation of large volumes of oil sands [3]. Slurry pipelines form a crucial part of the oil sands industry, accounting for millions of tonnes of solids flow per day [4].

Slurry pipelines are used in nearly all parts of the oil sands extraction process, from hydrotransport of oil sands ore to transporting middlings and underflow streams generated from separation vessels. Slurry pipelines are even used during the transportation of extraction coarse tailings to treatment plants for further processing. Figure 1.1 highlights the use of slurry pipelines throughout a typical oil sands processing plant [5]. Since slurry pipelines are crucial to the oil sands industry, it is important to understand the different types of slurries and the current models used to explain slurry flow behavior.

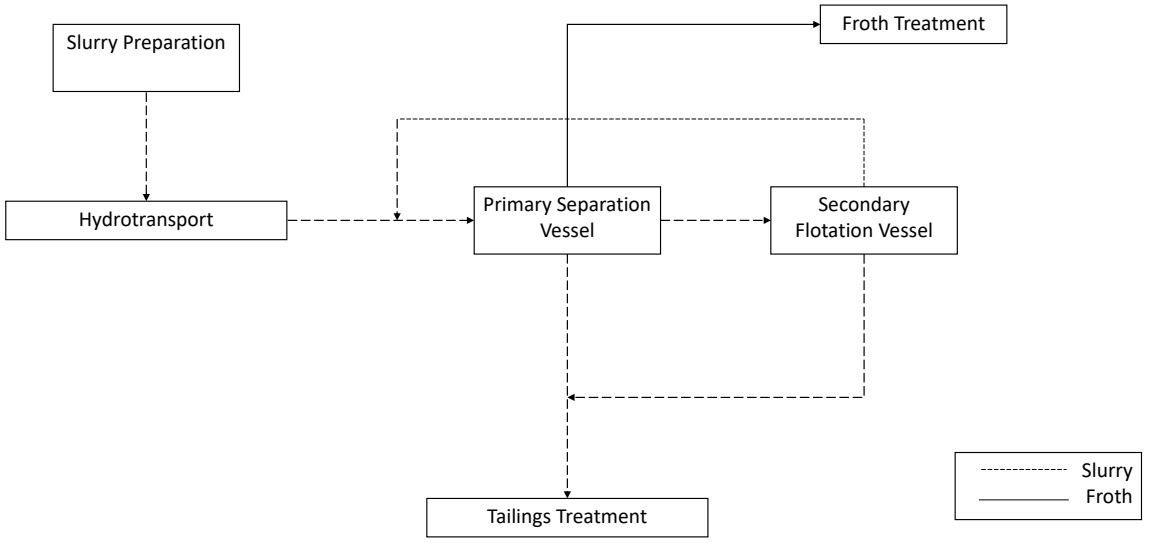

Figure 1.1: Slurry pipelines in a typical oil sands processing plant [5]

1.2 Slurry Flow in Industry

1.2.1 Types of Slurries

Slurries are broadly divided into heterogeneous and homogeneous slurries [6]. The distinctive feature of homogeneous slurries is the uniform concentration throughout the pipe during flow. The solid particles are always completely suspended in the liquid and the friction losses can be modeled using a fluid rheology approach [6]. On the other hand, the concentration of solids in a heterogeneous slurry varies depending on the vertical position in the pipe even under fully developed conditions [6]. The solids are not necessarily suspended and a minimum velocity is required to prevent particle deposition. This velocity is called the deposition velocity and is a crucial design parameter discussed in Section 1.2.3 [7]. In heterogeneous slurries, the fluid rheology alone can no longer be used to predict pressure losses in a pipeline. This is because coarse particles also contribute to frictional losses due to particle-particle interactions and particle-wall interactions [6]. Given the distinct features of heterogeneous slurries, models used for homogeneous slurries can no longer be applied and a more robust model is needed to understand flow of heterogeneous slurries.

1.2.2 SRC Two-Layer Model

The Saskatchewan Research Council (SRC) Two Layer Model was developed by Gillies et al. [8] who recognized the need for a comprehensive model to explain heterogeneous slurry flow in the oil sands industry. It was originally developed based on the results of experiments conducted by the SRC Pipeline Technology Center. It is now widely used by the oil sands industry and other industries around the world to predict pressure losses in heterogeneous slurry flow pipelines [4].

Since slurries contain both coarse and fine particles, the model divides slurries into two main components: the carrier fluid and the coarse particles. Figure 1.2 illustrates this division of components. The carrier fluid is defined as the liquid along with the fine particles (typically <44 μm)[6] that are fully suspended in the liquid. The fine particles alter the liquid's density and viscosity and hence, together with the liquid medium, are considered one: the carrier fluid. The coarse particles, on the contrary, are assumed to be suspended in the carrier fluid [7].

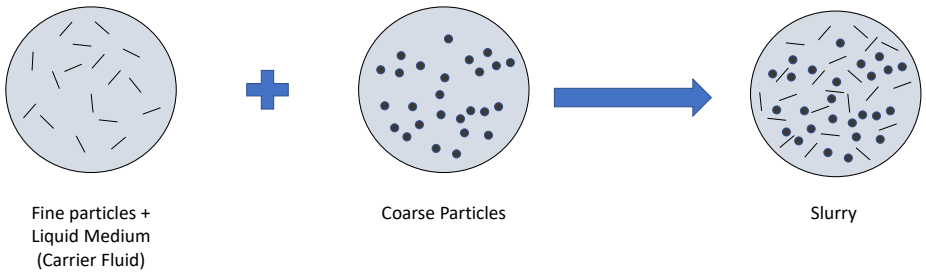

Figure 1.2: The SRC Two-Layer Model (adapted from Sanders and Gillies [6])

One of the key input parameters for the model is the carrier fluid viscosity, which is discussed in the following section.

1.2.3 Importance of Carrier Fluid Viscosity

As mentioned previously, the SRC Two Layer Model is widely used by industries around the world to design heterogeneous slurry pipelines [4]. This model provides engineers with two key design parameters:

1. Deposition Velocity
2. Pressure Gradient

The deposition velocity is the velocity at which solid particles begin to form a stationary deposit at the bottom of a pipe. This is typically undesirable and thus considered to be the lower limit of operating velocities for pipelines [7]. Failure to operate above the deposition velocity can cause increased pipeline wear and plugging of pipelines, leading to shutdowns [9]. The SRC Two Layer Model also provides engineers with accurate predictions of pressure losses in a slurry pipeline. This is also a crucial design parameter. The pressure loss is needed to accurately determine pumping requirements for pipelines. Inadequately sized pumps can also increase operating costs greatly because of energy wasted while pumping fluids at velocities much higher than the minimum required. Operating at unnecessarily high velocities can also increase pipeline wear rates due to increased particle-wall collisions [10]. This can lead to pipeline failures and large financial losses [11]. The carrier fluid viscosity can have a drastic effect on both these parameters. Higher carrier fluid viscosities generally lead to lower deposition velocities for heterogeneous slurries as illustrated in Figure 1.3 (replotted with data from Smith [12]). This means that slurries with more viscous carrier fluids have a lower deposition velocity and can be operated at lower velocities. On the other hand, higher carrier fluid viscosities also provide somewhat larger pressure gradients in pipelines. This information is crucial when determining pumping requirements for pipelines. The SRC Two Layer Model is the industry standard in designing slurry pipelines and the carrier fluid viscosity forms a key part of the model [4]. Hence, it is important to provide reliable and accurate carrier fluid viscosity values to ensure proper applications of the SRC Two Layer Model.

The carrier fluid viscosity also plays a key role in the performance of separation vessels at an extraction plant. Once the oil sand slurry has been transported to the processing plant using pipelines, it is sent to a primary separation vessel to begin extracting bitumen. In the hydrotransport pipeline, bitumen droplets attach to air bubbles and these aggregates

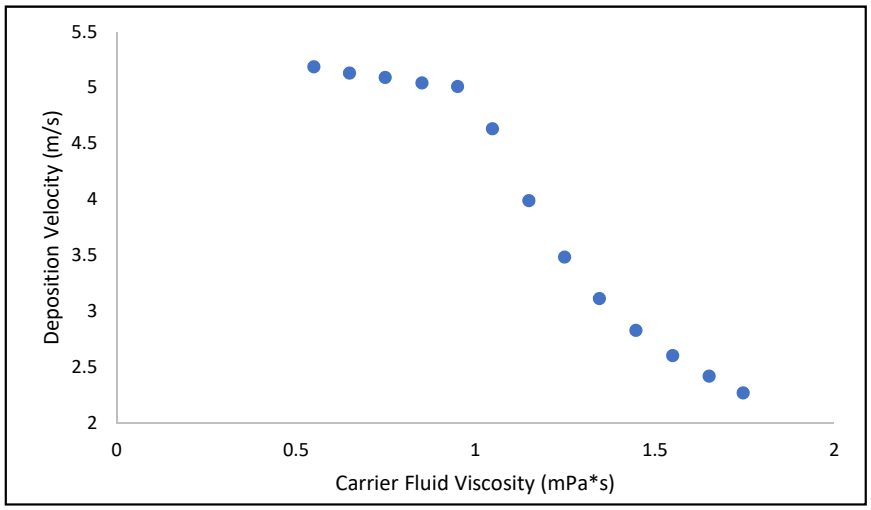

Figure 1.3: Carrier fluid viscosity and deposition velocity of 180 μm coarse particles in a 30% slurry through a 0.68 m pipeline. Replotted with data from Smith [12].

rise to the top of the vessel creating a froth which is recovered for further processing. The flotation of bitumen has been shown to be dependent on the viscosity of the carrier fluid [5]. Highly viscous carrier fluids hinder the flotation of bitumen which leads to poor recovery [5]. Hence, a process aid may be introduced to lower viscosity and optimize bitumen froth recovery [13]. This makes accurate carrier fluid viscosity values essential to the proper performance and operation of separation vessels.

1.3 Challenges to Determining Carrier Fluid Viscosities

Ideally, a parameter as important as the carrier fluid viscosity would be measured directly on site especially since the viscosity of the carrier fluid can change rapidly depending on the quality of the ore being mined. This, however, is impractical for many reasons. Current technology mostly limits the measurement of carrier fluid viscosities to off-line techniques which require samples to be extracted from pipelines and sent for analysis. The necessary equipment and personnel training is also often lacking on site. For these reasons, operations' personnel resort to empirical correlations to predict carrier fluid viscosities.

The issue with the use of empirical correlations is the inadvertent extrapolation which has occurred over time. For example, one of the most commonly used equations by

industry is [14]:

$$\mu_r = \frac{\mu_m}{\mu_l} = \exp(12.5 * C_s) \tag{1.1}$$

where μ_r is the viscosity of the carrier fluid relative to the viscosity of water at 25°C and C_s is the concentration of fine solids in the carrier fluid. While this equation is currently used in the oil sands industry to predict carrier fluid viscosities for all heterogeneous slurries, it was originally obtained using rheology measurements on mature fine tailings [7]. Equation 1.1 was intended to be an approximation, especially due to the large amount of scatter in the experimental results [7]. Accordingly, the authors strongly recommended future work be completed to account for other factors that may be causing the scatter in the MFT rheology measurements [6].

A study was completed by Smith [12] to expand Equation 1.1 by accounting for the aggregating behavior of particles in oil sand slurries. The results obtained by Smith [12] reiterated the need to include factors in addition to solids concentration when predicting carrier fluid viscosities. This project aims to build on the work conducted by Smith [12] and incorporate factors to account for particle and fluid properties when predicting carrier fluid viscosities.

1.4 Project Objectives

As mentioned previously, there are significant challenges to determining carrier fluid viscosities. This presents a significant hurdle to effective implementation of the SRC Two Layer Model in designing slurry pipelines. Hence, the objectives of this project are:

1. To measure carrier fluid viscosities of oil sand slurries.
2. To identify and analyze particle and fluid properties which contribute to the carrier fluid viscosity.
3. To develop an empirical model which can be used by industry to predict carrier fluid viscosities with reasonable accuracy.

The following chapter discusses, in greater detail, the challenges currently facing industry in determining carrier fluid viscosities. Current literature and recent research on carrier fluid viscosities are also discussed and critically analyzed to identify additional

factors to account for particle and fluid properties that contribute to the carrier fluid viscosities.

Chapter 2

Literature review

2.1 Introduction

Viscosity models for slurries have been incrementally expanded over time but are inapplicable or too inaccurate for effective application in the oil sands industry. The importance of accurate carrier fluid viscosity predictions is discussed in detail in this chapter. Also, the shortcomings and reasons behind the inaccurate predictions of currently used models to predict carrier fluid viscosities are analyzed. The factors necessary to improve current models are discussed, along with the theoretical impact of each factor on the viscosity of the carrier fluid. Finally, the different techniques available for measuring viscosity along with the advantages and disadvantages of each are also explained in this chapter.

2.2 Carrier Fluid Viscosity in Industry

As discussed previously, the oil sands present unique challenges in transportation and processing. The carrier fluid viscosity plays a key role in both operations. The SRC Two Layer Model is used to design and optimize slurry pipelines. The carrier fluid viscosity is a crucial input parameter for the SRC Two Layer Model and has an impact on key design parameters such as the deposition velocity and pressure gradient in slurry pipelines. These parameters are essential to proper design and operation of pipelines because they establish the boundaries of acceptable operating conditions [7]. Operating below the deposition velocity can lead to plugging of pipelines which may force shutdowns and losses in revenue [4]. On the other hand, operating too far above the deposition velocity leads to

higher operating costs and inefficient use of energy. This can also lead to increased pipeline wear rates due to higher particle-wall collisions [10]. Thus, engineers strive to operate at the optimum velocity to minimize deposition and cost while maximizing throughput. Hence, accurate carrier fluid viscosity values must be available to engineers to effectively apply the SRC Two Layer Model.

The carrier fluid viscosity also plays a key role in the processing plant once the slurry has been successfully transported from the ore. Almost all plants use primary separation vessels (PSV) for bitumen extraction from the oil sands slurries [15]. The primary separation vessels rely on the difference in densities to separate the bitumen-air aggregates from coarse particles. The more dense coarse particles settle to the bottom of the vessel whereas the less dense bitumen-air aggregates rise to the top of the vessel. The bitumen droplets must rise through the carrier fluid to form a froth which is then collected for further treatment [15]. The Stokes terminal rise velocity for spherical droplets of diameter d in laminar flow is given by [5]:

$$v_\infty = \frac{(\rho_a - \rho_f) g d^2}{18 \mu_f} \tag{2.1}$$

As seen in equation 2.1 the rise velocity (v) is inversely proportional to the viscosity of the carrier fluid (μ_f). More detailed versions of equation 2.1 are also available to account for hindering effects and non-ideal systems [5]. Equation 2.1 highlights the crucial role of the carrier fluid viscosity in the flotation of bitumen droplets. Schramm [13] conducted experiments on a Syncrude pilot separation vessel and found a drastic difference in the rise velocity of bitumen droplets based on the viscosity of the carrier fluid. In the central region of the vessel, which is critical for separation efficiency, bitumen droplets required 100 minutes to rise to the froth at a carrier fluid viscosity of 110 mPa*s. On the other hand, the same droplets required only 5 minutes to float to the froth region when the viscosity was reduced to 4.0 mPa*s using a processing aid [13]. This is crucial because the residence time for primary separation vessels is approximately 45 minutes [13]. More viscous carrier fluids could lead to incomplete bitumen recovery and large volumes of bitumen being lost in the middlings and underflow streams of separation vessels. Secondary flotation vessels, which are used to further extract bitumen from PSV middlings streams, also rely on the flotation of bitumen by attachment to air bubbles [5]. Hence, accurate viscosity values would help to ensure more optimal performance of all separation vessels and maximize

overall bitumen recovery for an entire processing plant.

2.3 Viscosity Correlations

The SRC Two Layer Model requires accurate carrier fluid viscosities for effective design of slurry pipelines. Similarly, accurate carrier fluid viscosities are also necessary for optimum design and operation of separation vessels at a processing plant. The best way to accomplish this would be to perform viscosity measurements on site. As discussed earlier, this is unrealistic for multiple reasons. Viscosity values can vary rapidly depending on the type of ore being processed at the time and presently no techniques exist to provide on-line real time viscosity values. This means that samples must be collected from a pipeline and sent for analysis which can take hours or days. This makes real time optimizations unrealistic. Also, conducting viscosity measurements accurately requires specific equipment and well-established procedures, which may not be available on site. Hence, engineers in industry resort to the use of empirical correlations to determine carrier fluid viscosities.

Carrier fluid viscosity is often reported in dimensionless terms, relative to the viscosity of the suspending pure liquid eg. water:

$$\mu_r = \frac{\mu_f}{\mu_w} \tag{2.2}$$

where μ_r is relative viscosity, μ_f is the carrier fluid viscosity and μ_w is the viscosity of water at the process temperature. One of the earliest equations for viscosity of dilute solid-liquid suspensions was derived by Einstein in 1906 [16]. This equation was derived under very strict limitations to the solid particles: non-interacting, rigid and spherical. The strict constraints required for this equation severely limit its applications in real-world situations. Einstein's equation is written as:

$$\mu_r = 1 + 2.5C \tag{2.3}$$

where C is the concentration of particles in suspension and μ_r is the relative viscosity. Since then, many researchers have attempted to expand the Einstein equation to higher concentrations for better applications in industry [17–21]. However, most of this work has been conducted on spherical particles. The carrier fluid in oil sand slurries, on the other

hand, primarily contains clay particles which are non-spherical and highly aggregating. Work done by Broughton and Windebank [22] highlighted this key difference and showed that viscosities of kaolin clay suspensions disagreed strongly with the viscosities predicted using Equation 2.3 due to their aggregating behavior [22]. They concluded that the Einstein equation should only be used for large spherical particles where no particle interactions occur [22]. Since then, many studies have been conducted to expand the Einstein's equation to flocculating particles. In 1999, A.D. Thomas conducted experiments with mineral ore slurries and introduced an experimentally determined constant to account for particle interactions [23]. An exponential relationship was found between the overall fines concentration[23]:

$$\mu_r = \exp(\frac{C_s}{BC_{max}}) \tag{2.4}$$

The need for experiments to determine the constant in Equation 2.4 emphasizes the complicated interactions occurring in slurries with flocculating particles. A similar exponential relationship was found by Shook et al. [7] when conducting viscosity measurements on mature fine tailings (MFT). The equation derived by Shook et al. [7] is:

$$\mu_r = \exp(12.5C_s) \tag{2.5}$$

where C_s is the volume fraction of fine particles less than 44 μm and μ_r is relative viscosity as defined in Equation 2.2 [7]. This equation is often used to determine carrier fluid viscosities in the oil sands industry. However, Sanders and Gillies [6] strongly advise against the indiscriminate application of this equation for multiple reasons. First, the equation was developed only using mature fine tailings and using it for all oil sands slurries without any corrections would be inappropriate [6]. Second, the viscosity measurements also had a large degree of variability despite numerous MFT samples having identical solids concentration [6, 7]. This strongly suggests the presence of other factors, besides fine solids concentration, contributing to the viscosity of the carrier fluid. More recently, Asadi Shahmirzadi [24] conducted viscosity measurements on pure clay and water mixtures and correlated viscosity with the concentration of aggregates instead of fine solids. The correlation derived by Asadi Shahmirzadi [24] is:

$$\mu_r = 17.7C_{agg} + 1 \tag{2.6}$$

where C_{agg} is defined as the concentration of aggregates in the fluid. The strong correlation found between concentration of aggregates and viscosity proves the importance of particle interactions in flow behavior of clay and water mixtures. However, the work done in this study was limited to pure kaolin clay in water which made it inapplicable to oil sands slurries. Work done by Smith [12] confirmed that assumptions of pure kaolin clay and pure water were not acceptable for carrier fluids in oil sands slurries. Smith [12] concluded that unlike in idealized clay-water suspensions, additional factors like water chemistry can vary greatly in carrier fluid samples. The viscosity results found by Smith [12] are shown in Figure 2.1. It is clear that the viscosity is being affected by factors besides fine solids concentration. Smith [12] used the concentration of calcium ions in addition to the overall fines solids concentration to predict carrier fluid viscosities:

$$\mu_r = 1.2 + 30.0C_s - 1356.8[Ca^{2+}] \tag{2.7}$$

However, the poor fit of the model and limited sample set suggest that there remains a need for incorporation of other factors that contribute to the viscosity of carrier fluids. Unfortunately, no other equations currently exist to account for factors besides fine solids concentration when predicting carrier fluid viscosities. This study aims to expand previous work by Smith [12] by incorporating two factors besides fine solids concentration when predicting carrier fluid viscosities: clay activity and water chemistry. These factors and their respective impacts on viscosity are discussed in the following sections.

2.4 Clay Activity

Although kaolinite is commonly accepted as the model clay for oil sands [24], studies have shown significant diversity in the overall clay compositions. Analyses conducted by Kaminsky et al. [25] showed that the composition of clays in oil sand slurries can vary significantly between streams in the extraction process. The variation in clay composition can be clearly seen in Figure 2.2. Additionally, numerous studies conducted over the years have reported different clay composition of oil sands depending on the sample type and ore location [25]. While most literature suggests kaolinite to be the predominant clay in oil sands, the results on the presence and composition of mixed layer clays and other clays have varied. Hence, in the interest of an all-encompassing viscosity correlation, one cannot

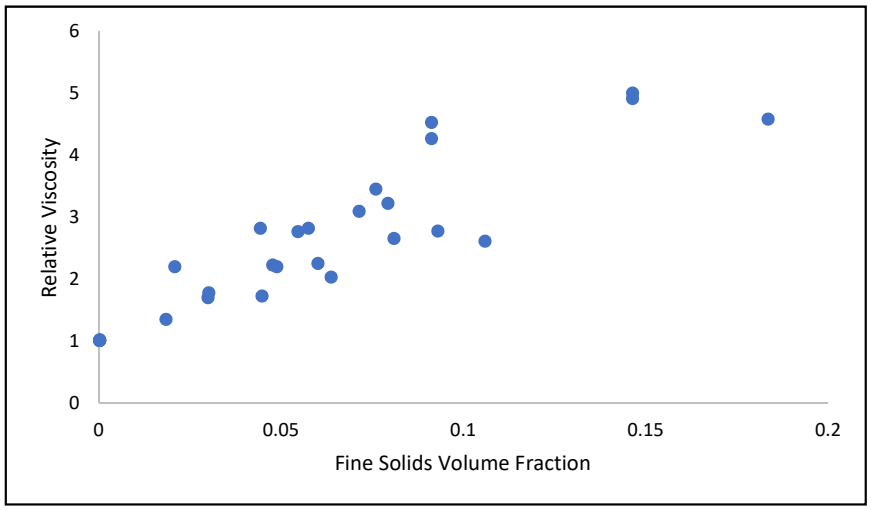

Figure 2.1: Carrier fluid viscosity and fine solids concentration for oil sand slurries found by Smith [12]. Replotted with data from Smith [12].

ignore the effects of the different clays present. This fact becomes even more important once the contribution of different clays is closely considered. Specifically, smectite, is known to significantly alter behaviors of slurries. Smectite is a three-layered clay as opposed to two-layered clays like kaolinite and illite [5]. Isomorphic substitution occurs in all clay particles which provides a positive or negative surface charge to the clays. This isomorphic substitution is relatively small for kaolinite particles and yields a low surface charge [5]. On the other hand, in smectite particles, isomorphic substitution occurs at multiple layers leading to a stronger negative surface charge on smectite particles [5]. The isomorphic substitution occurring in smectite weakens the interlayer bonding of the particles. This allows for more ion exchange in the interlayer, leading to swelling behavior and much higher cation exchange capacities [5].

Swelling behavior in smectites has been well documented in the literature. There are two different swelling mechanisms: hydration and osmotic swelling [26]. Hydration swelling involves the adsorption of water molecules on to the interlayer surfaces by hydrogen bonding. The trapped water increases the layer spacing from 10Åto 20Å. Osmotic swelling occurs in smectites saturated with cations. The driving forces behind osmotic swelling are surface charge density and localization. This type of swelling leads to interlayer spacing increases as high as 40Å[27].

The high swelling and high exchange capacities of smectite allow for more adsorption

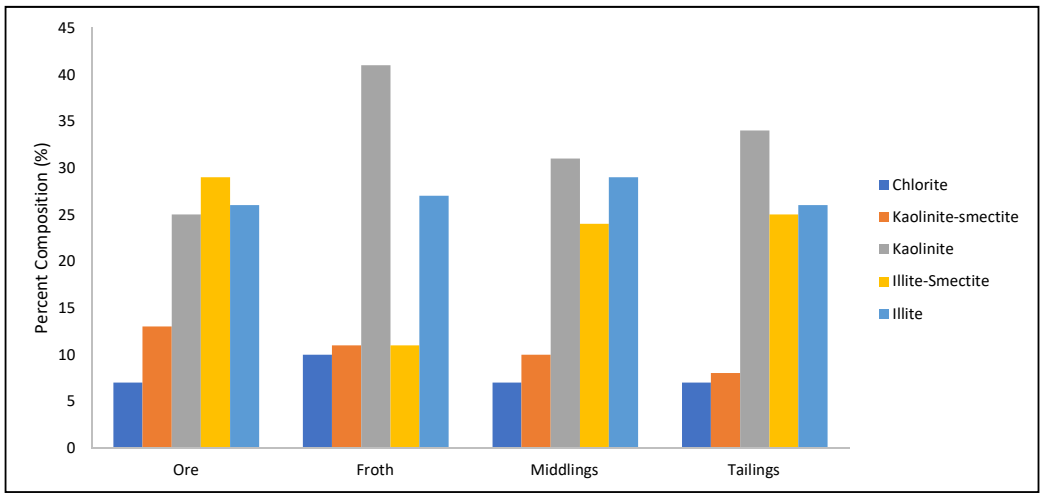

Figure 2.2: Composition of clay species in oil sands at different parts of a process [25]

of cations and larger volumes of trapped water which increases the apparent volume of clay in slurries [28]. The effects of these properties on viscosity are extreme. Studies conducted by Kasperski et al. [29] showed that even the presence of low volumes of swelling clays in a suspension significantly increased its viscosity despite constant overall solids concentrations. Figure 2.3 shows viscosity measurements conducted with varying compositions of montmorillonite (a category of swelling clays) and kaolinite clays in water. The effects of swelling clays on viscosity are clear. Similar trends were observed by Kameda and Morisaki [30].

In order to account for the presence of smectite and other swelling clays in oil sands, the cation exchange capacity (CEC) of the sample must be studied. The CEC has been established to be an accurate representation of the level of isomorphic substitution taking place in a clay [5]. The CEC of kaolinite and other non-swelling clays is in the range of 3-5 (meq/100g) whereas for swelling clays, like smectite, the CEC can be as high as 150 (meq/100g) [31]. The techniques to measure CEC are discussed in the following section.

2.4.1 Measurement Techniques

Due to the significant impacts of clay activity on processing units, numerous studies have been conducted to analyze clay activity. The most common techniques involve exchanging

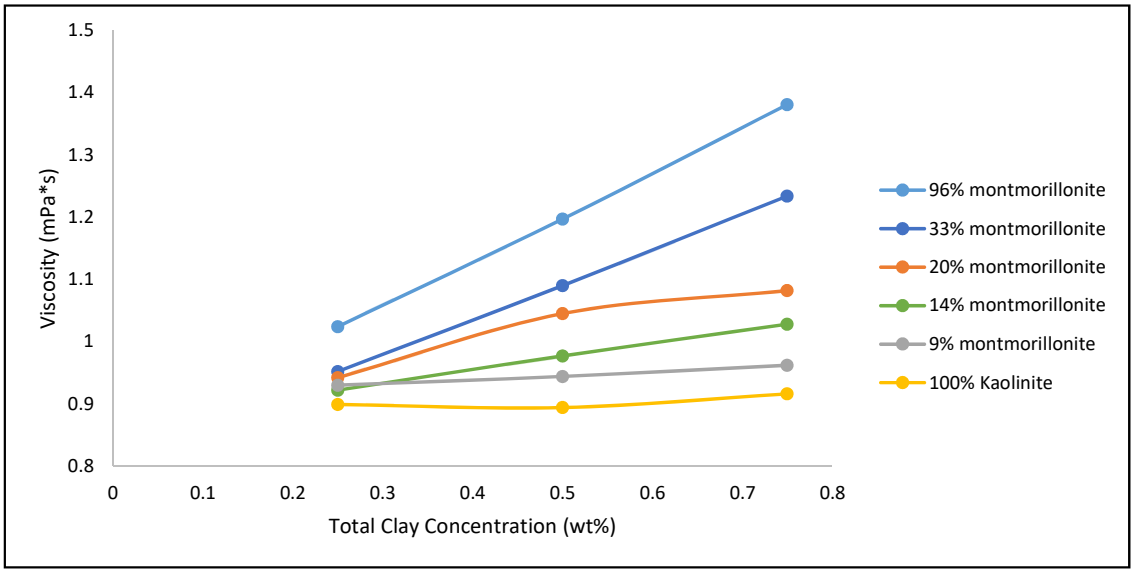

Figure 2.3: Viscosity of varying compositions (by mass) of montmorillonite and kaolinite suspensions in 0.010M of NaOH at 25°C [29]

cations from ammonium acetate or copper(II)-trien sulfate with the naturally occurring ions on clay surfaces to determine CEC [32]. Another technique uses methylene blue dye to determine an equivalent index [33]. This technique measures the amount of methylene blue dye absorbed onto the surfaces of clay particles through titration. The particles are dispersed and titration is conducted until no more dye is absorbed onto the surface of the clays. This endpoint is detected using the halo method. A drop of the titrated solution is placed on a filter paper and the operator attempts to identify a blue halo around the drop. A permanent halo is indicative of the endpoint and that complete absorption of methylene blue has occurred. A temporary halo or no halo are indications that the endpoint has not been reached and titration is continued until a permanent halo appears [33]. The final volume of titration at the end point is then used to calculate the amount of methylene blue absorbed on the surface of the clays. As expected, this endpoint method has a very high degree of operator bias and makes it very difficult to provide repeatable data. An analysis conducted by Currie et al. [34] found that endpoint detection was one of the leading causes of error in the methylene blue procedure. Hence, an alternative procedure was used in this study.

This project utilizes copper triethylenetetramine (Cu-trien) to exchange naturally present cations on the surface of the clays with the copper complex ions: $Cu(trien)^{2+}$ [35]. This method was originally developed by Meier [32] in 1999 and has since been widely applied by industry due to the ease and simplicity of the procedure. The procedure used in this study specifically, was developed by Syncrude R&D. One of the biggest advantages of the copper-trien method is that it allows for the use of a spectrometer to determine the concentration of copper-trien ions remaining in solution after absorption on clay surfaces is complete [36]. The particles to be studied are dispersed and mixed with excess copper trieylenetetramine solution. The high affinity of copper-trien ions for clay particles allows for rapid exchange of ions to take places [32]. Sodium bicarbonate acts as a pH buffer during experimentation and helps maintain dispersion of particles. Finally, an absorbency reading is taken of the solution to determine the amount of ions that were absorbed on to the clays. The use of a spectrometer removes the significant amount of operator error associated with other procedures like the methylene blue index. The exchange capacity is then calculated using:

$$CEC = \frac{2 * (C_i - C_f) * m_{liquid}}{m_{sample} * \rho_{liquid}} * 100 \tag{2.8}$$

where C_i and C_f are the initial and final concentration of copper-trien in solution. The mass of the liquid used for dispersion and mass of solids analyzed are represented by m_{liquid} and m_{sample} respectively.

2.5 Water Chemistry

Another important factor in carrier fluid rheology is water chemistry, which has been shown to be a crucial factor in viscosity of many clay and water suspensions [37, 38]. Work done by Asadi Shahmirzadi [24] showed the effect of pH on aggregation and dispersion behavior of clays. The water pH significantly impacts the surface charges of clay particles. This is because the surface charge on the edges of clay particles is strongly dependent on pH [5]. At low pH conditions, the surface charges on the edges turns positive due to protonation, which causes strong attraction to the permanent negative charges on the basal layers [5]. This leads to strong aggregation tendencies of the clay particles. At high pH conditions, the surface charges on the edges turns negative due to de-protonation and this

leads to repulsion with the permanent negative charges on the basal layers. This causes particle dispersion [39]. The aggregation and dispersion behavior of particles is illustrated in Figure 2.4. Under aggregated conditions, clay particles occupy much larger volumes in mixtures and trap additional water within their structures. This causes an increase in the viscosity of the suspension. Asadi Shahmirzadi [24] showed the drastic effect pH can have on the aggregation behavior of clay particles and in turn the viscosity of clay and water mixtures. This effect can be seen in Figure 2.5.

Similarly, previous work done by Smith [12] showed that the presence of divalent cations can affect viscosities of carrier fluid samples. This is because divalent ions affect the surface charge of clay particles. Divalent ions like Ca^{2+} perform the same function as hydrogen ions during protonation by adsorbing on to the surface of the clays. This compresses the negative electric double layer and allows the van-der-Waals attractive force to dominate leading to aggregation [39]. This in turn leads to an increase in viscosity as the aggregates become larger and more water becomes trapped in their structures. Work done by Smith [12] also found that process water can contain high concentrations of divalent ions like calcium and magnesium which can drastically affect viscosities. Thus, it is important to account for water chemistry of carrier fluid samples when determining viscosity. The different techniques and methods available to measure viscosity are analyzed in the following section.

2.6 Rheometry

2.6.1 Techniques

The two techniques most commonly used in industry to measure viscosities are based on laminar tube flow or concentric cylinder shearing [7]. The primary advantage to concentric cylinder rheometers over laminar pipe flow is the easier setup. Concentric cylinder rheometers require less space and sample volume to conduct high quality viscosity measurements. However, a disadvantage of concentric cylinder rheometers is the limited range of shear stress available. In order to extrapolate results from concentric cylinder rheometers to industrial scale pipelines, it is important to maintain shear stress in the same ranges as industrial applications [41]. This is often a challenge due to device constraints. Also, special care must be taken to ensure that flow remains laminar throughout a

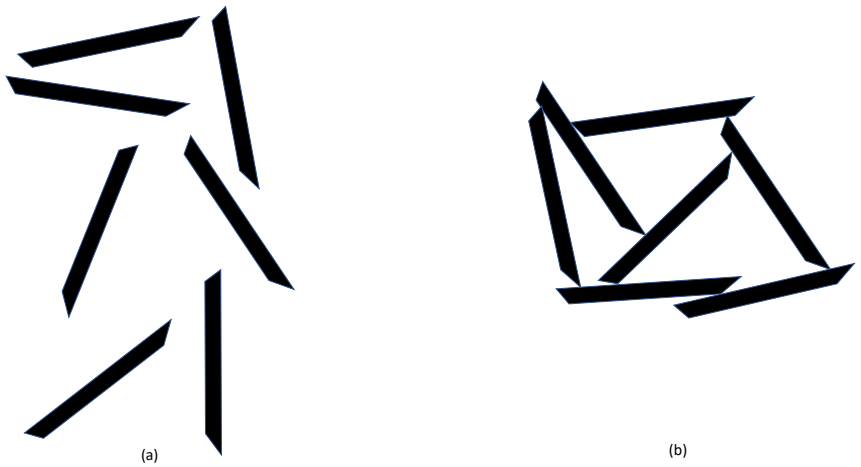

Figure 2.4: (a) Dispersed clay particles at high pH conditions. (b) Aggregated clay particles at low pH conditions [40]

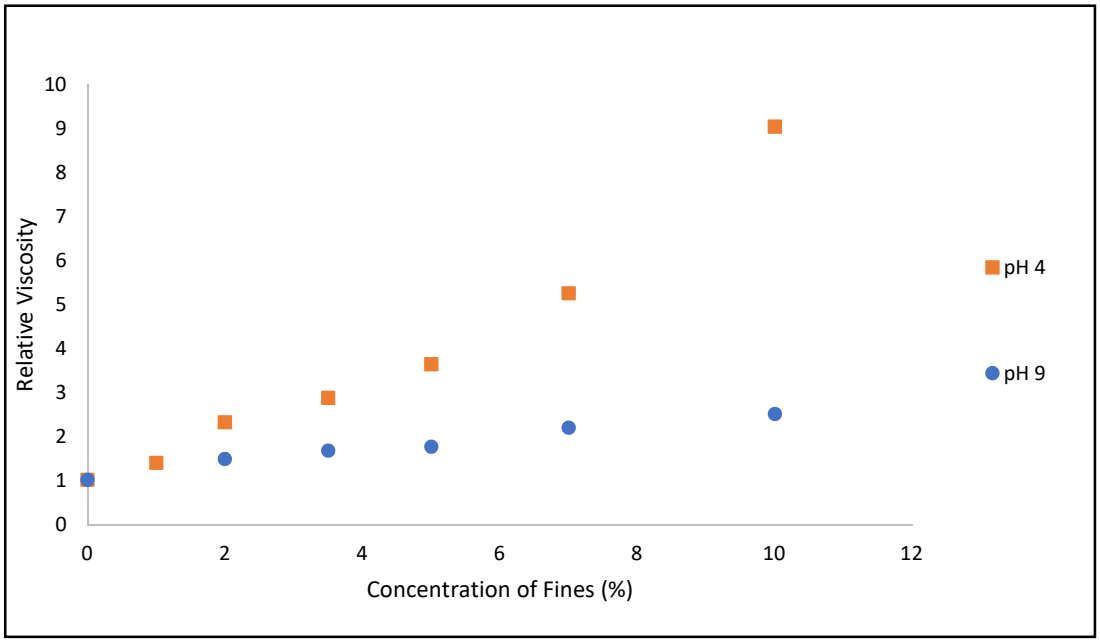

Figure 2.5: Effect of pH on viscosity of clay and water mixtures. Replotted with data from Asadi Shahmirzadi [24].

measurement. This is required in order to avoid secondary flows, known as Taylor vortices, from occurring in the fluid which lead to erroneous viscosity values [12]. Another challenge with concentric cylinder rheometers is that users must take deliberate steps to eliminate any time dependent behavior of fluids which would not be occurring in industrial pipelines. Hence, Shook et al. [7] recommend conducting confirmatory measurements using pipe flow tests prior to industrial application. The ease of operation and low sample volume requirement make concentric cylinder rheometers most common for rheometry. The concentric cylinder rheometers operate on the basis of a rotating inner geometry and a stationary outer cup. The rotating geometry provides the shear to the fluid at a specified spindle speed. An overhead motor measures the torque required to rotate the geometry at each spindle speed and shear stress and shear rates are then determined. Different geometries are available for various applications. The two most commonly used geometries for fluids are the DIN concentric cylinder viscometer (CCV) and double gap geometries. The DIN concentric cylinder geometry is ideal for fluids with medium range viscosities [42]. It involves a rotating spindle inside of a stationary cup as seen in Figure 2.6. The double gap geometry is ideal for fluids with very low (water-like) to medium range viscosities [42]. The double gap geometry uses two moving walls sandwiched between two stationary walls of the cup as seen in Figure 2.6. The primary advantage of the double gap geometry is that higher torque values can be achieved for the same spindle speeds compared to DIN concentric cylinders, hence delaying the onset of turbulence [42]. This leads to more accurate viscosity measurements for fluids with lower range viscosities.

2.6.2 Fluid Models

In order to conduct viscosity measurements, a fluid model must be applied to the sample. Numerous fluid models exist to explain different types of fluid behavior. Figure 2.7 shows some commonly used fluid models [43]. Most clay-water suspensions have been known to behave as Newtonian fluids at low concentrations and Bingham fluids at higher concentrations [24]. Newtonian fluids exhibit a linear relationship between the shear rate being applied and shear stress exhibited by the fluid. The viscosity is then determined using [44]:

$$\mu = \frac{\tau}{\dot{\gamma}} \tag{2.9}$$

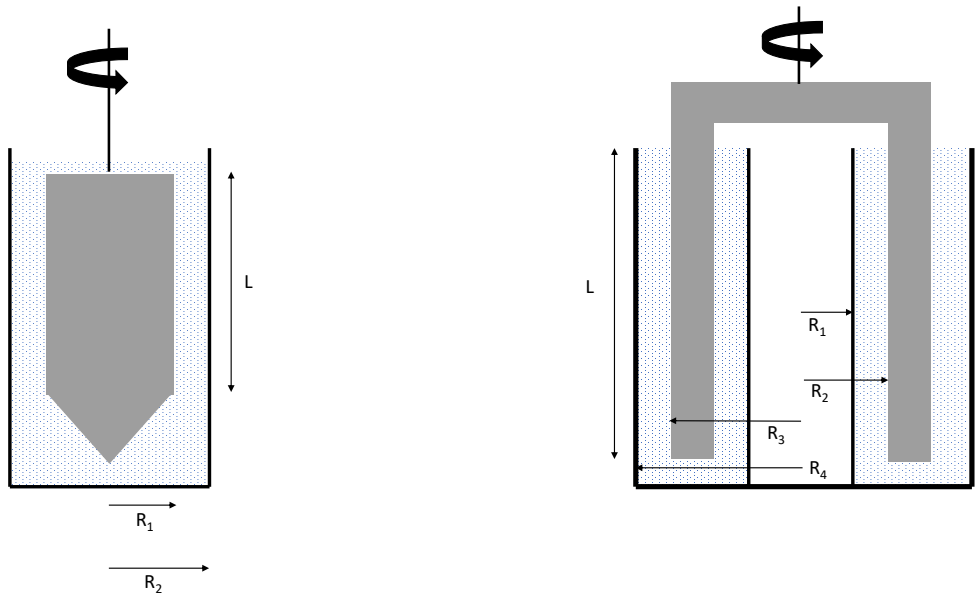

Figure 2.6: DIN concentric cylinder (CCV) and double gap geometries.

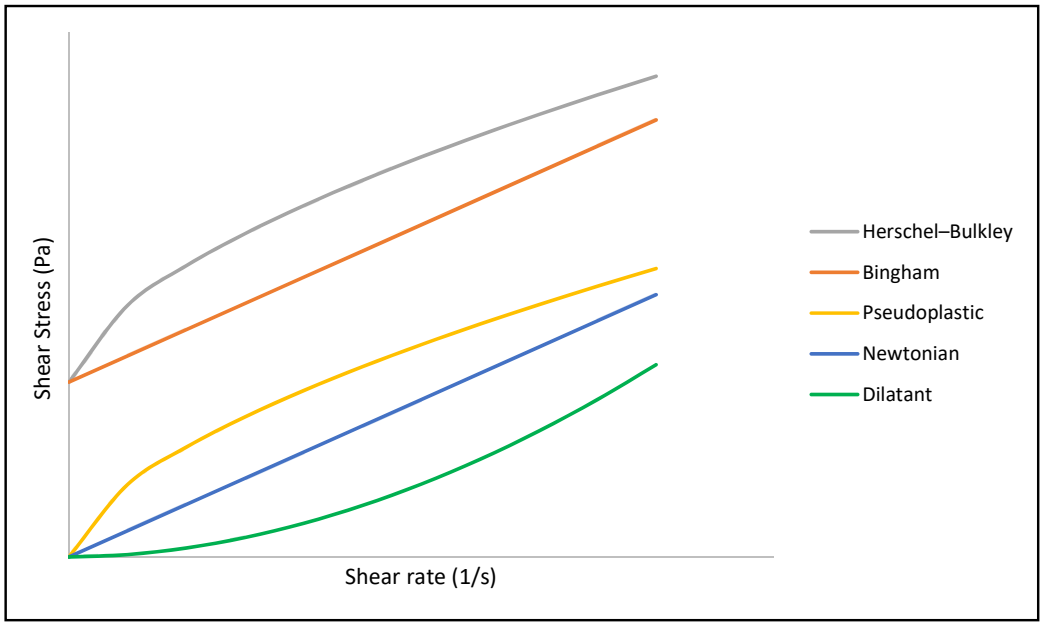

Figure 2.7: Commonly used rheological models

where τ is defined as shear stress and $\dot{\gamma}$ is defined as the shear rate. Since rheometers measure torque and spindle speed, not shear stress and shear rate, it is important to consider the equivalent equation in terms of torque and spindle speed. For DIN concentric cylinders this is given by [7]:

$$\omega = \frac{T}{4\pi L\mu}[\frac{1}{R_1^2} - \frac{1}{R_2^2}] \tag{2.10}$$

where ω is the spindle speed in rad/s and T is the torque in N*m. The radii (R_1 and R_2) and length L are defined in Figure 2.6. For double gap geometries, stress and strain constants, K_σ and $K_{\dot{\gamma}}$ are used [45]:

$$\tau = T * K_\sigma \tag{2.11}$$

$$\dot{\gamma} = \omega * K_{\dot{\gamma}} \tag{2.12}$$

where

$$K_\sigma = \frac{1}{2\pi L c_L (R_2^2 + R_3^2)} \tag{2.13}$$

$$K_{\dot{\gamma}} = \frac{1}{1 - \frac{R_3^2}{R_4^2}} + \frac{1}{\frac{R_2^2}{R_1^2} - 1} \tag{2.14}$$

where c_L is a geometry constant (R_2/R_1). The radii and length are measured as shown in Figure 2.6. The constants defined in Equations 2.13 and 2.14 were used in this study when analyzing viscosities for the double gap geometry. It has been shown in previous studies that the manufacturer recommended constants assume Newtonian fluid behavior during viscosity measurements [46, 47]. Given the slight non-Newtonian behavior shown by the carrier fluid samples, the manufacturer recommended constants were utilized in this study and the exact impact of the constants remains unknown. It is recommended that future work be conducted to investigate, in depth, the effect of these constants on viscosities of non-Newtonian fluids.

As mentioned previously, it is important to maintain laminar flow in a concentric cylinder and avoid Taylor vortices. Shook and Roco [41] determined a critical angular velocity at which the onset of Taylor vortices can be expected. This velocity is given by

$$\omega_{crit} = \frac{45\mu}{[\frac{R_1+R_2}{2}]^{0.5} * (R_2 - R_1)^{1.5}\rho} \tag{2.15}$$

where μ and ρ are the viscosity and density of the fluid respectively [41, 48]. Although this equation is primarily designed for use with Newtonian fluids, it has been used as a guideline to look for the onset of Taylor vortices in Bingham fluids, with reasonable accuracy [12].

As mentioned previously, clay and water mixtures have also been known to behave as Bingham fluids at higher concentrations. For such fluids, the relationship between shear stress and shear rate is:

$$\tau = \mu_p \dot{\gamma} + \tau_y \tag{2.16}$$

where μ_p is the plastic viscosity and τ_y is the Bingham yield stress [44]. Bingham fluids follow a linear relationship between shear stress and shear rate after the yield stress is overcome as seen in Figure 2.8. Equation 2.10 is derived for Bingham fluids to include a yield stress term[7]:

$$\omega = \frac{T}{4\pi L \mu_p}\left[\frac{1}{R_1^2} - \frac{1}{R_2^2}\right] - \frac{\tau_y}{\mu_p} \ln\left[\frac{R_2}{R_1}\right] \tag{2.17}$$

Another factor to consider for concentric cylinder rheometry is incomplete shearing across the gap when dealing with yield stress fluids. This occurs when the shear stress being applied is less than the yield stress. In order to avoid this, the torque values must be maintained above a value which provides a shear stress higher than the yield stress at the outside cup wall [41]. For DIN concentric cylinders, this can be determined using:

$$T_{min} = 2\pi L \tau_y R_2^2 \tag{2.18}$$

Equation 2.18 is also used in this project to estimate the minimum torque required to operate above the yield stress for double gap geometries by replacing R_2 with R_4.

2.7 Summary of Key Findings

The carrier fluid viscosity has been established as a crucial parameter in designing pipelines and operating process vessels. The carrier fluid viscosity plays a major role in determining the pressure loss in pipelines and is necessary to calculate the minimum operating velocity and prevent particle deposition. The carrier fluid viscosity also plays a crucial role in the flotation of bitumen-air aggregates during bitumen extraction from oil sands. Despite the importance of the carrier fluid viscosity, the literature provides limited equations to

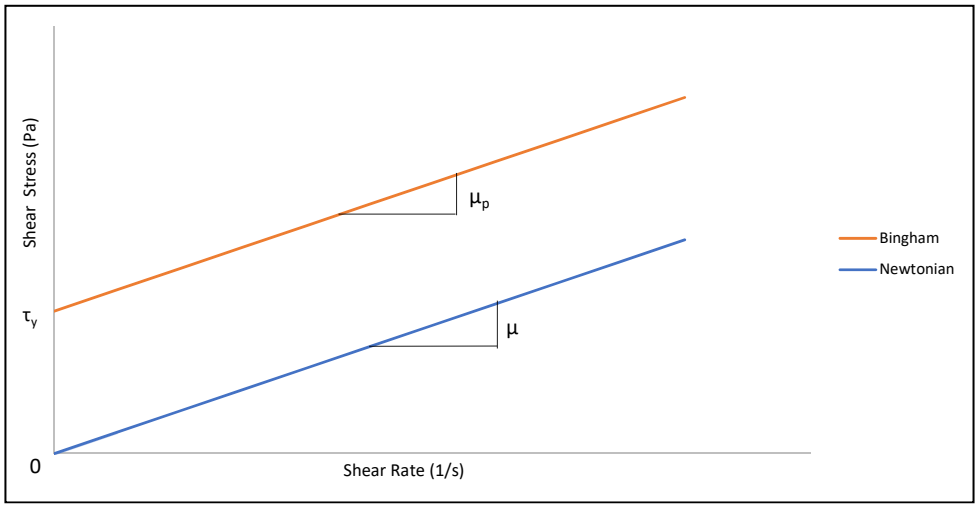

Figure 2.8: The Bingham Yield Stress

industry professionals to predict viscosities. Work has been done in the past to show that the viscosity of the carrier fluid is not accurately represented by the fine solids concentration. Viscosities often vary greatly despite similar fine solids concentrations. Previous work with clay suspensions suggests that the presence of active clays can cause large increases in viscosities at similar solids concentrations and should be accounted for using a clay activity parameter. The aggregating behavior of particles has also been well documented and shown to be strongly impacted by water chemistry conditions. Hence, the current study focuses on quantifying the effects of clay activity and water chemistry on viscosity. This will then be used in conjunction with the effects of fine solids concentrations to accurately predict carrier fluid viscosities. The viscosity measurements are conducted with two different geometries in a rotational rheometer. The differences in the two geometries and techniques to interpret results from each have been outlined.

Chapter 3

Materials and Methods

3.1 Industrial Samples

The samples used for analysis were provided by Syncrude Canada Ltd. from their North Mine plant. The process used by the Syncrude plant and streams used to collect samples are shown in Figure 3.1. The process uses primary separation vessels (PSV) to extract bitumen froth. The froth is then sent to deaerators and subsequently to froth treatment. The middlings and underflow stream of the PSV are sent to the tailings oil recovery (TOR) vessel for further processing. The TOR froth is recycled to the feed of the PSV, the middlings are sent to Mildred Lake Settling Basin and underflow are pumped to tailings treatment. The samples were collected under various operating conditions. This provided a diverse set of samples for analysis. Samples were provided in four bottles of 250mL each, for a total volume of 1L per sample. The sampling locations included the hydrotransport stream, the middlings and underflow stream of the primary separation vessels, the middlings and underflow stream of the TOR vessels and the tailings stream. An effort was made to analyze samples from specific dates and times during diverse plant performance conditions based on information provided by Syncrude.

3.2 Sample Preparation

The steps required to prepare samples for measurements are detailed in this section and a concise procedure for each step is provided. A detailed safe work procedure (SWP) is provided in Appendix A.

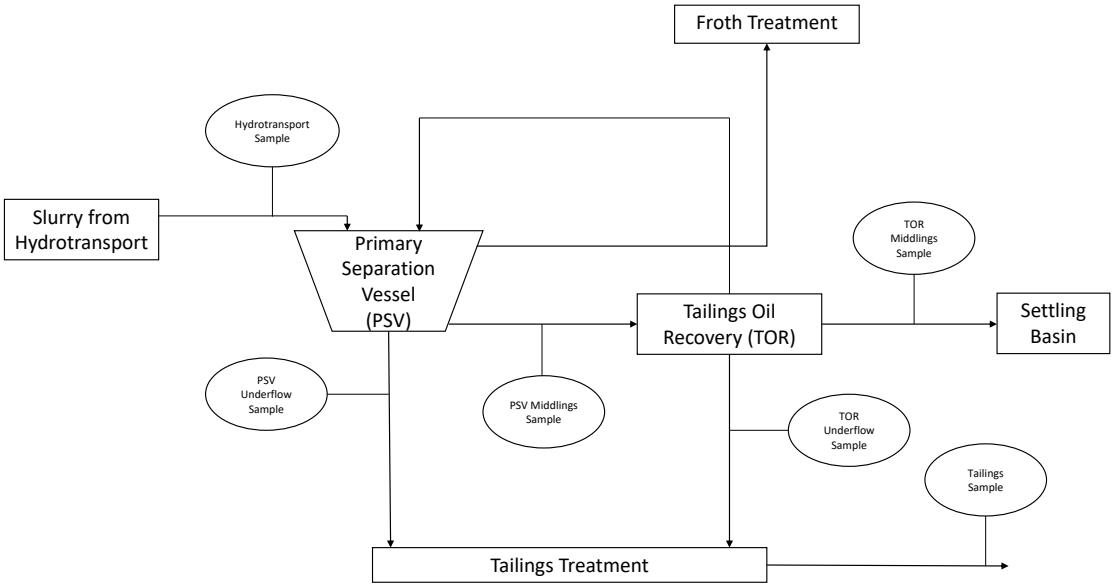

Figure 3.1: Process flow diagram and sample collections points [15].

3.2.1 Sieving

Sieving was used to separate the carrier fluid from the slurry. A NO. 200 USA Standard Test Sieve (75 μm mesh size) was used to separate the coarse particles greater than 75 μm from the carrier fluid. The sieving of a typical sample is shown in Figure 3.2. The volume of carrier fluid collected ranged from 200ml - 600mL depending on the type of sample being sieved and the amount of coarse particles present. The procedure used is as follows:

1. Place a NO. 200 test sieve over a collection pan.
2. Vigorously shake sample bottles to ensure no particles are settled at the bottom. Gently pour approximately 250mL of slurry on to the sieve.
3. Stir the slurry on sieve with a spatula to promote sieving. Be careful not to damage the sieve.
4. Remove coarse particles from sieve as necessary and repeat steps 2-3 until all slurry has been sieved
5. Once sieving is complete, collect carrier fluid from pan into a labeled container. Remove coarse particles from sieve.
6. Wash sieve and pan with solvent and soap as needed.

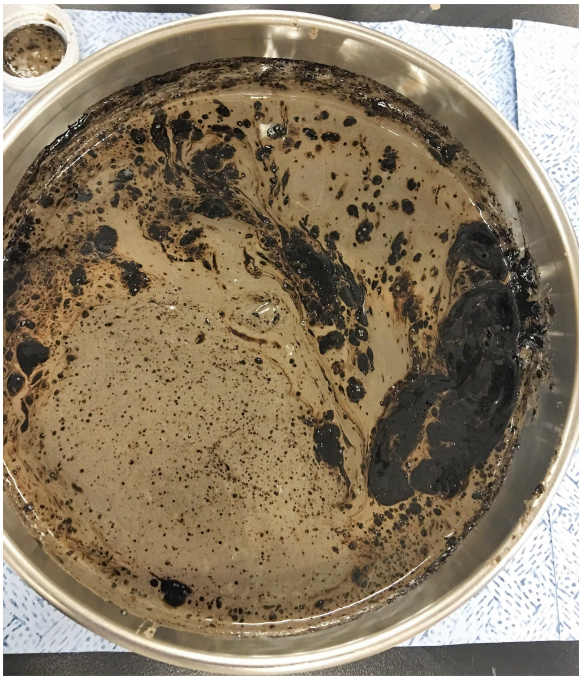

Figure 3.2: Sieving of oil sand slurries

3.2.2 QuickBit Analysis

In order to determine the amount of bitumen present in the carrier fluid after sieving, the QuickBit analysis was used. The QuickBit analysis was developed by Smith [12] as a modified version of the Dean Stark extraction. The full Dean Stark extraction is a lengthy procedure which is widely used in industry to obtain bitumen free solids and determine the exact composition of slurries [49, 50]. However, for the applications of this study a rapid method of determining bitumen content of slurries was necessary and hence, the QuickBit analysis was employed. The QuickBit analysis relies on the separation of bitumen and solids in a slurry due to the difference in densities. Two test tubes containing equal volumes of toluene and carrier fluid each, are centrifuged at 3400 rpm using a tabletop centrifuge (Hamilton Bell Model No. 1505). This causes the toluene and bitumen to rise to the top of the test tube and the solids to settle to the bottom. The toluene and bitumen layer is then extracted and the mass of bitumen is measured to determine bitumen content of the fluid.

The procedure used for QuickBit Analysis is as follows [12]:

1. In two 15 mL test tubes, add 5 mL slurry sample and 5 mL toluene to each.

2. Cap the test tubes and shake vigorously for approximately 5 minutes, or until

mixture is homogeneous.

3. Place test tubes in centrifuge in a balanced position. Run centrifuge at 3400 RPM for 15 minutes and visually inspect for two layers of fluid. Continue to centrifuge if two distinct layer are not visible.

4. For bitumen determination:

   (a) Weigh 1 piece of Whatman 5 Qualitative filter paper, record mass.

   (b) Using a syringe, remove 2 mL of the bitumen and toluene phase. Place 2 mL sample onto filter paper. Allow 45 minutes to dry and weigh filter paper with bitumen.

   (c) The bitumen content is the difference in mass between Steps (b) and (a) multiplied by 2.5. (5mL of carrier fluid was added to each test tube and 2mL of bitumen layer was removed; hence, multiplying by 2.5 provides bitumen content of 5mL of carrier fluid)

   (d) The mass of bitumen in the total volume of carrier fluid can then be calculated as:

$$m_{bitcarrierfluid} = m_{bitin5mL} * \frac{V_{totalcarrierfluid}}{5mL} \tag{3.1}$$

   where $m_{bitin5mL}$ is the bitumen content in 5mL of carrier fluid calculated from Step (c) and $V_{totalcarrierfluid}$ is the total volume of the carrier fluid to be analyzed in mL.

5. Dispose remaining oil phase in clearly marked disposal container.

6. Repeat Steps 4-5 with second test tube to improve repeatability

3.2.3 Bitumen Removal

Once the bitumen content of the carrier fluid has been determined, Gradek reusable hydrocarbon sorbent (RHS) beads are used to remove the bitumen. Gradek RHS beads are made of a highly oliophilic and hydrophobic co-polymer which attracts the bitumen on the surface of the beads when exposed to bitumen containing slurries [51]. The beads are spheroids with diameters in the range of 12 to 20 mm and specific gravities in the range of 0.08 to 0.35. In tests conducted by the manufacturer on high grade oil sands, recovery

of bitumen at 20°C has been as high as 87% [51]. The recovery is even further improved to 99% when the agitation temperature is increased to 40°C [51]. Hence, the procedure used involves heating the jar containing the carrier fluid and RHS beads to 45°C. A baffle is introduced into the jar and the jar is mixed on a tumbler to maximize the exposure of beads to any bitumen present in the fluid. The tumbler used is a Lortone Inc. rotary tumbler with a fixed speed of 70 rpm. Previous work done by Smith [12] found six cycles of extraction and a ratio of 6:1 of beads and bitumen to be ideal for maximum bitumen removal of carrier fluid samples. Thus, these steps are repeated five additional times with fresh RHS beads for every cycle. The primary advantage of the Gradek beads is that they can be reused for up to 600 cycles without any reduction in activity [51]. Hence, the beads were regenerated after every sample for reuse. The procedure used for bitumen removal and bead regeneration is as follows:

1. Add carrier fluid sample to a glass jar.
2. Calculate mass of beads required by multiplying mass of bitumen in carrier fluid from QuickBit analysis in Section 3.2.2 by 6. Smith [12] found the beads to bitumen ratio of 6:1 to be optimum for maximum bitumen removal.
3. Place jar in hot water bath (preheated to 45°C) for 10 minutes.
4. Remove jar from hot water bath and add metal baffle to jar. Use tumbler to mix fluid and beads for 10 minutes.
5. Remove jar from tumbler and extract beads from mixture by straining. Store beads for regeneration.
6. Repeat above Steps 3-5 until six cycles are complete.
7. To perform bead regeneration:
   (a) Pour 200mL of naphtha into a jar. Add approximately 40g of beads to jar.
   (b) Add metal baffle to jar and begin mixing in tumbler for 10 minutes.
   (c) Remove jar from tumbler and strain beads. Rinse to clean beads.
   (d) Place beads in an oven preheated to 75°C for 10 minutes to evaporate any remaining naphtha.
   (e) Repeat above steps (a)-(d) until all spent beads have been regenerated.

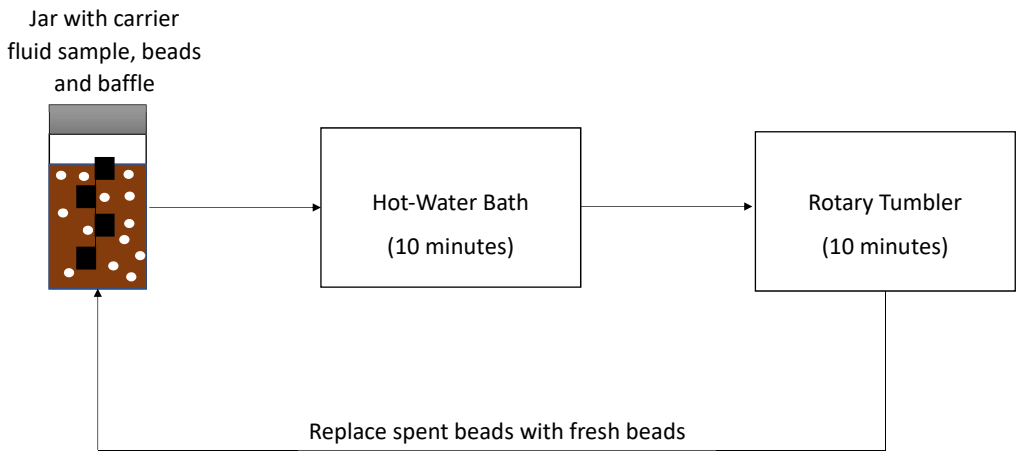

Figure 3.3: Removal of bitumen from carrier fluid

The process of bitumen removal from carrier fluid samples is shown in Figure 3.3.

3.3 Rheometry

Rheometry was primarily conducted using a TA instruments Discovery DHR-2 instrument. An accompanying water temperature control system was utilized to maintain constant temperatures. The DHR-2 is a shear rate controlled instrument which measures the torque required to attain a certain angular velocity in a fluid. The torque range for the DHR-2 is between 0.01 μNm and 200 mNm with a resolution of 0.1 nNm. The angular velocity range is 1.4E-9 rad/s to 300 rad/s [45]. Two types of geometries were used in this study. The double gap cylinder and DIN concentric cylinder geometries (CCV) were discussed in detail in Section 2.6. The specifications of both geometries are shown in Table 3.1.

A detailed safe work procedure for rheology measurements is available in Appendix A. The procedure used for rheology measurements is as follows:

1. Pour the carrier fluid sample into a 1L beaker. Mix the carrier fluid sample using an overhead mixer and 45°pitched blade turbine (PBT) impeller for 1 hour at 400 RPM.

2. Open air supply valve to rheometer.

Table 3.1: Specifications for the two types of geometries used in this study

Dimension	Double Gap	CCV
Cup Diameter (mm)	36.99 & 30.20	30.40
Bob Diameter (mm)	35.00 & 32.03	28.00
Bob Length (mm)	54.98	42.03
Gap length (mm)	0.950	1.2
Sample volume (mL)	13	16

3. Remove bearing lock.
4. Inspect water level and connections for temperature control system.
5. Turn on rheometer, computer and temperature control system.
6. Turn on software.
7. Perform instrument inertial calibration.
8. Attach desired geometry and verify geometry selection on software.
9. Perform geometry inertial and frictional calibrations.
10. Perform geometry rotational mapping.
11. Set temperature to 25°C and wait for temperature to reach steady state.
12. Set zero-gap.
13. Create new procedure by adding procedure steps in order:
    (a) Shear conditioning at 25 rad/s for 60s
    (b) Flow sweep up from 0.1 rad/s to 20 rad/s
    (c) Flow sweep down from 20 rad/s to 0.1 rad/s
    (d) Set steady state sensing to 5 consecutive points, tolerance to 5% and point time to 3s
14. Load appropriate volume of sample and lower head to geometry gap.
15. Begin test.

16. Once test is complete, save data and raise head to loading gap.

17. Remove geometry and dispose sample in appropriately labeled waste container.

18. Clean geometry with soap and warm water.

19. Shutdown rheometer, computer and temperature control system.

20. Attach bearing lock.

21. Shutoff air supply.

22. Plot torque vs. angular velocity for both flow sweep up and down with a linear best fit line. Determine viscosity and yield stress from slope and y-intercept for DIN concentric cylinder geometry (CCV) using:

$$\omega = \frac{T}{4\pi L \mu_p}\left[\frac{1}{R_1^2} - \frac{1}{R_2^2}\right] - \frac{\tau_y}{\mu_p}\ln\left[\frac{R_2}{R_1}\right] \tag{3.2}$$

For double gap geometry measurements, use Equations 2.11-2.14 to determine viscosity and yield stress.

3.4 Measuring Fine Solids Concentration

Three different techniques were evaluated to determine the fine solids concentrations in the carrier fluid samples. In order to identify the best technique for this study, mixtures of known amounts of pure kaolin clay and water were prepared and the results of each technique were compared to the true concentrations of each slurry. The results of each are discussed in the following chapter. The techniques and brief descriptions are listed below.

3.4.1 Pycnometer

A pycnometer is a device used to measure densities of fluids by measuring the mass of a precise volume of sample. The primary advantages are that it requires minimum sample volume and has a short analysis time. The steps required are as follow:

1. Weigh a dry, clean pycnometer and record mass.

2. Load sample into pycnometer using a pipette.

3. Insert stopper into pycnometer slowly, allowing liquid to overflow.

4. Wipe off excess fluid carefully.

5. Reweigh pycnometer with liquid.

6. Subtract the mass of the empty pycnometer (Step 1) from mass in Step 5 to determine mass of sample (m_{sample}).

7. Determine density and solids volume fraction using:

$$\rho_f = \frac{m_{sample}}{V_{pycnometer}} \tag{3.3}$$

$$C_s = \frac{\rho_f - \rho_w}{\rho_s - \rho_w} \tag{3.4}$$

where C_s is the solids volume fraction, ρ_f is the density of the sample calculated from Equation 3.3, ρ_s is the density of the solids and ρ_w is the density of water at 25°C. $V_{pycnometer}$ is the volume of sample in the pycnometer which is provided by the manufacturer but should be verified using ultrapure water or other fluids with known densities.

3.4.2 Volumetric Flask Method

The second method studied is the volumetric flask method which requires the operator to measure the volume and mass of a sample to determine the composition. The steps required for this method are as follows:

1. Weigh a clean and dry volumetric flask and record mass.

2. Pour sample into volumetric flask till the meniscus is at the designated volume line.

3. Record new mass of sample and flask.

4. Subtract mass of empty flask (step 1) from mass of sample and flask (step 3) to determine mass of sample.

5. Determine solids volume fraction using Equations 3.3 and 3.4.

3.4.3 Filter Paper Method

The final method used to calculate solids volume fraction is the filter paper method which involves evaporating a specific amount of sample and measuring the mass of solids to determine the composition. The steps required for this method are as follows:

1. Set up funnel over a 1L volumetric flask. Connect a vacuum pump to the flask using plastic tubing and ensure a proper seal. Use para-film to improve seal if necessary.
2. Measure mass of fluid to be filtered.
3. Measure mass of Fischer 8 (pore size 20 micrometers) filter paper.
4. Place Fischer 8 filter paper on funnel and switch on vacuum pump.
5. Slowly pour fluid onto filter paper and allow filtration till completion.
6. Carefully lift filter paper once filtration is complete and dry using an oven for one hour at 110°.
7. Record mass of filter paper and solids.
8. Repeat Steps 3-7 with Whatman 1 (pore size 11 micrometers), Whatman 5 (pore size 2.5 micrometers) and Millipore membrane (pore size 0.22 micrometers) filter papers.
9. Subtract mass of filter papers from mass of filter paper and sample respectively to determine total mass of solids.
10. Calculate solids volume fractions as:

$$C_s = \frac{\frac{m_s}{\rho_s}}{\frac{m_s}{\rho_s} + \frac{m_f - m_s}{\rho_w}} \tag{3.5}$$

where m_s is the mass of dry solids from all the filter papers, m_f is the mass of the fluid, ρ_s is the density of the solids and ρ_w is the density of water at 25°C.

3.5 Measuring Clay Activity

Clay activity was measured using the copper trien method. The procedure was provided by Syncrude Canada Ltd. In order to extract clean, dry solids for CEC measurements,

solids were extracted using vacuum filtration. A GAST vacuum pump (DOA-P708-AA) was used along with a GCA Corp. Precision oven (Ogden Manufacturing, Pittsburgh, PA, USA). A Microsonix 4000 was used to disperse solids to promote ion exchange. It provides a maximum output of 600W at an amplitude of 120 μm. The solution was then filtered and the absorbance was measured using a Perkins-Elmer Lambda 900 spectrometer. A step by step procedure is as follows:

1. Begin filtration of carrier fluid sample by placing a Fischer 8 filter paper on a funnel above a volumetric flask.
2. Connect vacuum pump to flask and switch on pump.
3. Slowly pour desired amount of carrier fluid on filter paper.
4. Allow filtration until completion (2.5-3 hours).
5. Carefully remove filter paper from funnel and allow to dry.
6. Repeat Steps 1-5 with Whatman 1 (pore size 11 micrometers), Whatman 5 (pore size 2.5 micrometers) and Millipore membrane (pore size 0.22 micrometers) filter papers. Store filtrate water in labeled containers for water chemistry analysis.
7. Dry solids in oven for 2 hours at 110°C.
8. Allow solids to cool in fume hood.
9. Prepare CuTrien solution by adding 1.09g of triethylenetetramine to a 250mL volumetric flask. Add 1.87g of copper (II) sulfate pentahydrate and bring the flask to volume.
10. Prepare buffer solution by adding 1.26g of sodium bicarbonate to a 1L volumetric flask and bringing to volume with ultrapure water. Adjust the pH to 9.6 by adding 1M sodium hydroxide solution dropwise.
11. Label and weigh empty jars and lids for unknown samples, method blank (MB), quality control (QC) samples and standards.
12. Add 1.5g of solids to respective sample jars.
13. Re-weigh jars with solids and record mass.

14. Add 3mL of isopropyl alcohol to each jar.
15. Add 40mL of bicarbonate to unknown sample, MB and QC jars.
16. Sonicate QC, MB and unknown samples for 4 minutes at 100% amplitude.
17. If necessary wipe solids off sonicator probe with minimum amount of bicarbonate solution.
18. Carefully remove jars after sonication is complete.
19. Add 30mL, 50mL and 80mL of bicarbonate to standards 1,2 and 3 respectively.
20. Add 10mL of CuTrien solution to each jar except standard 3.
21. Shake jars in high speed shaker for 20 minutes.
22. Reweigh jar with solids and liquids and record final mass.
23. Using a syringe, extract 3mL of each sample and filter into 1.5mL cuvettes with 0.1μm syringe filter.
24. Turn on spectrometer and software.
25. Set absorbance scan from 400nm to 800nm at 1nm/s.
26. Zero the spectrometer with ultrapure water.
27. Measure absorbance of three previously prepared standards to determine calibration curve.
28. Measure absorbance of MB, QC and samples.
29. Shutdown spectrometer and software.
30. Dispose samples in labeled waste container.

Chapter 4

Results and Discussion

4.1 Overview

This chapter discusses the results obtained from the analyses conducted on carrier fluid samples. The results of fine solids concentration measurements and viscosity measurements are critically analyzed and compared to similar studies described in the literature. The repeatability and accuracy of the various techniques are also discussed in each section. Based on these results, samples are identified and selected for clay activity and water chemistry analyses. The clay activity and water chemistry analyses results are presented and discussed. The final section in this chapter focuses on identifying relationships between clay activity, water chemistry, fine solids concentration and viscosity and determining a correlation based on such relationships to predict carrier fluid viscosities.

4.2 Fine Solids Concentration Measurements

As discussed in the previous chapter, three techniques were compared to determine carrier fluid solids content. In order to test each technique, analysis was completed using previously prepared Kaolin clay suspensions of known compositions. These results are outlined in the following section.

4.2.1 Technique Comparison using Kaolin Suspensions

As shown in Table 4.1, the three techniques studied provided generally acceptable results for solids content measurements of model Kaolin suspensions. However, the volumetric

Table 4.1: Comparison of the different solids volume fraction measurement techniques using Kaolin suspensions

True Volume Fraction	Pycnometer	Volumetric Flask	Filter Paper
3%	2.8%	2.8%	2.9%
3%	3.1%	2.8%	3.0%
4%	3.9%	4.1%	4.0%
4%	4.0%	3.6%	4.1%
5%	4.9%	5.5%	5.1%
5%	5.0%	4.9%	5.2%
7.5%	7.5%	7.8%	7.6%
7.5%	7.6%	7.2%	7.7%
10%	10.1%	8.9%	10.0%
10%	10.2%	10.9%	10.5%

flask method was not very repeatable. This may be due to the increased operator error in measuring the exact volume of a sample manually. This error is eliminated by the use of a pycnometer which allows for identical volumetric measurements with each test. The filter paper method was highly repeatable and accurate but too time consuming to be conducted for all industrial samples. The filter paper method was also sample destructive and required larger volumes of samples for accurate measurement. The pycnometer provided repeatable and accurate results while requiring the least time and sample volume to complete measurements. Hence, the pycnometer was chosen to conduct solids volume fraction measurements of all industrial slurry samples.

4.2.2 Carrier Fluid Composition Results

The concentration of fine solids was analyzed for 93 samples using the pycnometer. The number of samples and average concentrations for each stream are shown in Table 4.2. The results offer valuable insight into the general composition of each stream in a typical oil sands processing plant. This information is critical, for example, in designing pipelines to carry various streams between vessels.

Overall, the hydrotransport samples contained the highest concentration of fine solids and the TOR middlings samples contained the lowest concentration. The PSV Middlings,

Table 4.2: Average fine solids concentration (v/v) of carrier fluid samples by stream

Stream Location And Identifier	Number of samples	Average Concentration (v/v)
Hydrotransport (HYDR)	14	15.4%
PSV Middlings (PSVM)	12	7.7%
PSV Underflow (PSVU)	15	7.9%
TOR Middlings (TORM)	22	2.7%
TOR Underflow (TORU)	26	7.2%
Tailings (TAIL)	4	5.7%

PSV Underflow and TOR Underflow had similar compositions on average. The overall range of fine solids concentration was 1.2% (v/v) to 18.2% (v/v). The concentration of fine solids in carrier fluid samples found in this study are in the same range as the previous work done by Smith [12] on carrier fluids. Smith [12] found carrier fluid samples to contain between 1.8% (v/v) to 18.4% (v/v) fine solids.

Four samples were diluted to lower concentrations in order to further investigate the effect of fine solids concentration on carrier fluid viscosity. The dilutions were performed with process water extracted from the samples using filtration, as discussed in Section 3.2.4. The diluted concentrations are shown in Table 4.3. Table 4.3 also shows each sample's unique identifier which includes the stream name and date of collection followed by the sample's solids concentration.

Table 4.3: Concentrations of diluted samples

Sample Identifier (Original)	Original Concentration	Sample Identifier (Diluted)	Diluted Concentrations
TORU-0809-84	8.4%	TORU-0809-47	4.7%
TORU-0809-84	8.4%	TORU-0809-63	6.3%
PSVM-0807-76	7.6%	PSVM-0807-27	2.7%
PSVM-0807-76	7.6%	PSVM-0807-54	5.4%
TORU-0806-70	7.0%	TORU-0806-38	3.8%
TORU-0806-70	7.0%	TORU-0806-50	5.0%
PSVU-0801-105	10.5%	PSVU-0801-46	4.6%
PSVU-0801-105	10.5%	PSVU-0801-81	8.1%

4.3 Rheometry Results

4.3.1 Shear Behavior

A disadvantage of rotational rheometry is that certain time dependent behavior of fluids is more pronounced [7]. Such time dependent behavior would not be an issue in industry due to the high shear conditions experienced in a pump prior to the fluid entering a pipeline [7]. Hence, these effects needed to be eliminated prior to measurements to avoid results that do not reflect actual in pipe conditions. In order to do so, a conditioning step was implemented prior to viscosity measurement. Ideal conditioning parameters had been devised by Asadi Shahmirzadi [24] and Smith [12] previously for concentric cylinder geometries. They found conditioning at 25 rad/s for 60 seconds successfully stabilized the fluid for viscosity measurements [12, 24]. These parameters were verified to be acceptable for the double gap geometry as shown in Figure 4.1.

During the viscosity measurements, steady state sensing was employed to verify stable torque values were recorded at each angular velocity. Aggregate formation and breakage is a dynamic process and requires time to achieve steady state at any given shear condition. Hence, parameters were selected to successfully establish conditions where the breakage and formation of aggregates had stabilized prior to the torque value being recorded. The two parameters controlled were percent tolerance of deviation between consecutive values and number of points used to calculate deviation. The effect of these parameters on measured viscosity is shown in Table 4.4. It is clear from Table 4.4 that an average time of 20 seconds is ideal for reaching steady state in terms of aggregate formation and breakage. Reducing the percent tolerance to increase accuracy had no effect on the viscosity values but increased the average time per point. On the other hand, increasing the number of values almost doubled the point time and provided higher viscosities. Longer measurement times increase the risk of settling occurring within a geometry which can lead to erroneous viscosity values. In order to avoid such a scenario and maintain accuracy, the percent tolerance and number of points were chosen at 5% and 5 respectively.

4.3.2 Accuracy and Repeatability

In order to determine the accuracy of the rheometer, measurements were completed using a standard oil, ultrapure water and sugar solution at 25°C. The results are shown in

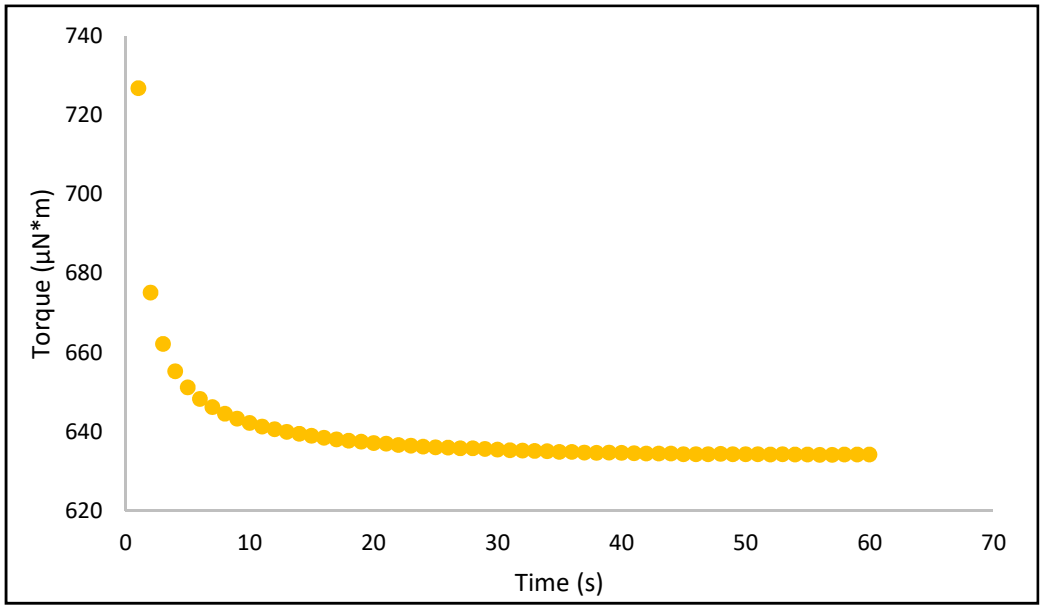

Figure 4.1: Conditioning of carrier fluid sample TORU-0801-99 at 25 rad/s for 60s

Table 4.5[1]. The double gap geometry provided more accurate results with an average error of 2.2%. Overall, the DIN concentric cylinder had an error of 12.4% which is similar to the 10.6% error found by Smith [12] for standard oils in a similar viscosity range.

The standard oil was also used to measure repeatability of the two geometries. The standard oil measurements were repeated four times with each geometry at 25 °C. Repeatability was also measured with carrier fluid sample TORM-0517-41. The absolute error of the measurements are shown in Table 4.6[2]. The viscosity measurements were more repeatable for the standard oil than the carrier fluid sample. Overall, both geometries displayed high levels of repeatability.

4.3.3 Data Analysis

As mentioned previously, the rheometer measures torque at each angular velocity during viscosity measurements. This data must then be interpreted using a fluid model to determine viscosity. Figure 4.2 shows torque and angular velocity results from the rheometer for sample PSVU-0727-68. The Bingham fluid model was found to be the best

[1]The double gap viscosities were calculated using the manufacturer recommended constants which assume Newtonian fluid behavior. The possible impact of these constants on the viscosity of non-Newtonian fluids is currently unknown.

[2]See previous note.

Table 4.4: Steady state sensing during viscosity measurements

Procedure	Relative Viscosity	Average Time per Point (s)
TORM-0517-28		
5% tolerance, 5 consecutive values	2.83	20.5
2% tolerance, 5 consecutive values	2.80	24.0
5% tolerance, 10 consecutive values	3.10	38.7
TORM-0729-35		
5% tolerance, 5 consecutive values	2.56	19.7
2% tolerance, 5 consecutive values	2.55	22.2
5% tolerance, 10 consecutive values	2.60	35.3

Table 4.5: Accuracy of different rheometer geometries

Sample	Viscosity at 25°C (mPa*s)	Double gap (mPa*s)	CCV (mPa*s)
Standard oil	4.60	4.50	5.00
Sugar solution	6.20	6.00	6.50
Ultrapure water	0.89	0.90	1.10

fit for the data. Once the slope had been determined from the linear best-fit line, the viscosity was calculated using Equation 2.17 for CCV. The yield stress was also calculated using the y-intercept in Equation 2.17 for CCV. Equations 2.11-2.14 were used to determine viscosity and yield stress values for the double gap measurements. As discussed previously, Bingham fluids behave linearly once the yield stress has been overcome. In industry, fluids experience high shear conditions in pipelines and therefore, in pipeline design the viscosity remains the most important parameter. The viscosity results for all other samples analyzed are included in Appendix B.

4.3.4 Effect of Geometry on Viscosity

The difference in the measured viscosities of the standards shown in Table 4.5[3]warranted an investigation into the causes of such a difference. It was found that the viscosity measurements on carrier fluid samples also showed notable differences between the

[3]The double gap viscosities were calculated using the manufacturer recommended constants which assume Newtonian fluid behavior. The possible impact of these constants on the viscosity of non-Newtonian fluids is currently unknown.

Table 4.6: Absolute error of different rheometer geometries

Sample	Viscosity (mPa*s)	Double gap	CCV
Standard oil	4.60	+/-0.03	+/-0.03
TORM-0517-41	3.80	+/-0.2	+/-0.4

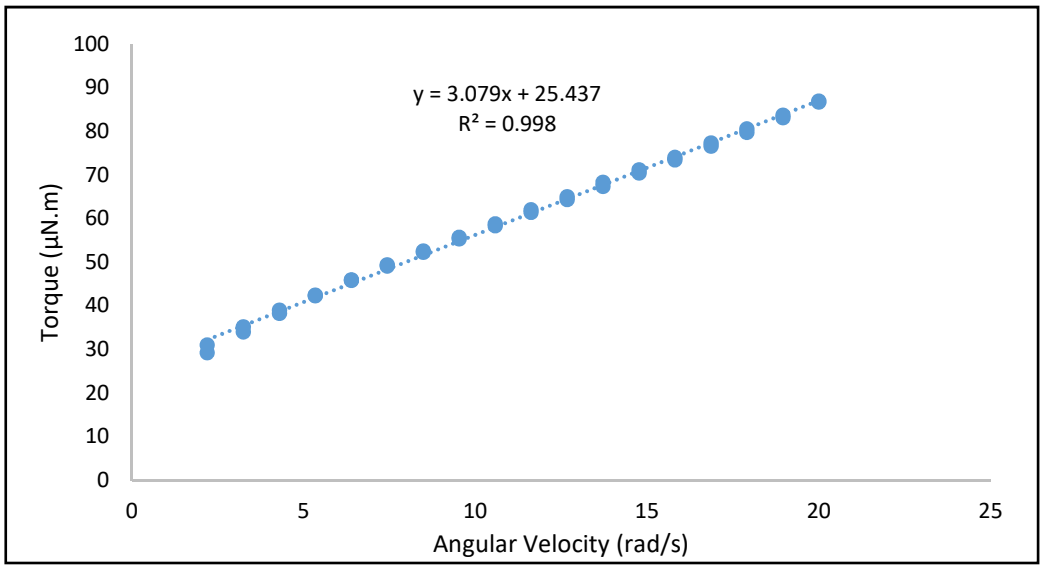

Figure 4.2: Flow sweep up and down results for PSVU-0727-68.

geometries. This is shown in Table 4.7[4]. The difference in viscosity results for all carrier fluid samples analyzed using both geometries is shown in Figure 4.3[5].

Two possible explanations were explored for this difference in viscosity measurements:

1. Gap width

2. Energy Input

During viscosity measurements of carrier fluid samples, special care must be taken to avoid a narrow gap between the cup inner wall and rotor outer wall [7]. This is because narrow gaps will interfere with aggregate formation and breakage and hence, provide

[4]The double gap viscosities were calculated using the manufacturer recommended constants which assume Newtonian fluid behavior. The possible impact of these constants on the viscosity of non-Newtonian fluids is currently unknown.

[5]See previous note.

Table 4.7: Difference in carrier fluid viscosities based on geometries

Sample	Double Gap (mPa*s)	CCV (mPa*s)
TORM-0516-17	1.61	2.80
TORU-0725-64	3.98	5.14
PSVU-0729-81	4.94	6.56
PSVU-0801-105	6.20	8.53
PSVM-0806-76	6.64	8.23
TORU-0820-100	6.31	7.74
TORU-0807-94	8.35	11.64

inaccurate viscosity results. A general rule of thumb is to maintain a gap 10 times the size of the largest aggregate [7]. To investigate the effect of gap size on viscosity, three carrier fluid samples were analyzed with four different gap widths. The 0.505 mm double gap and 1.643 mm CCV measurements were completed using an Anton Paar MCR 102 rheometer. The MCR 102 has a torque range of 5 nNm to 200 mNm and an angular velocity range of 10^{-8} rad/s to 314 rad/s [52]. The procedure was discussed in Section 3.3. The results are shown in Table 4.8[6]. The results show a general increase in viscosity with the gap length.

Table 4.8: Effect of gap size on relative viscosity

Sample	Double gap 0.505 mm	Double gap 0.955 mm	CCV 1.200 mm	CCV 1.643 mm
TAIL-0807-45	3.03	4.00	5.03	5.54
PSVM-0807-73	4.16	5.69	7.09	7.63
TORM-0516-24	1.69	2.14	2.76	3.59

However, the viscosity values also deviate more between geometries than between gap sizes. This suggests that geometry type, and not gap size, may be the leading cause in the deviation in viscosity measurements.

In order to investigate the effect of the geometry on viscosity, energy dissipation calculations were conducted. The primary advantage of double gap geometries is that

[6]The double gap viscosities were calculated using the manufacturer recommended constants which assume Newtonian fluid behavior. The possible impact of these constants on the viscosity is currently unknown.

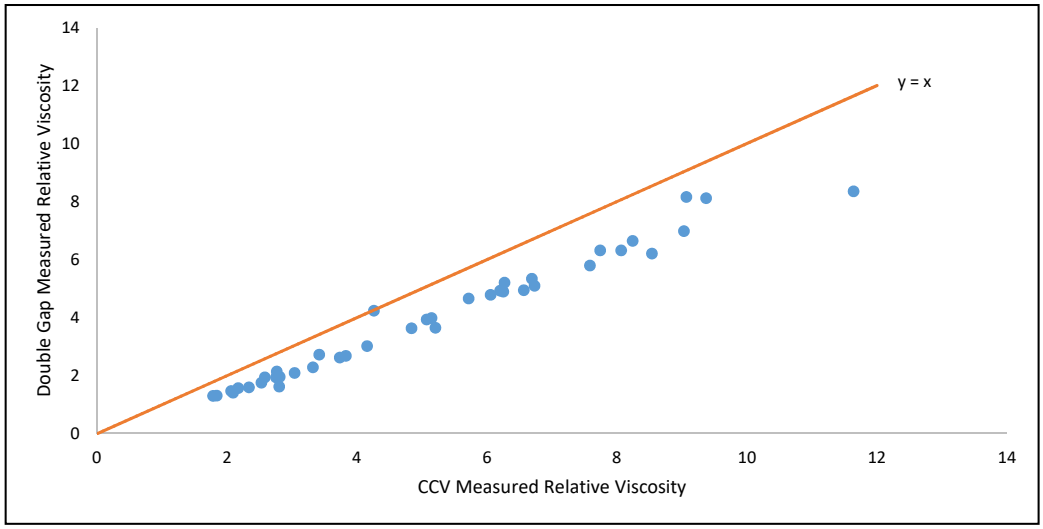

Figure 4.3: Difference in viscosities of carrier fluid samples based on geometries

higher torque values can be obtained during viscosity measurements. This in turn results in larger energy dissipation and total energy input to the sample. The rate of energy dissipated into a rheometer sample is given by [53]:

$$\epsilon = \frac{T * \omega}{m} \tag{4.1}$$

where ϵ is the rate of energy dissipated, T is the torque, ω is the angular velocity of the rotor and m is the mass of the sample. The total energy input can also be calculated as:

$$W = \epsilon * t \tag{4.2}$$

where t is the time at each torque value and W is the total energy input. A higher energy input has been shown to affect the structure of aggregates in clay and water mixtures [53, 54]. As expected, because the double gap geometry provides higher torque for the same angular velocity, the total energy input and rate of energy dissipation are also higher than for the concentric cylinder. Since double gap geometries were providing lower viscosity measurements than concentric cylinders, it was hypothesized that a relationship may exist between energy input or rate of energy dissipation and viscosity due to the

effect of energy input on aggregate size. A higher energy input would facilitate breakage of aggregates and hence, promote lower viscosities. In order to test this hypothesis, the concentric cylinder tests were repeated to match or significantly exceed the energy input and rate of dissipation values of the double gap measurements. The total energy input and rate of energy dissipation results are shown in Table 4.9[7]. As seen in Table 4.9, the

Table 4.9: Effect of total energy input and rate of energy dissipation on relative viscosity

Sample	Property	Double gap	CCV original	CCV modified
TAIL-0807-45	Relative Viscosity	4.00	5.03	5.01
	Energy Input	160 J/kg	35 J/kg	182 J/kg
	Rate of Energy Dissipation	0.60 W/kg	0.13 W/kg	0.81 W/kg
TORM-0516-24	Relative Viscosity	2.14	2.76	3.10
	Energy Input	23 J/kg	14 J/kg	245 J/kg
	Rate of Energy Dissipation	0.38 W/kg	0.08 W/kg	3.86 W/kg
PSVM-0807-73	Relative Viscosity	5.69	7.09	6.85
	Energy Input	247 J/kg	59 J/kg	277 J/kg
	Rate of Energy Dissipation	0.90 W/kg	0.21 W/kg	1.14 W/kg

increase in total energy input and rate of dissipation provided no consistent decrease in viscosity. The viscosity values remained within the margin of error established in Table 4.6 and showed no notable effect due to an increase in energy input and rate of dissipation. This result is especially interesting because of the prevalent use of concentric cylinder geometry to conduct viscosity measurements [12, 24, 53]. Due to the disparity in results, samples were sent out for analysis by an independent third party organization. The results agreed more closely with the double gap geometry than the concentric cylinder. This confirmation provided confidence in the double gap geometry results. The double gap geometry also provided lower error during measurements as opposed to the concentric cylinder geometry. Hence, the double geometry was selected for measurement of carrier fluid viscosities in this project.

[7]The double gap viscosities were calculated using the manufacturer recommended constants which assume Newtonian fluid behavior. The possible impact of these constants on the viscosity is currently unknown.

4.3.5 Viscosity and Fines Concentration

The viscosity was measured for 93 carrier fluid samples using the double gap geometry. The number of samples analyzed for each stream were given in Table 4.2. Overall, the viscosity values were highest for hydrotransport samples and lowest for TOR middlings samples. The carrier fluid viscosities and corresponding fines solids concentrations are shown in Figure 4.4[8]. The model currently used by industry to predict viscosities of carrier fluids and the correlation found by Smith [12] during carrier fluid viscosity measurements is also shown on Figure 4.4 [7, 12].

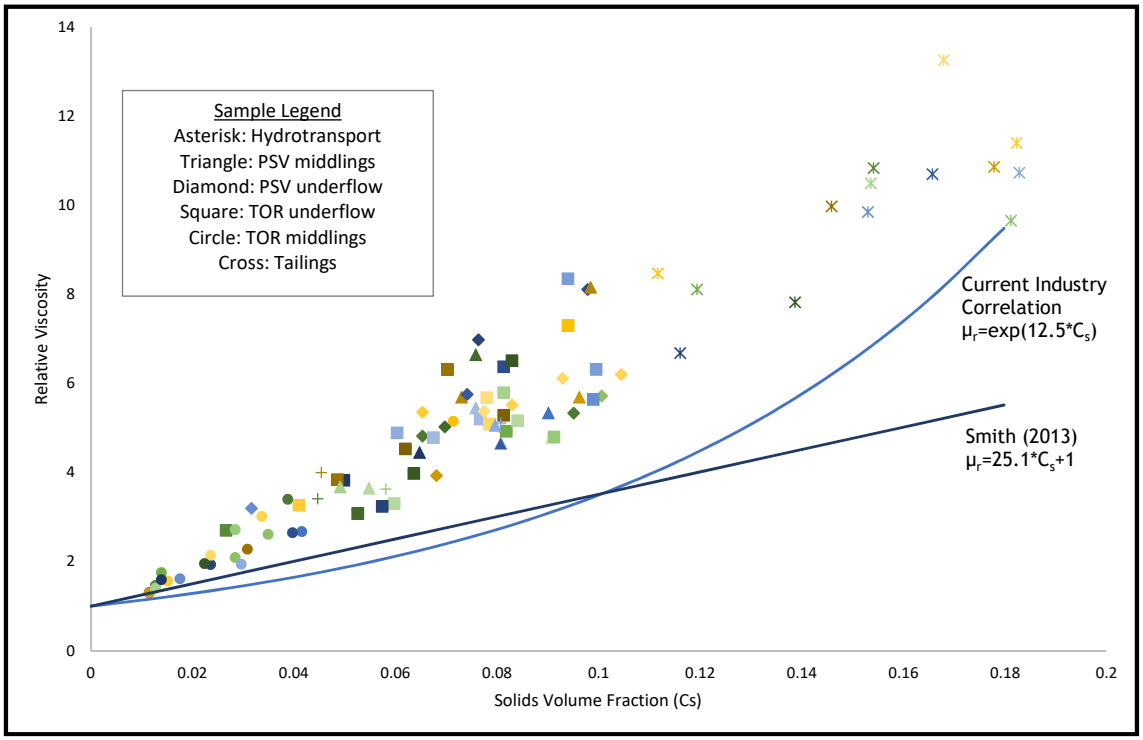

Figure 4.4: Relative viscosity and fine solids volume fraction of carrier fluid samples

As seen in Figure 4.4, the carrier fluid viscosities generally increase with the fine solids concentration. However, there is a large degree of variation at constant fine solids concentrations. This effect can be seen clearly with the viscosity of three samples shown in Table 4.10. The viscosity varies by as much as 70% despite little deviation in fine solids concentrations. This is important because a large deviation in viscosity values can require proportionate modifications in operating conditions to maintain optimum performance of

[8]The double gap viscosities were calculated using the manufacturer recommended constants which assume Newtonian fluid behavior. The possible impact of these constants on the viscosity of non-Newtonian fluids is currently unknown.

Table 4.10: Variations in viscosity at similar fines solids concentrations

Sample	Fines Solids Concentration	Relative Viscosity
TORU-0731-91	9.1%	4.80
TORU-0806-94	9.4%	7.30
TORU-0807-94	9.4%	8.35

pipelines and separation vessels. This shows that the fine solids concentration alone is not sufficient to determine the viscosity of the carrier fluid. It is also obvious from Figure 4.4 that the correlation currently used by industry to predict carrier fluid viscosities is highly inaccurate and under-predicts viscosities for almost all samples. This is unsurprising given the fact that this correlation was originally developed using mature fine tailings alone and had a large degree of scatter in predictions despite the small data set. Figure 4.4 shows that there is a need for additional analysis of factors besides fine solids concentrations (eg. clay activity, water chemistry) to better understand carrier fluids viscosity.

Dilutions were conducted to better understand the contribution of fine solids concentration. Samples were diluted by process water to preserve water chemistry conditions and dilution curves were plotted as shown in Figure 4.5[9]. Figure 4.5 also shows the correlation currently used by industry to predict carrier fluid viscosities [7]. The dilution curves were plotted for four different samples at concentrations shown in Table 4.3. Exponential relationships were seen between fine solids concentration and viscosities. However, it is important to note that the exponents were significantly higher than the relationship currently used by industry. This shows that the contribution of secondary factors can vary greatly and needs to be accounted for when predicting carrier fluid viscosities. The strong exponential fit ($R^2 = 0.94 - 0.99$) also suggest that once secondary parameters have been accounted for, predictions can be made with a high degree of accuracy.

4.4 Selection of Samples for Further Analysis

The viscosity results confirmed the original hypothesis that factors besides fine solids concentration have major contributions to the viscosity of the carrier fluid. Hence, clay activity and water chemistry analyses were conducted on selected samples. The samples

[9]The double gap viscosities were calculated using the manufacturer recommended constants which assume Newtonian fluid behavior. The possible impact of these constants on the viscosity is currently unknown.

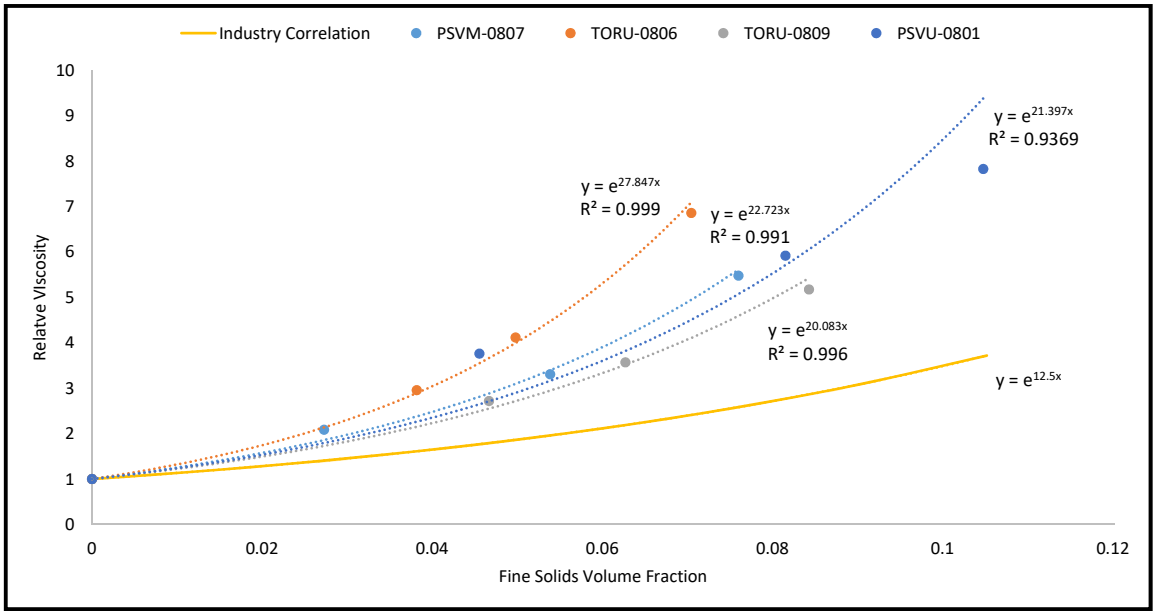

Figure 4.5: Effect of fine solids concentration on viscosity of carrier fluids

were selected to be representative of the complete sample set and an attempt was made to identify samples with dissimilar viscosities at similar fine solids concentrations. The relative viscosity and composition values for the 24 samples selected are shown in Figure 4.6[10]. As seen by the best-fit line in Figure 4.6, there is a large deviation in viscosities of samples selected based on fines solids concentration. The diverse range of viscosities and solids concentrations for the selected samples is also illustrated by Figure 4.6.

[10]The double gap viscosities were calculated using the manufacturer recommended constants which assume Newtonian fluid behavior. The possible impact of these constants on the viscosity of non-Newtonian fluids is currently unknown.

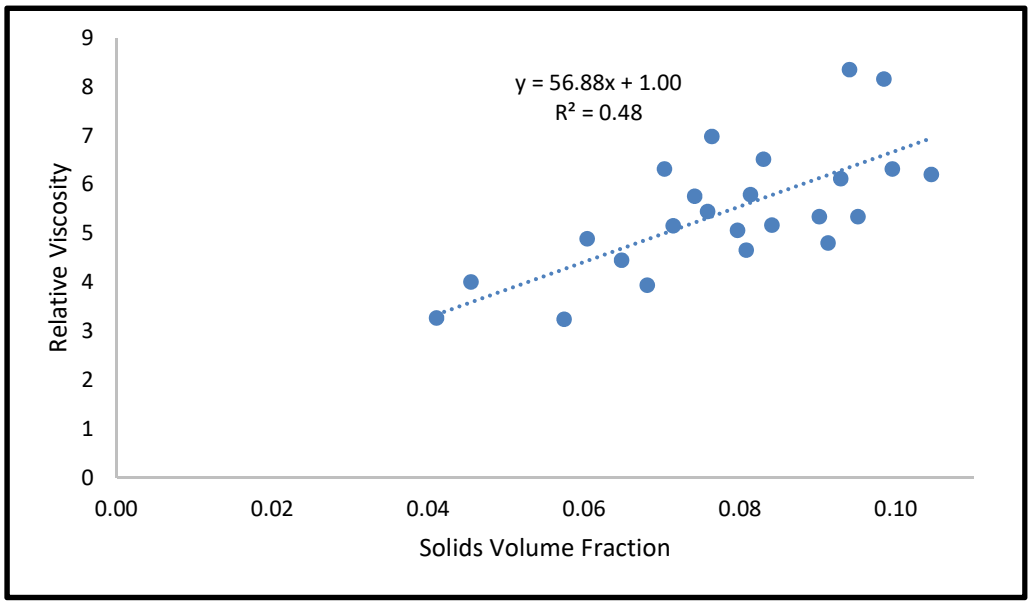

Figure 4.6: Fine solids concentration and viscosity of selected carrier fluid samples

4.5 Clay Activity Results

The procedure followed to determine clay activity was discussed in Section 3.5. Once the absorbance values had been determined, a three point calibration curve was used to determine the final CuTrien concentration. Three standards of varying CuTrien concentrations were analyzed with every batch of samples to determine the calibration curve. An example of a calibration curve is shown in Figure 4.7. In order to determine the accuracy of the procedure, quality control samples were also analyzed with every batch of unknown samples. The quality control samples used in this study were of Illite clay. The theoretical CEC value of pure Illite clay is 10-30 (meq/100g) [55]. Table 4.11 shows the CEC values for each test with Illite clay. As seen in Table 4.11, the procedure was highly repeatable with a

Table 4.11: CEC for Illite clay

Run	CEC value
1	11.05
2	11.16
3	11.29
4	10.94

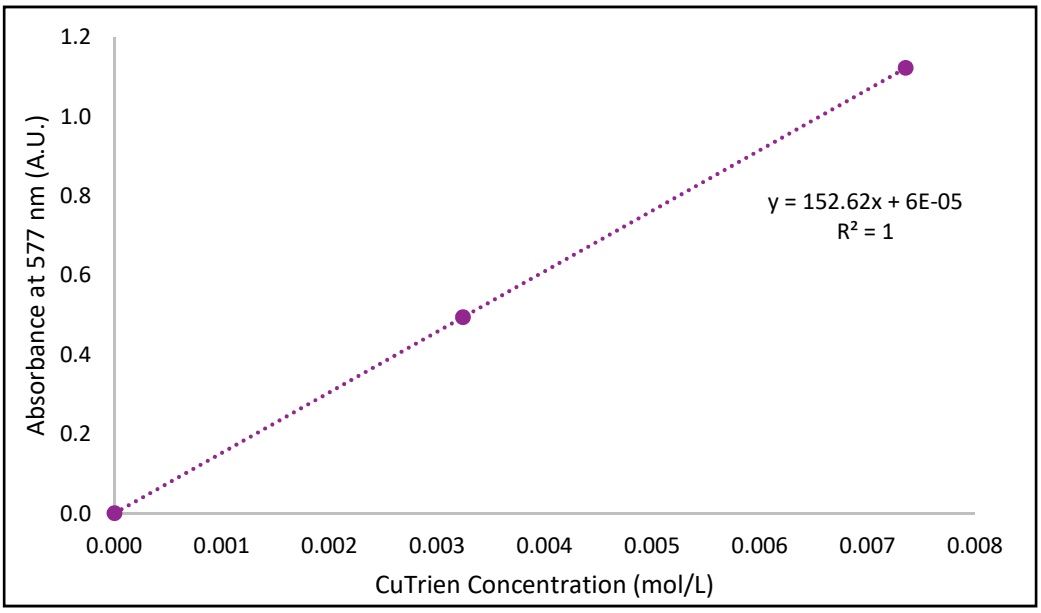

Figure 4.7: Calibration curve of three standards with varying concentrations of CuTrien at an absorbance of 577nm.

percent difference of less than 3.5%. The CEC value determined was slightly lower than the average theoretical value for the CEC of pure Illite clay. Overall, the CEC results for the Illite clay proved a high level of accuracy and repeatability of the procedure.

The CEC was determined for 24 carrier fluid samples. The solids were extracted and analyzed as discussed in Section 3.5. The CEC values for the samples are shown in Table 4.12. Overall, the results range between 9.8-18.1 meq/100g. It is interesting to note that this range falls closer to the average theoretical value for CEC of illite clays (20.7 meq/100g) than the average theoretical CEC value of kaolinite clays (4.6 meq/100g) [55]. This supports the original hypothesis that kaolinite alone cannot be assumed to be representative of clays in oil sands slurries.

Table 4.12: CEC of fine solids Carrier Fluid samples

Sample Identifier	Sample Name	CEC (meq/100g)
PSVU-0801-105	PSV Underflow Aug. 1st 20:04	18.1
TORU-0814-81	TOR Underflow Aug. 14th 02:01	13.2
PSVM-0807-76	PSV Middlings Aug. 7th 19:30	13.4
TORU-0820-100	TOR Underflow Aug. 20th 05:05	12.4
TORU-0809-84	TOR Underflow Aug. 9th 02:05	12.5
TORM-0810-71	TOR Middlings Aug. 10th 11:19	12.0
PSVM-0810-80	PSV Middlings Aug. 10th 13:33	11.7
PSVM-0809-65	PSV Middlings Aug. 9th 01:30	12.0
TORU-0806-70	TOR Underflow Aug 6th 17:00	13.7
PSVU-0727-68	PSV Underflow Jul. 27th 07:33	10.4
PSVU-0807-74	PSV Underflow Aug 7th 01:45	12.5
TAIL-0807-45	Tailings Aug. 7th 17:15	13.2
TORU-0731-91	TOR Underflow Jul. 31st 22:59	9.8
TORU-0816-57	TOR Underflow Aug. 16th 11:02	11.2
PSVM-0816-90	PSV Middlings Aug. 16th 22:42	10.1
TORU-0807-94	TOR Underflow Aug. 7th 11:05	11.9
PSVU-0730-95	PSV Underflow Jul. 30th 22:49	15.7
TORU-0808-60	TOR Underflow Aug. 8th 14:00	18.8
TORU-0808-41	TOR Underflow Aug. 8th 05:01	18.7
PSVU-0729-93	PSV Underflow Jul. 29th 16:57	12.0
PSVM-0727-81	PSV Middlings Jul. 27th 07:44	11.3
PSVU-0806-76	PSV Underflow Aug. 6th 16:31	15.3
TORU-0807-83	TOR Underflow Aug. 7th 17:03	13.6
PSVM-0807-98	PSV Middlings Aug. 7th 10:41	12.0

4.6 Water Chemistry Results

Water chemistry analysis was conducted by labs at Syncrude R&D using ion chromatography. The analysis included measurements of pH, conductivity and concentrations of Al^{3+},

K^+, Li^{2+}, F^-, Cl^-,NO_3^-, Ca^{2+}, Na^+, SO_4^{2-} and Mg^{2+}. Full water chemistry results for all samples are shown in Appendix C. A parameter previously used by industry to estimate overall water chemistry of samples is ionic strength [56]. Ionic strength is defined as

$$IS = \frac{1}{2}\sum c_i * Z_i^2 \tag{4.3}$$

where IS is ionic strength in mol/L, c_i is molar concentration of each ion and Z_i is the ionic charge [56]. The samples analyzed and the respective ionic charges are shown in Table 4.13. The overall range of ionic strength for the samples was between 0.052 to 0.083 mol/L. The ionic strength results in this study are considerably higher than ionic strength values found by Smith [12] for carrier fluid samples. Similarly, concentration of dissolved ions like Sodium, Chloride and Sulphate ions were also significantly higher in this study than those found by Smith [12]. Table 4.14 shows the average concentrations of dissolved ions found in this study relative to the water chemistry results found by Smith [12]. The difference in concentrations and ionic strength supports the primary hypothesis that water chemistry can affect carrier fluid viscosities. The samples studied by Smith [12] had relatively low dissolved ion concentrations and low viscosities; the samples analyzed in this study have considerably higher dissolved ion concentrations and ionic strengths and higher viscosities. The following sections discusses the viscosity correlations determined based on the clay activity, water chemistry and fine solids concentration results.

4.7 Viscosity Correlations

Carrier fluid viscosities were correlated to fine solids concentration initially. Linear regression analysis was conducted and a best fit line was developed. Figure 4.8[11] shows the best fit line and 40% confidence intervals. This correlation can be used by industry to approximate carrier fluid viscosities in the absence of CEC and ionic strength information with a reasonable level of accuracy. Analysis was also conducted on viscosity results from the concentric cylinder geometry. Samples analyzed using both geometries are shown in Figure 4.9[12]. Figure 4.9 highlights the effect of geometries on the viscosity correlations. The concentric cylinder provides a correlation with a higher coefficient than the double

[11] The double gap viscosities were calculated using the manufacturer recommended constants which assume Newtonian fluid behavior. The possible impact of these constants on the viscosity is currently unknown.

[12] See previous note.

Table 4.13: Ionic Strength of Carrier Fluid samples

Sample Identifier	Sample Name	Ionic Strength (mol/L)
PSVU-0801-105	PSV Underflow Aug. 1st 20:04	0.083
TORU-0814-81	TOR Underflow Aug. 14th 02:01	0.069
PSVM-0807-76	PSV Middlings Aug. 7th 19:30	0.066
TORU-0820-100	TOR Underflow Aug. 20th 05:05	0.060
TORU-0809-84	TOR Underflow Aug. 9th 02:05	0.077
TORM-0810-71	TOR Middlings Aug. 10th 11:19	0.076
PSVM-0810-80	PSV Middlings Aug. 10th 13:33	0.080
PSVM-0809-65	PSV Middlings Aug. 9th 01:30	0.070
TORU-0806-70	TOR Underflow Aug 6th 17:00	0.070
PSVU-0727-68	PSV Underflow Jul. 27th 07:33	0.068
PSVU-0807-74	PSV Underflow Aug 7th 01:45	0.076
TAIL-0807-45	Tailings Aug. 7th 17:15	0.052
TORU-0731-91	TOR Underflow Jul. 31st 22:59	0.067
TORU-0816-57	TOR Underflow Aug. 16th 11:02	0.056
PSVM-0816-90	PSV Middlings Aug. 16th 22:42	0.074
TORU-0807-94	TOR Underflow Aug. 7th 11:05	0.081
PSVU-0730-95	PSV Underflow Jul. 30th 22:49	0.073
TORU-0808-60	TOR Underflow Aug. 8th 14:00	0.075
TORU-0808-41	TOR Underflow Aug. 8th 05:01	0.063
PSVU-0729-93	PSV Underflow Jul. 29th 16:57	0.073
PSVM-0727-81	PSV Middlings Jul. 27th 07:44	0.057
PSVU-0806-76	PSV Underflow Aug. 6th 16:31	0.065
TORU-0807-83	TOR Underflow Aug. 7th 17:03	0.065
PSVM-0807-98	PSV Middlings Aug. 7th 10:41	0.077

gap correlation. It is also interesting to note that the correlations for both geometries have similar fits ($R^2 = 0.85$). Similarly, the samples selected for clay activity and water chemistry analysis showed large variations in viscosity with respect to fine solids concentrations. Figure 4.6 showed the fit for the 24 samples selected for CEC and water chemistry analysis.

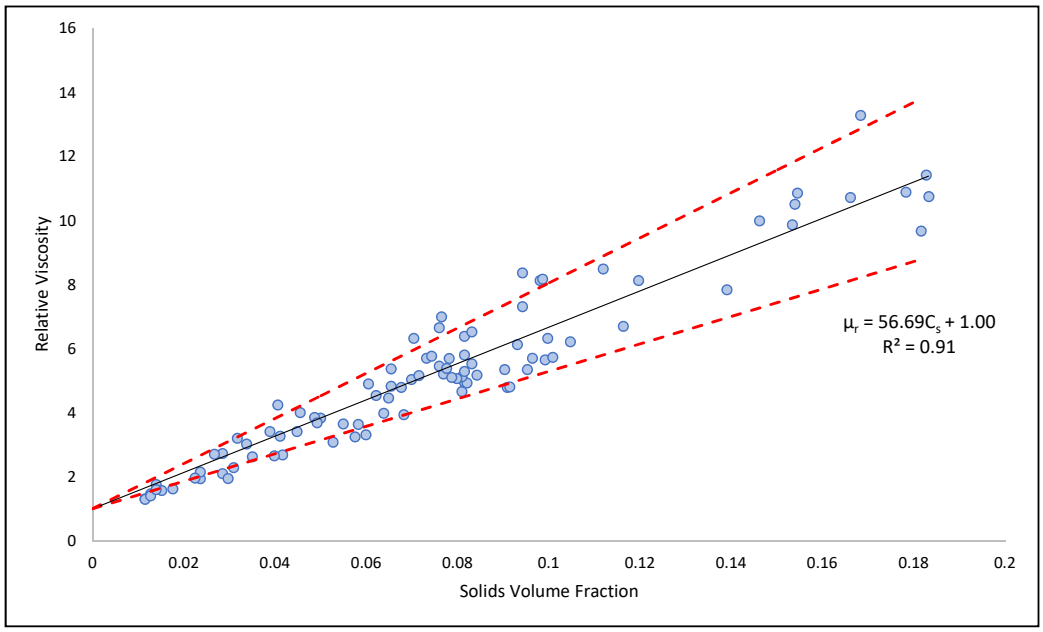

Figure 4.8: Carrier fluid viscosities with linear regression analysis.

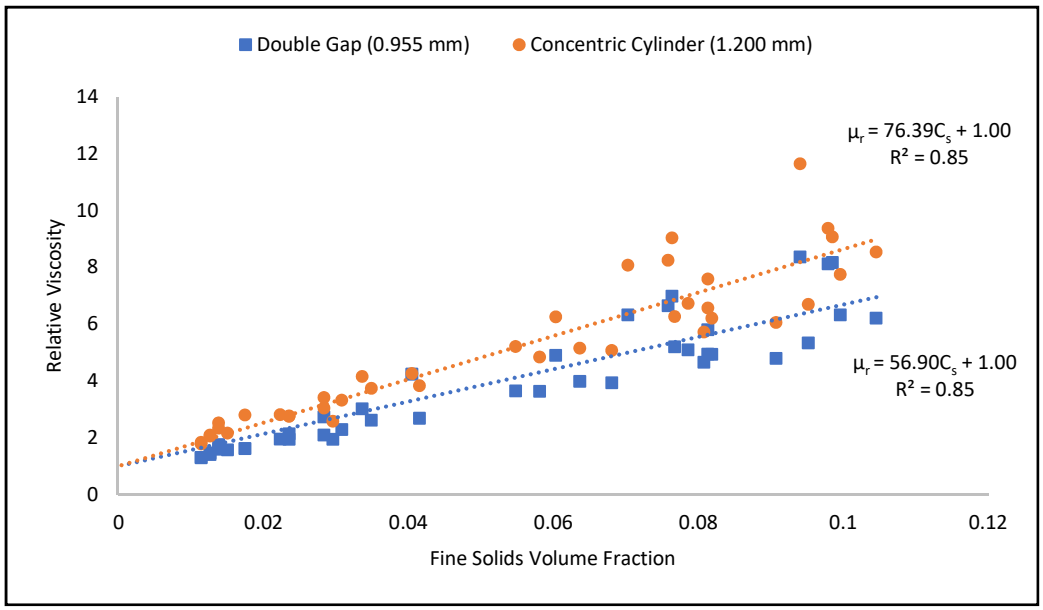

Figure 4.9: Effect of geometries on viscosity correlations

Table 4.14: Comparison of Water Chemistry results

Element	Current Study	Smith [12]
Na	1535	1009
Ca	18	17
SO_4	987	134
Mg	12	11
Cl	944	483
pH	8.96	8.85
Ionic Strength	0.070	0.039

The overall fit for predictions of carrier fluid viscosities by fine solids concentration alone was very poor ($R^2 = 0.48$). In order to develop an improved correlation to predict carrier fluid viscosities, secondary parameters like clay activity and water chemistry were incorporated along with fine solids concentration. Hence, regression analysis was repeated with clay activity and water chemistry parameters in an attempt to develop an improved viscosity correlation. The parameters incorporated and their respective fits are shown in Table 4.15. The detailed correlations are included in Appendix D. Table 4.15 shows that the incorporation of one other factor besides solids concentration marginally improved the overall fit in predicting viscosity. However, the fit remained poor with single additional parameters, and predictions could not be made with a high level of accuracy. Hence, further analysis was conducted with multiple factors besides fine solids concentration. The regression analysis was conducted by maintaining a constant y-intercept to ensure boundary conditions were met with relative viscosity being one at a solids concentration of zero. Previous work done by Smith [12] had shown water chemistry to have a major negative effect on carrier fluid viscosities. Hence, the regression analysis was conducted while allowing factors to maintain negative contributions to viscosity. Additionally, it was discussed in Section 2.4 that Kasperski et al. [29] had found large increases in viscosity when pure Kaolinite was mixed with more active clays. The increase in viscosity was not found to be linear as illustrated by Figure 2.3. Figure 2.3 suggested a change in suspension behavior as the activity of solids in suspension increased. Hence, a correlation was devised to account for different suspension behavior at more active clay conditions. A correlation was developed which was divided based on the CEC and ionic strength (IS) conditions:

Table 4.15: Fit of correlations with incorporation of factors besides fines solids concentration

Factor incorporated with Cs	Fit (R^2)
CEC	0.49
Ionic Strength	0.49
pH	0.48
Concentration of Al^{3+}	0.48
Concentration of SO_4^{2-}	0.57
Concentration of Ca^{2+}	0.48
Concentration of Na^{+}	0.47
Concentration of NO_3^{-}	0.49
Concentration of Cl^{-}	0.48
Concentration of F^{-}	0.50
Concentration of Mg^{2+}	0.49
Concentration of Li^{+}	0.50
Concentration of K^{+}	0.49
CEC and IS	0.50
All Divalent ions	0.70

For CEC<12.5 and IS<0.077

$$\mu_r = 40.22 * C_s + 0.06 * CEC + 1.58 * IS + 1 \tag{4.4}$$

For CEC<12.5 and IS>0.077

$$\mu_r = 197.72 * C_s - 1.36 * CEC + 56.21 * IS + 1 \tag{4.5}$$

For CEC>12.5 and IS<0.070

$$\mu_r = 144.46 * C_s + 0.43 * CEC - 184.22 * IS + 1 \tag{4.6}$$

For CEC>12.5 and IS>0.070

$$\mu_r = -16.62 * C_s - 0.50 * CEC + 191.20 * IS + 1 \tag{4.7}$$

This correlation provided much better predictions of carrier fluid viscosity, as shown in Figure 4.10[13]. It is however, interesting to note the variation in coefficients with different CEC and ionic strength conditions. For example, an observation that can be made by studying the correlation is that at low CEC and ionic strength values, the solids volume fraction dominates with very large coefficients when compared to CEC and IS. On the other hand, at very high CEC and ionic strength, the coefficient of solids volume fractions is negative. This implies that the contribution of fine solids concentration is negative to viscosity as opposed to ionic strength which has a large positive coefficient. This is unexpected and should be investigated further. Previous studies done by Shook et al. [7], Smith [12], Asadi Shahmirzadi [24] have shown no evidence of any negative effects of solids concentration. The large variations in coefficients for fine solids concentrations under different conditions also suggests the presence of more complicated behavior than anticipated here or explained by previous research. It can be assumed that the contribution of fine solids concentration can vary greatly depending on the water chemistry and clay activity levels in a suspension. This questions most previous work done in literature which always suggest a constant coefficient to account for the contribution of fine solids concentration. Similarly, the coefficient for ionic strength varies under different conditions which suggests that water chemistry may also have a greater or lesser impact on viscosity depending on CEC. It is important to note that Smith [12] found a negative coefficient for the correlation of calcium ion concentration and relative viscosity. The equation proposed in this study points to a deeper and more complicated relationship between each parameter than suggested by previous research. Overall, the correlation provides accurate predictions for carrier fluid viscosity with the addition of two parameters besides fine solids concentration. It comprehensively accounts for the contributions of each parameter under different conditions and shows that the variations in viscosities at similar fine solids concentration can be accounted for using particle interaction parameters like CEC and ionic strength.

[13]The double gap viscosities were calculated using the manufacturer recommended constants which assume Newtonian fluid behavior. The possible impact of these constants on the viscosity of non-Newtonian fluids is currently unknown.

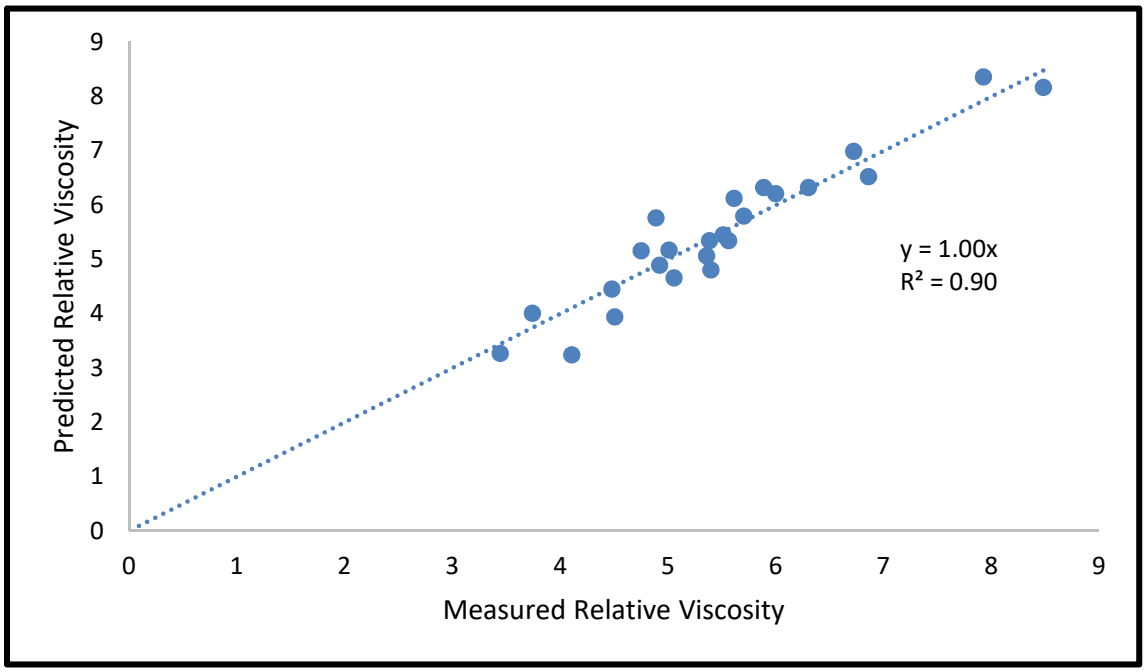

Figure 4.10: Correlation predictions of relative viscosity and measured relative viscosity

Chapter 5

Conclusions and Recommendations for Future Work

5.1 Conclusions

The primary objectives of this study, as stated in Section 1.4, were:

1. To measure carrier fluid viscosities of oil sand slurries.
2. To identify and analyze particle and fluid properties which contribute to carrier fluid viscosities.
3. To develop an empirical model for use by industry to predict carrier fluid viscosities with reasonable accuracy.

This study established a thorough database of carrier fluid viscosities. A diverse set of samples was analyzed which showed the large deviations which can exist in carrier fluid viscosities. The carrier fluid viscosities of samples studied were also consistently higher than predictions made by currently used models. This highlighted the gap that exists in currently used correlations. Viscosities were also shown to vary greatly at similar solids concentration proving the need for incorporation of clay activity and water chemistry factors in addition to concentration. Measurements were conducted using both double gap and concentric cylinder geometries and the difference in results was highlighted. This was a crucial finding due to the prevalence of concentric cylinder geometry in industry to measure carrier fluid viscosities. Potential causes of difference between the results were also explored.

Two factors were analyzed in addition to fines solids concentration for their effects on viscosity. Namely, cation exchange capacity (CEC), a measure of clay activity, and ionic strength, a measure of water chemistry, were found to be major contributing factors. Overall, CEC values were found to be closer to theoretical values for illite clay than kaolinite clay. Results also showed the presence of large amounts of divalent and monovalent ions in carrier fluid samples.

Finally, a correlation was established based on CEC, ionic strength and fine solids concentration to predict carrier fluid viscosities of oil sand slurries. The results of this study prove that the incorporation of particle interaction parameters like CEC and ionic strength can significantly improve predictions of carrier fluid viscosities for use in industry. This offers an excellent alternative to correlations that rely solely on solids concentrations to predict carrier fluid viscosities.

5.2 Recommendations for Future Work

It is recommended that additional work be done to investigate the difference in viscosity results of concentric cylinder and double gap geometries. It was shown that the correlations to predict viscosity also vary based on the geometries used to conduct the viscosity measurements. Further investigation is required to identify the reasons causing the discrepancies and to identify the geometry that may be most useful to make pipeline predictions using the SRC Two Layer Model. The effect of shear and strain constants on viscosity of non-Newtonian fluids should be investigated. The use of other geometries like cone and plate may also offer insight on the causes of such a difference. It is also recommended that pipe loop viscosity measurements be conducted at similar shear rates to confirm viscosity results from this study and to explore the effect of shear rates on viscosity.

Future work should also be conducted to confirm the relationships suggested by the model developed in this study. This can be done by conducting CEC and water chemistry analysis on the remaining carrier fluid samples used during viscosity and composition analyses in this study. This will help offer more insight on the behavior of particles in carrier fluid samples. It is also important to note that the carrier fluid samples analyzed in this study were all collected from the Syncrude North Mine plant. It is recommended that samples be analyzed from other oil sands ores and operations with varying clay activity

properties. This will establish a thorough sample set with different CEC levels and help verify the results of this study before any potential application in industry.

It is further recommended that the impact of particle interactions be studied in-situ since the results of this study suggest complicated particle interactions at high clay activity and water chemistry conditions. This can be achieved using a device similar to a particle video microscope (PVM) which allows the operator to observe the aggregation behavior of particles directly. The aggregation behavior may offer insight on the reason behind the decreasing contribution of solids concentration to viscosity at higher CEC and ionic strength. Future investigations should also focus on the mineralogy of clays present in carrier fluid samples. While this study used CEC to measure the activity of clays present in samples, it would be also be beneficial to utilize techniques like x-ray diffraction (XRD) which offer specific content level of clays. This would be a more time consuming but accurate way of relating the viscosity to composition of individual clay components. It could also be used to confirm the results provided in this study on activity levels of clays in carrier fluid samples.

References

[1] Natural Resources Canada. Oil Resources. URL https://www.nrcan.gc.ca/energy/oil-sands/18085.

[2] Canadian Association of Petroleum Producers. Canada's Energy Resources. URL https://www.capp.ca:443/canadian-oil-and-natural-gas/canadas-petroleum-resources.

[3] M. Pazouki. An Experimental Study on Oil Sand Lump Ablation. URL https://era.library.ualberta.ca/items/bfc169c8-d7f0-47fe-9cf8-efd0130599f9.

[4] R. S. Sanders, J. Schaan, R. Hughes, and C. Shook. Performance of Sand Slurry Pipelines in the Oil Sands Industry. 82(4):850–857, . doi:10.1002/cjce.5450820427.

[5] J. H. Masliyah, Z. Xu, and J. A. Czarnecki. *Handbook on Theory and Practice of Bitumen Recovery from Athabasca Oil Sands*. Kingsley Knowledge Pub. ISBN 978-1-926832-03-6 978-1-926832-16-6. OCLC: 697934334.

[6] R. S. Sanders and R. G. Gillies. Hydrotransport. In *Handbook on Theory and Practice of Bitumen Recovery from Athabasca Oil Sands. Volume 2. Industrial Practice*. Kingsley Knowledge Publishing. ISBN 978-1-926832-16-6.

[7] C. A. Shook, R. G. Gillies, and R. S. Sanders. *Pipeline Hydrotransport : With Applications in the Oil Sand Industry /*. SRC Pipe Flow Technology Centre,. ISBN 978-1-895880-20-5.

[8] R. G. Gillies, C. A. Shook, and K. C. Wilson. An improved two layer model for horizontal slurry pipeline flow. 69(1):173–178. doi:10.1002/cjce.5450690120.

[9] B. Bbosa, E. DelleCase, M. Volk, and E. Ozbayoglu. A comprehensive deposition velocity model for slurry transport in horizontal pipelines. 7(1):303–310. doi:10.1007/s13202-016-0259-1.

[10] A. J. S. . Buchan and A. J. . . Spearing. The effect of corrosion on the wear rate of steel pipelines conveying backfill slurry. 94(2):37–45.

[11] K. Bakx. What causes pipeline spills in Canada? | CBC News. URL https://www.cbc.ca/news/business/cepa-2016-safety-report-1.3654640.

[12] J. L. Smith. Measurement of Carrier Fluid Viscosities for Oil Sand Extraction and Tailings Slurries. URL https://era.library.ualberta.ca/items/1f84dad5-3053-4ef7-b3d1-2494241fadcd.

[13] L. L. Schramm. The Influence Of Suspension Viscosity On Bitumen Rise Velocity And Potential Recovery In The Hot Water Flotation Process For Oil Sands. 28(03), . doi:10.2118/89-03-07.

[14] S. Sanders, J. Munkler, and R. Sumner. Viscometer and Pipeloop Tests of Syncrude Fine Tailings. In *Pipeline Symposium*, .

[15] V. Wolff. Bitumen Separation. In *Handbook on Theory and Practice of Bitumen Recovery from Athabasca Oil Sands. Volume 2. Industrial Practice*. Kingsley Knowledge Publishing. ISBN 978-1-926832-16-6.

[16] A. Einstein. Eine neue Bestimmung der Moleküldimensionen. 324(2):289–306. doi:10.1002/andp.19063240204.

[17] K. Toda and H. Furuse. Extension of Einstein's viscosity equation to that for concentrated dispersions of solutes and particles. 102(6):524–528. doi:10.1263/jbb.102.524.

[18] M. Kunitz. AN EMPIRICAL FORMULA FOR THE RELATION BETWEEN VISCOSITY OF SOLUTION AND VOLUME OF SOLUTE. 9(6):715–725. doi:10.1085/jgp.9.6.715.

[19] D. G. Thomas. Transport characteristics of suspension: VIII. A note on the viscosity of Newtonian suspensions of uniform spherical particles. 20(3):267–277, . doi:10.1016/0095-8522(65)90016-4.

[20] S. G. Ward and R. L. Whitmore. Studies of the viscosity and sedimentation of suspensions Part 1. - The viscosity of suspension of spherical particles. 1(11):286–290. doi:10.1088/0508-3443/1/11/303.

[21] A. A. Zavitsas. A Different Interpretation of Einstein's Viscosity Equation Provides Accurate Representations of the Behavior of Hydrophilic Solutes to High Concentrations. 116(33):10055–10069. doi:10.1021/jp306248a.

[22] G. Broughton and C. S. Windebank. Agglomeration and Viscosity in Dilute Suspensions. 30(4):407–409. doi:10.1021/ie50340a009.

[23] A. D. Thomas. The Influence of Coarse Particles on the Rheology of Fine Particle Slurries. In *Proceedings of Rheology in the Mineral Industry II*, pages 113–123, .

[24] A. Asadi Shahmirzadi. The Effect of Fine Flocculating Particles and Fine Inerts on Carrier Fluid Viscosity. URL https://era.library.ualberta.ca/items/57e97631-5e91-491b-9e51-8cd33188c729.

[25] H. A. W. Kaminsky, T. H. Etsell, D. G. Ivey, and O. Omotoso. Distribution of clay minerals in the process streams produced by the extraction of bitumen from Athabasca oil sands. 87(1):85–93. doi:10.1002/cjce.20133.

[26] P. F. Luckham and S. Rossi. The colloidal and rheological properties of bentonite suspensions. 82(1):43–92. doi:10.1016/S0001-8686(99)00005-6.

[27] L. Georgehowarth. RHEOLOGICALSTUDIES OF BENTONITEDISPERSIONS. page 377.

[28] T. Kasongo, Z. Zhou, Z. Xu, and J. Masliyah. Effect of clays and calcium ions on bitumen extraction from athabasca oil sands using flotation. 78(4):674–681. doi:10.1002/cjce.5450780409.

[29] K. Kasperski, C. Hepler, and L. G. Hepler. Viscosities of dilute aqueous suspensions of montmorillonite and kaolinite clays. 64:1919–1924. doi:10.1139/v86-316.

[30] J. Kameda and T. Morisaki. Sensitivity of Clay Suspension Rheological Properties to pH, Temperature, Salinity, and Smectite-Quartz Ratio. 44. doi:10.1002/2017gl075334.

[31] J. K. Mitchell. *Fundamentals of Soil Behavior*.

[32] L. Meier. Determination of the Cation Exchange Capacity (CEC) of Clay Minerals Using the Complexes of Copper(II) Ion with Triethylenetetramine and Tetraethylenepentamine. 47:386–388. doi:10.1346/CCMN.1999.0470315.

[33] H. Kaminsky. DEMYSTIFYING THE METHYLENE BLUE INDEX.

[34] R. Currie, H. Mian, S. Bansal, and I. Khan. An Investigation of the Methylene Blue Titration Method for Clay Activity of Oil Sands Samples. URL https://era.library.ualberta.ca/items/b831aa15-7986-4c6f-a7e8-439f02b1b59d.

[35] P. Bohác, L. Delavernhe, E. Zervas, F. Königer, R. Schuhmann, and K. Emmerich. Cation exchange capacity of bentonite in a saline environment. 100:407–413. doi:10.1016/j.apgeochem.2018.12.019.

[36] A. Steudel, P. G. Weidler, R. Schuhmann, and K. Emmerich. Cation Exchange Reactions of Vermiculite with Cu-Triethylenetetramine as Affected by Mechanical and Chemical Pretreatment. 57:486–493. doi:10.1346/CCMN.2009.0570409.

[37] C. G. Litzenberger. Rheological study of kaolin clay slurries.

[38] Z. Zhou, O. Worku, L. Wang, Z. Xu, and J. H. Masliyah. Viscosity of mixed clay suspensions. 3:54–61.

[39] A. S. Michaels and J. C. Bolger. Particle Interactions in Aqueous Kaolinite Dispersions. 3(1):14–20. doi:10.1021/i160009a003.

[40] M. Marefatallah. Effect of Sonication on the Particle Size of Kaolinite Clays.

[41] C. A. Shook and M. C. Roco. *Slurry Flow: Principles and Practice*. Elsevier. ISBN 978-1-4832-9220-5.

[42] T. G. Mezger. *The Rheology Handbook: For Users of Rotational and Oscillatory Rheometers*. Vincentz Network GmbH & Co KG. ISBN 978-3-87870-174-3.

[43] R. S. Sanders. Course Notes - Fluid-Particle Systems and Applications.

[44] R. B. Bird, W. E. Stewart, and E. N. Lightfoot. *Transport Phenomena*. Wiley. ISBN 978-0-471-41077-5.

[45] TA Instruments. DHR-2 User Manual.

[46] A. Nosrati, J. Addai-Mensah, and W. Skinner. Rheology of aging aqueous muscovite clay dispersions. 66(2):119–127. doi:10.1016/j.ces.2010.06.028.

[47] P. Estellé, C. Lanos, and A. Perrot. Processing the Couette viscometry data using a Bingham approximation in shear rate calculation. 154(1):31–38. doi:10.1016/j.jnnfm.2008.01.006.

[48] G. I. Taylor. Fluid Friction between Rotating Cylinders. I. Torque Measurements. 157: 546–564. doi:10.1098/rspa.1936.0215.

[49] E. W. Dean and D. D. Stark. A Convenient Method for the Determination of Water in Petroleum and Other Organic Emulsions. 12(5):486–490. doi:10.1021/ie50125a025.

[50] J. Starr, J. T. Bulmer, and Syncrude Canada Ltd. *Syncrude Analytical Methods for Oil Sand and Bitumen Processing*. Edmonton : Alberta Oil Sands Technology and Research Authority.

[51] T. Gradek and T. Gradek. Hydrocarbon extraction by oleophilic beads from aqueous mixtures. URL https://patents.google.com/patent/US20100072110A1/en.

[52] Rheometer: MCR 102, MCR 302, MCR 502 :: Anton-Paar.com. URL https://www.anton-paar.com/ca-en/products/details/rheometer-mcr-102-302-502/.

[53] Y. Sun. Recovery of Thickened Kaolinite Suspension Properties Through Shear.

[54] R. Neelakantan. Effect of Shear Energy Input on the Rheology of Flocculant- Dosed Kaolinite Suspensions.

[55] K. Cheng and Z. Heidari. A new method for quantifying cation exchange capacity in clay minerals. 161:444–455. doi:10.1016/j.clay.2018.05.006.

[56] L. L. Schramm. Suspensions: Basic Principles. In *Suspensions: Fundamentals and Applications in the Petroleum Industry*, volume 251 of *Advances in Chemistry*, pages 3–44. American Chemical Society, . ISBN 978-0-8412-3136-8. doi:10.1021/ba-1996-0251.ch001.

Appendix A

Safe Work Procedure (SWPs)

A.1 Safe Work Procedure for Sample Preparation of Carrier Fluid Samples

The safe work procedure used for sample preparation of carrier fluid samples is attached.

SAFE WORK PROCEDURE (SWP) FOR CARRIER FLUID PREPARATION FROM SLURRY SAMPLES

Location: CME 2-156, University of Alberta

Job title: Sample Preparation of Carrier Fluid Samples	**Date Updated:** January 19, 2019
Written by: Ghassan I. Khan	**Conducted by:**
	Ghassan I. Khan

Required personal protective equipment (PPE) and laboratory equipment: Safety glasses, nitrile gloves, lab coat, full length pants, closed toe shoes, fume hood
Hazards present: • Toluene (Systematic IUPAC name: Methylbenzene) is a hazardous irritant when ingested, inhaled, or when in contact with skin or eyes. When handling toluene, do so under the fume hood with gloves and safety glasses. For extended contact, use viton gloves. Refer to toluene MSDS for additional information. • Spilling fluid near electronic devices can cause damage to them; ensure absorbent paper towels are on hand at all times. • Naphtha should be handled with caution under a fume hood during reusable hydrocarbon sorbent (RHS) beads regeneration. Nitrile gloves can be used to handle naphtha. Refer to naphtha MSDS for additional information.
First aid measures: Antiseptic wash, gauze pads, adhesive tapes, bandages, instant cold pack, spill kit, and burn relief gel.

Carrier Fluid Separation

The following is a step-by-step procedure detailing the removal of coarse particles from slurry to collect carrier fluid.

Step	Description and Sequence of SWP Steps	Potential Hazards / Notes
1	• Ensure absorbent paper towel is laid down under work area in case of spill. • Retrieve the 200-mesh sieve (75 microns opening) and collection pan. Ensure sieve is properly secured over collection pan. • Shake raw slurry container to disperse settled particles. Pour the slurry sample onto the 200-mesh sieve (75 microns opening).	Spill hazard; have adsorbent papers on hand.
2	• Shake sieve and collection pan until all applicable liquid and fines have passed through the mesh. The liquid and fine particles in collection pan are known as the carrier fluid. • Pour carrier fluid into sample container. Label the container clearly.	Fine mesh is prone to clogging. Pour raw slurry slowly and shake gently.
3	• Carefully collect the solids left on the sieve and store them for further analysis in a container. This could be collected by scooping out the remaining solids. • Clearly label the container with size of the particles (e.g. >75µm), date, and sample number.	Be careful not to damage or tear the sieve while scooping the left over solids.
4	Remove 10 mL of carrier fluid for QuickBit testing.	Quickbit testing procedure is detailed below.

QuickBit Testing

The following procedure is used for QuickBit analysis to determine bitumen content of the carrier fluid.

Step	Description and Sequence of SWP Steps	Potential Hazards / Notes
1	In two 15 mL test tubes, add 5 mL carrier fluid sample and 5 mL toluene to each. Two test tubes are needed to balance the centrifuge.	Toluene is a volatile irritant. Complete this step under the fume hood or wear a vapor respirator.
2	Cap the test tubes and shake. Shake vigorously for approximately 5 minutes, or until mixture is homogeneous.	
3	• Place test-tubes in centrifuge in balanced positions (cross positions). • Run centrifuge at 3400 RPM for 15 minutes and visually inspect for two layers of fluid. Continue centrifuging if two distinct layers are not visible.	Centrifuge may vibrate and move. Never leave running equipment unattended.
4	• Using a syringe and needle, remove 2 mL of the upper phase (oil phase). • Weigh 1 piece of Whatman 5 Qualitative filter paper, record weight. (i) *Initial weight* = _____*g* • Place 2 mL sample onto filter paper. Allow time to dry. Once dried, weigh paper again, and record. (ii) *Final weight* = _____*g* • The bitumen weight is the difference between ii and i. *Bitumen weight* = _____*g* • This weight, multiplied by 2.5, is the mass of bitumen per 5 mL sample. *Bitumen per 5 ml sample* = _____*g*	
5	Dispose remaining oil phase in clearly marked disposal container. Repeat step 4 for second test tube to confirm bitumen content.	

Bitumen Removal

This procedure relies on information obtained from QuickBit testing. Please ensure QuickBit analysis is performed before starting this step.

Step	Description and Sequence of SWP Steps	Potential Hazards / Notes
1	The hot water bath takes a long time to warm up. Set the temperature to 45 °C well in advance to avoid waiting.	Ensure the water level in the bath is appropriate.
2	Remove 400 mL of carrier fluid and place into a glass jar with a metal baffle already placed inside.	
3	Add RHS beads to the jar at a 6:1 bead-to-bitumen ratio by mass. *Bitumen per 5 ml sample = _____g* *(from step 4 of the QuickBit Testing procedure)* x *80* = _____*g (bitumen in 400 ml sample)* x *6* = _____*g (mass of RHS beads required)*	These calculations are for 400 mL carrier fluid; they can change depending on the volume of carrier fluid remaining upon reaching this step[14].
4	Heat the jar containing beads and carrier fluid using the hot water bath set at 45 °C for 10 minutes.	Spill hazard; have adsorbent papers on hand.
5	• Place jar on the rotating mixer and mix for 10 minutes at 70 RPM. • Remove the jar and allow the RHS beads to rise to the top of the container.	
6	• Strain liquid into a beaker using large metal mesh strainer. Retain beads for regeneration. • Repeat steps 3-5 an additional five times to complete bitumen removal.	
7	Regeneration of RHS beads: 1. Wash RHS beads in fume hood with Coleman Naphtha Camp Fuel. Wipe excess Camp fuel with paper towel and allow the beads to dry in a fume hood. Carefully dispose Naphtha camp fuel in properly labelled container. 2. Heat the dried beads in the vacuum oven at 75 °C for 10 minutes to get rid of all remaining Naphtha. The vacuum oven should be connected to a pump that can generate a vacuum in order to minimize exposure to fumes. The pressure measured should be around -7 kPa.	• Naphtha (used for beads regeneration) should be handled with extra care under the fume hood. • Use vacuum oven only. Using regular oven to heat flammable materials like naphtha camp fuel is very dangerous and can lead to a fire.
8	Once bitumen removal is complete, proceed to analysis.	

[14] Assuming a uniform concentration (mass of bitumen per volume of sample) throughout the carrier fluid, the mass of bitumen in any volume of sample can be calculated using:

$$m_{V_{Carrier\ Fluid}} = m_{5\ mL\ of\ Carrier\ Fluid} \times \left(\frac{V_{Carrier\ Fluid}}{5\ mL}\right)$$

A.2 Safe Work Procedure for Viscosity Measurements of Carrier Fluid Samples

The safe work procedure used for viscosity measurements of carrier fluid samples is attached.

SAFE WORK PROCEDURE (SWP) FOR CARRIER FLUID VISCOSITY MEASUREMENTS OF SLURRY SAMPLES

Location: CME 2-156, University of Alberta

Job title: Viscosity Measurements of Carrier Fluid Samples	**Date Updated:** January 19, 2019
Written by: Ghassan I. Khan	**Conducted by:**
	Ghassan I. Khan

Required personal protective equipment (PPE) and laboratory equipment:
Safety glasses, nitrile gloves, lab coat, full length pants, closed toe shoes, fume hood
Hazards present: • Spilling fluid near electronic devices can cause damage to them; ensure absorbent paper towels are always on hand. • Absence of water in the temperature control system of the rheometer and hot water bath can cause short circuiting of the equipment; resulting in damage to said equipment and potential harm to personnel. The liquid level on all applicable instruments must be double checked and, if necessary, filled prior to each use.
First aid measures: Antiseptic wash, gauze pads, adhesive tapes, bandages, instant cold pack, spill kit, and burn relief gel.

Rheometry
The following procedure is for measuring the rheological properties of carrier fluid samples.

Step	Description and Sequence of SWP Steps	Potential Hazards / Notes
1	Mix the carrier fluid sample using an overhead mixer and 45 degrees pitch blade impeller at 400 RPM for 1 hour.	
2	Once solution is ready to be tested, open valve to rheometer air supply and verify pressure is 32 psi.	Low air pressure does not allow the system to run and causes serious damage to the instrument
3	Remove bearing lock from rheometer and ensure the spindle bearing moves freely.	.
4	Turn on computer, rheometer and temperature control system. Click on instrument software and verify rheometer and computer connection is active Check liquid level in the temperature control tank.	The water level must be up to the lower part of the neck. If it is not enough, use de-ionized water to top up.
5	Calibrate rheometer without any attached geometry: calibration menu > calibration tab > “Calibrate”> “Accept”	.
6	Attach appropriate geometry to rheometer bearing. Click Geometry menu> select geometry	Always tighten the shaft from above. Avoid putting any pressure on the geometry.
7	Perform instrument mapping: Calibration menu> rotational mapping tab> precision mapping, 2 iterations> “Calibrate”	
8	Adjust temperature set-point to 25°C Wait for equilibrium. Check the temperature reading under the instrument display for a constant value.	
9	Perform zero gap measurement. Click Instrument menu> “Zero Gap Click “Start”.	
10	Once zero gap measurement is complete, click Instrument menu> Click “Raise to Loading Gap”.	
11	Experiment menu> create test procedure appropriate for sample Add the following steps: • Shear conditioning step for 60s at 25 rad/s • Flow sweep up from 0.1 rad/s to 20 rad/s • Flow sweep down from 20 rad/s to 0.1 rad/s • Activate steady state sensing and set parameters to 5 consecutive values for 5%	
12	Using a large syringe, add 17 mL of sample to the rheometer cup for CCV and 13 mL for double gap geometry. Click “Go to Geometry Gap”. Once rotor is in place, click the START button on the Home menu.	
13	For each sample, plot torque vs. angular velocity and use the appropriate equation to calculate viscosity from the slope of	

	graphs. For CCV this equation is: $$w = \frac{T}{4\pi L\mu}\left[\frac{1}{R1^2} - \frac{1}{R2^2}\right] - \frac{\tau}{\mu} ln \frac{R2}{R1}$$ For double gap geometry, refer to section 2.6.2.	
14	• Once test is complete, click raise to loading gap in geometry menu. • Remove cup and dispose sample in appropriately labeled container. • Clean cup and geometry with soap and warm water. Dry with paper towel.	Always tighten or loosen rotor with the screw on top of the rheometer.
15	• Turn off computer, rheometer, and temperature control system. • Replace bearing lock and turn off rheometer air supply. • Carefully place rheometer geometries back into holders.	

Before leaving the lab, tidy the lab area. Wash all equipment and hang on drying rack. Ensure all waste is properly labelled and placed in the appropriate waste disposal area. Contact Terry Runyon to inform her of waste that needs to be disposed.

A.3 Safe Work Procedure for Determination of CEC for Carrier Fluid Samples

SAFE WORK PROCEDURE (SWP) FOR CEC DETERMINATION OF SLURRY SAMPLES
Location: CME 2-156

Job title: CEC Determination of Carrier Fluid Samples	**Date Updated:** July 2nd, 2019
Written by: Ghassan I. Khan	**Conducted by:** Ghassan I. Khan

Required personal protective equipment (PPE) and laboratory equipment: Safety glasses, nitrile gloves, lab coat, full length pants, closed toe shoes, fume hood
Hazards present: • Strong bases such as sodium hydroxide (NaOH) are caustic and must be handled with caution. Contact with the fluid will lead to chemical burns. Use appropriate gloves and safety glasses at all times. Refer to MSDS for more information. • The sonicator enclosure must be closed while the sonicator is running to provide protection from noise. Use ear protection for extended exposure.
First aid measures: Antiseptic wash, gauze pads, adhesive tapes, bandages, instant cold pack, spill kit, and burn relief gel.

Solids and Solutions Preparation

A step-by-step procedure detailing the preparation of solid samples and solutions required for experimentation.

Step	Description and Sequence of SWP Steps	Potential Hazards / Notes
	Solids Preparation	
1	• Place 1.5g of dry, bitumen free solids in styrene plastic containers.	
2	• Dry the solids in a vacuum oven at 90ºC for 2 hours.	
3	• Remove solids from vacuum oven and allow to cool in fume hood.	Use gloves as container will be very hot
	0.030 M CuTrien Solution Preparation	
4	• Add 1.08g of triethylenetetramine to a 250 mLvolumetric flask using a disposable pipette.	Fresh CuTrien solution must be prepared daily to avoid solution degradation.
5	• Add 1.87g of copper (II) sulfate pentahydrate to a 50mL beaker. • Verify mass is accurate • Add enough ultrapure water to beaker to dissolve copper (II) sulfate pentahydrate. Use stirring to promote dissolution solids. • Once solids are completely dissolved, pour solution into volumetric flask with triethylenetetramine.	
6	• Bring solution to volume with ultrapure water • Store at room temperature and use within 24 hours of preparation	
	0.015 M $NaHCO_3$ Solution Preparation	
7	• Add 1.26g of $NaHCO_3$ to a 1L volumetric flask • Bring to volume with ultrapure water	
8	• Transfer this solution to a beaker with a magnetic stir bar • Add pH probe to solution in beaker and record pH of solution	
9	Add 1M NaOH using a disposable pipette until pH is 9.6	
10	• Transfer buffer solution to a suitable storage container • Use within 24 hours of preparation	

CEC Procedure

The procedure used to measure the exchange capacity of solids in carrier fluid samples.

Step	Description and Sequence of SWP Steps	Potential Hazards / Notes
1	Label three 4oz. jars as standards 1,2 and 3. Label one jar each for samples being analyzed including two quality control samples. Also label one jar as a blank.	
2	Weigh each jar and record mass of jars with lids. • Weigh each jar and record mass of jars with lids. • Add previously dried samples to respective jars and record mass of jars with solids.	
3	• Add 3mL of isopropyl alcohol to each jar • Add 30mL, 80mL and 50mL of bicarbonate buffer to standards 1,2 and 3 respectively. Add 40mL of bicarbonate buffer to samples and blank jars.	
4	• Set the sonic probe approximately 1cm from the bottom of the jar. • Sonicate each sample except standards for 4 minutes at 100% amplitude (600W)	Use ear protection as necessary.
5	• Add 10mL of Cu-trien solution to all jars except standard 3. • Place jars in shaker for 30 minutes.	
6	Record final mass of jars	
7	Filter 3mL of each sample, blank and standard using a 0.1 micrometer syringe filter into a cuvette for absorbance analysi.	

Spectrometer Procedure
The procedure used to measure the absorbance using a spectrometer is outlined.

Step	Description and Sequence of SWP Steps	Potential Hazards / Notes
1	• Turn on spectrometer and computer. • Turn on spectrometer software and verify active connection between device and computer. • Verify absorbance setting is selected. • Select a wavelength range from 400nm to 800nm.	
2	• Place cuvette with ultrapure water in cuvette holder • Zero spectrometer at 577nm	
3	• Place jar on the rotating mixer and mix for 10 minutes. • Remove the jar and allow the RHS beads to rise to the top of the container. • Once previous step is complete, proceed to measure absorbance as follows: 1. Standard 1 2. Standard 2 3. Standard 3 4. Quality Control 1 5. Method Blank 6. All unknown samples 7. Method Blank 8. Quality Control 2 If more than 10 unknown samples are being analyzed, perform method blank after every 10 samples.	
4	Once all absorbance measurements are complete, export data and turn off spectrometer.	
5	• Pour all unused solutions and samples into appropriately labeled waste containers • Wash cuvettes and jars with soap and water and dry for future use	
6	• Derive calibration curve using three standards • Use calibration curve to convert absorbance readings to final concentrations and calculate CEC as outlined in equation 2.8	

Appendix B

Rheometry Results

B.1 Concentric Cylinder Geometry

The Torque vs. angular velocity graphs for all samples analyzed with concentric cylinder geometry are attached.

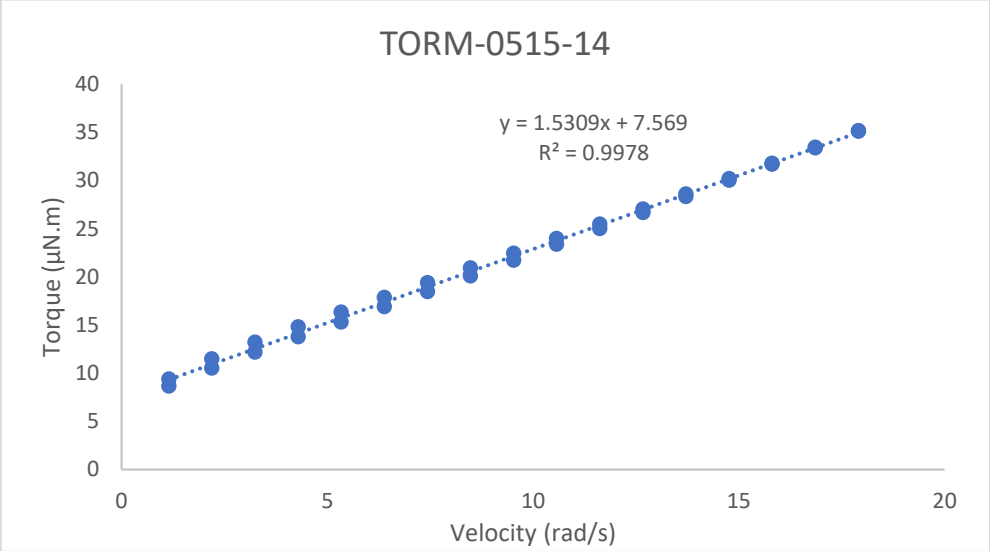
TORM-0515-14
y = 1.5309x + 7.569
R² = 0.9978
Torque (µN.m)
Velocity (rad/s)
0
5
10
15
20
25
30
35
40

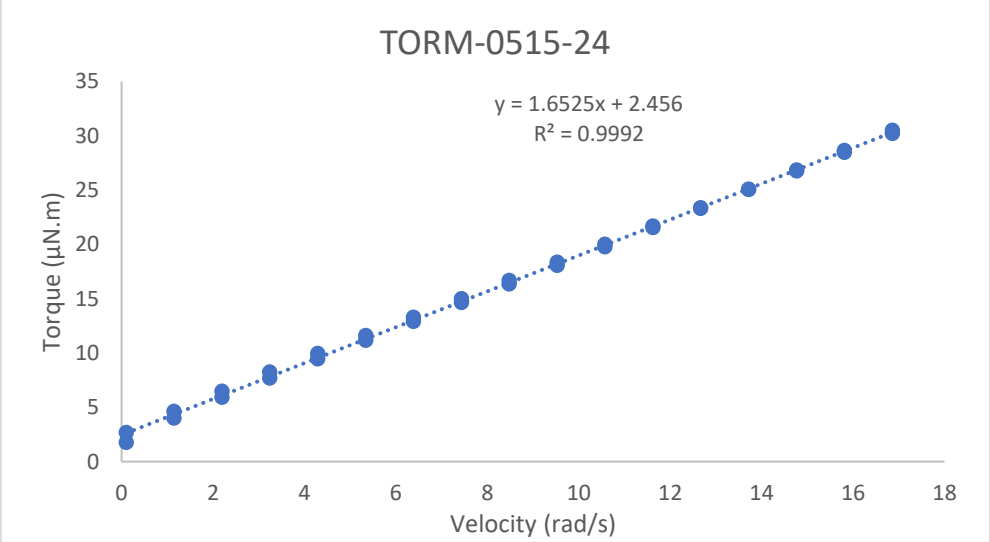
TORM-0515-24
y = 1.6525x + 2.456
R² = 0.9992
Torque (µN.m)
Velocity (rad/s)
0
2
4
6
8
10
12
14
16
18
0
5
10
15
20
25
30
35

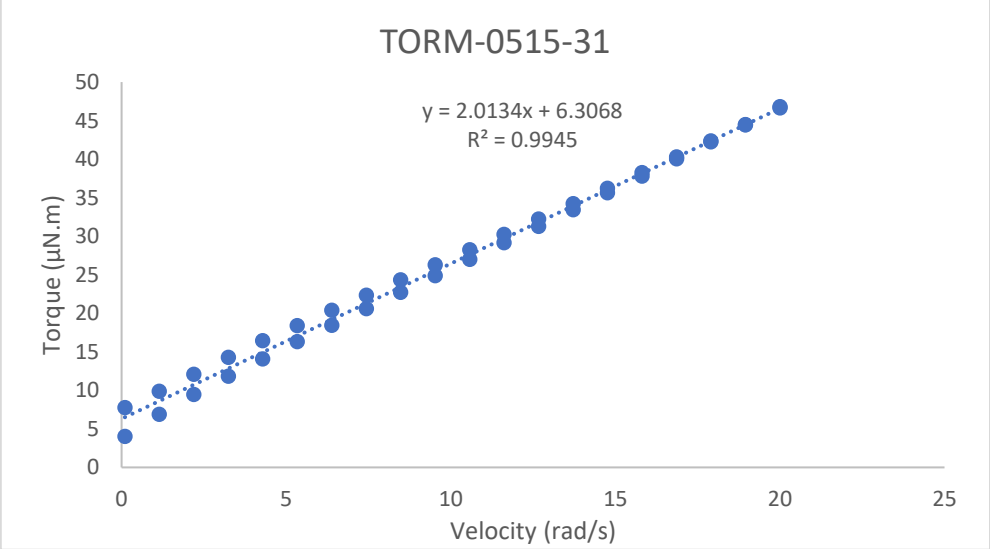
TORM-0515-31
y = 2.0134x + 6.3068
R² = 0.9945
Torque (µN.m)
Velocity (rad/s)
0
5
10
15
20
25
0
5
10
15
20
25
30
35
40
45
50

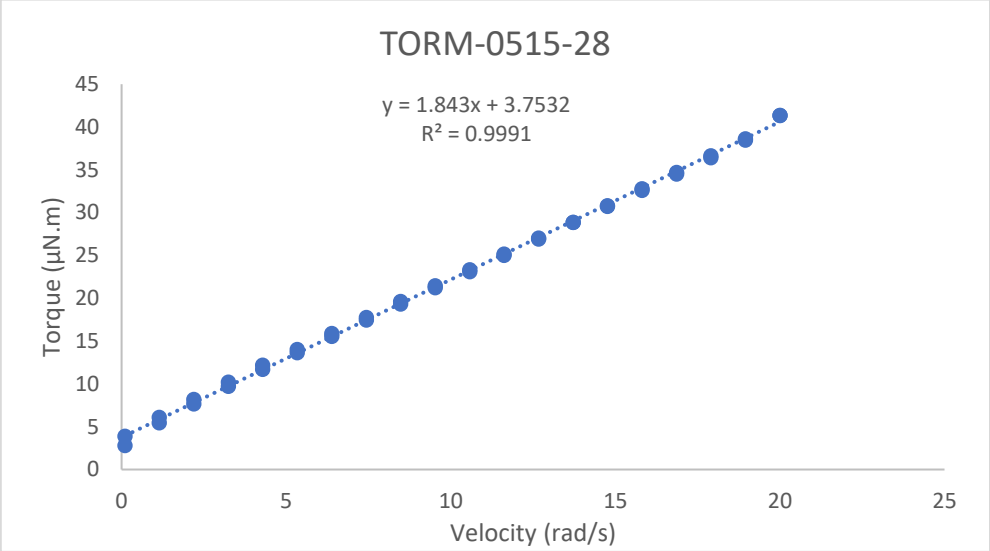
TORM-0515-28
y = 1.843x + 3.7532
R² = 0.9991
Torque (µN.m)
Velocity (rad/s)
0
5
10
15
20
25
30
35
40
45

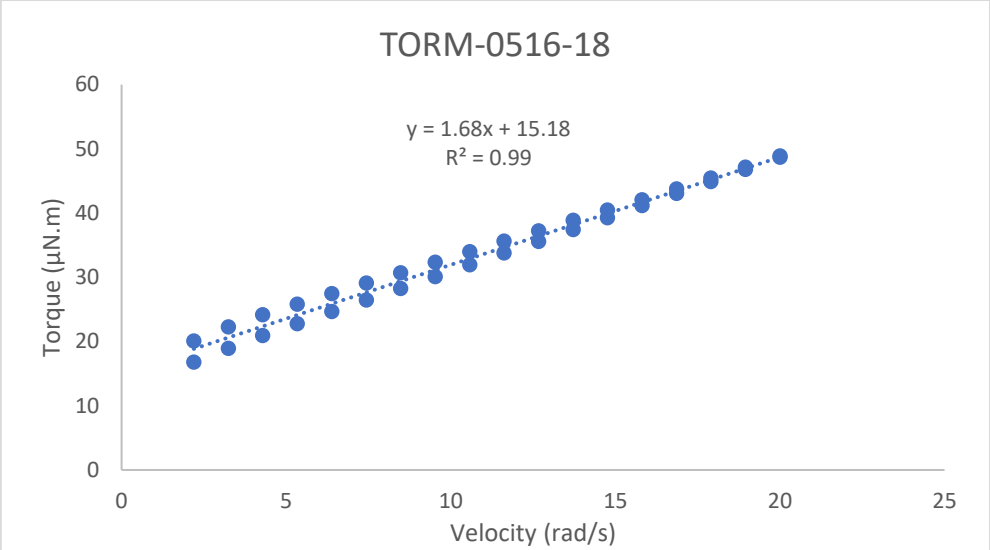
TORM-0516-18
y = 1.68x + 15.18
R² = 0.99
Torque (µN.m)
Velocity (rad/s)
0
10
20
30
40
50
60

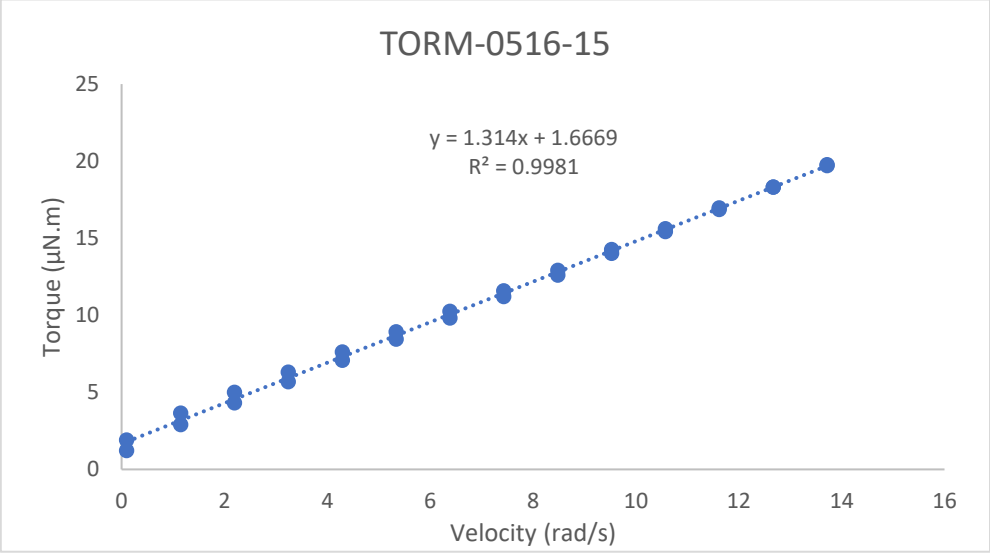
TORM-0516-15
y = 1.314x + 1.6669
R² = 0.9981
Torque (µN.m)
Velocity (rad/s)
0
5
10
15
20
25
2
4
6
8
12
14
16

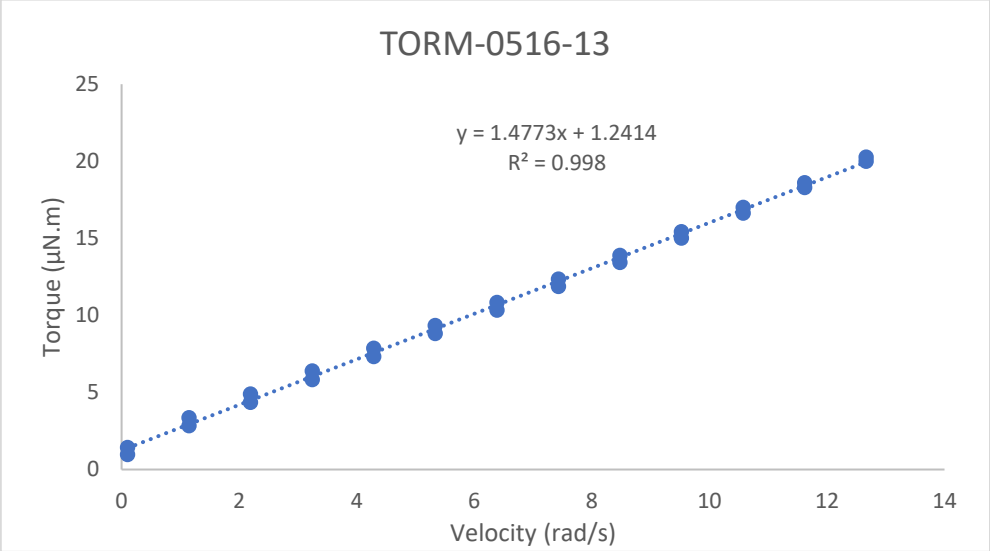
TORM-0516-13
y = 1.4773x + 1.2414
R² = 0.998
Torque (µN.m)
Velocity (rad/s)
0
5
10
15
20
25
0
2
4
6
8
10
12
14

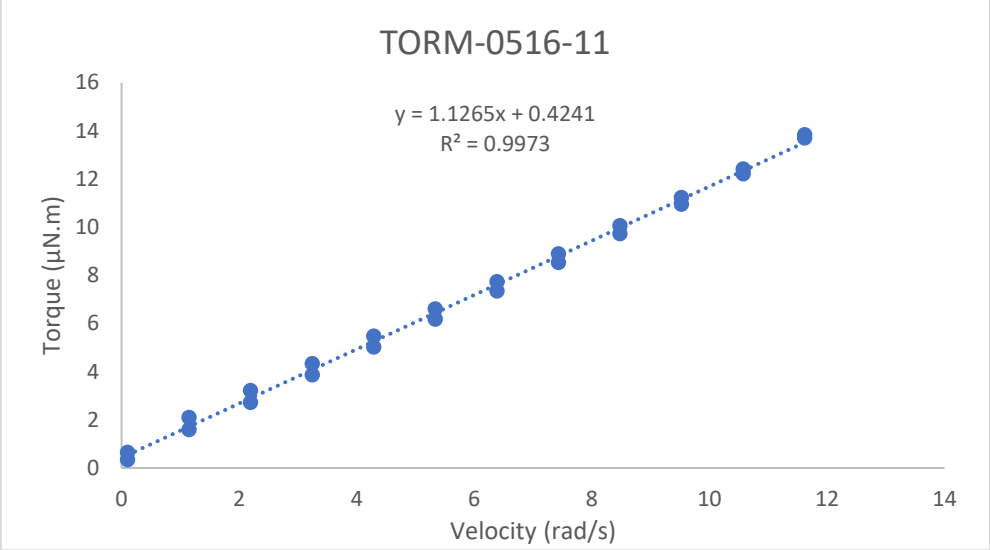
TORM-0516-11
y = 1.1265x + 0.4241
R² = 0.9973
Torque (µN.m)
Velocity (rad/s)
0
2
4
6
8
10
12
14
16
0
2
4
6
8
10
12
14

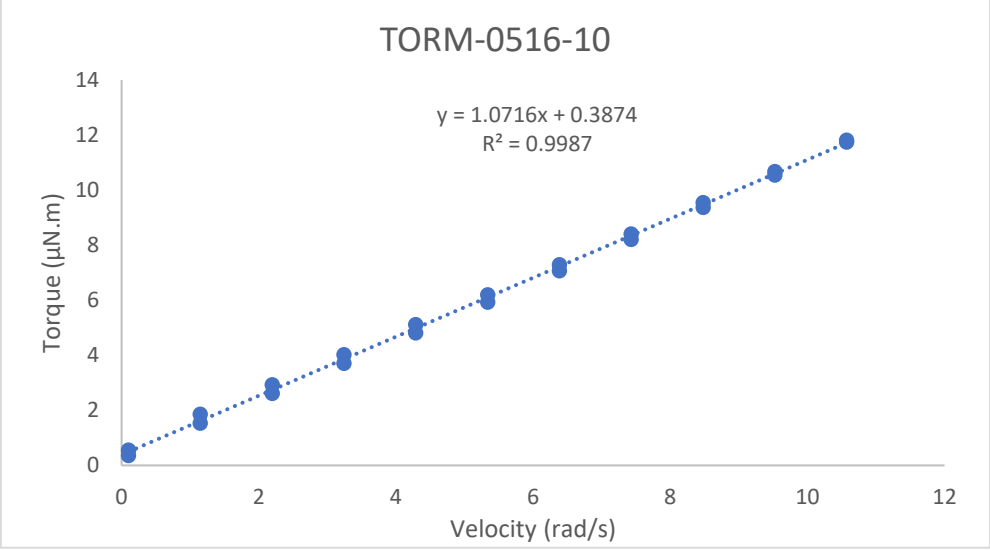
TORM-0516-10
y = 1.0716x + 0.3874
R² = 0.9987
Torque (µN.m)
Velocity (rad/s)
0
2
4
6
8
10
12
14
0
2
4
6
8
10
12

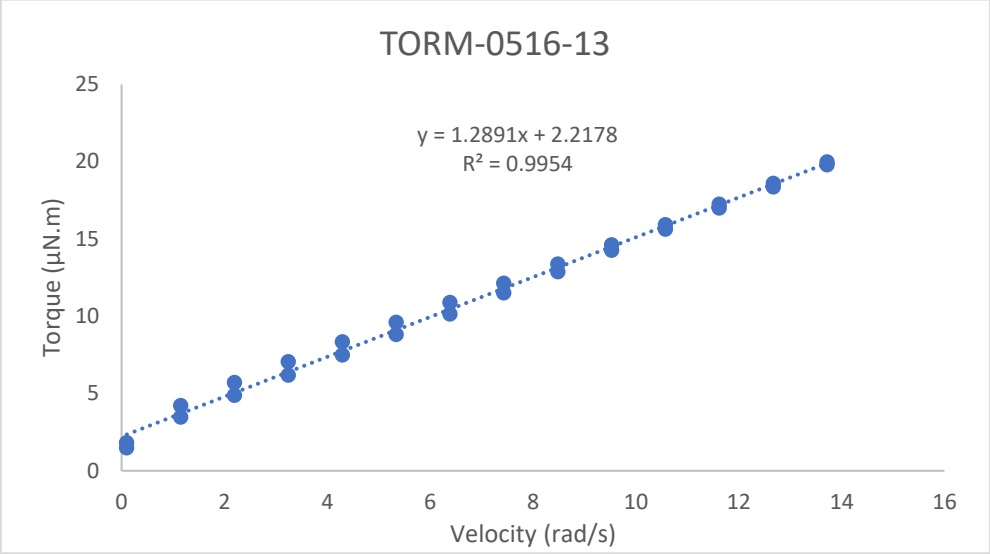
TORM-0516-13
y = 1.2891x + 2.2178
R² = 0.9954
Torque (µN.m)
Velocity (rad/s)
0
5
10
15
20
25
0
2
4
6
8
10
12
14
16

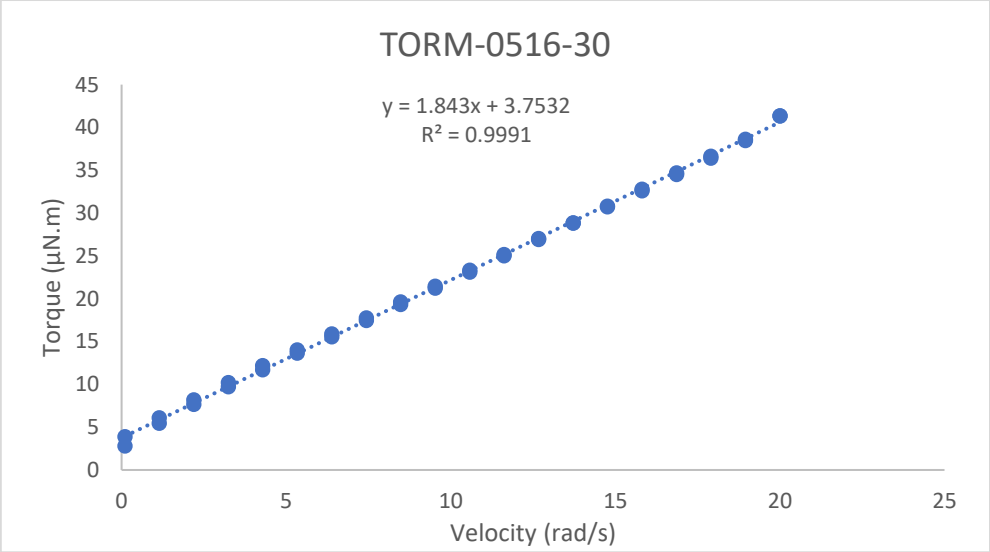
TORM-0516-30
y = 1.843x + 3.7532
R² = 0.9991
Torque (µN.m)
Velocity (rad/s)
0
5
10
15
20
25
30
35
40
45
0
5
10
15
20
25

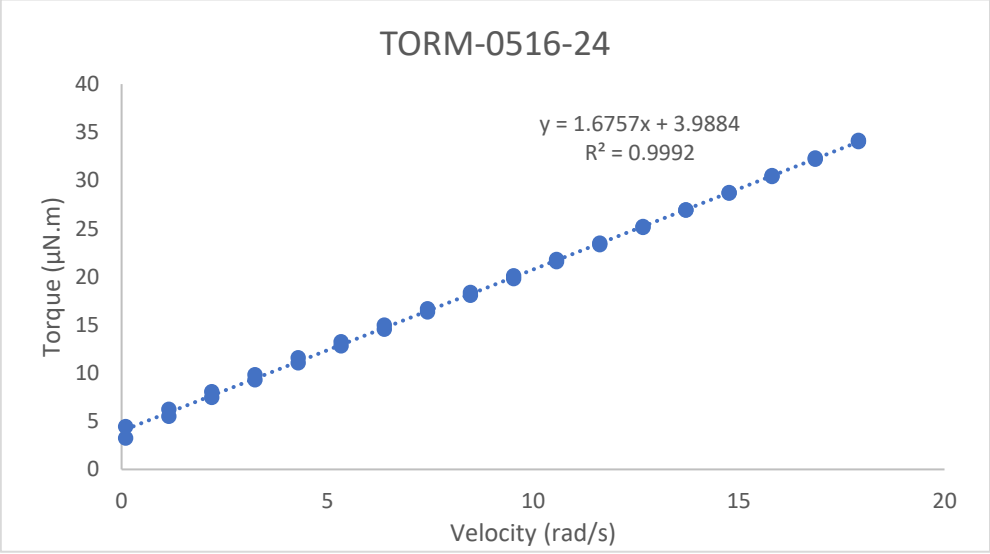
TORM-0516-24
y = 1.6757x + 3.9884
R² = 0.9992
Torque (µN.m)
Velocity (rad/s)
0
5
10
15
20
25
30
35
40
0
5
10
15
20

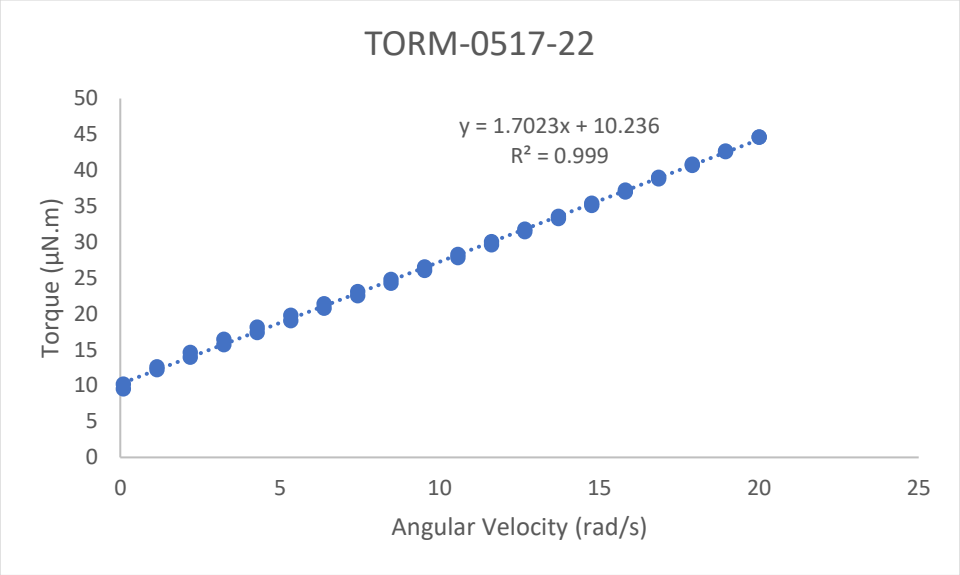
TORM-0517-22
y = 1.7023x + 10.236
R² = 0.999
Torque (µN.m)
Angular Velocity (rad/s)
0
5
10
15
20
25
30
35
40
45
50

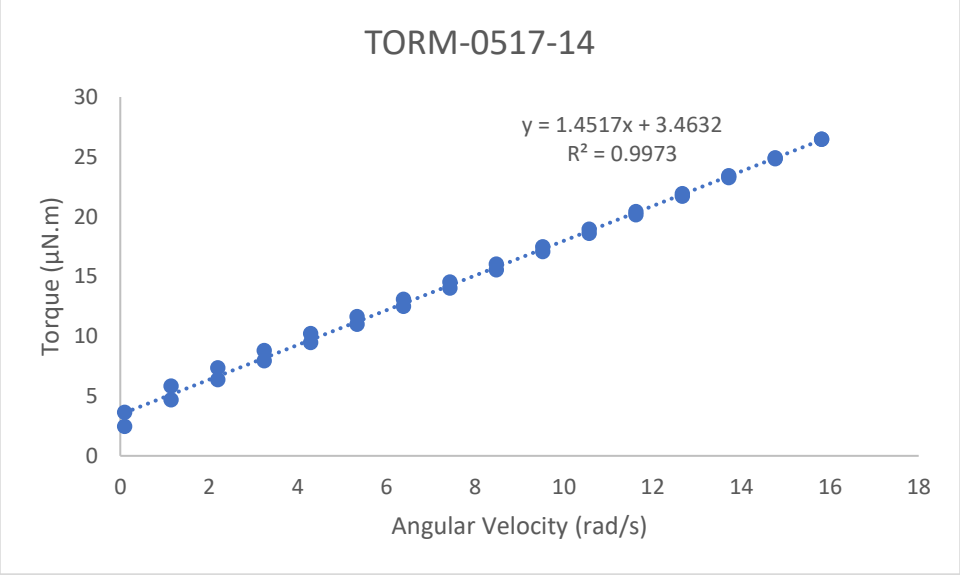
TORM-0517-14
y = 1.4517x + 3.4632
R² = 0.9973
Torque (µN.m)
Angular Velocity (rad/s)
0
2
4
6
8
10
12
14
16
18
0
5
10
15
20
25
30

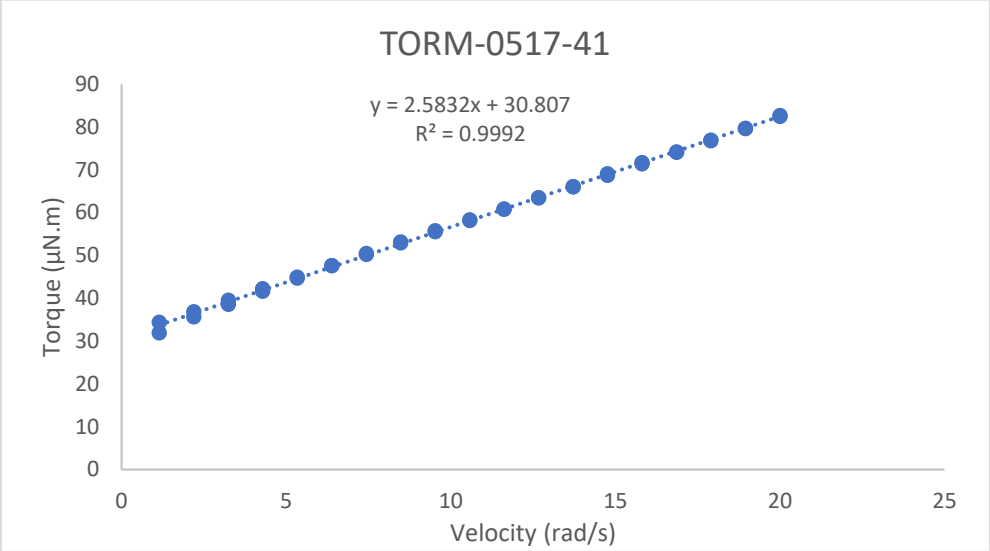
TORM-0517-41
y = 2.5832x + 30.807
R² = 0.9992
Torque (µN.m)
Velocity (rad/s)
0
10
20
30
40
50
60
70
80
90
0
5
10
15
20
25

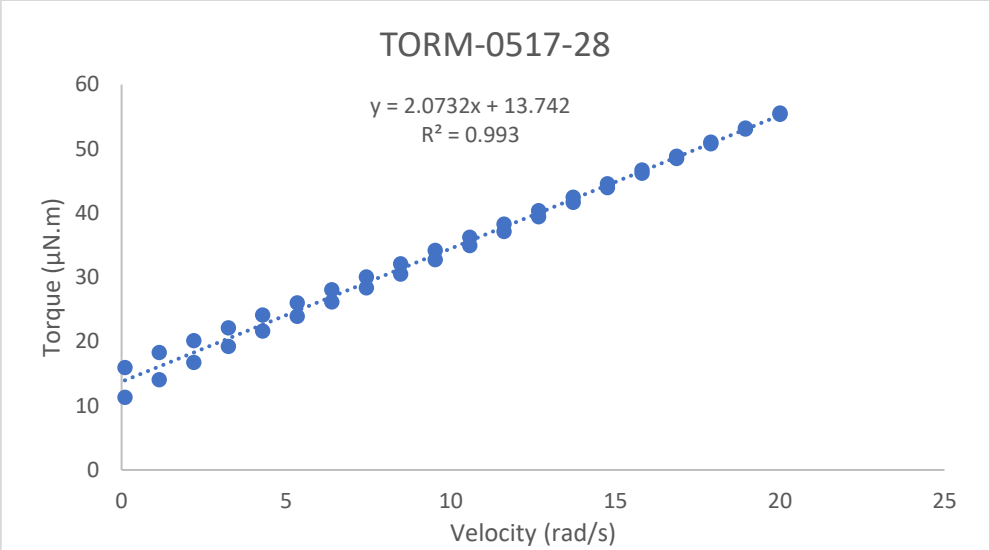
TORM-0517-28
y = 2.0732x + 13.742
R² = 0.993
Torque (µN.m)
Velocity (rad/s)
0
10
20
30
40
50
60
0
5
10
15
20
25

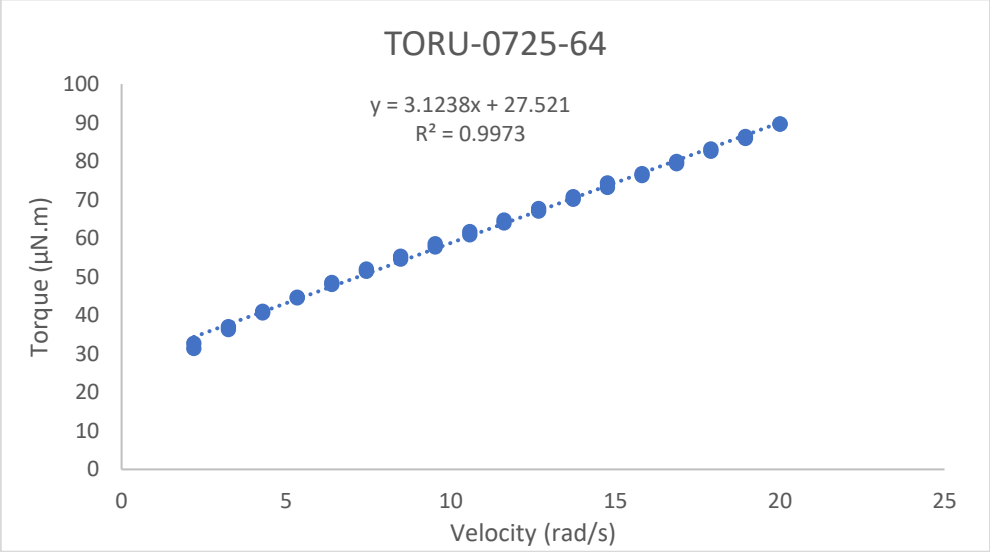
TORU-0725-64
y = 3.1238x + 27.521
R² = 0.9973
Torque (µN.m)
Velocity (rad/s)
0
10
20
30
40
50
60
70
80
90
100
0
5
10
15
20
25

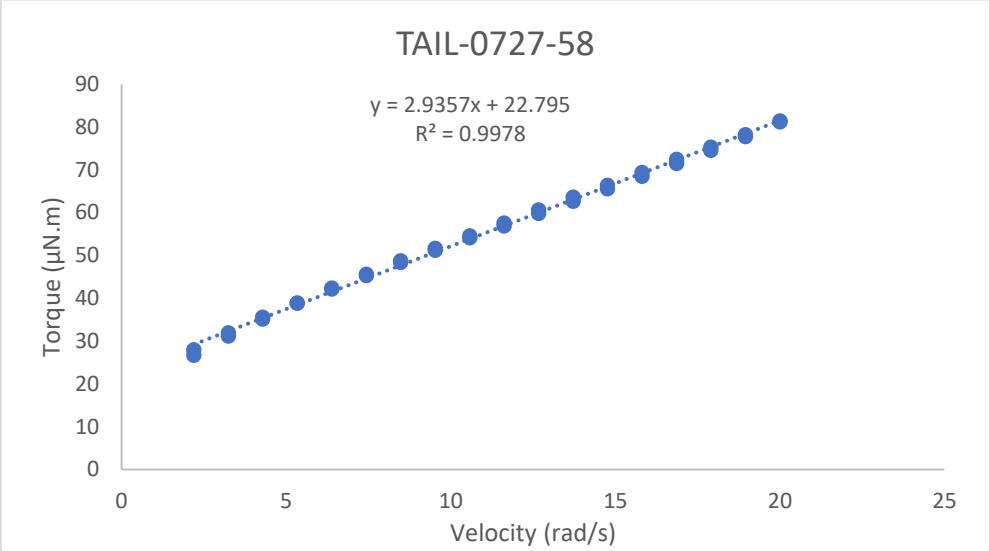
TAIL-0727-58
y = 2.9357x + 22.795
R² = 0.9978
Torque (µN.m)
Velocity (rad/s)
0
10
20
30
40
50
60
70
80
90
0
5
10
15
20
25

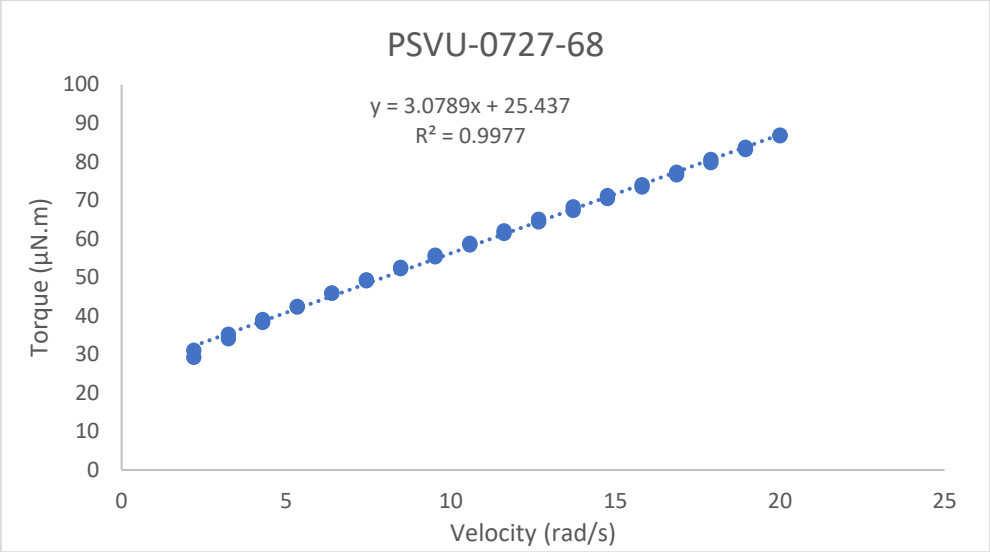
PSVU-0727-68
y = 3.0789x + 25.437
R² = 0.9977
Torque (µN.m)
Velocity (rad/s)
0
10
20
30
40
50
60
70
80
90
100
0
5
10
15
20
25

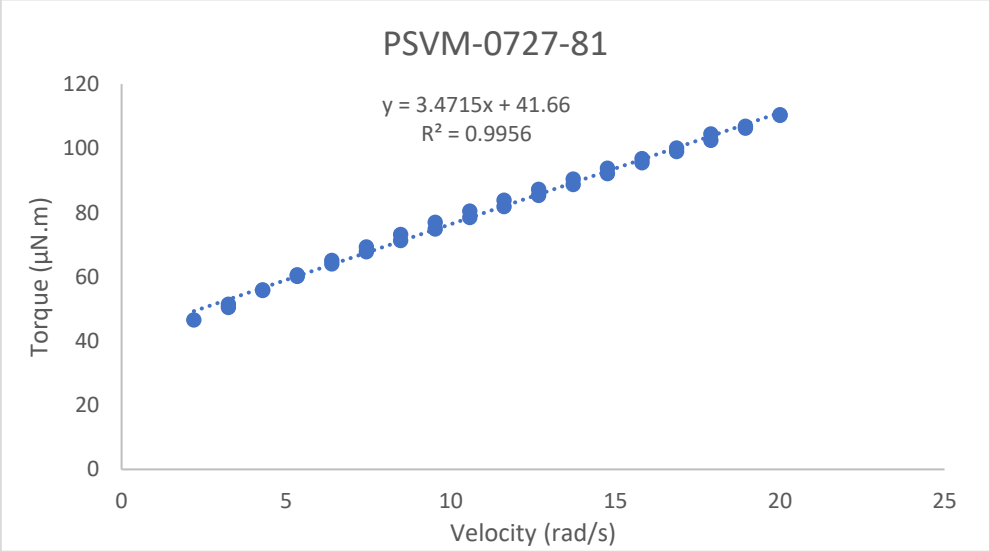
PSVM-0727-81
y = 3.4715x + 41.66
R² = 0.9956
Torque (µN.m)
Velocity (rad/s)
0
20
40
60
80
100
120
0
5
10
15
20
25

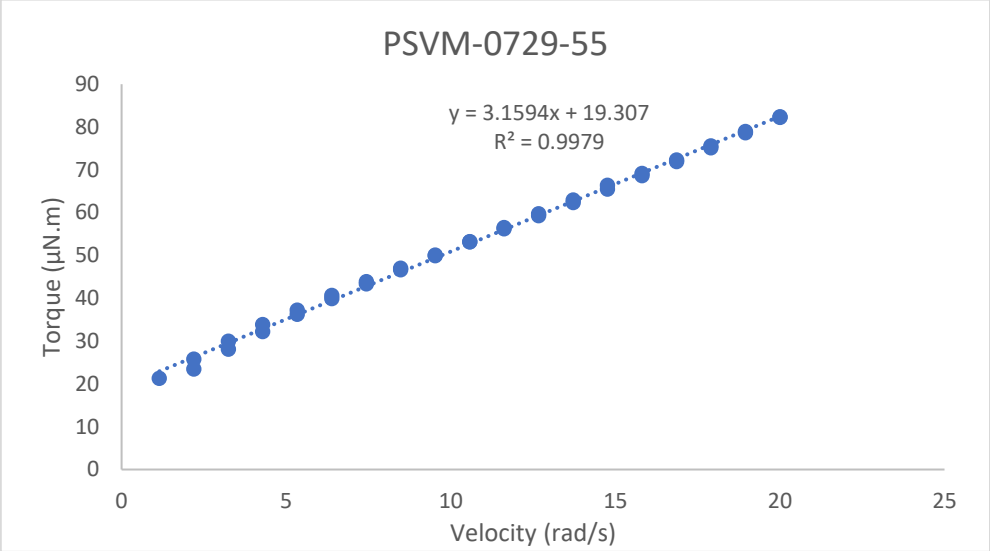
PSVM-0729-55
y = 3.1594x + 19.307
R² = 0.9979
Torque (µN.m)
Velocity (rad/s)
0
10
20
30
40
50
60
70
80
90
0
5
10
15
20
25

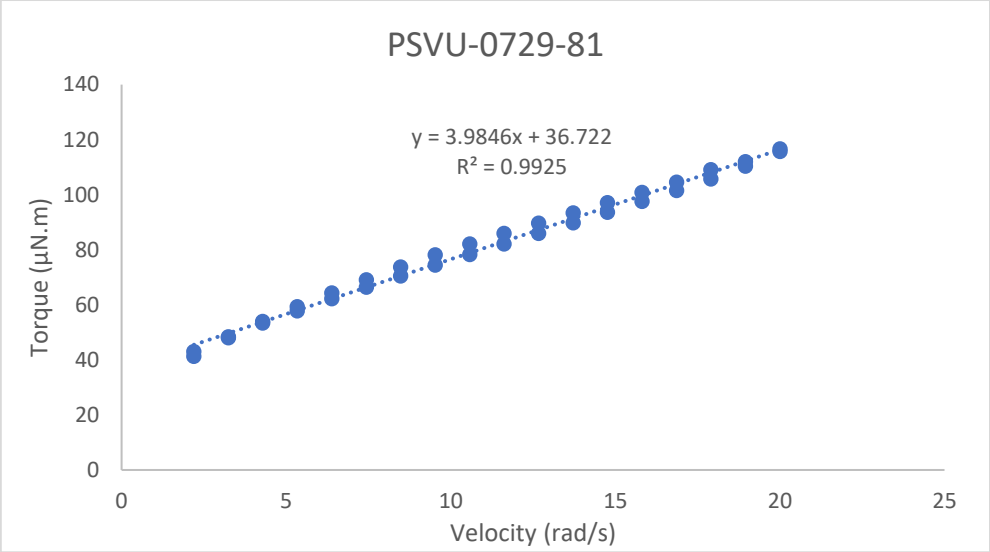
PSVU-0729-81
y = 3.9846x + 36.722
R² = 0.9925
Torque (µN.m)
Velocity (rad/s)
0
20
40
60
80
100
120
140
0
5
10
15
20
25

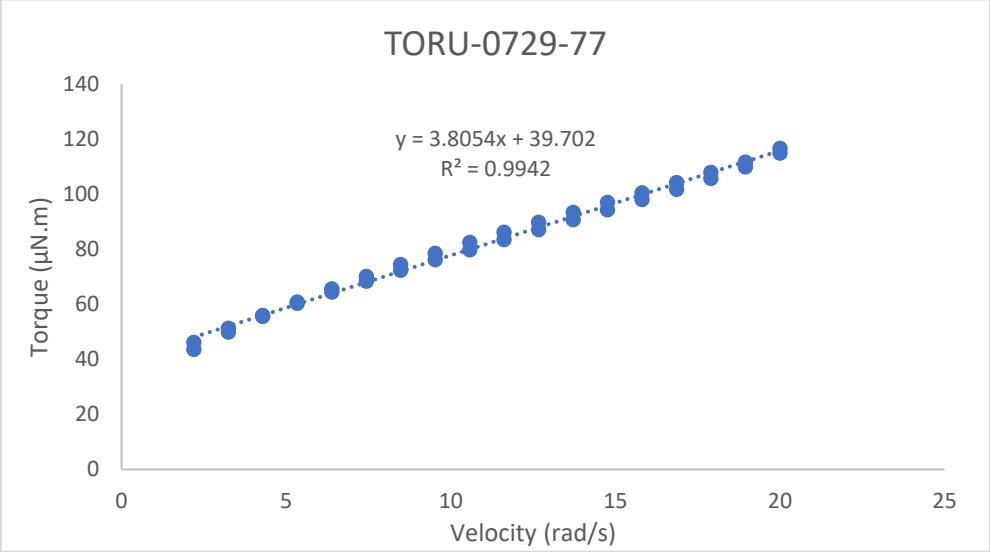
TORU-0729-77
y = 3.8054x + 39.702
R² = 0.9942
Torque (µN.m)
Velocity (rad/s)
0
20
40
60
80
100
120
140
0
5
10
15
20
25

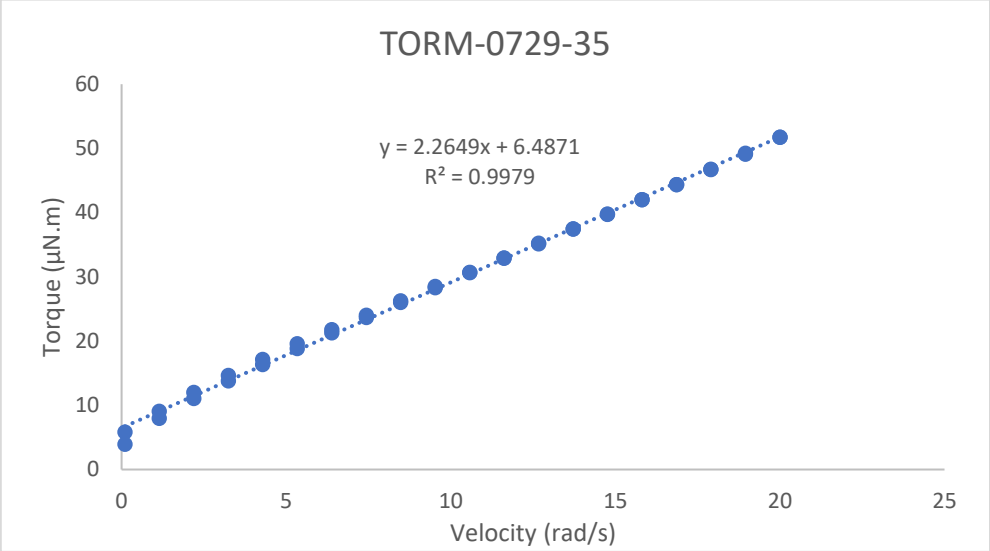
TORM-0729-35
y = 2.2649x + 6.4871
R² = 0.9979
Torque (µN.m)
Velocity (rad/s)
0
10
20
30
40
50
60
0
5
10
15
20
25

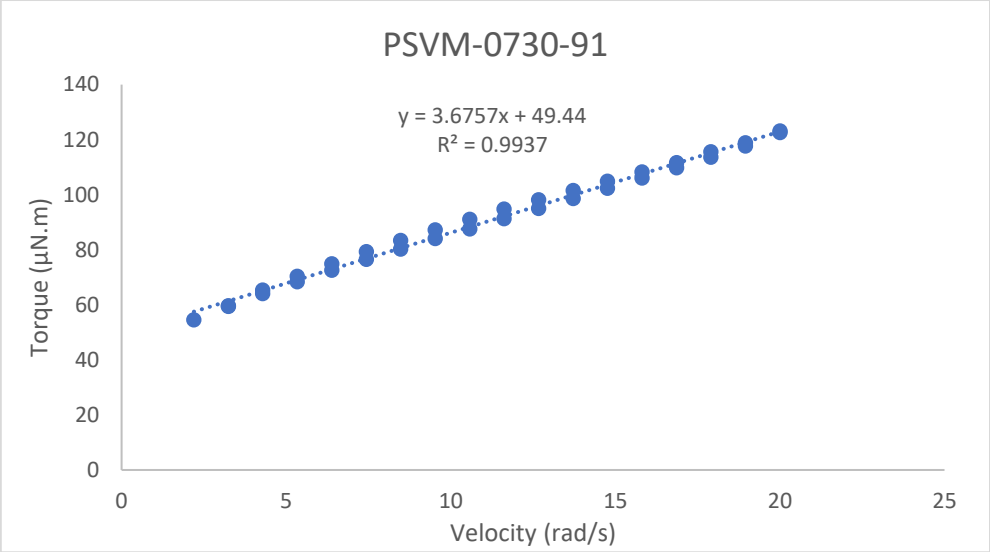
PSVM-0730-91
y = 3.6757x + 49.44
R² = 0.9937
Torque (µN.m)
Velocity (rad/s)
0
20
40
60
80
100
120
140
0
5
10
15
20
25

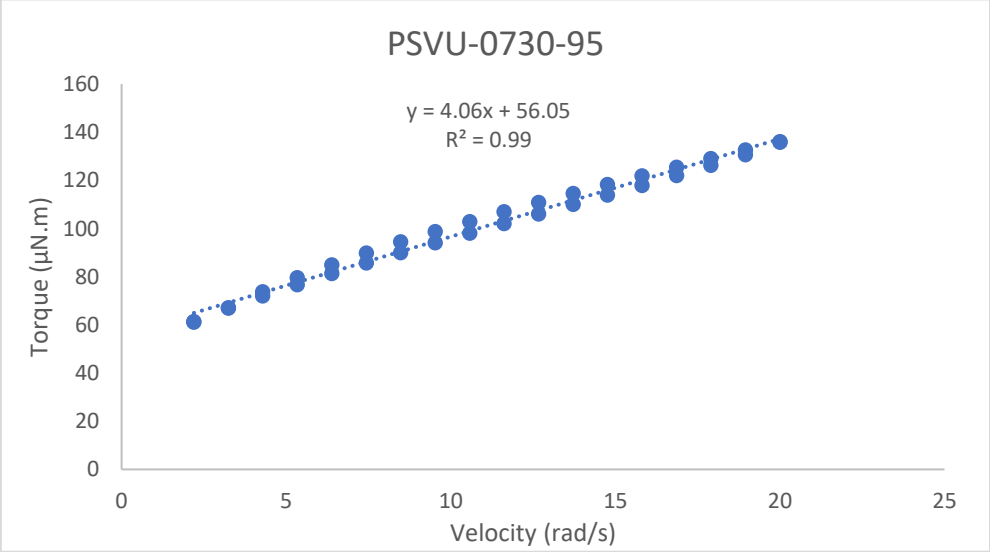
PSVU-0730-95
y = 4.06x + 56.05
R² = 0.99
Torque (µN.m)
Velocity (rad/s)
0
20
40
60
80
100
120
140
160
0
5
10
15
20
25

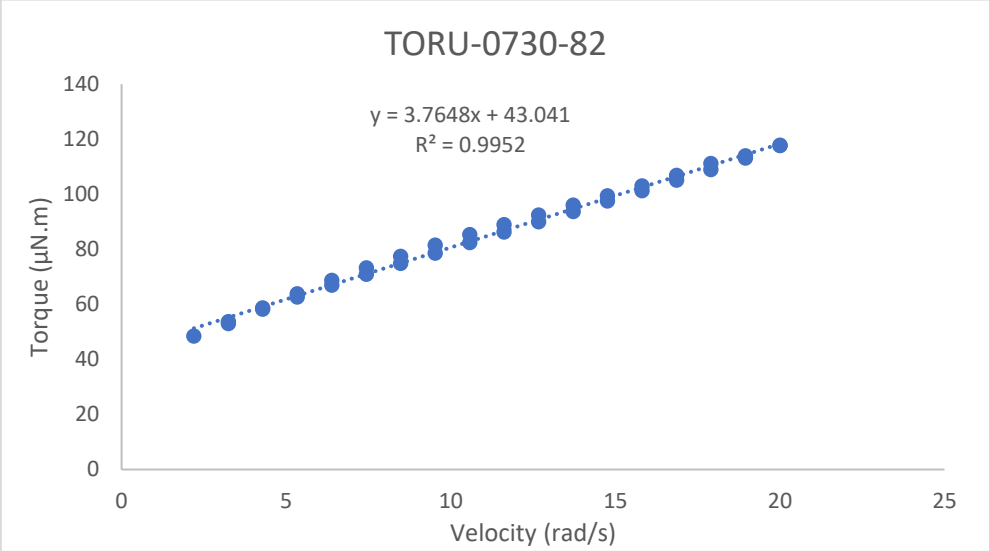
TORU-0730-82
y = 3.7648x + 43.041
R² = 0.9952
Torque (µN.m)
Velocity (rad/s)
0
20
40
60
80
100
120
140
0
5
10
15
20
25

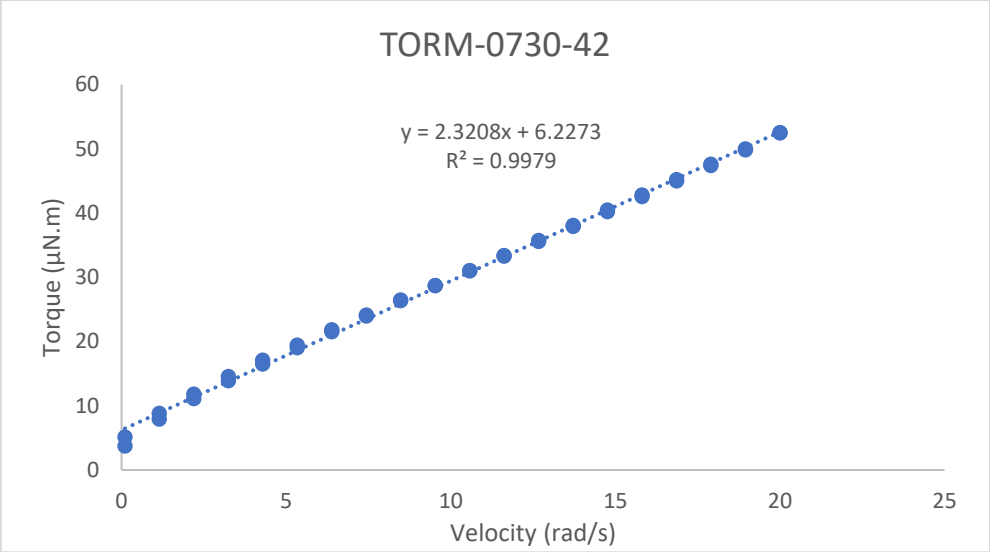
TORM-0730-42
y = 2.3208x + 6.2273
R² = 0.9979
Torque (µN.m)
Velocity (rad/s)
0
10
20
30
40
50
60
0
5
10
15
20
25

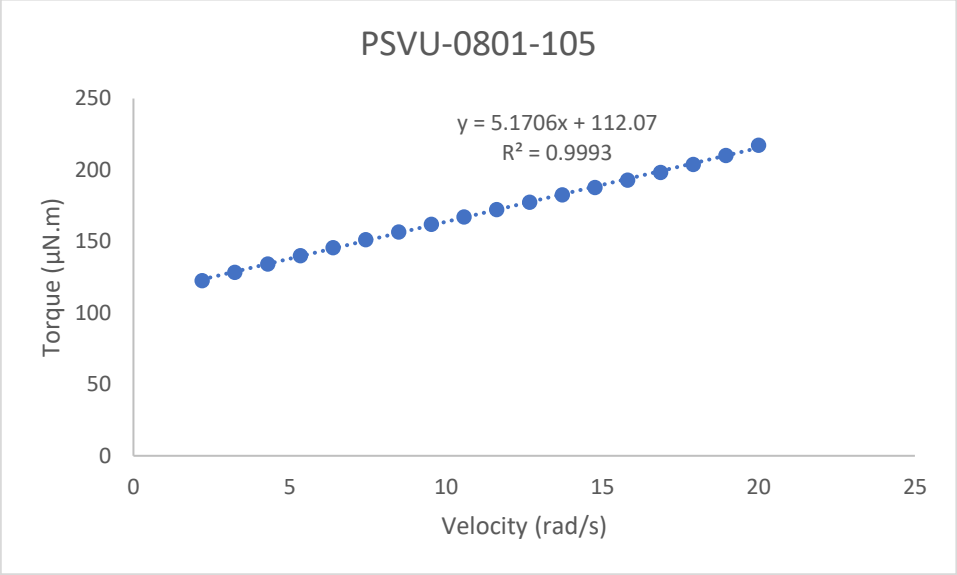
PSVU-0801-105
y = 5.1706x + 112.07
R² = 0.9993
Torque (µN.m)
Velocity (rad/s)
0
50
100
150
200
250
0
5
10
15
20
25

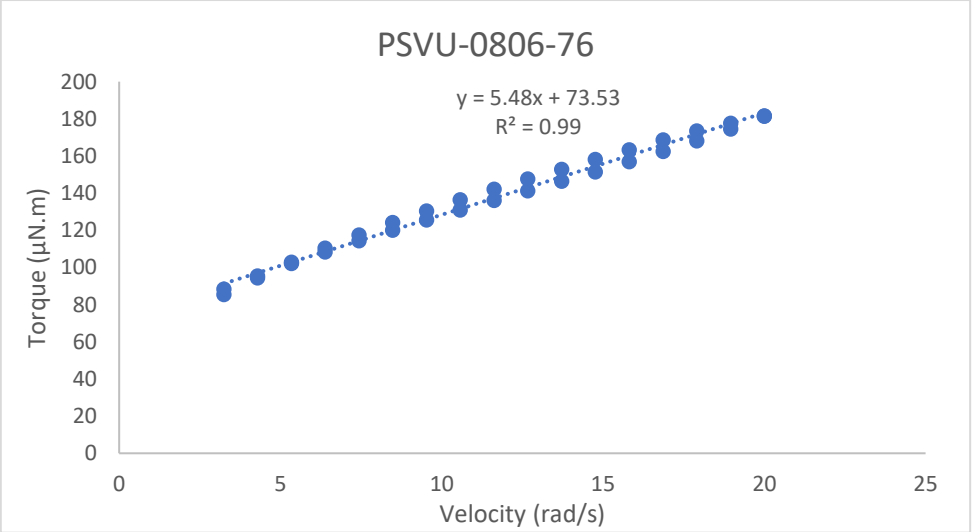
PSVU-0806-76
y = 5.48x + 73.53
R² = 0.99
Torque (µN.m)
Velocity (rad/s)
0
20
40
60
80
100
120
140
160
180
200
0
5
10
15
20
25

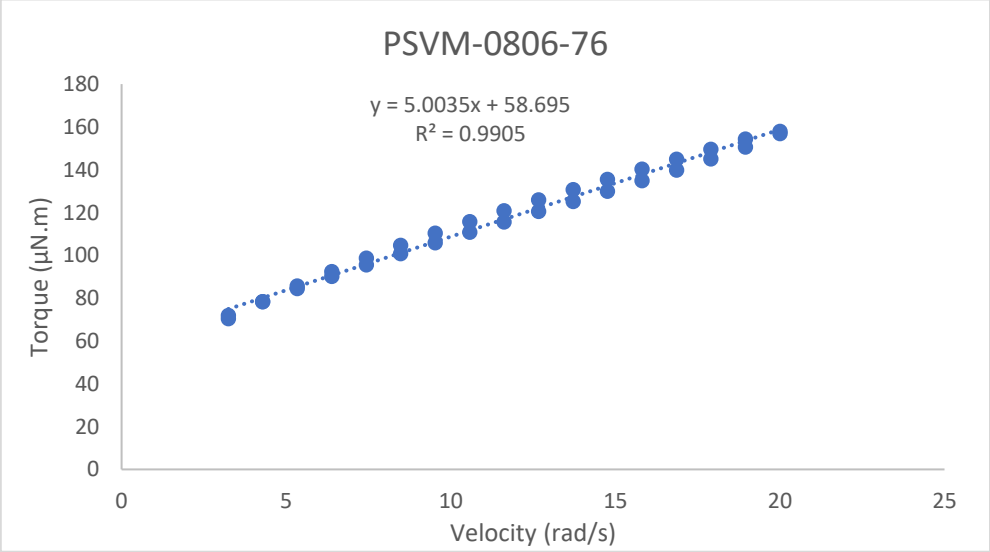
PSVM-0806-76
y = 5.0035x + 58.695
R² = 0.9905
Torque (µN.m)
Velocity (rad/s)
0
20
40
60
80
100
120
140
160
180
0
5
10
15
20
25

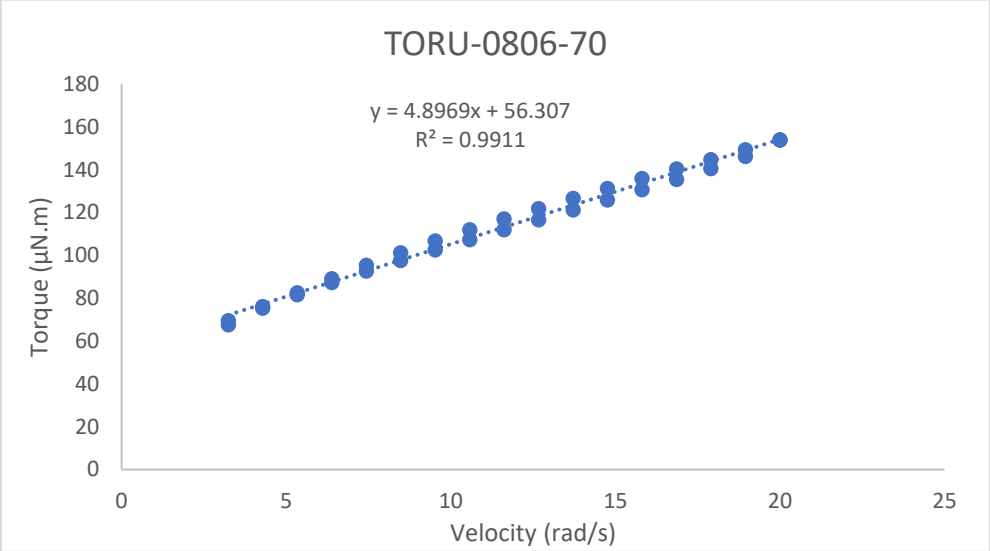
TORU-0806-70
y = 4.8969x + 56.307
R² = 0.9911
Torque (µN.m)
Velocity (rad/s)
0
20
40
60
80
100
120
140
160
180
0
5
10
15
20
25

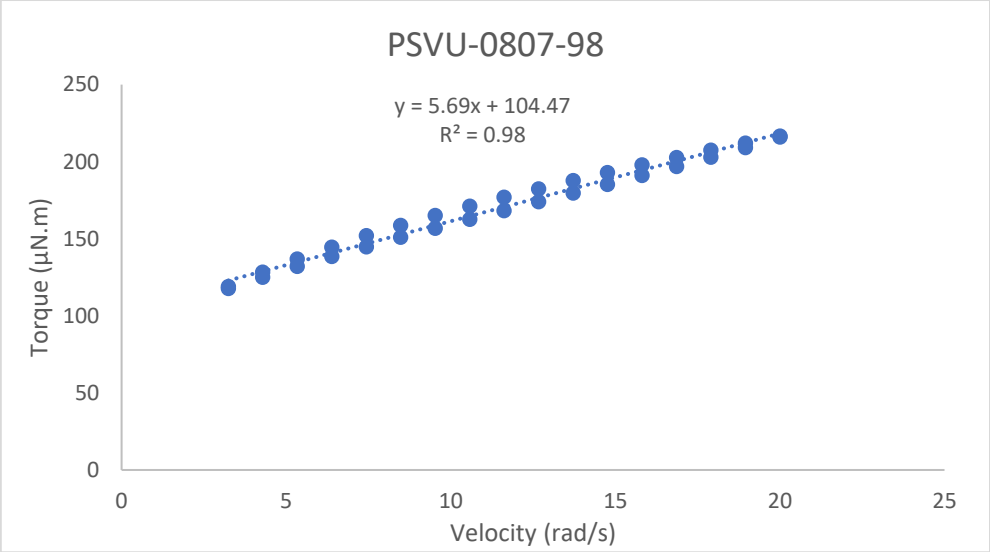
PSVU-0807-98
y = 5.69x + 104.47
R² = 0.98
Torque (µN.m)
Velocity (rad/s)
0
50
100
150
200
250
0
5
10
15
20
25

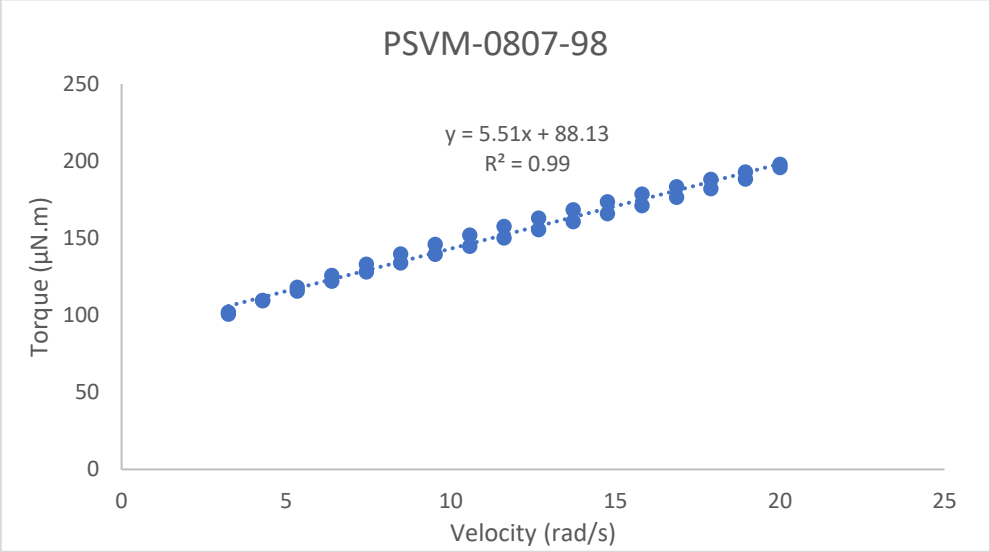
PSVM-0807-98
y = 5.51x + 88.13
R² = 0.99
Torque (µN.m)
Velocity (rad/s)
0
50
100
150
200
250
0
5
10
15
20
25

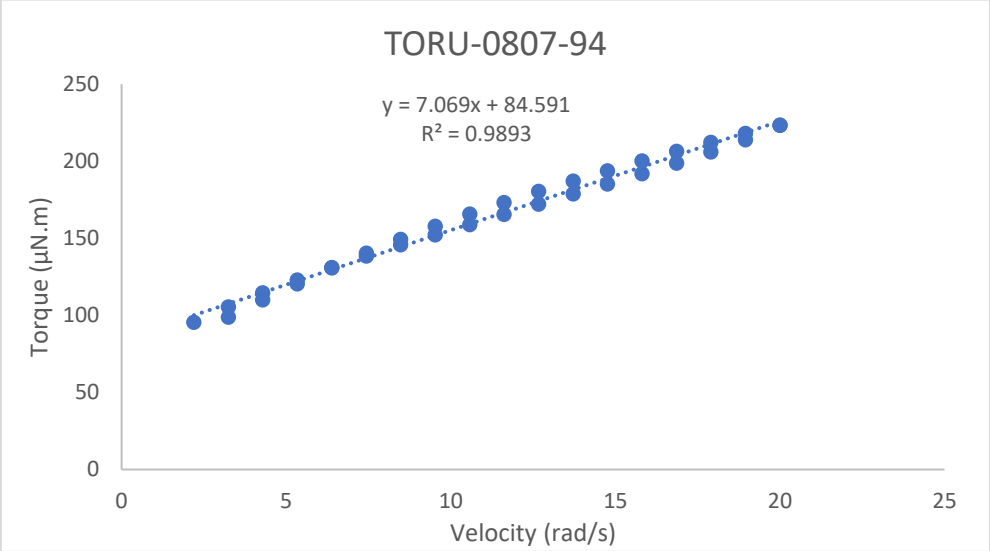
TORU-0807-94
y = 7.069x + 84.591
R² = 0.9893
Torque (µN.m)
Velocity (rad/s)
0
50
100
150
200
250
0
5
10
15
20
25

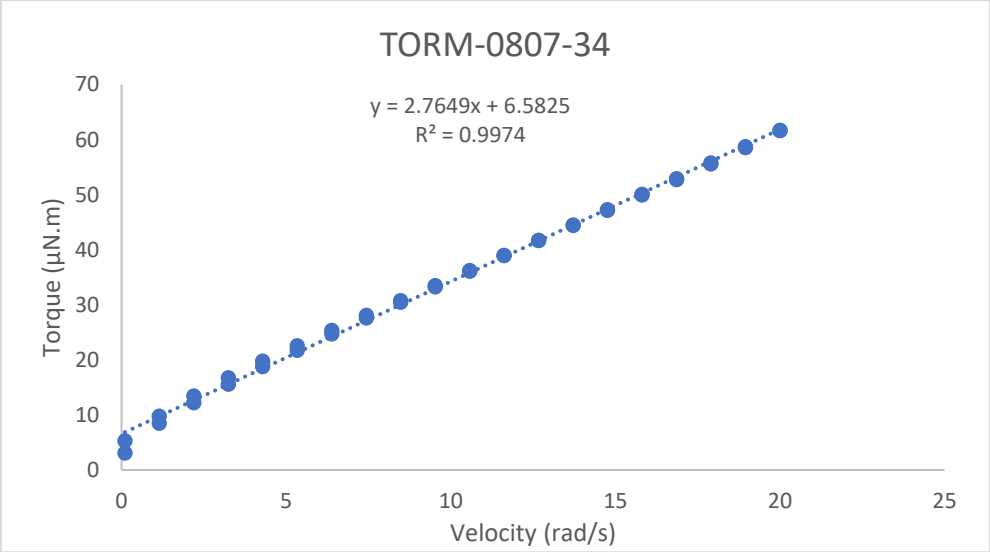
TORM-0807-34
y = 2.7649x + 6.5825
R² = 0.9974
Torque (µN.m)
Velocity (rad/s)
0
10
20
30
40
50
60
70
0
5
10
15
20
25

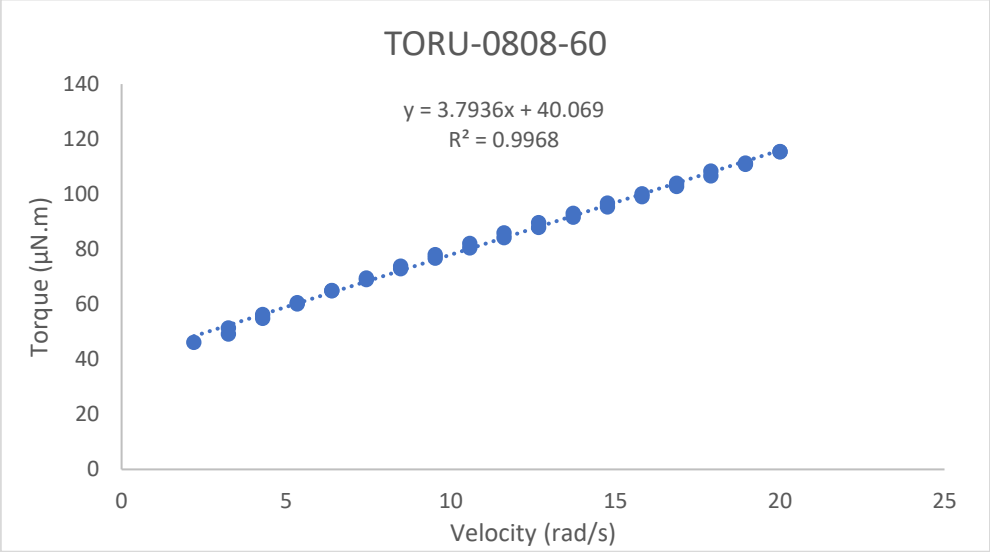
TORU-0808-60
y = 3.7936x + 40.069
R² = 0.9968
Torque (µN.m)
Velocity (rad/s)
0
20
40
60
80
100
120
140
0
5
10
15
20
25

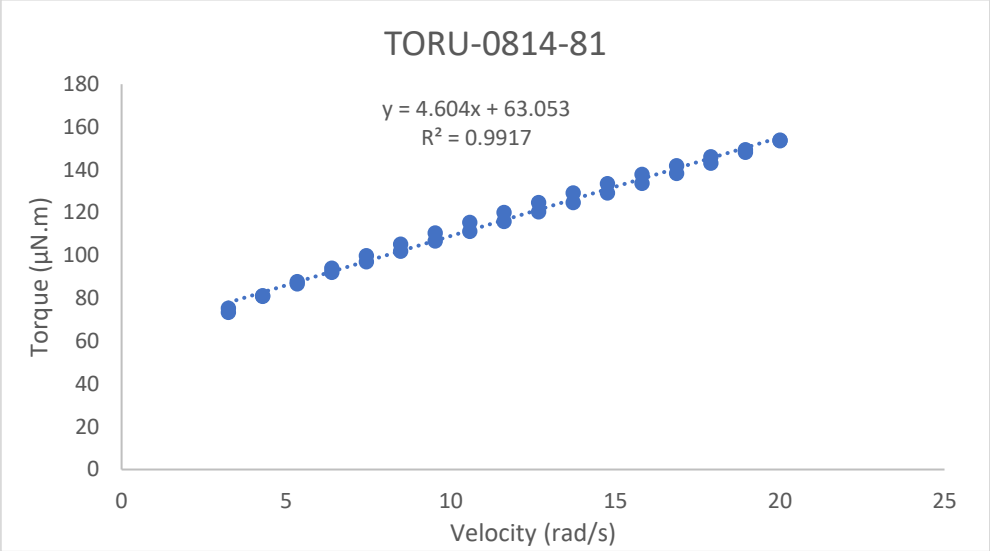
TORU-0814-81
y = 4.604x + 63.053
R² = 0.9917
Torque (µN.m)
Velocity (rad/s)
0
20
40
60
80
100
120
140
160
180
0
5
10
15
20
25

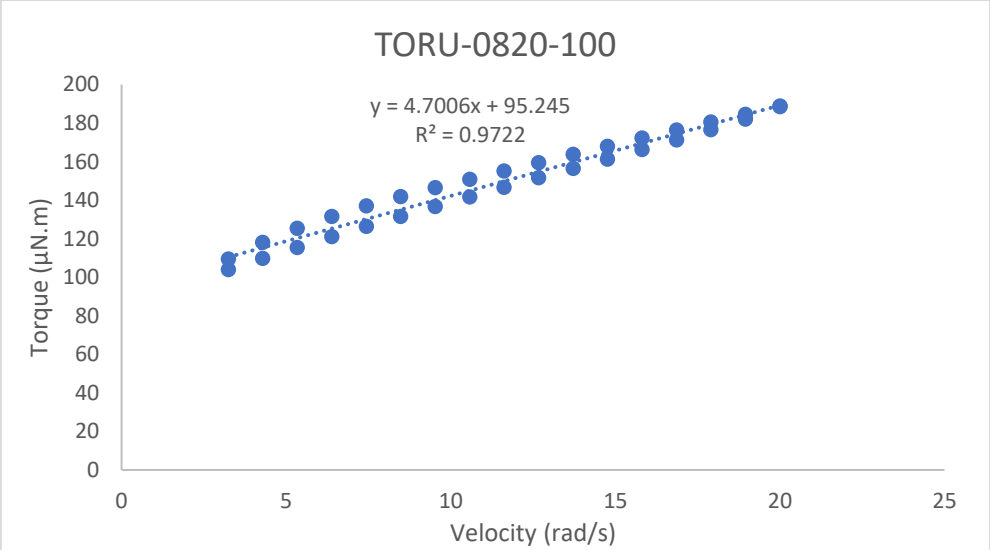
TORU-0820-100
y = 4.7006x + 95.245
R² = 0.9722
Torque (µN.m)
Velocity (rad/s)
0
20
40
60
80
100
120
140
160
180
200
0
5
10
15
20
25

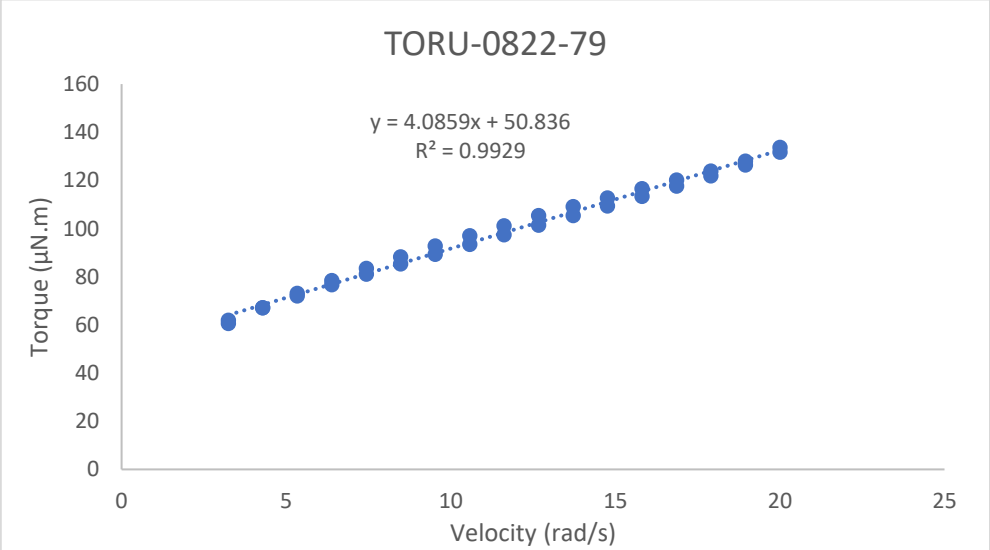
TORU-0822-79
y = 4.0859x + 50.836
R² = 0.9929
Torque (µN.m)
Velocity (rad/s)
0
20
40
60
80
100
120
140
160
0
5
10
15
20
25

B.2 Double Gap Geometry

The shear stress vs. shear rate graphs for all samples analyzed with the double gap geometry are attached.

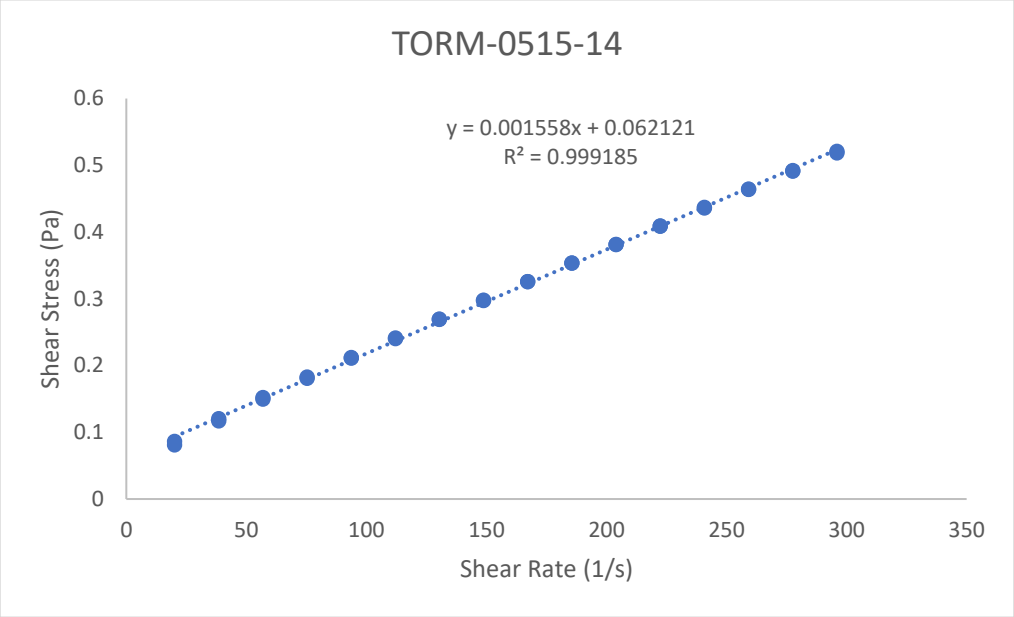
TORM-0515-14
y = 0.001558x + 0.062121
R² = 0.999185
Shear Stress (Pa)
Shear Rate (1/s)
0
0.1
0.2
0.3
0.4
0.5
0.6
0
50
100
150
200
250
300
350

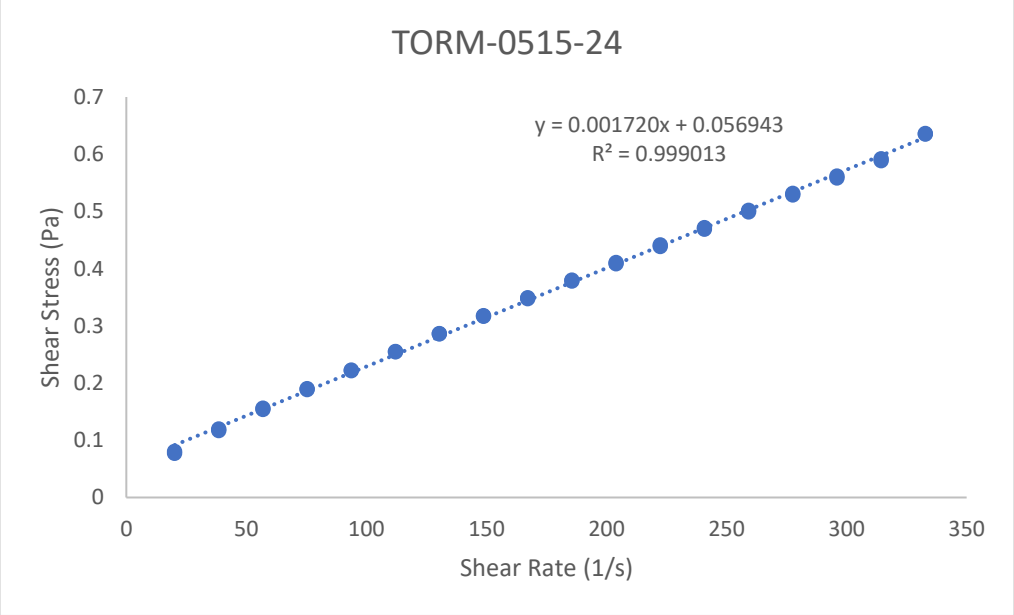
TORM-0515-24
y = 0.001720x + 0.056943
R² = 0.999013
Shear Stress (Pa)
Shear Rate (1/s)
0
0.1
0.2
0.3
0.4
0.5
0.6
0.7
0
50
100
150
200
250
300
350

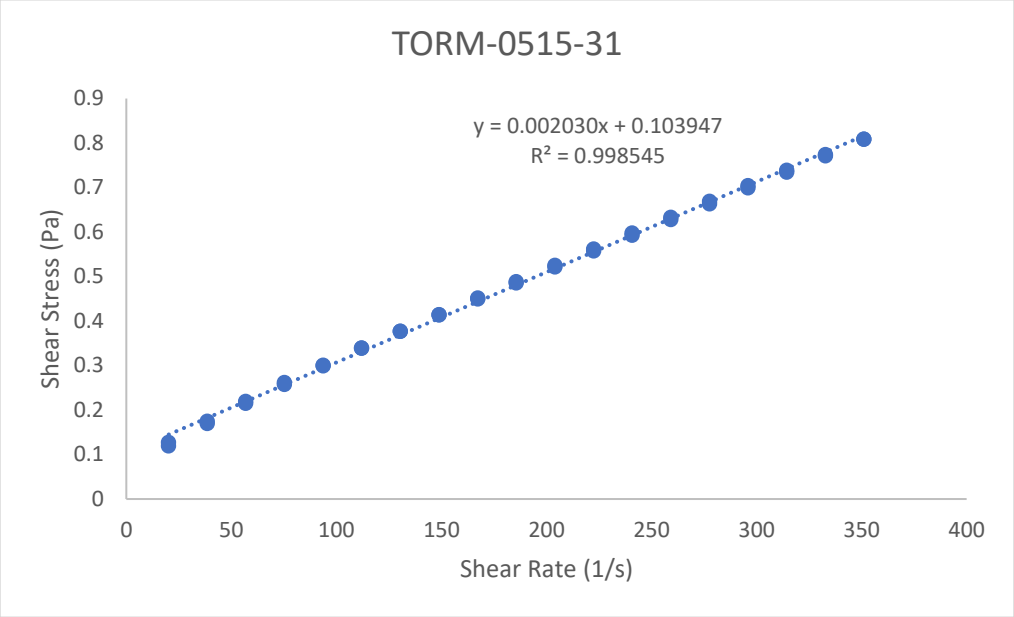
TORM-0515-31
y = 0.002030x + 0.103947
R² = 0.998545
Shear Stress (Pa)
Shear Rate (1/s)
0
0.1
0.2
0.3
0.4
0.5
0.6
0.7
0.8
0.9
0
50
100
150
200
250
300
350
400

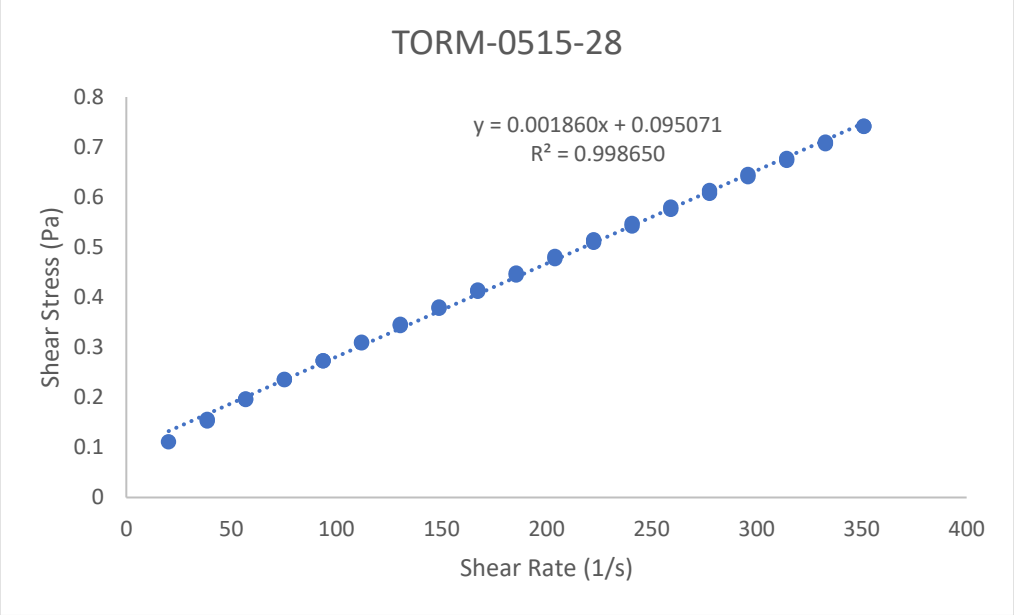
TORM-0515-28
y = 0.001860x + 0.095071
R² = 0.998650
Shear Stress (Pa)
Shear Rate (1/s)
0
0.1
0.2
0.3
0.4
0.5
0.6
0.7
0.8
0
50
100
150
200
250
300
350
400

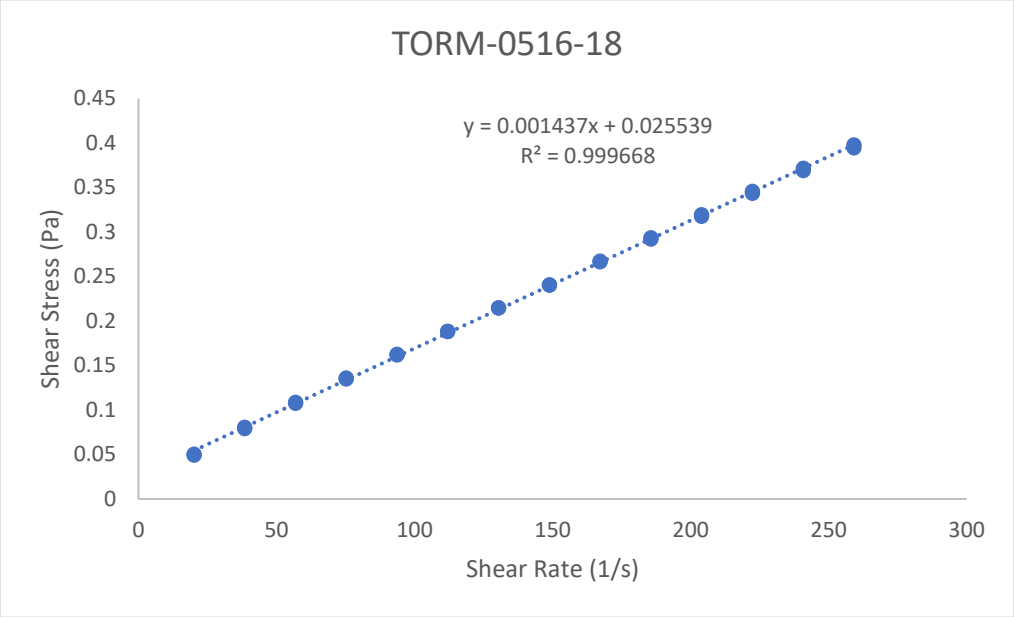
TORM-0516-18
y = 0.001437x + 0.025539
R² = 0.999668
Shear Stress (Pa)
Shear Rate (1/s)
0.45
0.4
0.35
0.3
0.25
0.2
0.15
0.1
0.05
0
0
50
100
150
200
250
300

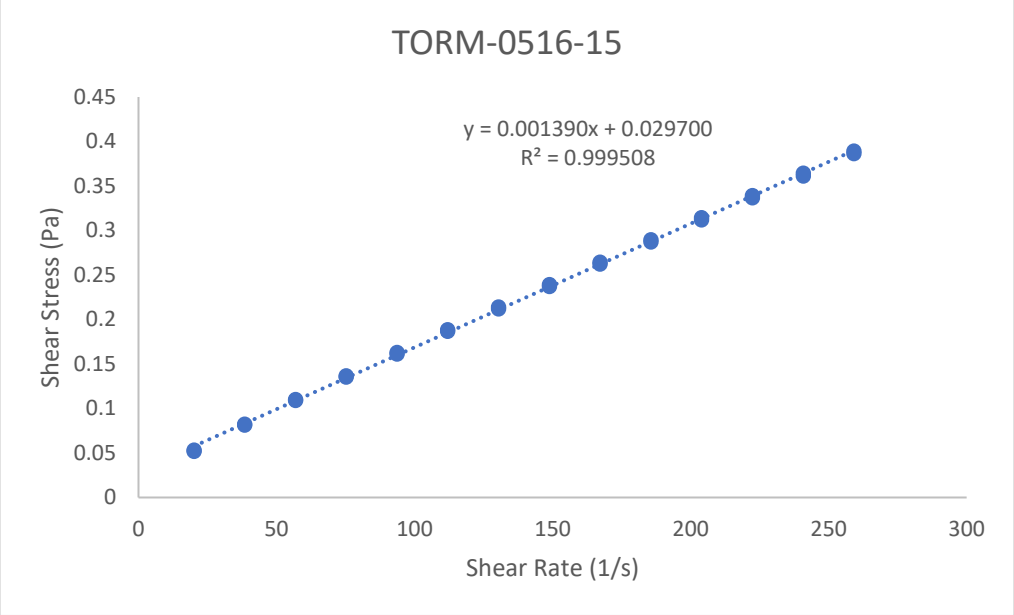
TORM-0516-15
y = 0.001390x + 0.029700
R² = 0.999508
Shear Stress (Pa)
Shear Rate (1/s)
0.45
0.4
0.35
0.3
0.25
0.2
0.15
0.1
0.05
0
0
50
100
150
200
250
300

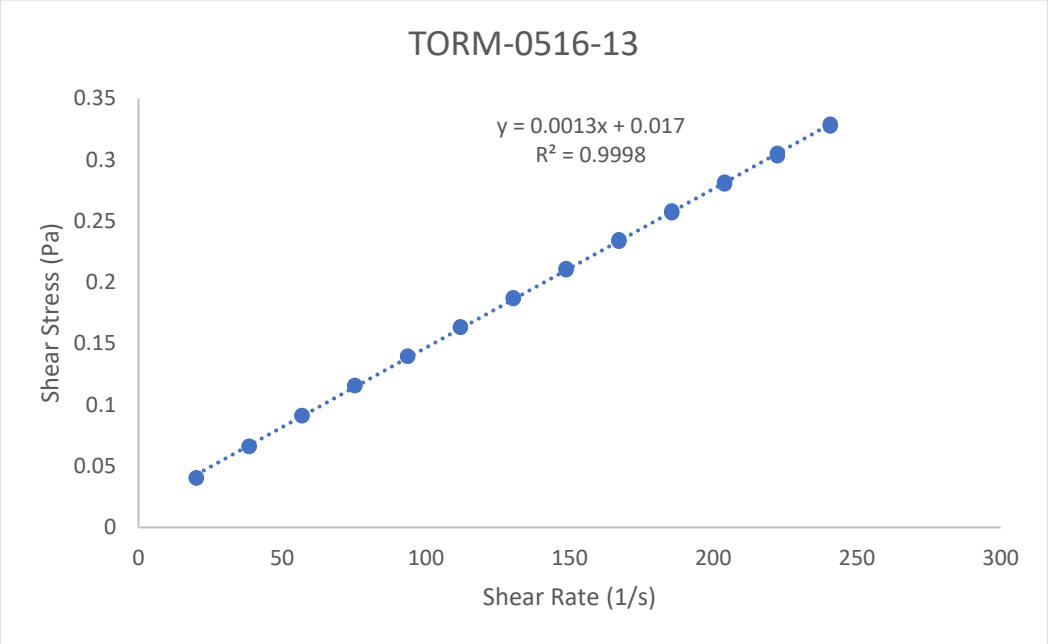
TORM-0516-13
y = 0.0013x + 0.017
R² = 0.9998
Shear Stress (Pa)
Shear Rate (1/s)
0.35
0.3
0.25
0.2
0.15
0.1
0.05
0
0
50
100
150
200
250
300

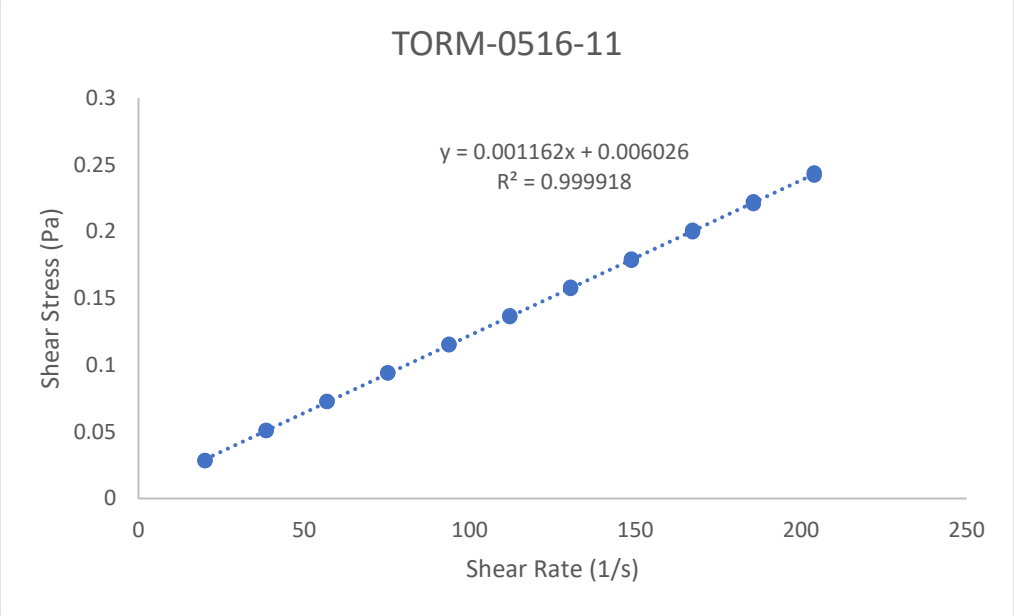
TORM-0516-11
y = 0.001162x + 0.006026
R² = 0.999918
Shear Stress (Pa)
Shear Rate (1/s)
0.3
0.25
0.2
0.15
0.1
0.05
0
0
50
100
150
200
250

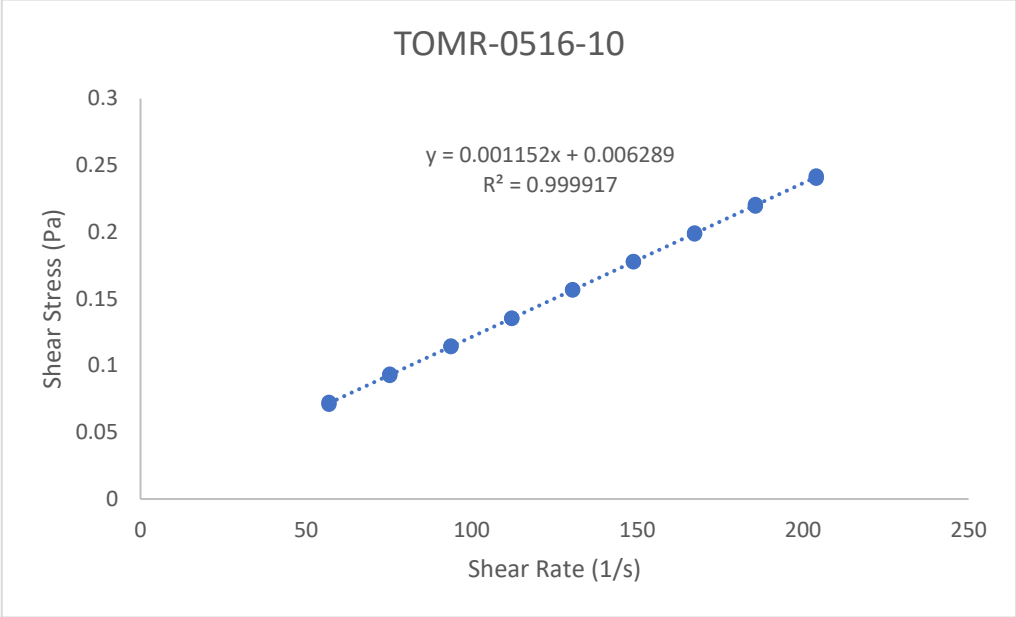
TOMR-0516-10
y = 0.001152x + 0.006289
R² = 0.999917
Shear Stress (Pa)
Shear Rate (1/s)
0
0.05
0.1
0.15
0.2
0.25
0.3
0
50
100
150
200
250

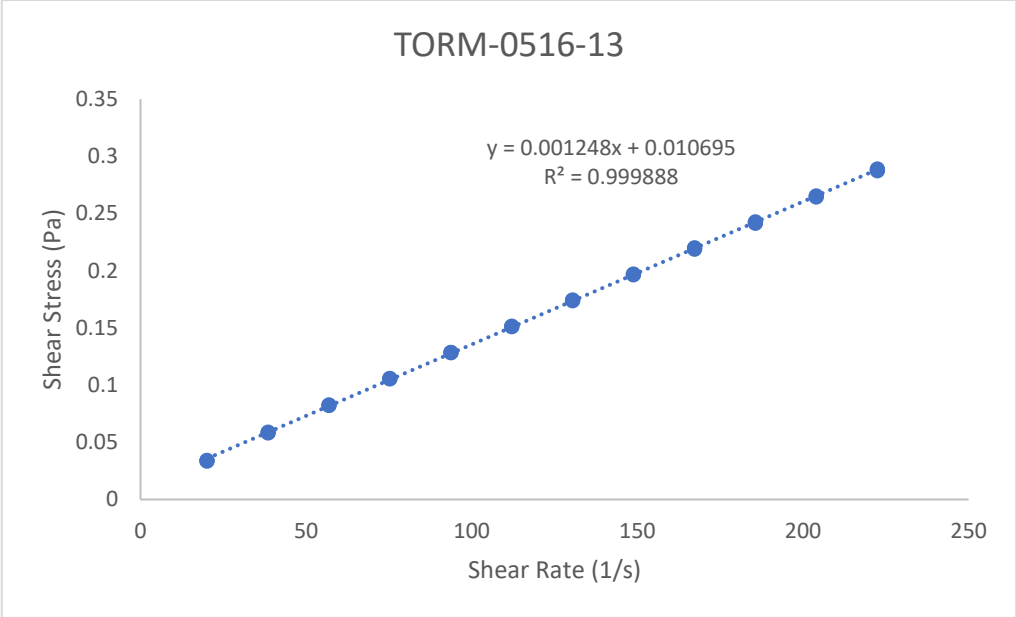
TORM-0516-13
y = 0.001248x + 0.010695
R² = 0.999888
Shear Stress (Pa)
Shear Rate (1/s)
0
0.05
0.1
0.15
0.2
0.25
0.3
0.35
0
50
100
150
200
250

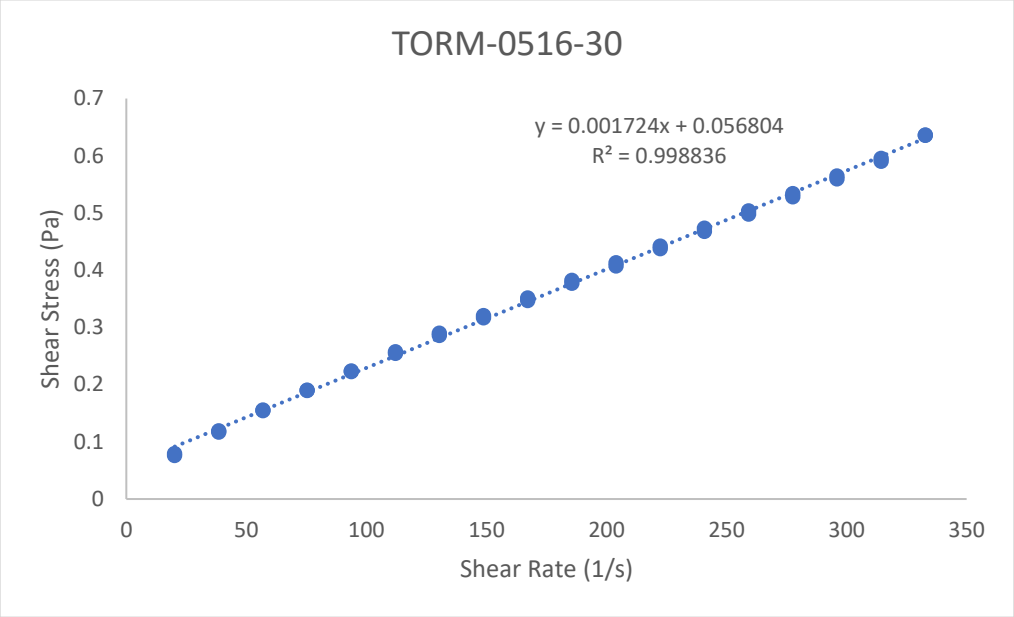
TORM-0516-30
y = 0.001724x + 0.056804
R² = 0.998836
Shear Stress (Pa)
Shear Rate (1/s)
0
0.1
0.2
0.3
0.4
0.5
0.6
0.7
0
50
100
150
200
250
300
350

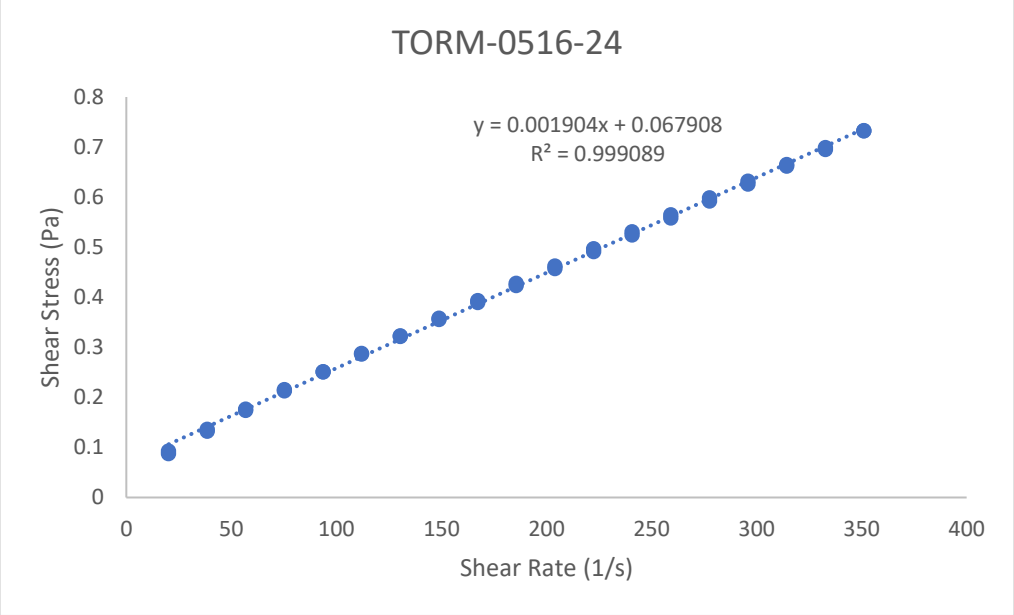
TORM-0516-24
y = 0.001904x + 0.067908
R² = 0.999089
Shear Stress (Pa)
Shear Rate (1/s)
0
0.1
0.2
0.3
0.4
0.5
0.6
0.7
0.8
0
50
100
150
200
250
300
350
400

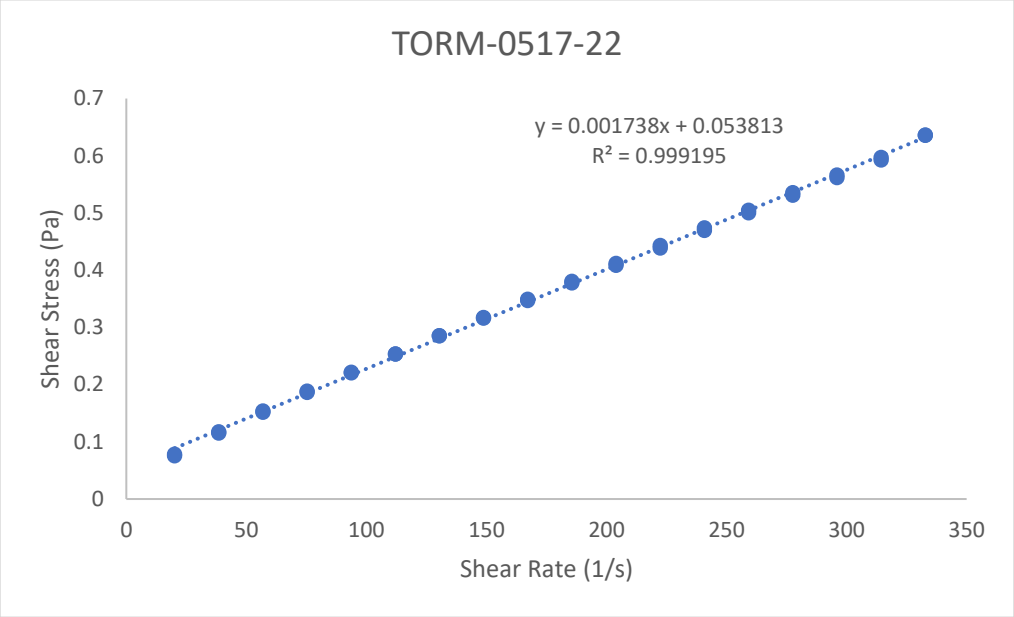
TORM-0517-22
y = 0.001738x + 0.053813
R² = 0.999195
Shear Stress (Pa)
Shear Rate (1/s)
0
0.1
0.2
0.3
0.4
0.5
0.6
0.7
0
50
100
150
200
250
300
350

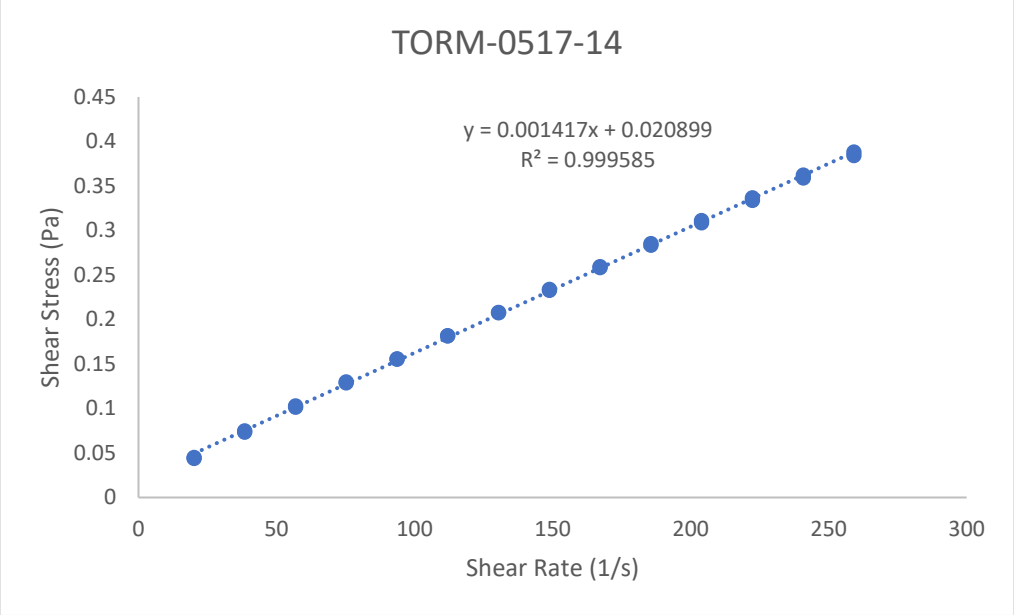
TORM-0517-14
y = 0.001417x + 0.020899
R² = 0.999585
Shear Stress (Pa)
Shear Rate (1/s)
0
0.05
0.1
0.15
0.2
0.25
0.3
0.35
0.4
0.45
0
50
100
150
200
250
300

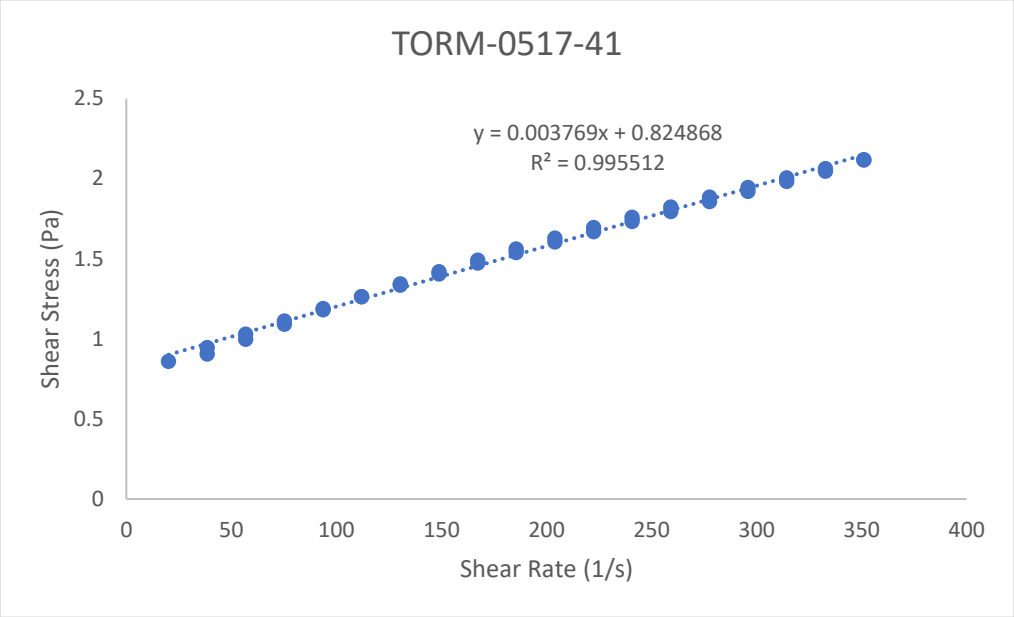
TORM-0517-41
y = 0.003769x + 0.824868
R² = 0.995512
Shear Stress (Pa)
Shear Rate (1/s)
0
0.5
1
1.5
2
2.5
0
50
100
150
200
250
300
350
400

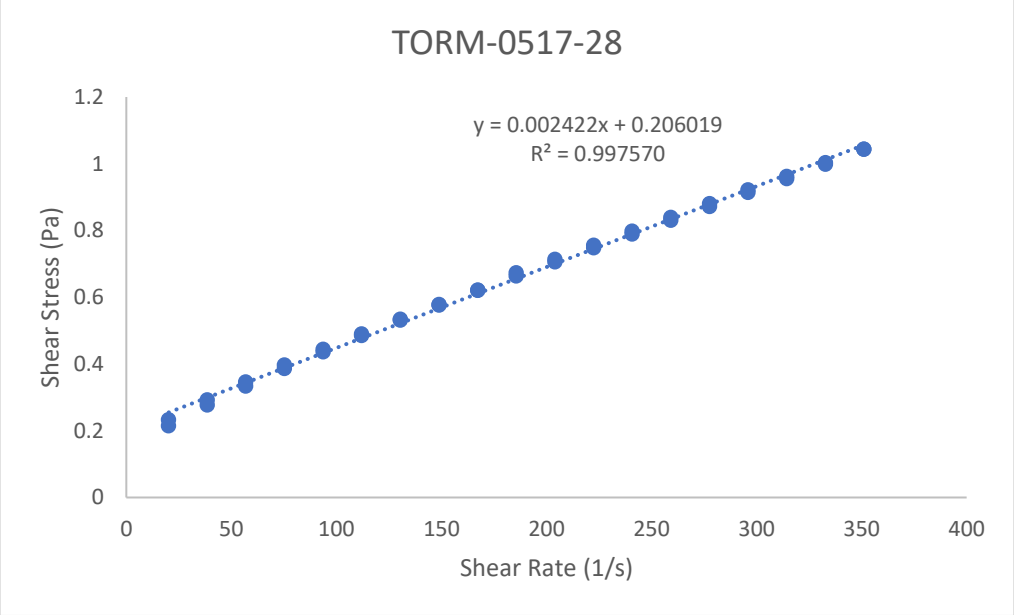
TORM-0517-28
y = 0.002422x + 0.206019
R² = 0.997570
Shear Stress (Pa)
Shear Rate (1/s)
0
0.2
0.4
0.6
0.8
1
1.2
0
50
100
150
200
250
300
350
400

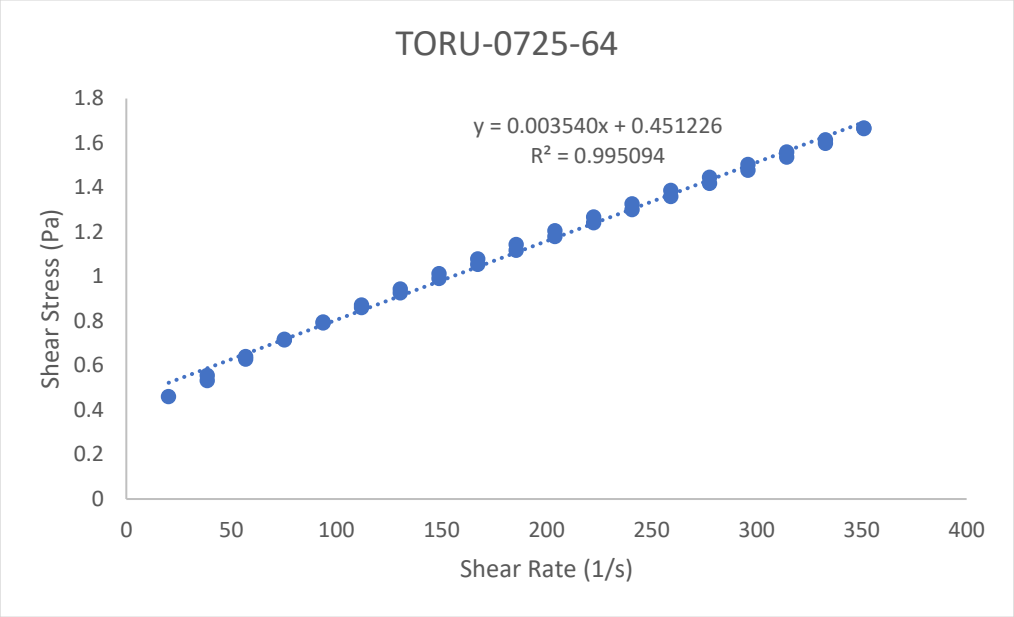
TORU-0725-64
y = 0.003540x + 0.451226
R² = 0.995094
Shear Stress (Pa)
Shear Rate (1/s)
0
0.2
0.4
0.6
0.8
1
1.2
1.4
1.6
1.8
0
50
100
150
200
250
300
350
400

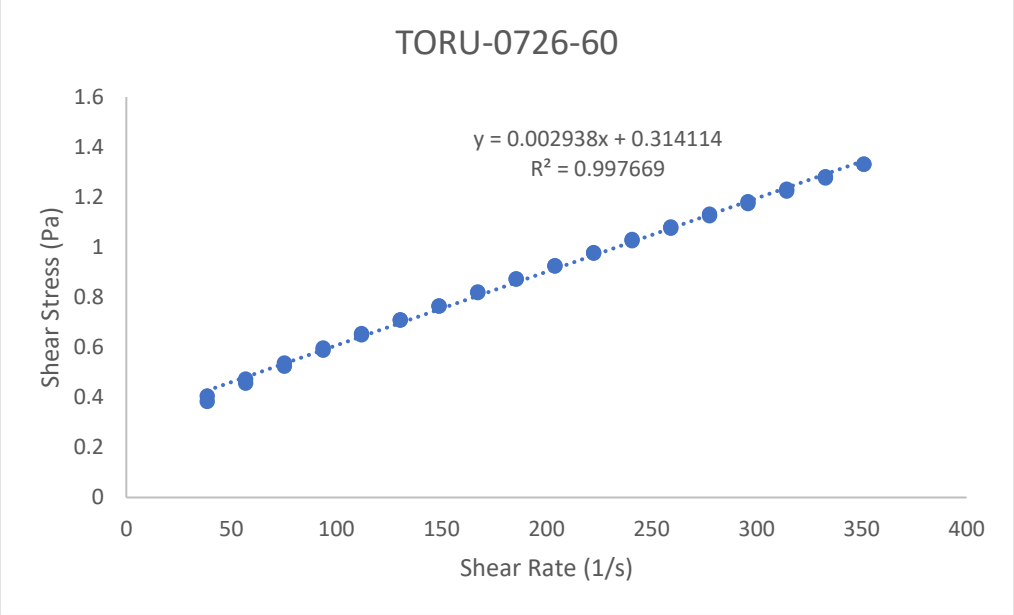
TORU-0726-60
y = 0.002938x + 0.314114
R² = 0.997669
Shear Stress (Pa)
Shear Rate (1/s)
0
0.2
0.4
0.6
0.8
1
1.2
1.4
1.6
0
50
100
150
200
250
300
350
400

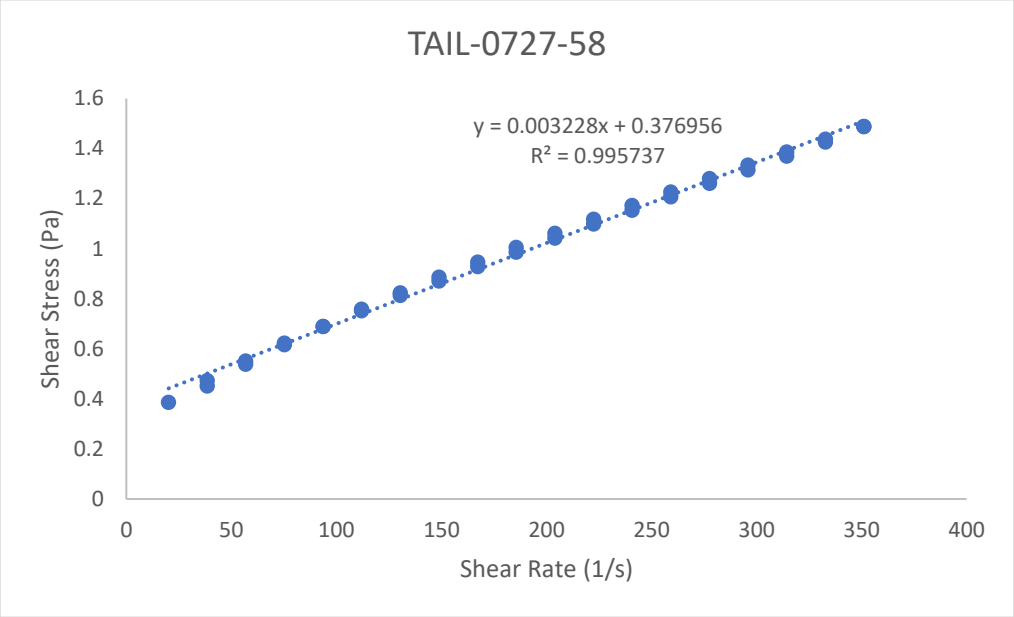
TAIL-0727-58
y = 0.003228x + 0.376956
R² = 0.995737
Shear Stress (Pa)
Shear Rate (1/s)
0
0.2
0.4
0.6
0.8
1
1.2
1.4
1.6
0
50
100
150
200
250
300
350
400

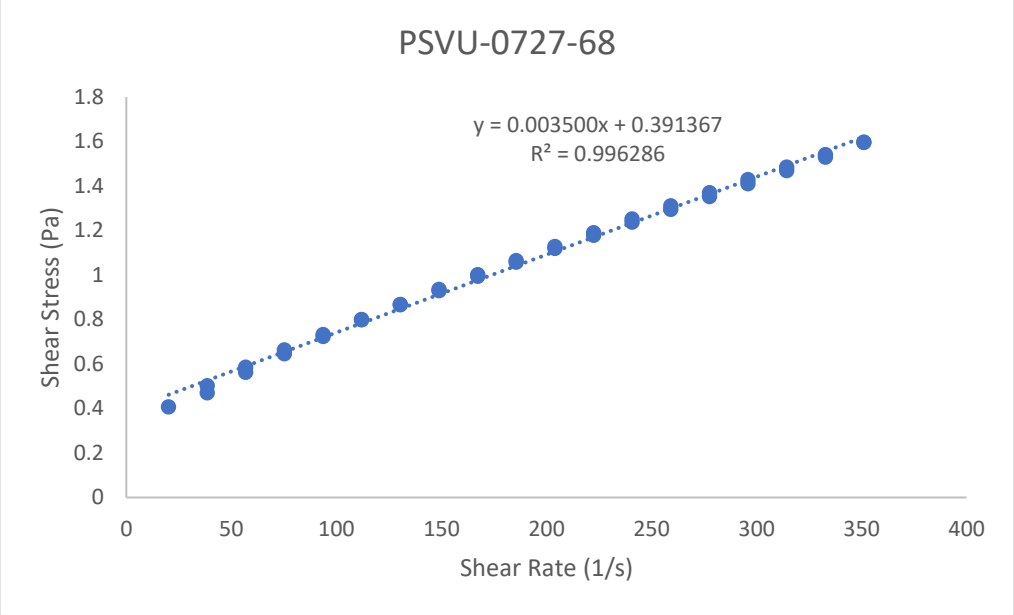
PSVU-0727-68
y = 0.003500x + 0.391367
R² = 0.996286
Shear Stress (Pa)
Shear Rate (1/s)
0
0.2
0.4
0.6
0.8
1
1.2
1.4
1.6
1.8
0
50
100
150
200
250
300
350
400

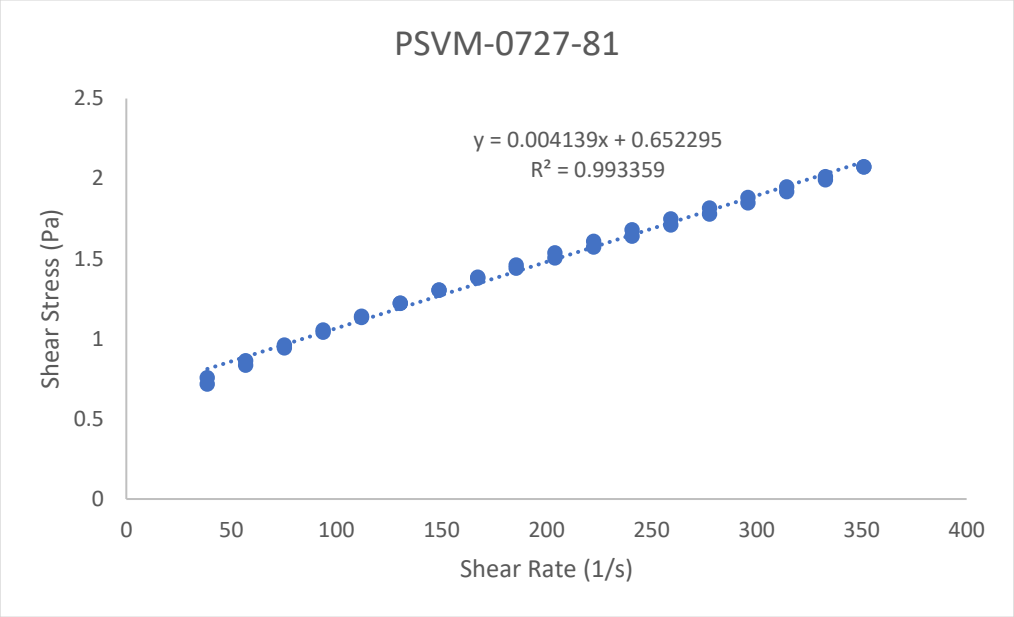
PSVM-0727-81
y = 0.004139x + 0.652295
R² = 0.993359
Shear Stress (Pa)
Shear Rate (1/s)
0
0.5
1
1.5
2
2.5
0
50
100
150
200
250
300
350
400

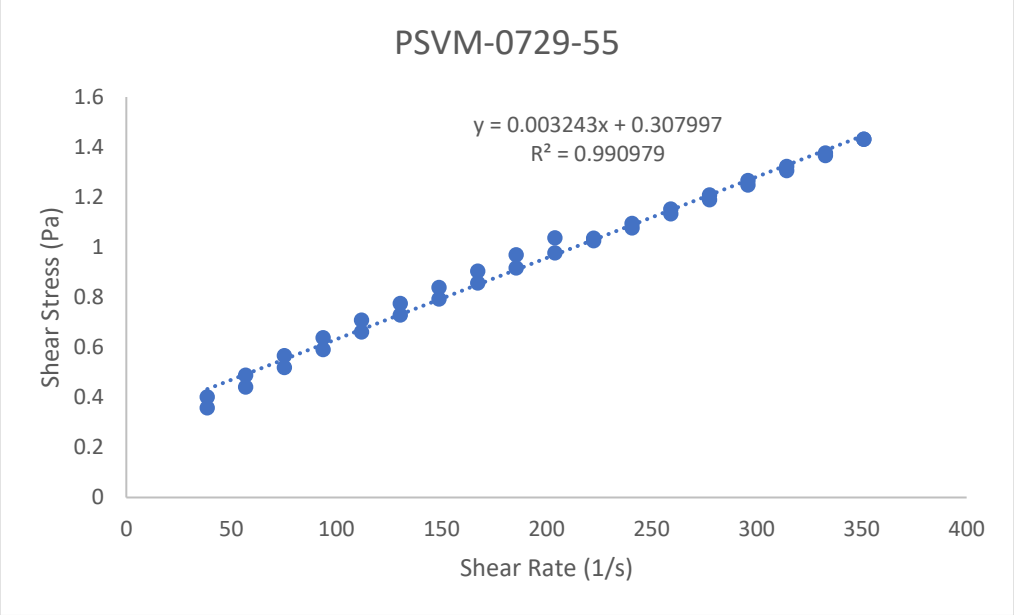
PSVM-0729-55
y = 0.003243x + 0.307997
R² = 0.990979
Shear Stress (Pa)
Shear Rate (1/s)
0
0.2
0.4
0.6
0.8
1
1.2
1.4
1.6
0
50
100
150
200
250
300
350
400

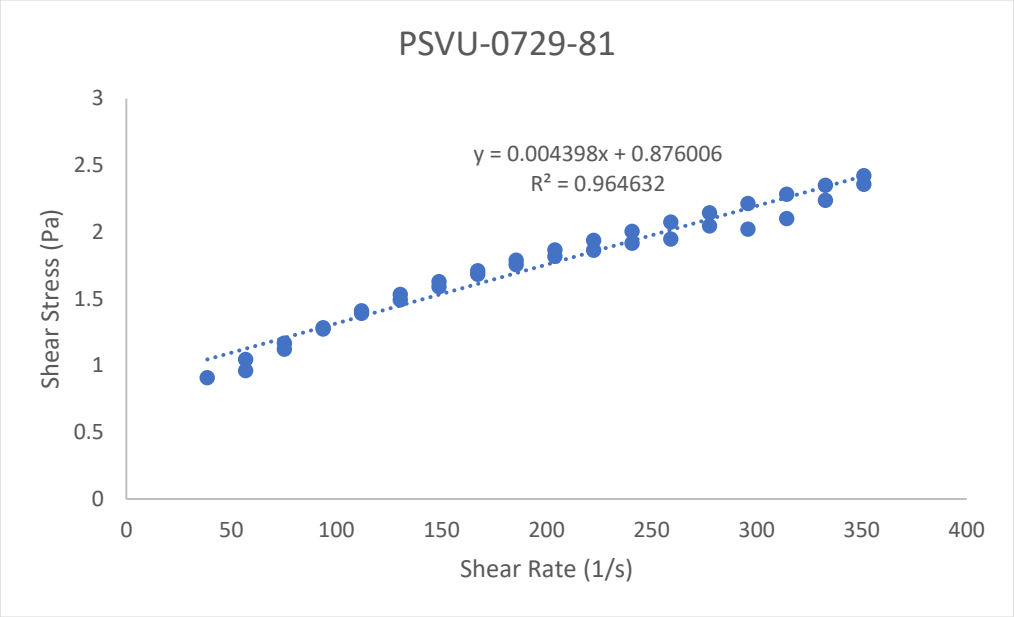
PSVU-0729-81
y = 0.004398x + 0.876006
R² = 0.964632
Shear Stress (Pa)
Shear Rate (1/s)
0
0.5
1
1.5
2
2.5
3
0
50
100
150
200
250
300
350
400

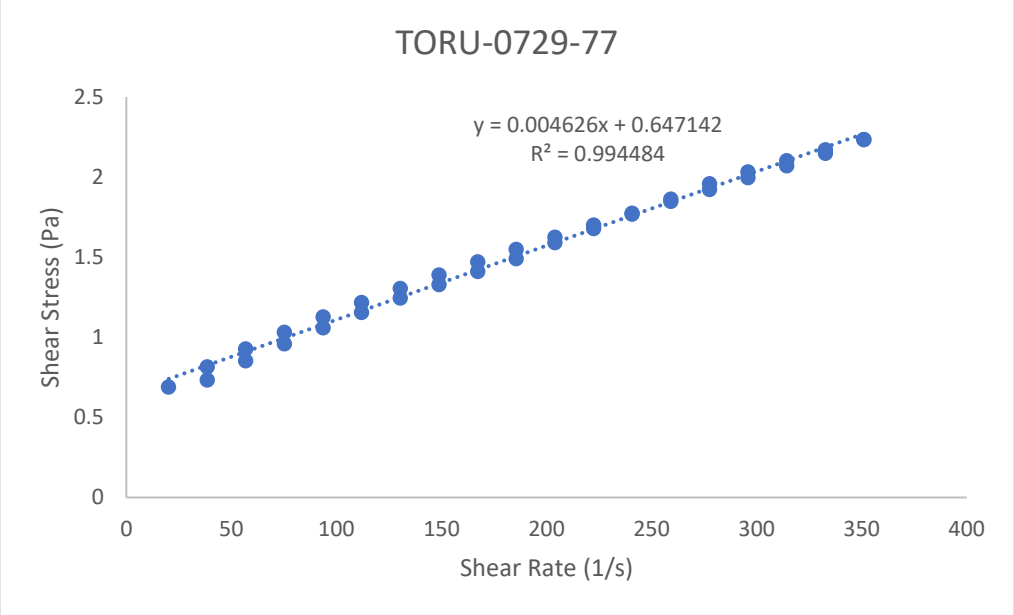
TORU-0729-77
y = 0.004626x + 0.647142
R² = 0.994484
Shear Stress (Pa)
Shear Rate (1/s)
0
0.5
1
1.5
2
2.5
0
50
100
150
200
250
300
350
400

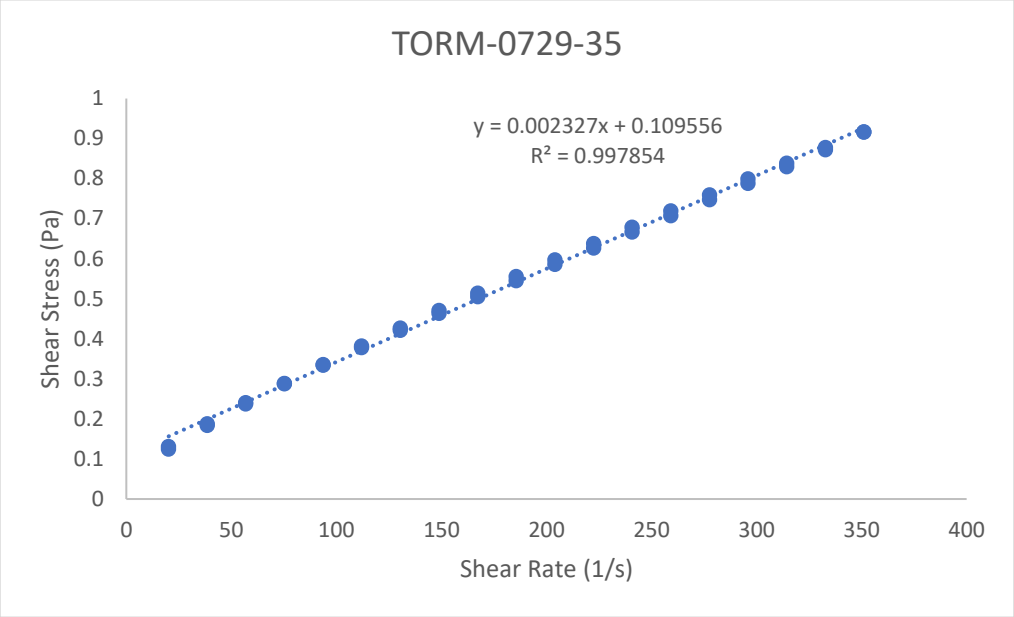
TORM-0729-35
y = 0.002327x + 0.109556
R² = 0.997854
Shear Stress (Pa)
Shear Rate (1/s)
0
0.1
0.2
0.3
0.4
0.5
0.6
0.7
0.8
0.9
1
0
50
100
150
200
250
300
350
400

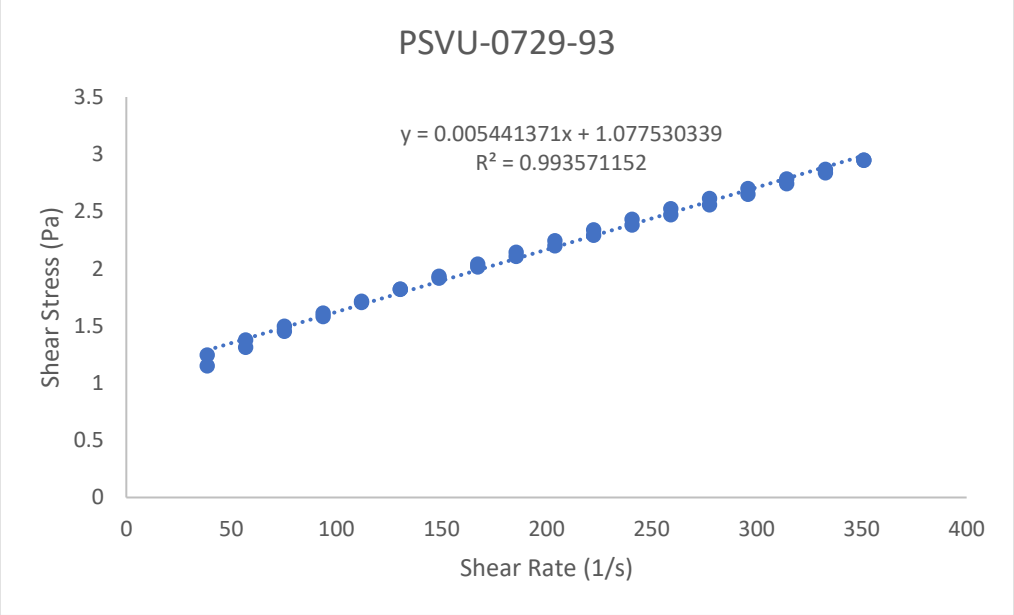
PSVU-0729-93
y = 0.005441371x + 1.077530339
R² = 0.993571152
Shear Stress (Pa)
Shear Rate (1/s)
0
0.5
1
1.5
2
2.5
3
3.5
0
50
100
150
200
250
300
350
400

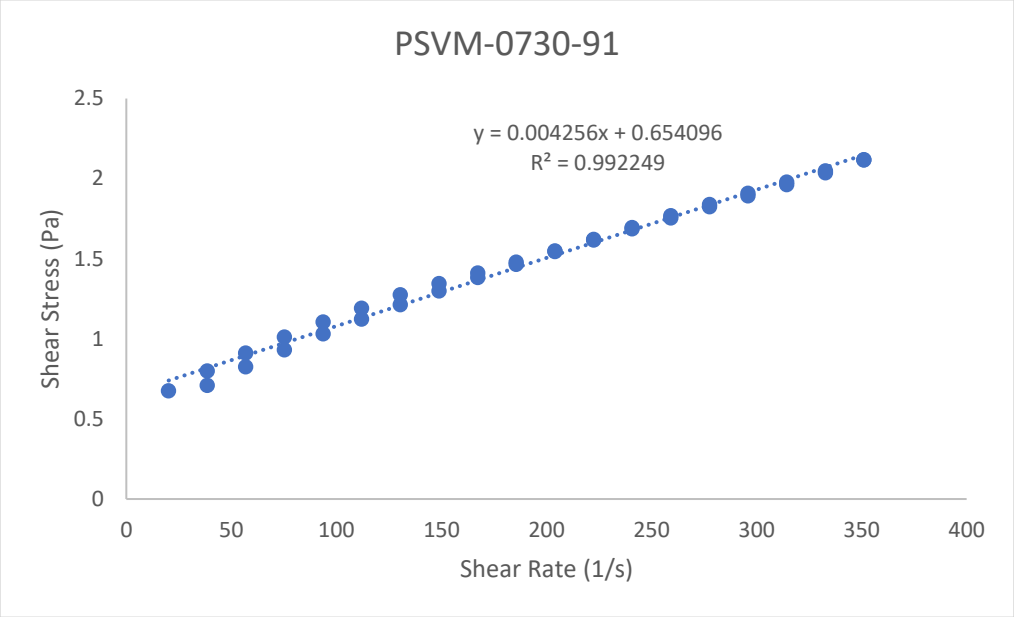
PSVM-0730-91
y = 0.004256x + 0.654096
R² = 0.992249
Shear Stress (Pa)
Shear Rate (1/s)
0
0.5
1
1.5
2
2.5
0
50
100
150
200
250
300
350
400

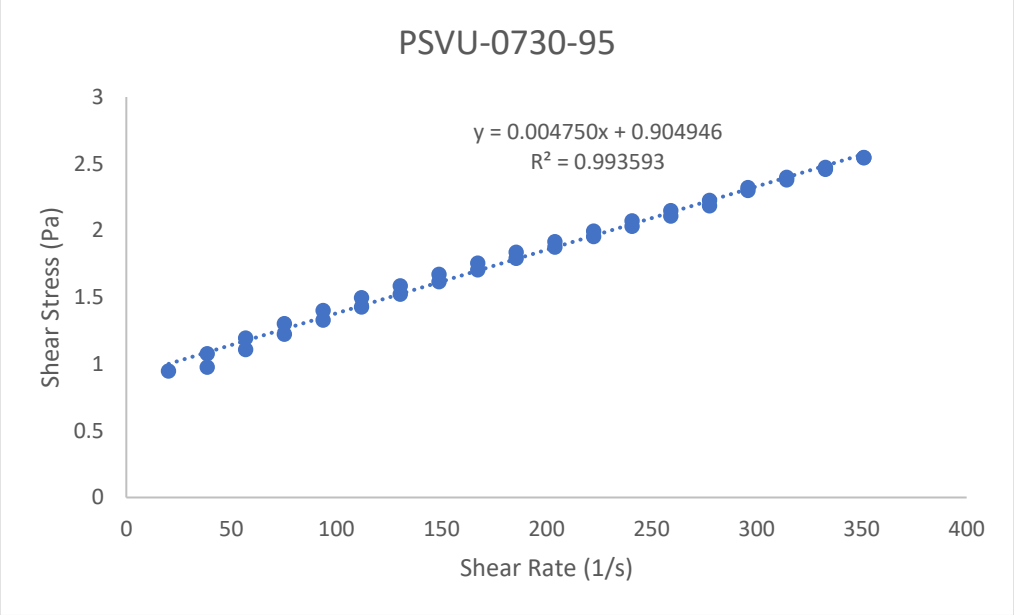
PSVU-0730-95
y = 0.004750x + 0.904946
R² = 0.993593
Shear Stress (Pa)
Shear Rate (1/s)
0
0.5
1
1.5
2
2.5
3
0
50
100
150
200
250
300
350
400

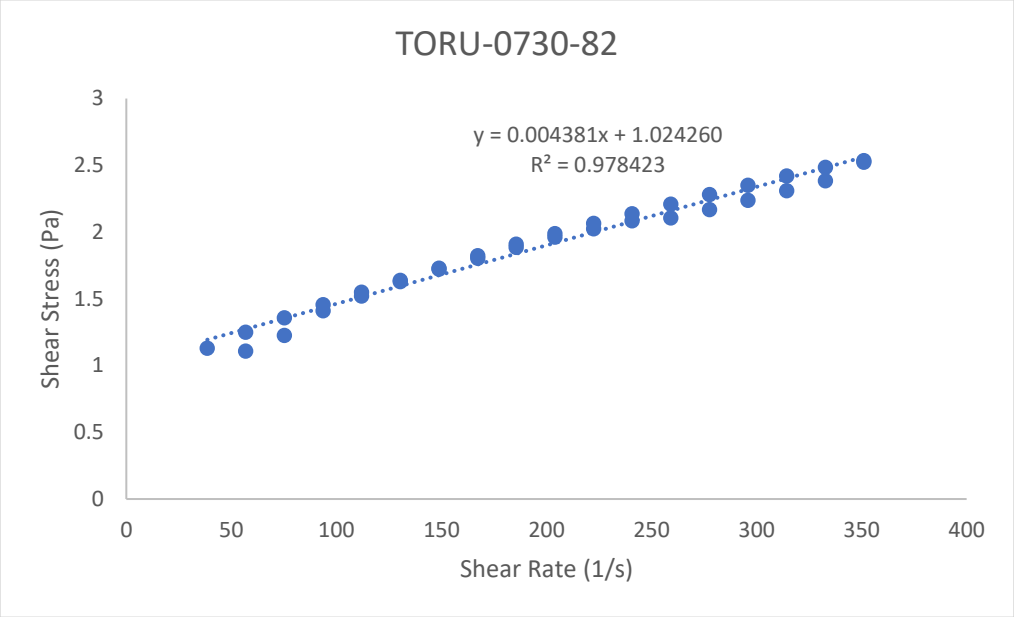
TORU-0730-82
y = 0.004381x + 1.024260
R² = 0.978423
Shear Stress (Pa)
Shear Rate (1/s)
0
0.5
1
1.5
2
2.5
3
0
50
100
150
200
250
300
350
400

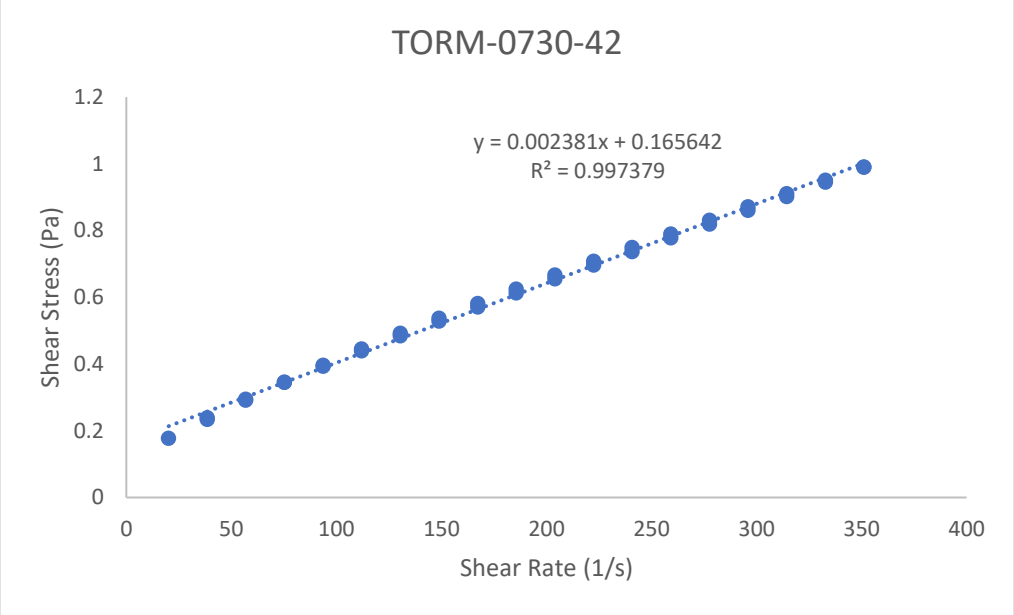
TORM-0730-42
y = 0.002381x + 0.165642
R² = 0.997379
Shear Stress (Pa)
Shear Rate (1/s)
0
0.2
0.4
0.6
0.8
1
1.2
0
50
100
150
200
250
300
350
400

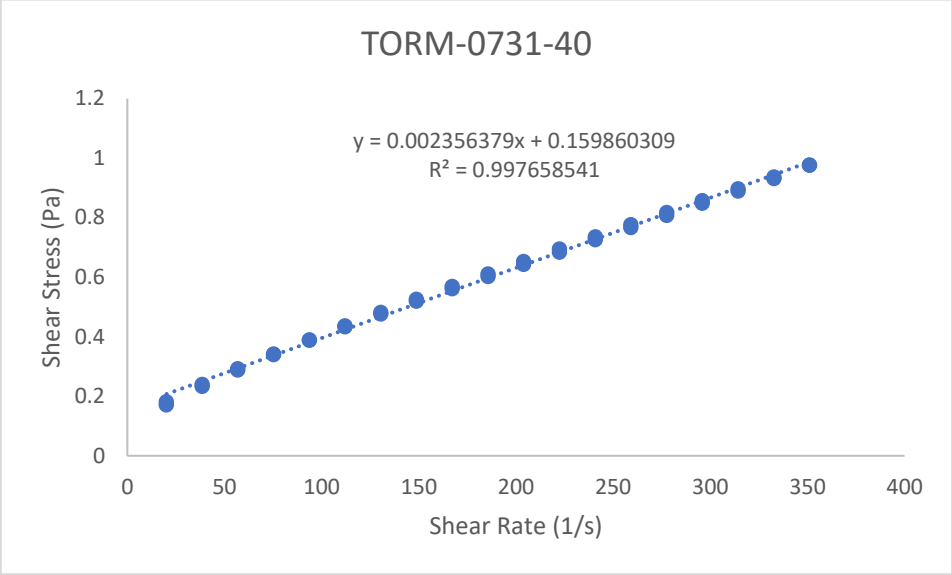
TORM-0731-40
y = 0.002356379x + 0.159860309
R² = 0.997658541
Shear Stress (Pa)
Shear Rate (1/s)
0
0.2
0.4
0.6
0.8
1
1.2
0
50
100
150
200
250
300
350
400

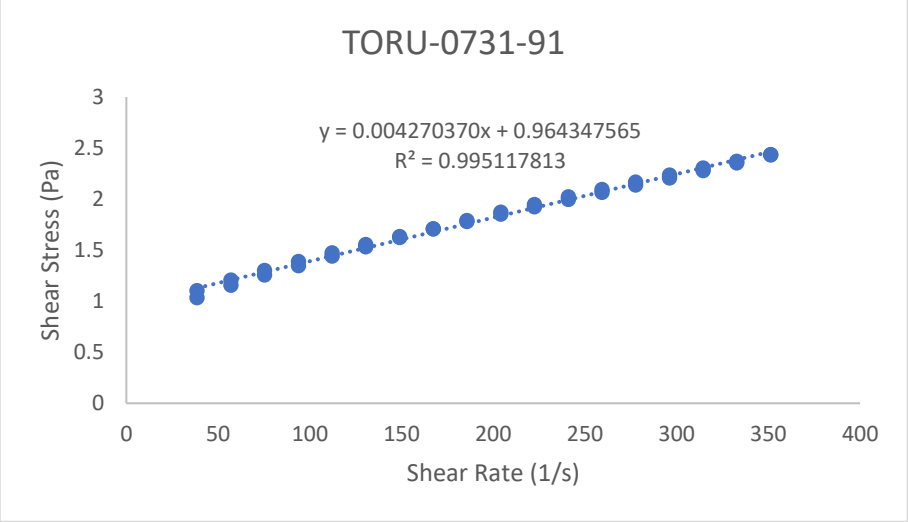
TORU-0731-91
y = 0.004270370x + 0.964347565
R² = 0.995117813
Shear Stress (Pa)
Shear Rate (1/s)
0
0.5
1
1.5
2
2.5
3
0
50
100
150
200
250
300
350
400

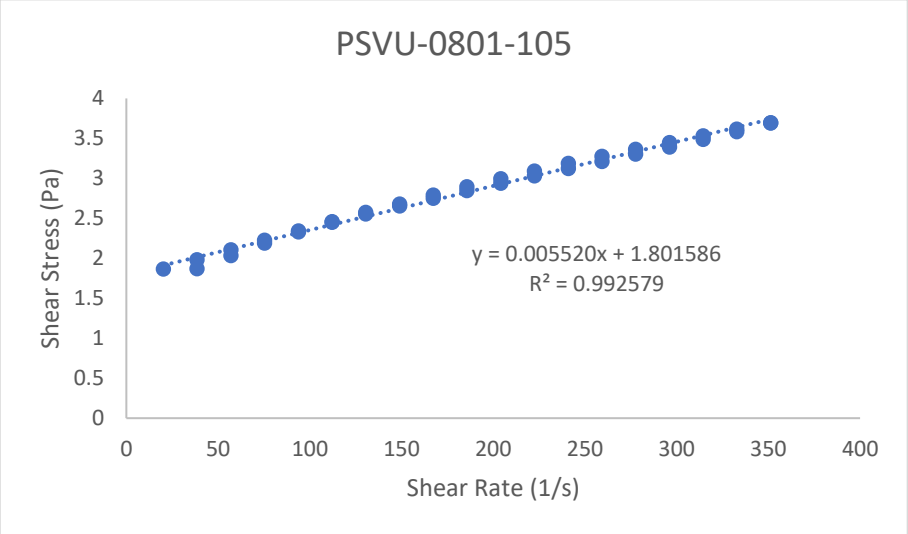
PSVU-0801-105
y = 0.005520x + 1.801586
R² = 0.992579
Shear Stress (Pa)
Shear Rate (1/s)
0
0.5
1
1.5
2
2.5
3
3.5
4
0
50
100
150
200
250
300
350
400

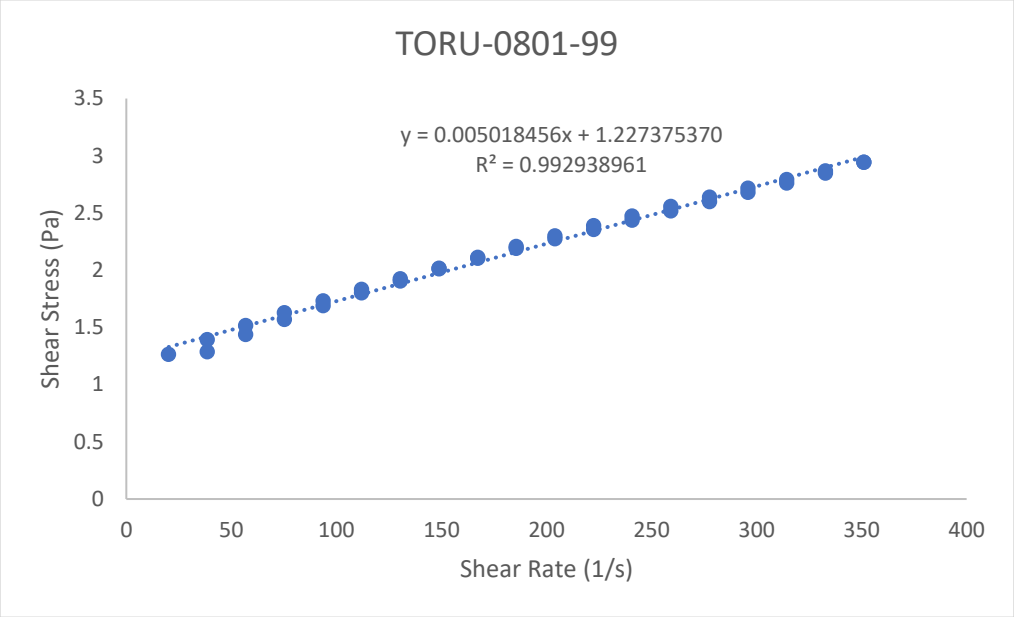
TORU-0801-99
y = 0.005018456x + 1.227375370
R² = 0.992938961
Shear Stress (Pa)
Shear Rate (1/s)
0
0.5
1
1.5
2
2.5
3
3.5
0
50
100
150
200
250
300
350
400

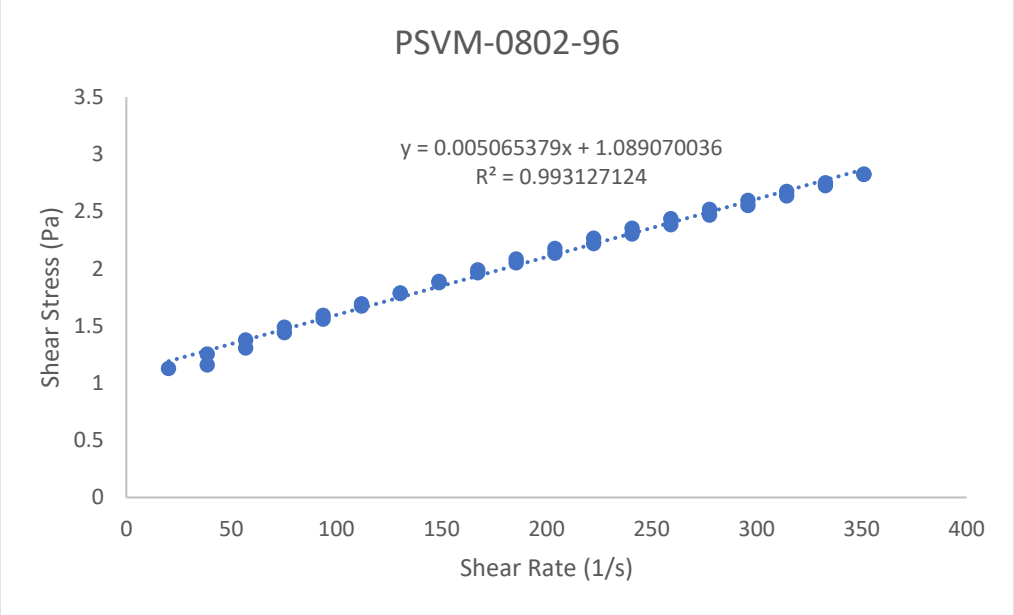
PSVM-0802-96
y = 0.005065379x + 1.089070036
R² = 0.993127124
Shear Stress (Pa)
Shear Rate (1/s)
0
0.5
1
1.5
2
2.5
3
3.5
0
50
100
150
200
250
300
350
400

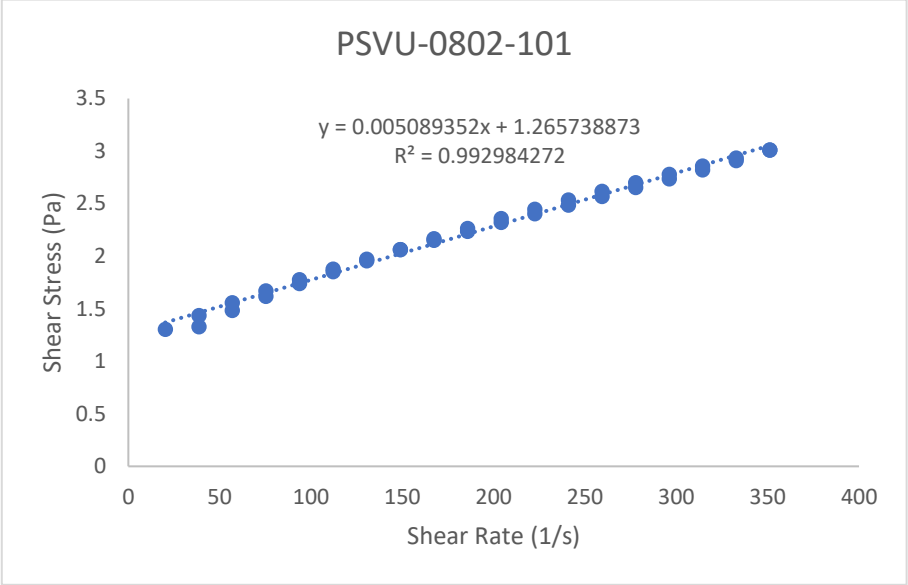
PSVU-0802-101
y = 0.005089352x + 1.265738873
R² = 0.992984272
Shear Stress (Pa)
Shear Rate (1/s)
0
0.5
1
1.5
2
2.5
3
3.5
0
50
100
150
200
250
300
350
400

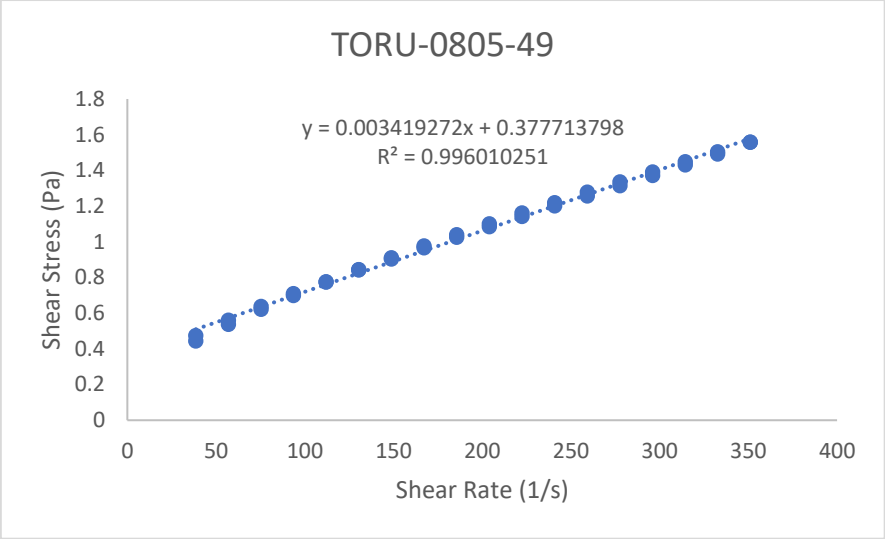
TORU-0805-49
y = 0.003419272x + 0.377713798
R² = 0.996010251
Shear Stress (Pa)
Shear Rate (1/s)
0
0.2
0.4
0.6
0.8
1
1.2
1.4
1.6
1.8
0
50
100
150
200
250
300
350
400

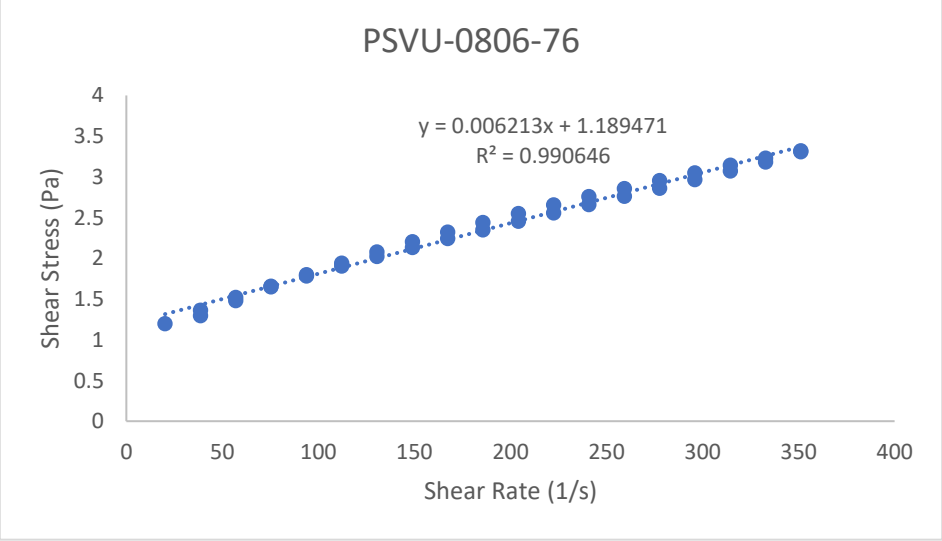
PSVU-0806-76
y = 0.006213x + 1.189471
R² = 0.990646
Shear Stress (Pa)
Shear Rate (1/s)
0
0.5
1
1.5
2
2.5
3
3.5
4
0
50
100
150
200
250
300
350
400

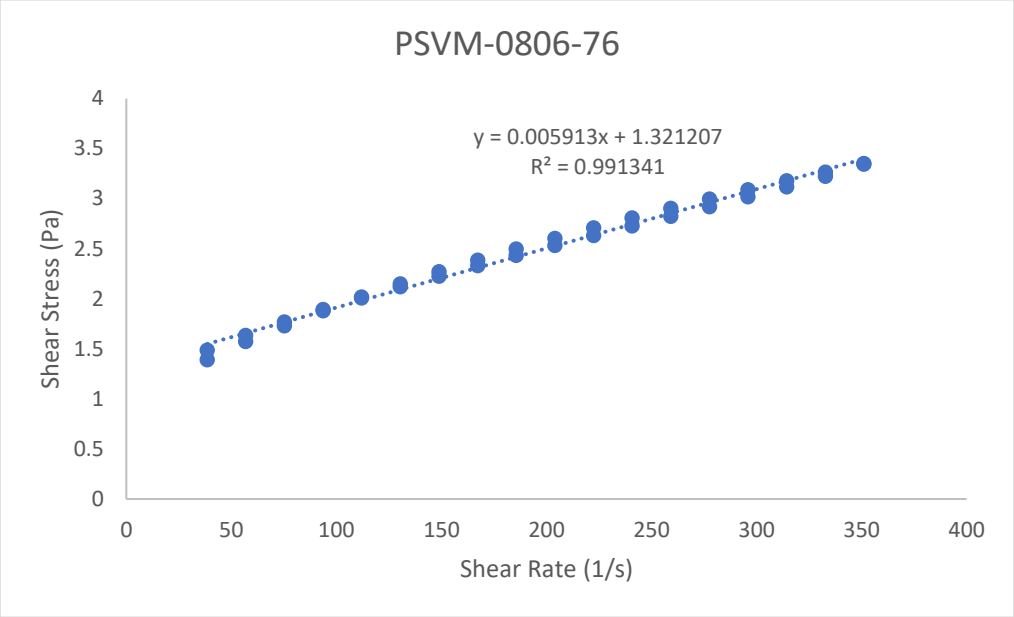
PSVM-0806-76
y = 0.005913x + 1.321207
R² = 0.991341
Shear Stress (Pa)
Shear Rate (1/s)
0
0.5
1
1.5
2
2.5
3
3.5
4
0
50
100
150
200
250
300
350
400

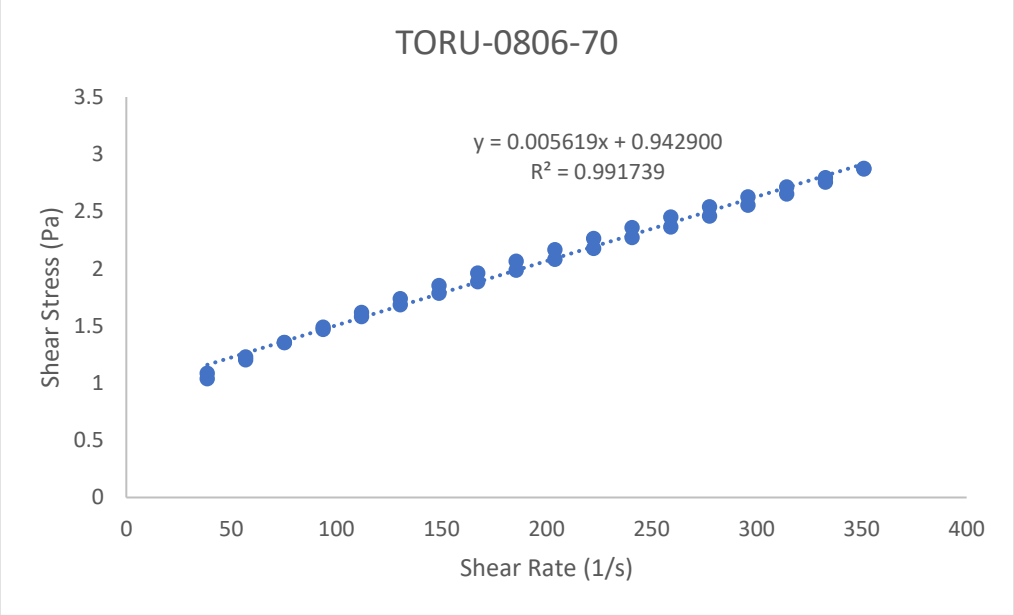
TORU-0806-70
y = 0.005619x + 0.942900
R² = 0.991739
Shear Stress (Pa)
Shear Rate (1/s)
0
0.5
1
1.5
2
2.5
3
3.5
0
50
100
150
200
250
300
350
400

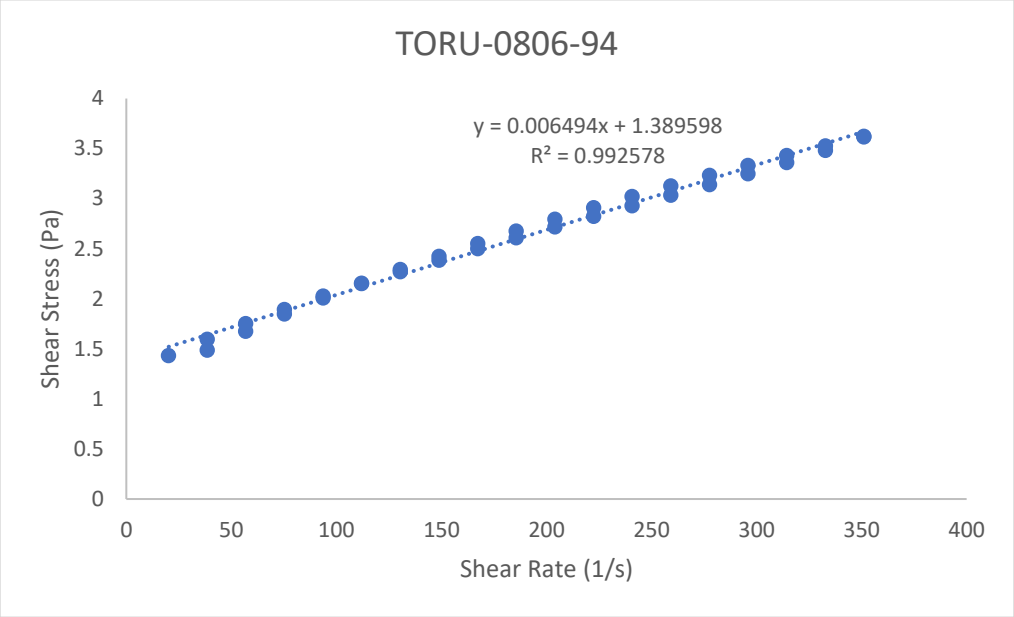
TORU-0806-94
y = 0.006494x + 1.389598
R² = 0.992578
Shear Stress (Pa)
Shear Rate (1/s)
0
0.5
1
1.5
2
2.5
3
3.5
4
0
50
100
150
200
250
300
350
400

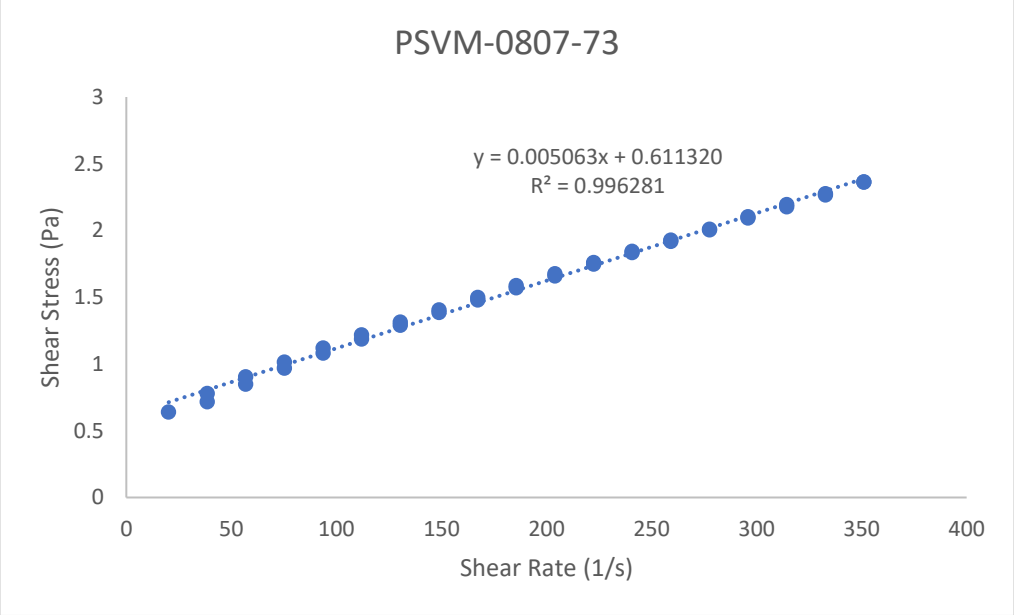
PSVM-0807-73
y = 0.005063x + 0.611320
R² = 0.996281
Shear Stress (Pa)
Shear Rate (1/s)
0
0.5
1
1.5
2
2.5
3
0
50
100
150
200
250
300
350
400

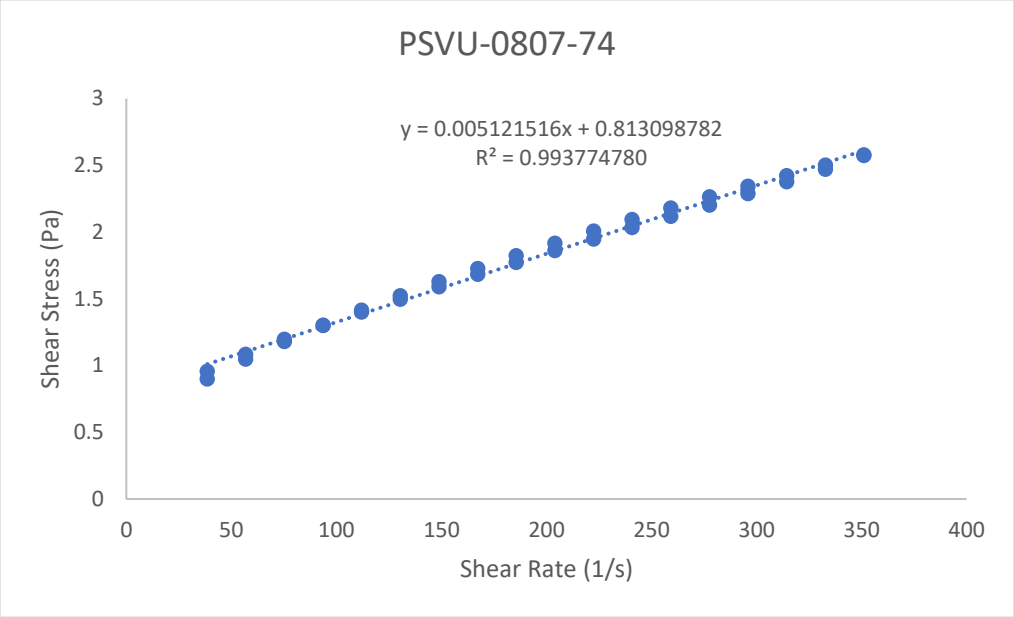
PSVU-0807-74
y = 0.005121516x + 0.813098782
R² = 0.993774780
Shear Stress (Pa)
Shear Rate (1/s)
0
0.5
1
1.5
2
2.5
3
0
50
100
150
200
250
300
350
400

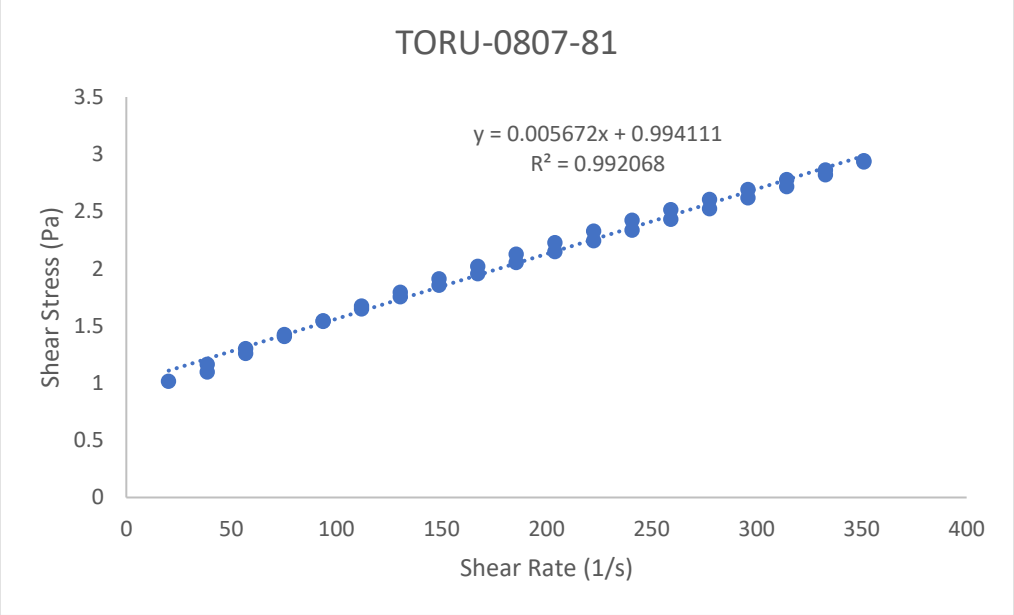
TORU-0807-81
y = 0.005672x + 0.994111
R² = 0.992068
Shear Stress (Pa)
Shear Rate (1/s)
0
0.5
1
1.5
2
2.5
3
3.5
0
50
100
150
200
250
300
350
400

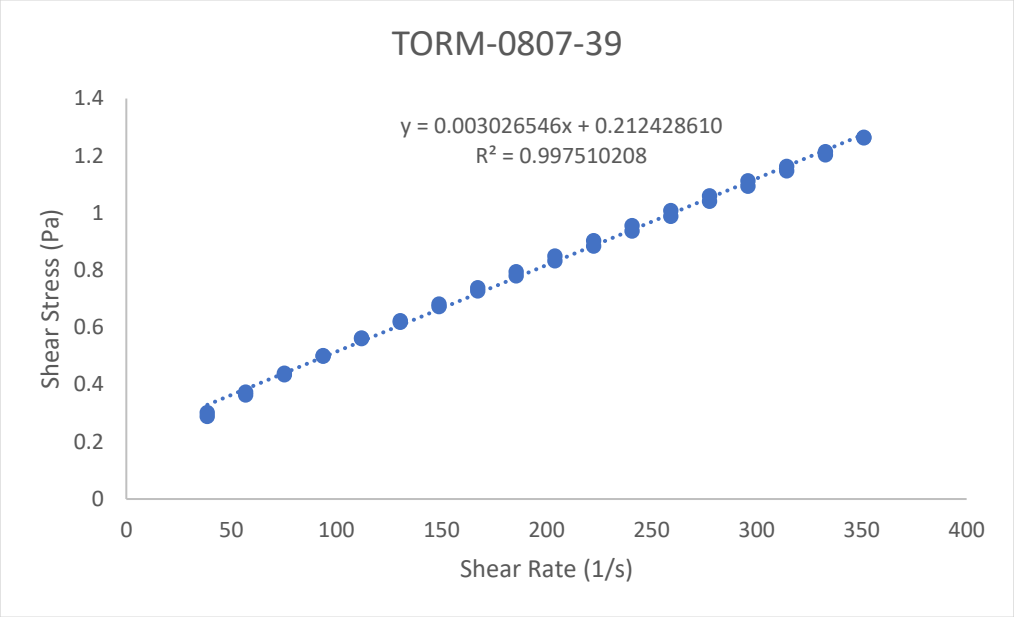
TORM-0807-39
y = 0.003026546x + 0.212428610
R² = 0.997510208
Shear Stress (Pa)
Shear Rate (1/s)
0
0.2
0.4
0.6
0.8
1
1.2
1.4
0
50
100
150
200
250
300
350
400

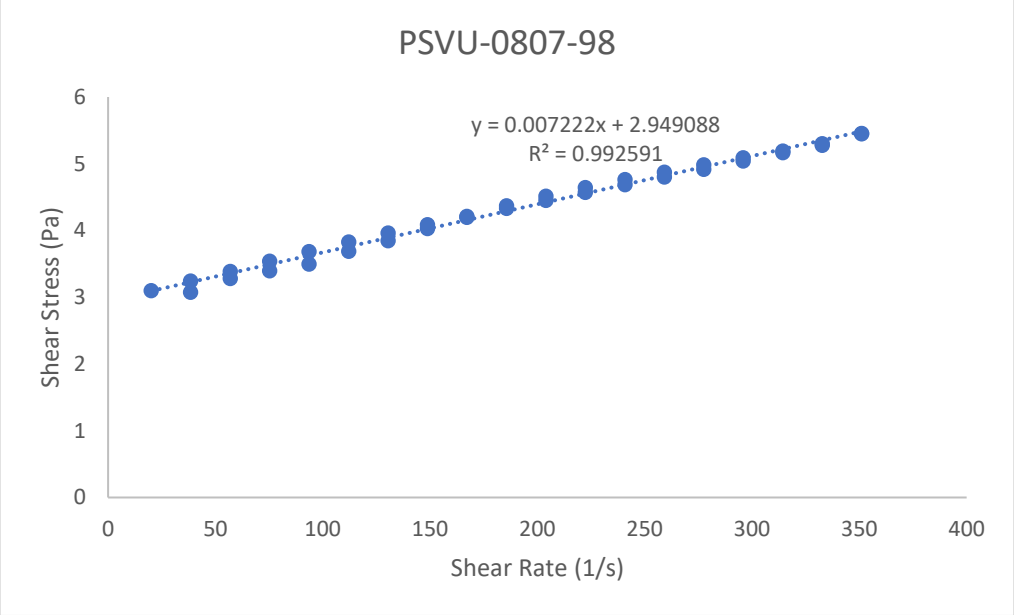
PSVU-0807-98
y = 0.007222x + 2.949088
R² = 0.992591
Shear Stress (Pa)
Shear Rate (1/s)
0
1
2
3
4
5
6
0
50
100
150
200
250
300
350
400

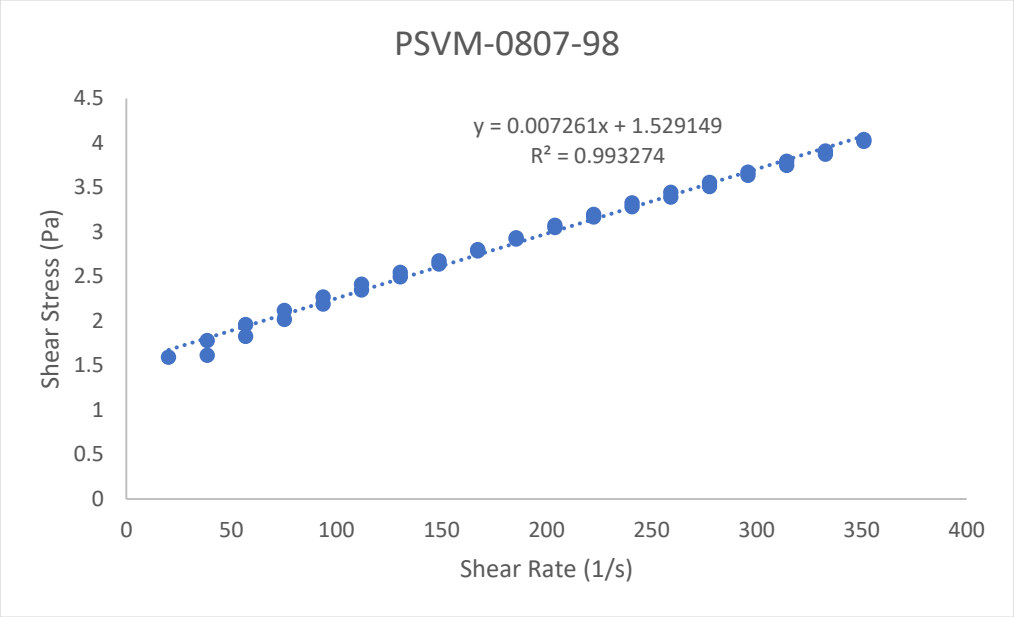
PSVM-0807-98
y = 0.007261x + 1.529149
R² = 0.993274
Shear Stress (Pa)
Shear Rate (1/s)
0
0.5
1
1.5
2
2.5
3
3.5
4
4.5
0
50
100
150
200
250
300
350
400

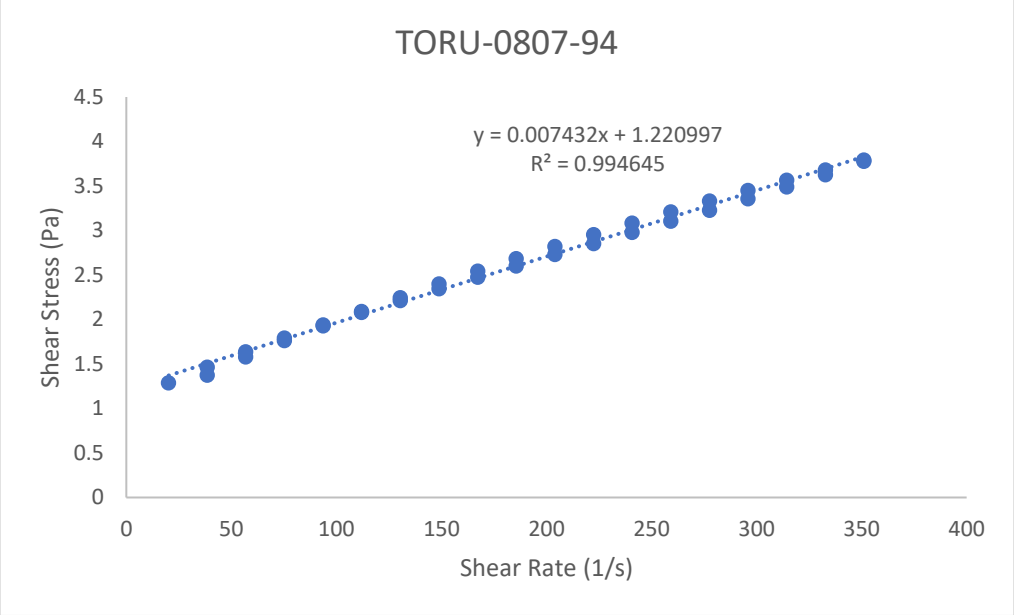
TORU-0807-94
y = 0.007432x + 1.220997
R² = 0.994645
Shear Stress (Pa)
Shear Rate (1/s)
0
0.5
1
1.5
2
2.5
3
3.5
4
4.5
0
50
100
150
200
250
300
350
400

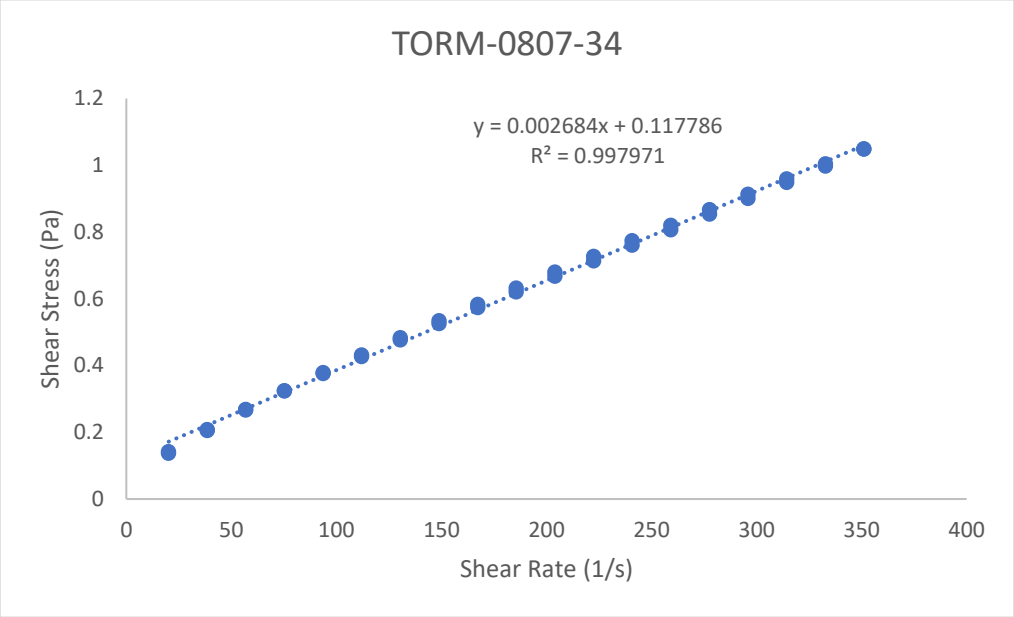
TORM-0807-34
y = 0.002684x + 0.117786
R² = 0.997971
Shear Stress (Pa)
Shear Rate (1/s)
0
0.2
0.4
0.6
0.8
1
1.2
0
50
100
150
200
250
300
350
400

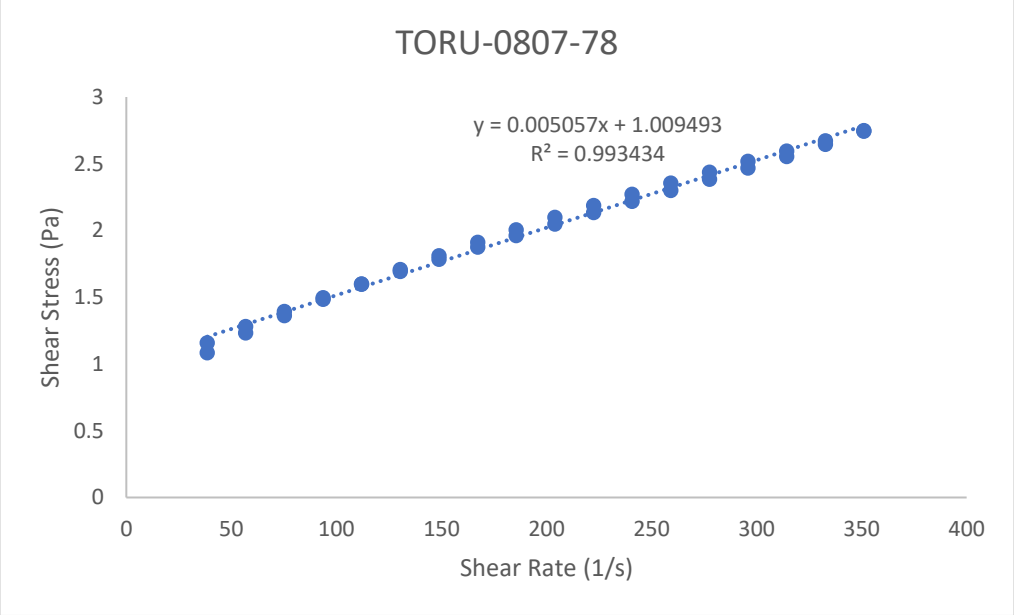
TORU-0807-78
y = 0.005057x + 1.009493
R² = 0.993434
Shear Stress (Pa)
Shear Rate (1/s)
0
0.5
1
1.5
2
2.5
3
0
50
100
150
200
250
300
350
400

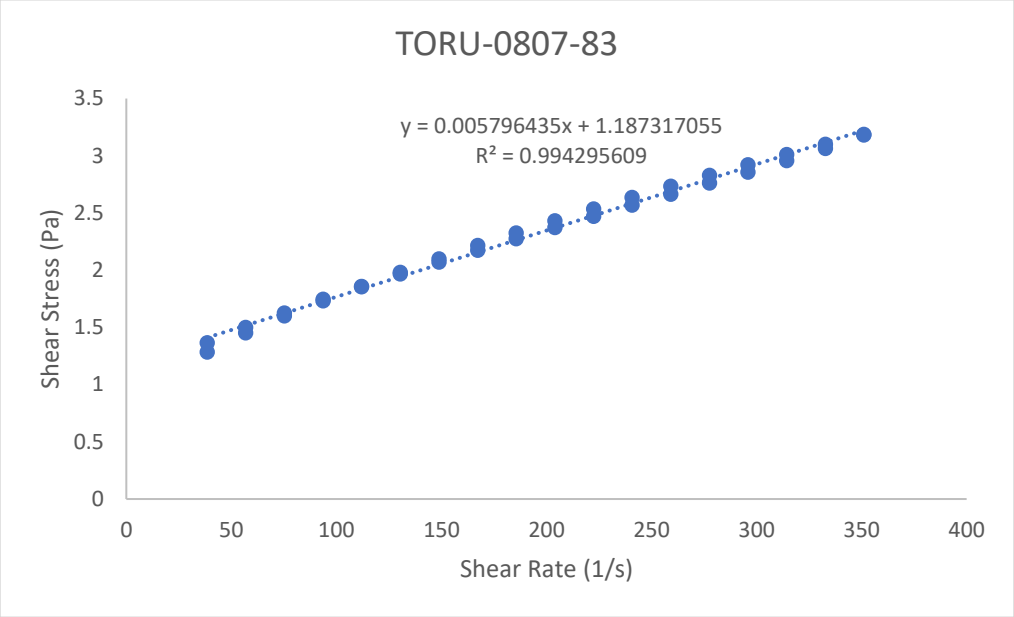
TORU-0807-83
y = 0.005796435x + 1.187317055
R² = 0.994295609
Shear Stress (Pa)
Shear Rate (1/s)
0
0.5
1
1.5
2
2.5
3
3.5
0
50
100
150
200
250
300
350
400

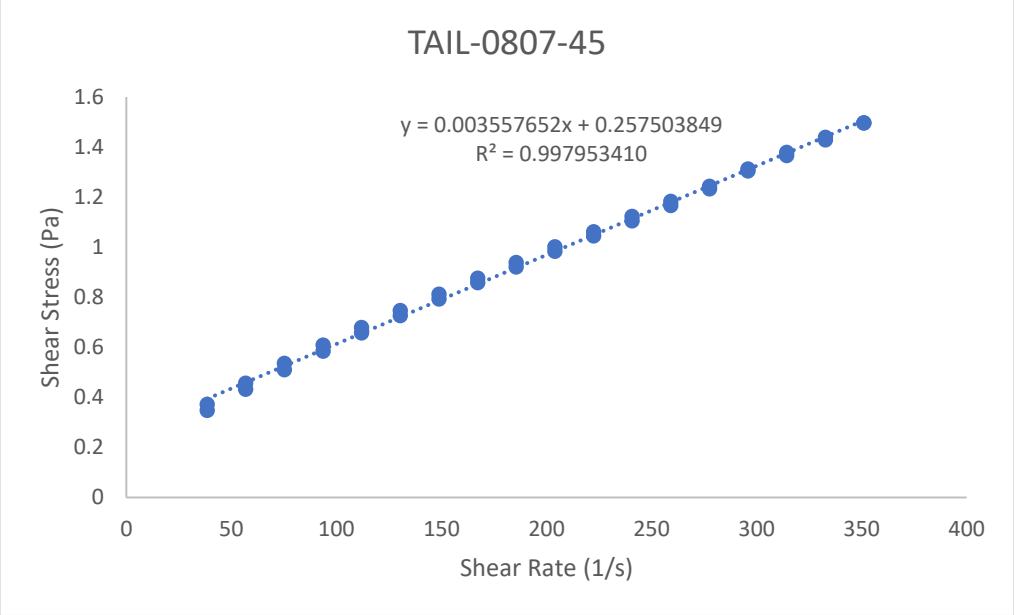
TAIL-0807-45
y = 0.003557652x + 0.257503849
R² = 0.997953410
Shear Stress (Pa)
Shear Rate (1/s)
0
0.2
0.4
0.6
0.8
1
1.2
1.4
1.6
0
50
100
150
200
250
300
350
400

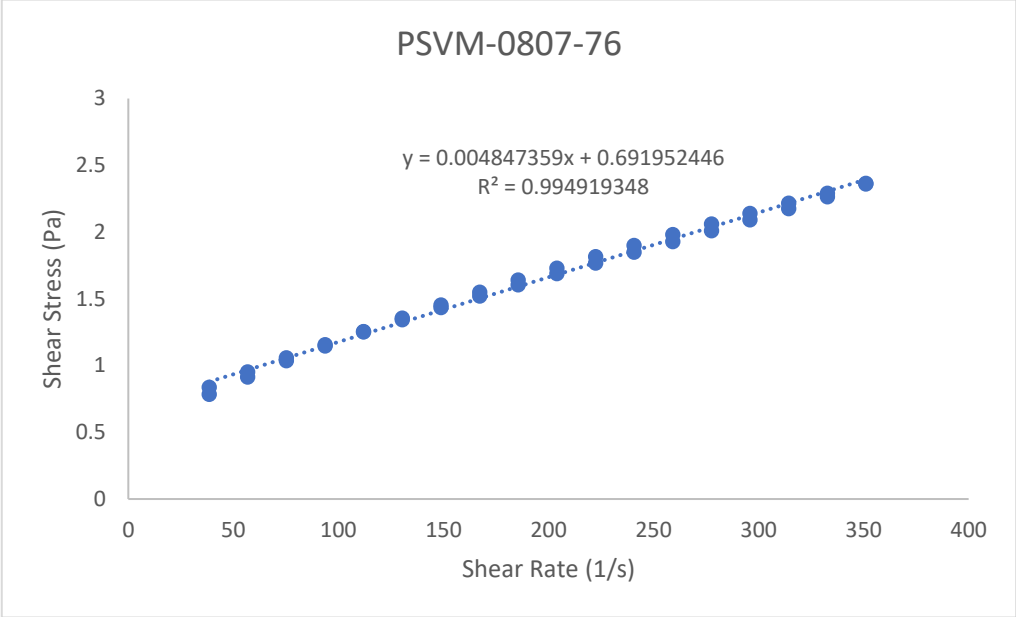
PSVM-0807-76
y = 0.004847359x + 0.691952446
R² = 0.994919348
Shear Stress (Pa)
Shear Rate (1/s)
0
0.5
1
1.5
2
2.5
3
0
50
100
150
200
250
300
350
400

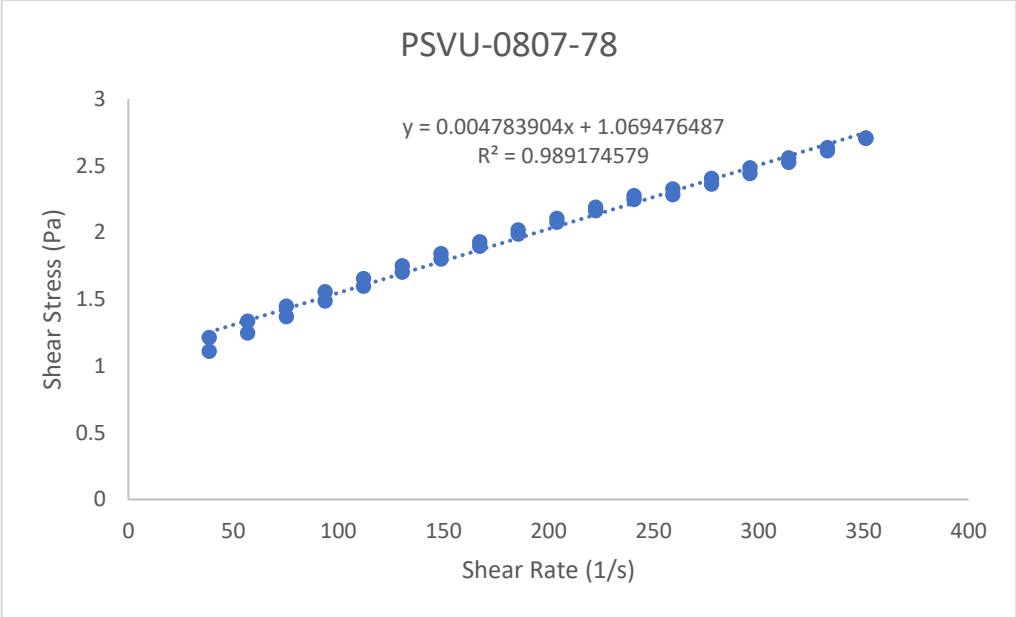
PSVU-0807-78
y = 0.004783904x + 1.069476487
R² = 0.989174579
Shear Stress (Pa)
Shear Rate (1/s)
0
0.5
1
1.5
2
2.5
3
0
50
100
150
200
250
300
350
400

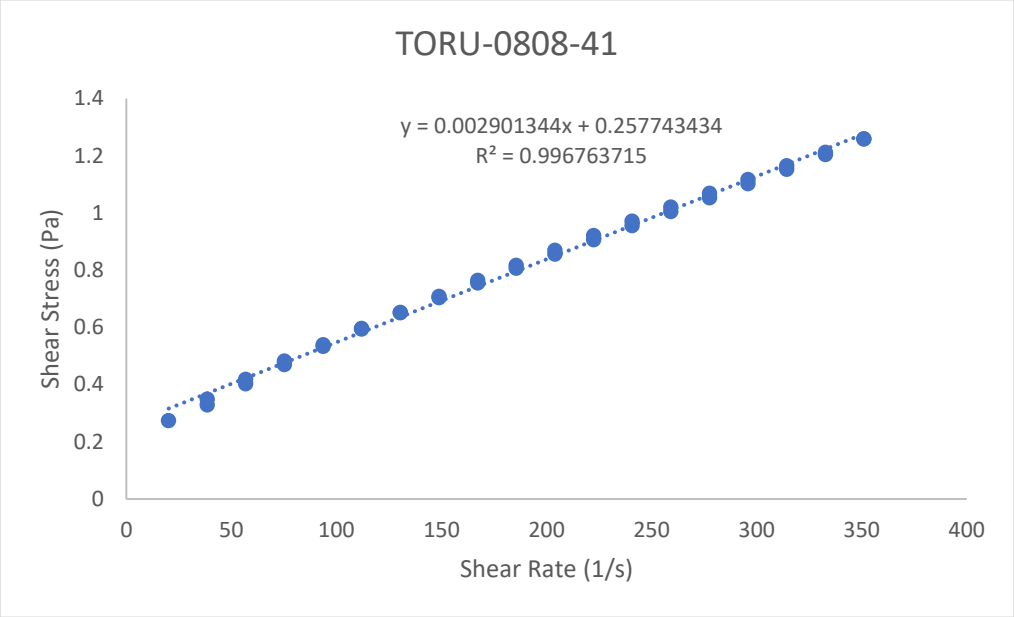
TORU-0808-41
y = 0.002901344x + 0.257743434
R² = 0.996763715
Shear Stress (Pa)
Shear Rate (1/s)
0
0.2
0.4
0.6
0.8
1
1.2
1.4
0
50
100
150
200
250
300
350
400

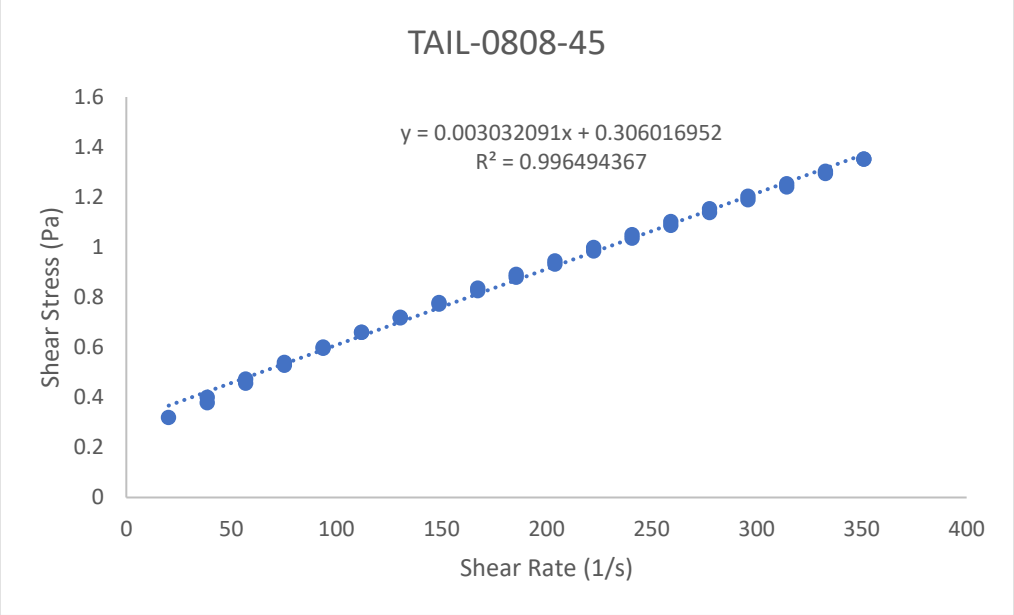
TAIL-0808-45
y = 0.003032091x + 0.306016952
R² = 0.996494367
Shear Stress (Pa)
Shear Rate (1/s)
0
0.2
0.4
0.6
0.8
1
1.2
1.4
1.6
0
50
100
150
200
250
300
350
400

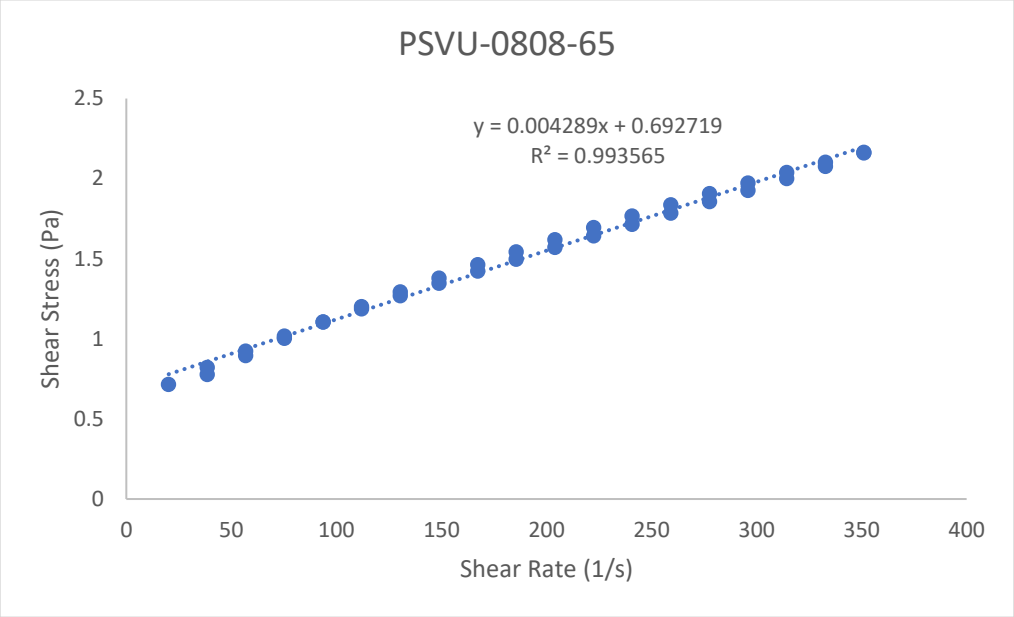
PSVU-0808-65
y = 0.004289x + 0.692719
R² = 0.993565
Shear Stress (Pa)
Shear Rate (1/s)
0
0.5
1
1.5
2
2.5
0
50
100
150
200
250
300
350
400

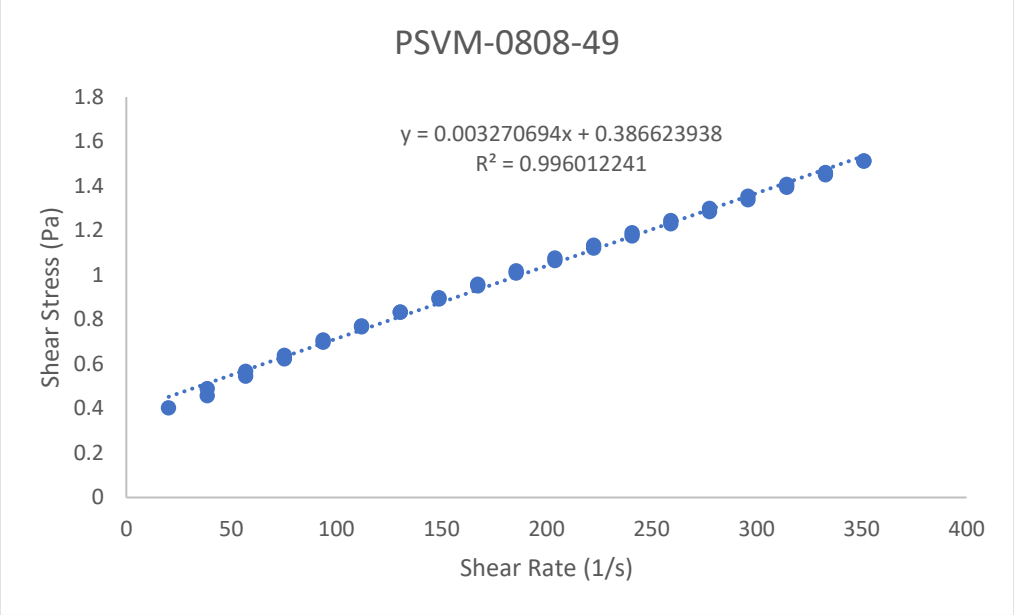
PSVM-0808-49
y = 0.003270694x + 0.386623938
R² = 0.996012241
Shear Stress (Pa)
Shear Rate (1/s)
0
0.2
0.4
0.6
0.8
1
1.2
1.4
1.6
1.8
0
50
100
150
200
250
300
350
400

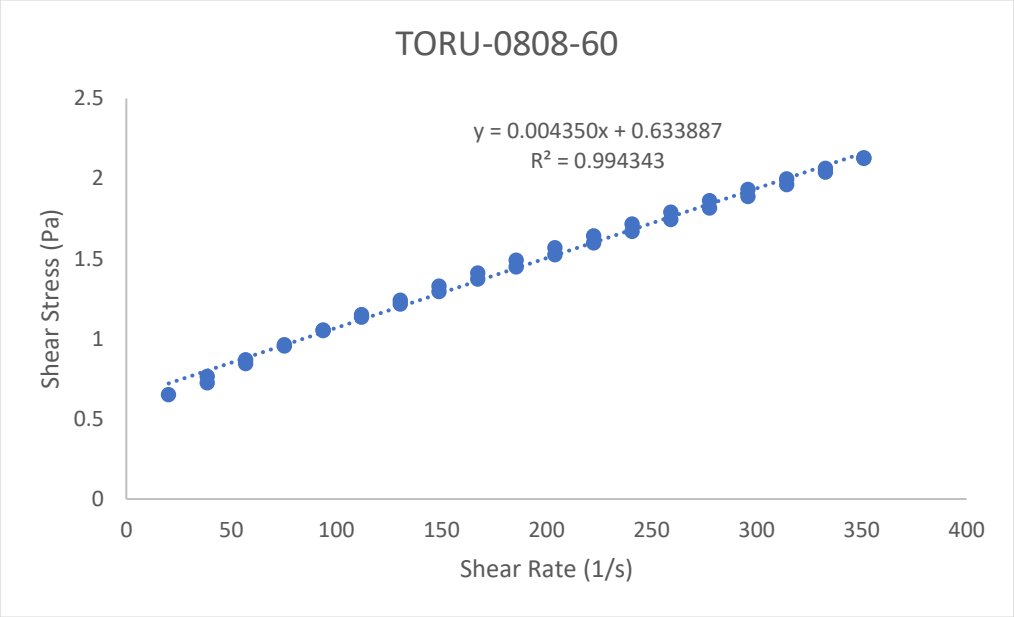
TORU-0808-60
y = 0.004350x + 0.633887
R² = 0.994343
Shear Stress (Pa)
Shear Rate (1/s)
0
0.5
1
1.5
2
2.5
0
50
100
150
200
250
300
350
400

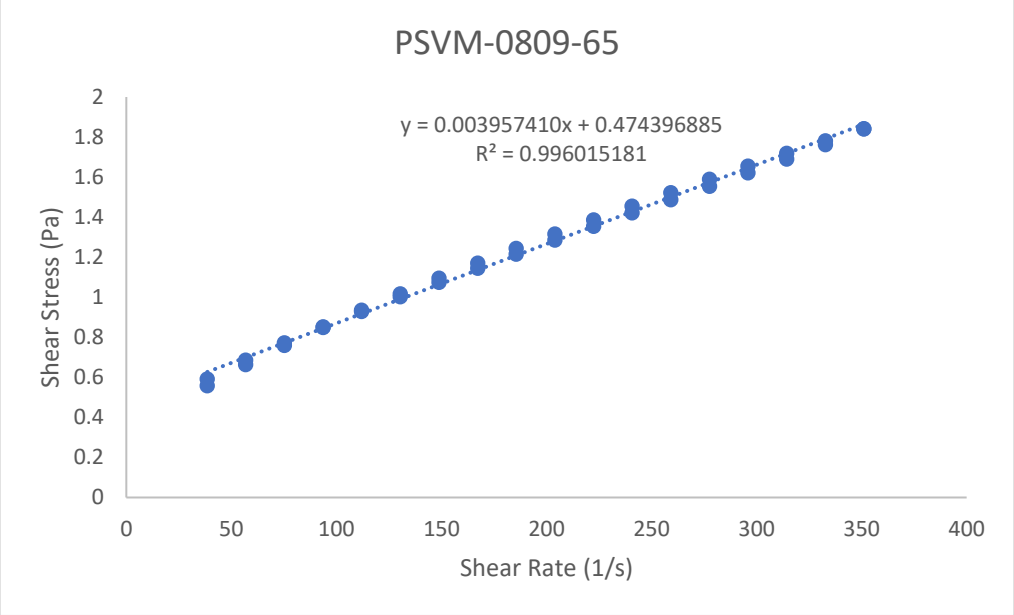
PSVM-0809-65
y = 0.003957410x + 0.474396885
R² = 0.996015181
Shear Stress (Pa)
Shear Rate (1/s)
0
0.2
0.4
0.6
0.8
1
1.2
1.4
1.6
1.8
2
0
50
100
150
200
250
300
350
400

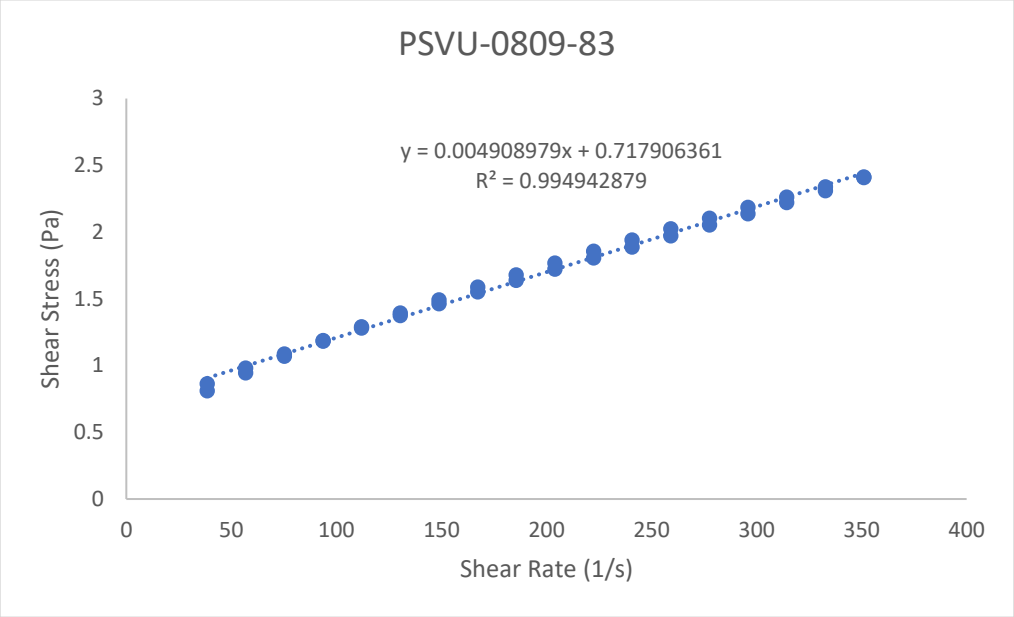
PSVU-0809-83
y = 0.004908979x + 0.717906361
R² = 0.994942879
Shear Stress (Pa)
Shear Rate (1/s)
0
0.5
1
1.5
2
2.5
3
0
50
100
150
200
250
300
350
400

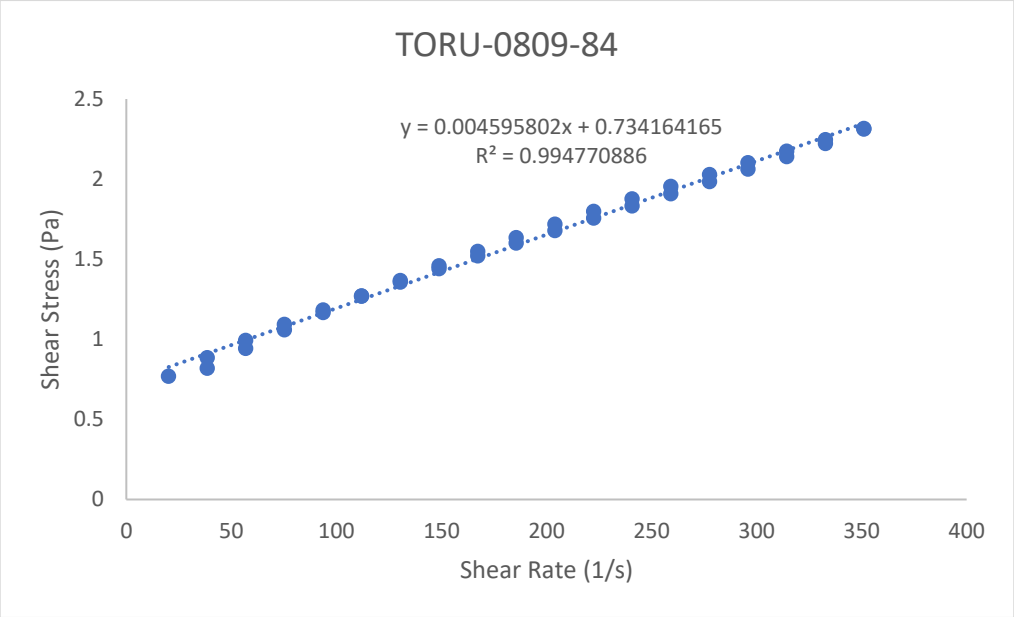
TORU-0809-84
y = 0.004595802x + 0.734164165
R² = 0.994770886
Shear Stress (Pa)
Shear Rate (1/s)
0
0.5
1
1.5
2
2.5
0
50
100
150
200
250
300
350
400

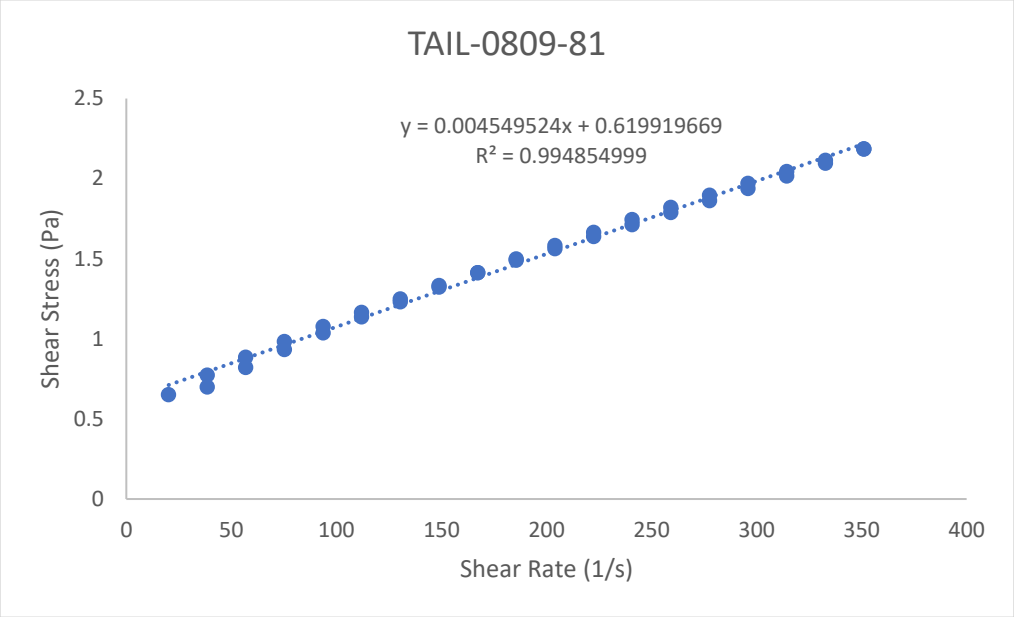
TAIL-0809-81
y = 0.004549524x + 0.619919669
R² = 0.994854999
Shear Stress (Pa)
Shear Rate (1/s)
0
0.5
1
1.5
2
2.5
0
50
100
150
200
250
300
350
400

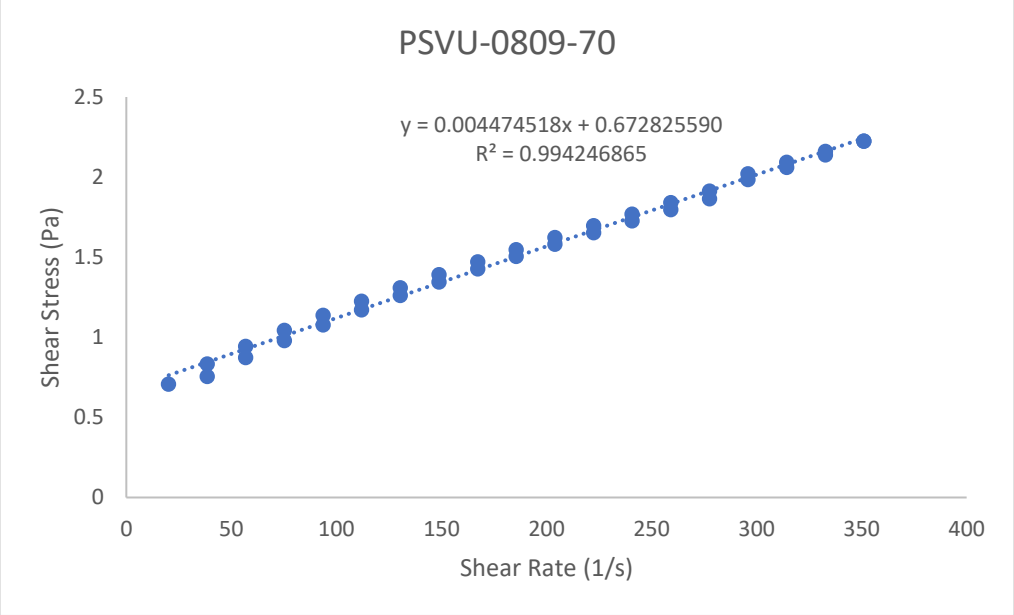
PSVU-0809-70
y = 0.004474518x + 0.672825590
R² = 0.994246865
Shear Stress (Pa)
Shear Rate (1/s)
0
0.5
1
1.5
2
2.5
0
50
100
150
200
250
300
350
400

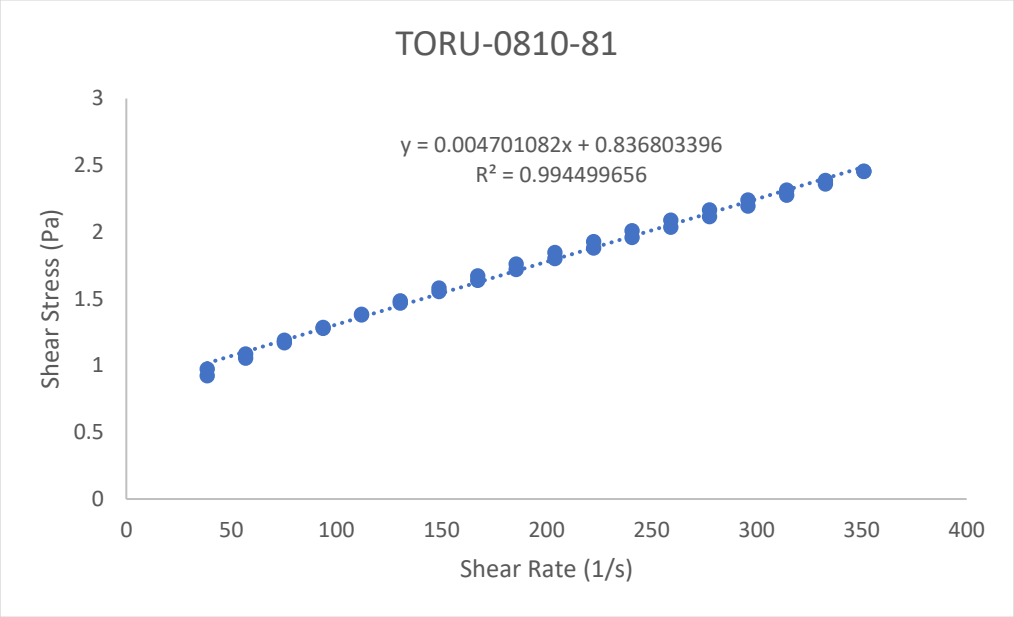
TORU-0810-81
y = 0.004701082x + 0.836803396
R² = 0.994499656
Shear Stress (Pa)
Shear Rate (1/s)
0
0.5
1
1.5
2
2.5
3
0
50
100
150
200
250
300
350
400

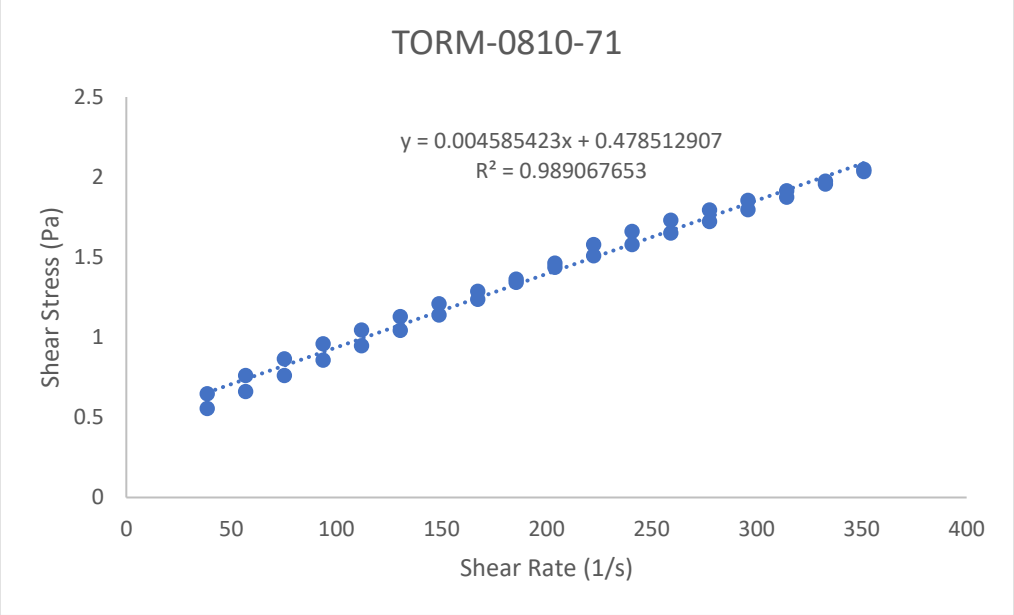
TORM-0810-71
y = 0.004585423x + 0.478512907
R² = 0.989067653
Shear Stress (Pa)
Shear Rate (1/s)
0
0.5
1
1.5
2
2.5
0
50
100
150
200
250
300
350
400

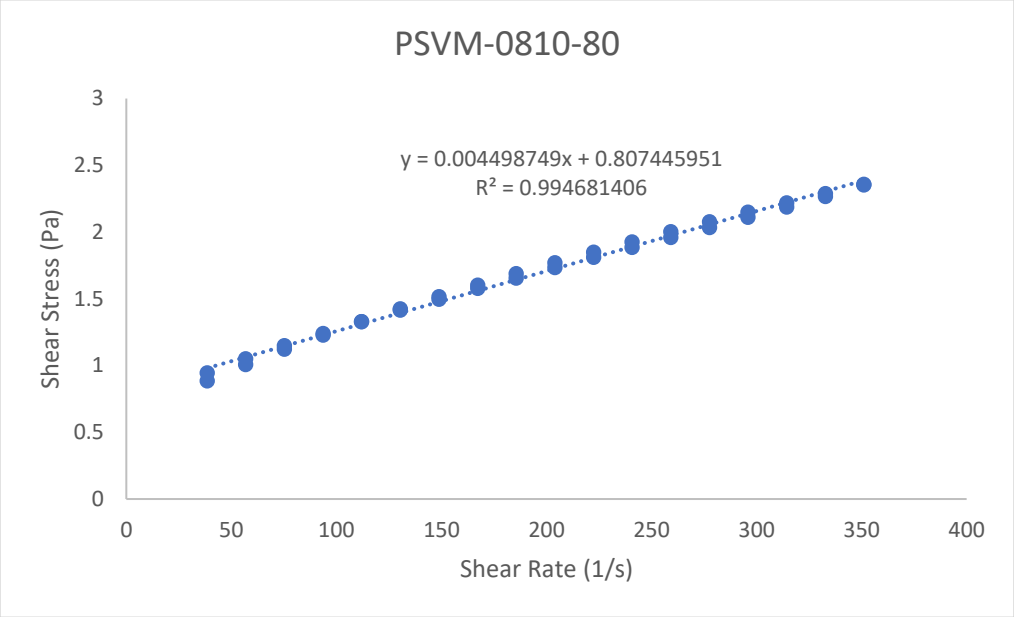
PSVM-0810-80
y = 0.004498749x + 0.807445951
R² = 0.994681406
Shear Stress (Pa)
Shear Rate (1/s)
0
0.5
1
1.5
2
2.5
3
0
50
100
150
200
250
300
350
400

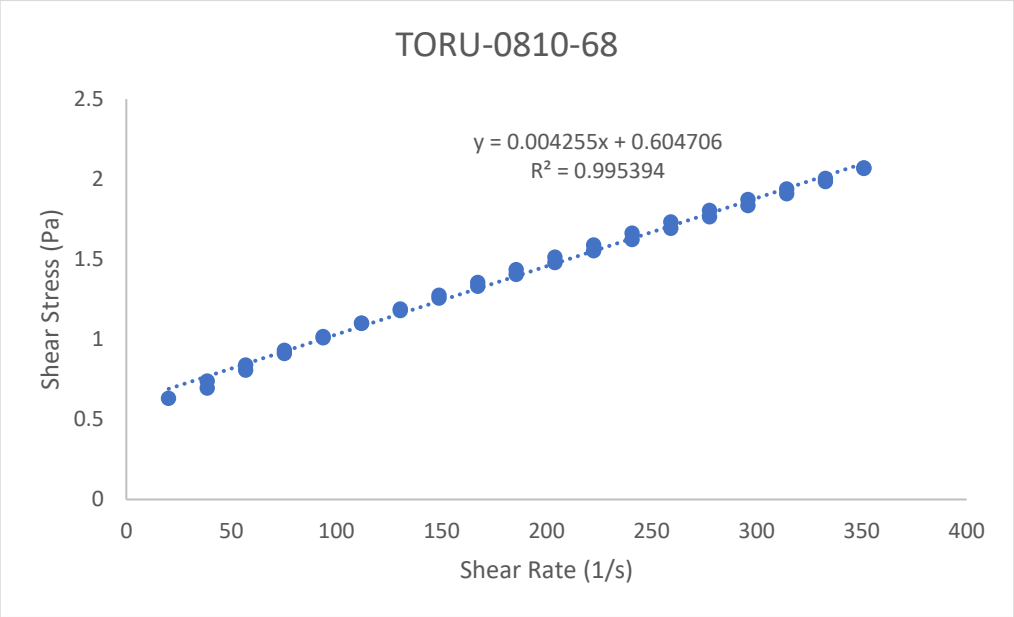
TORU-0810-68
y = 0.004255x + 0.604706
R² = 0.995394
Shear Stress (Pa)
Shear Rate (1/s)
0
0.5
1
1.5
2
2.5
0
50
100
150
200
250
300
350
400

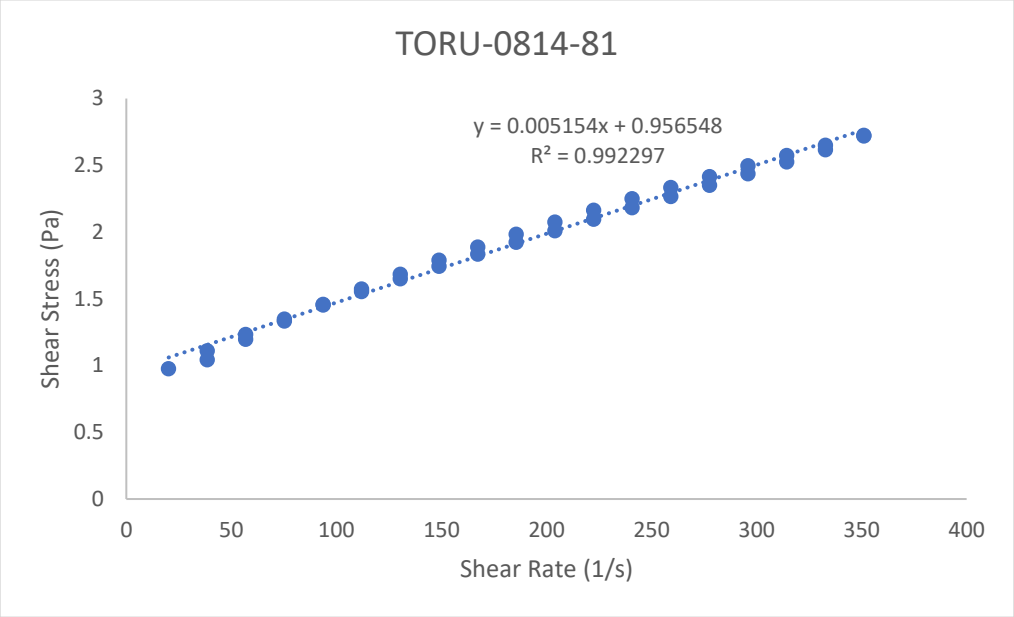
TORU-0814-81
y = 0.005154x + 0.956548
R² = 0.992297
Shear Stress (Pa)
Shear Rate (1/s)
0
0.5
1
1.5
2
2.5
3
0
50
100
150
200
250
300
350
400

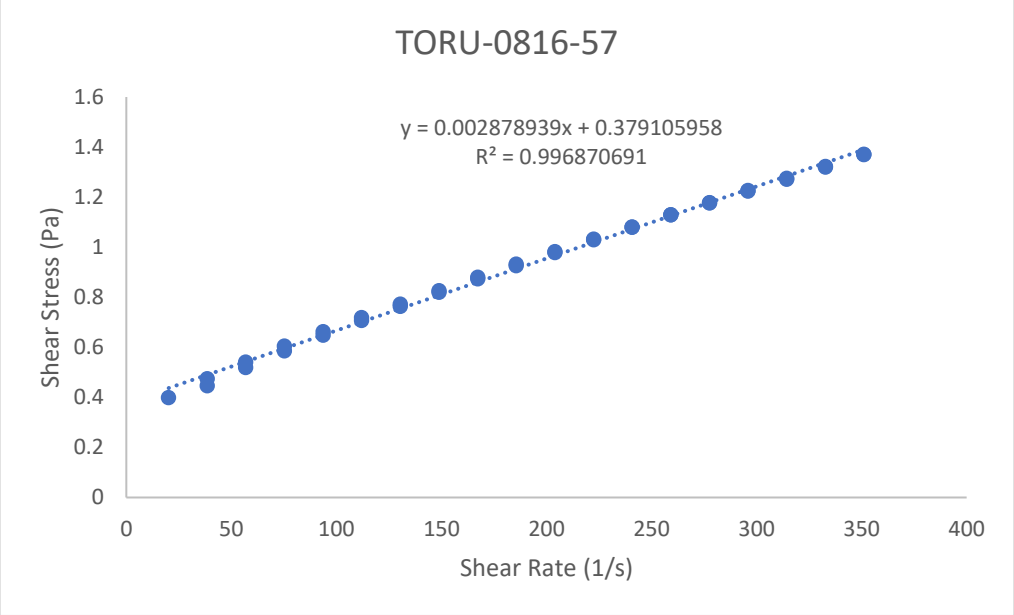
TORU-0816-57
y = 0.002878939x + 0.379105958
R² = 0.996870691
Shear Stress (Pa)
Shear Rate (1/s)
0
0.2
0.4
0.6
0.8
1
1.2
1.4
1.6
0
50
100
150
200
250
300
350
400

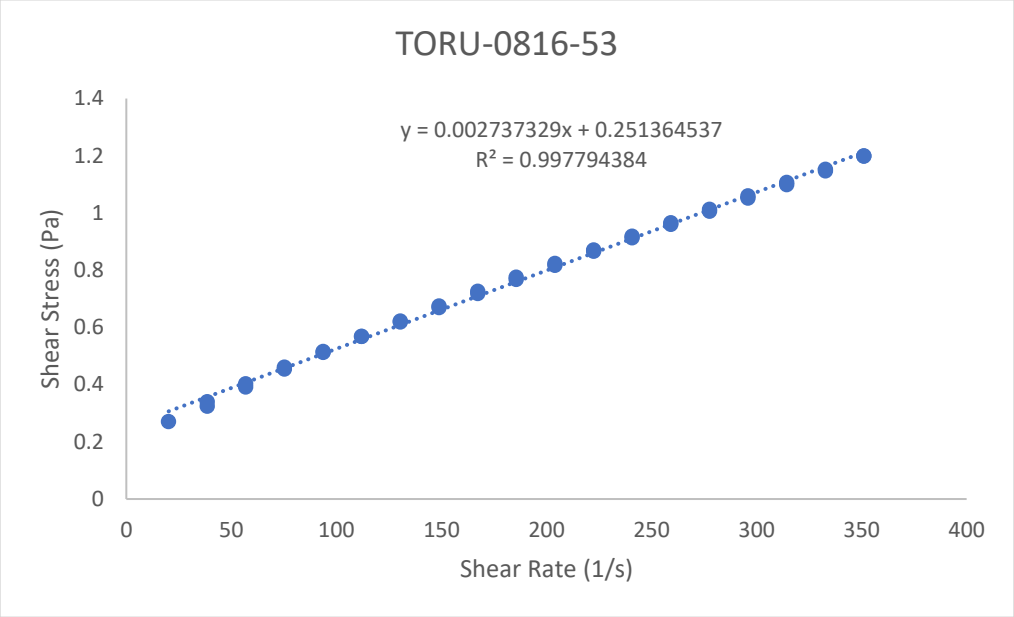
TORU-0816-53
y = 0.002737329x + 0.251364537
R² = 0.997794384
Shear Stress (Pa)
Shear Rate (1/s)
0
0.2
0.4
0.6
0.8
1
1.2
1.4
0
50
100
150
200
250
300
350
400

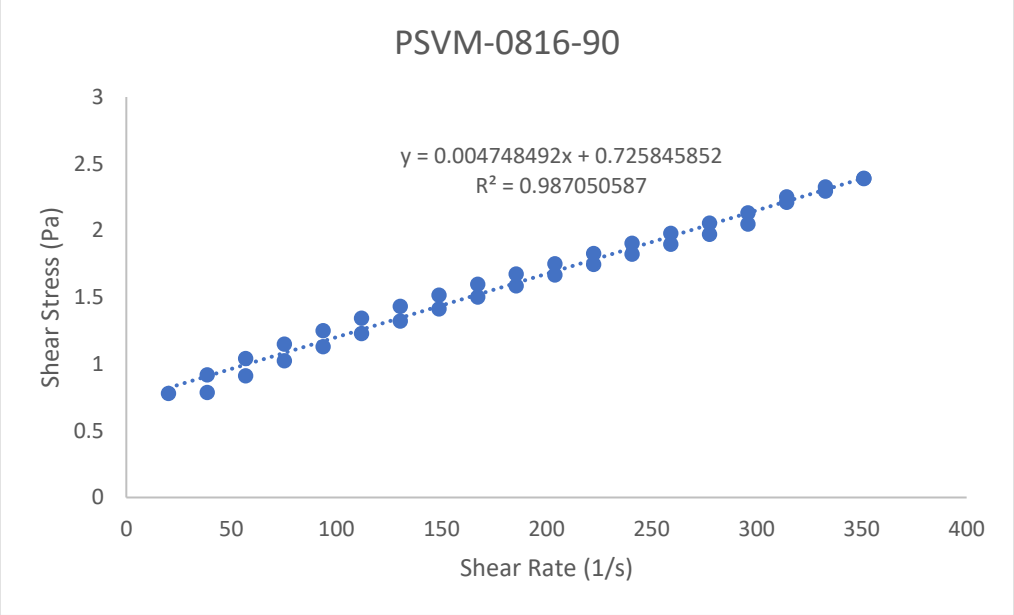
PSVM-0816-90
y = 0.004748492x + 0.725845852
R² = 0.987050587
Shear Stress (Pa)
Shear Rate (1/s)
0
0.5
1
1.5
2
2.5
3
0
50
100
150
200
250
300
350
400

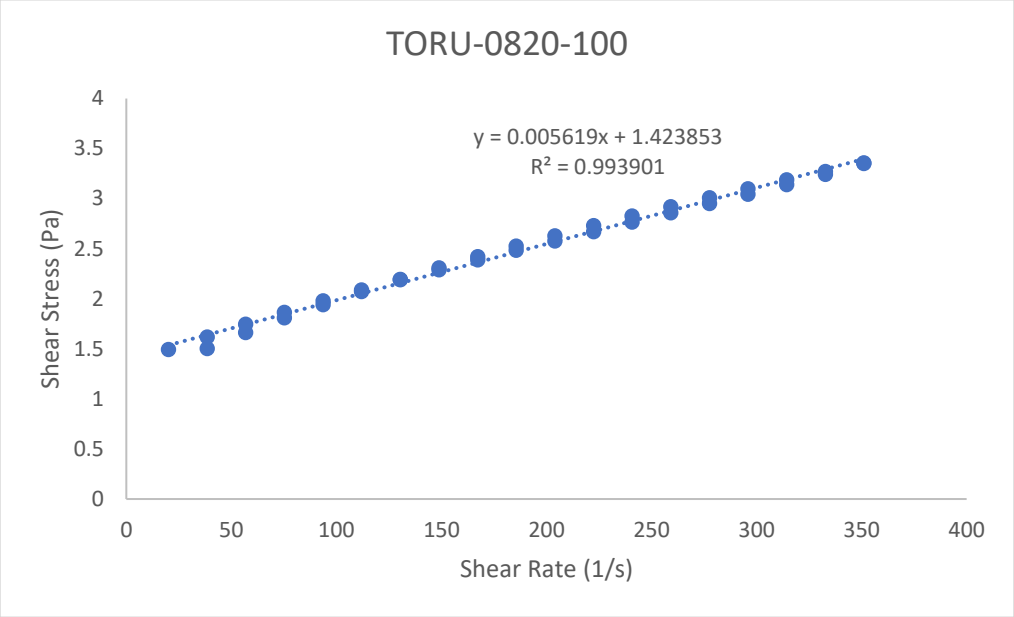
TORU-0820-100
y = 0.005619x + 1.423853
R² = 0.993901
Shear Stress (Pa)
Shear Rate (1/s)
0
0.5
1
1.5
2
2.5
3
3.5
4
0
50
100
150
200
250
300
350
400

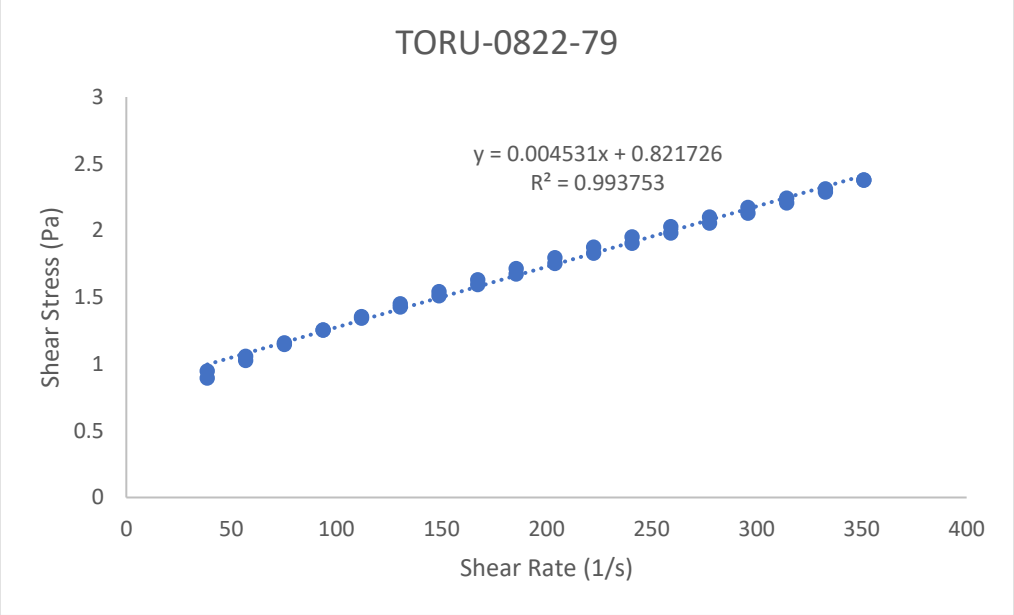
TORU-0822-79
y = 0.004531x + 0.821726
R² = 0.993753
Shear Stress (Pa)
Shear Rate (1/s)
0
0.5
1
1.5
2
2.5
3
0
50
100
150
200
250
300
350
400

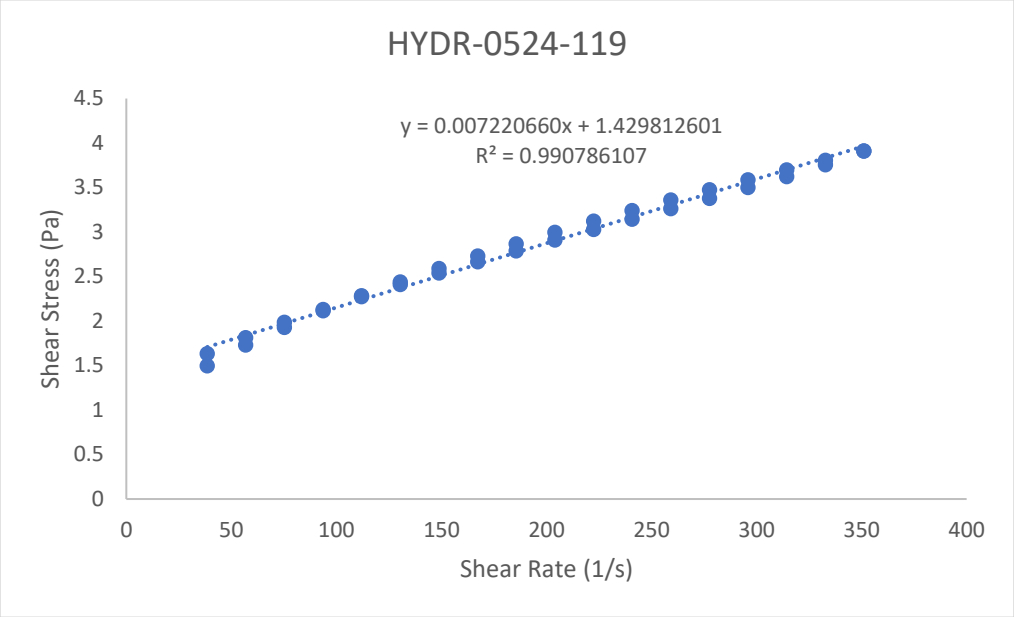
HYDR-0524-119
y = 0.007220660x + 1.429812601
R² = 0.990786107
Shear Stress (Pa)
Shear Rate (1/s)
0
0.5
1
1.5
2
2.5
3
3.5
4
4.5
0
50
100
150
200
250
300
350
400

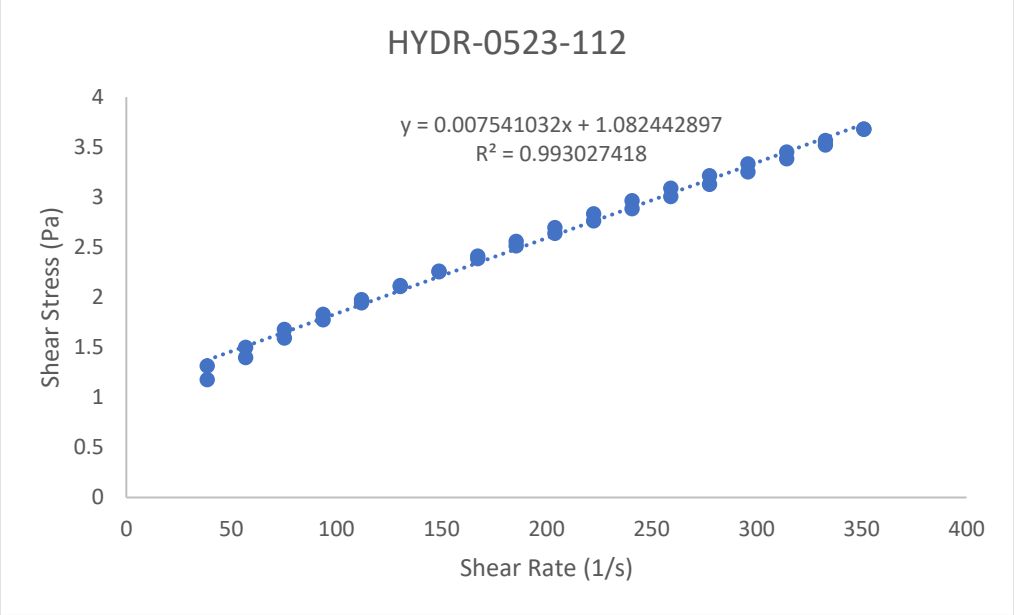
HYDR-0523-112
y = 0.007541032x + 1.082442897
R² = 0.993027418
Shear Stress (Pa)
Shear Rate (1/s)
0
0.5
1
1.5
2
2.5
3
3.5
4
0
50
100
150
200
250
300
350
400

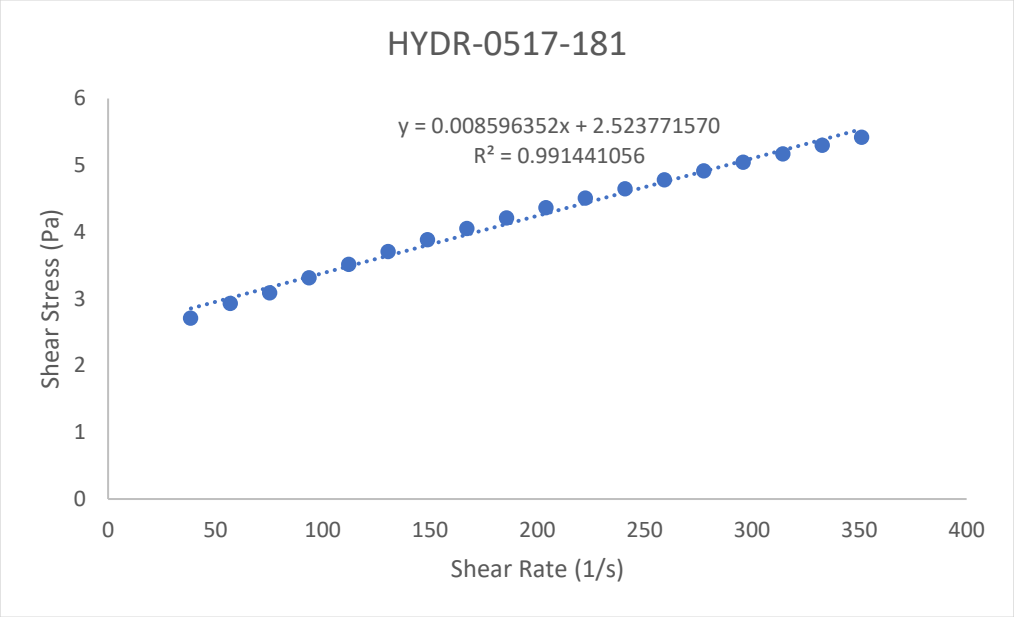
HYDR-0517-181
y = 0.008596352x + 2.523771570
R² = 0.991441056
Shear Stress (Pa)
Shear Rate (1/s)
0
1
2
3
4
5
6
0
50
100
150
200
250
300
350
400

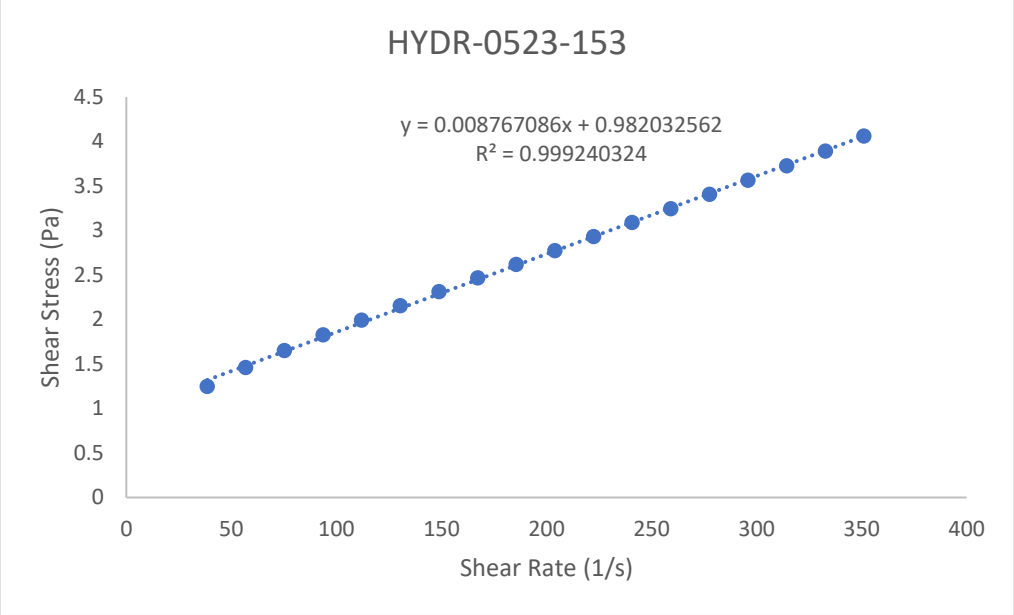
HYDR-0523-153
y = 0.008767086x + 0.982032562
R² = 0.999240324
Shear Stress (Pa)
Shear Rate (1/s)
0
0.5
1
1.5
2
2.5
3
3.5
4
4.5
0
50
100
150
200
250
300
350
400

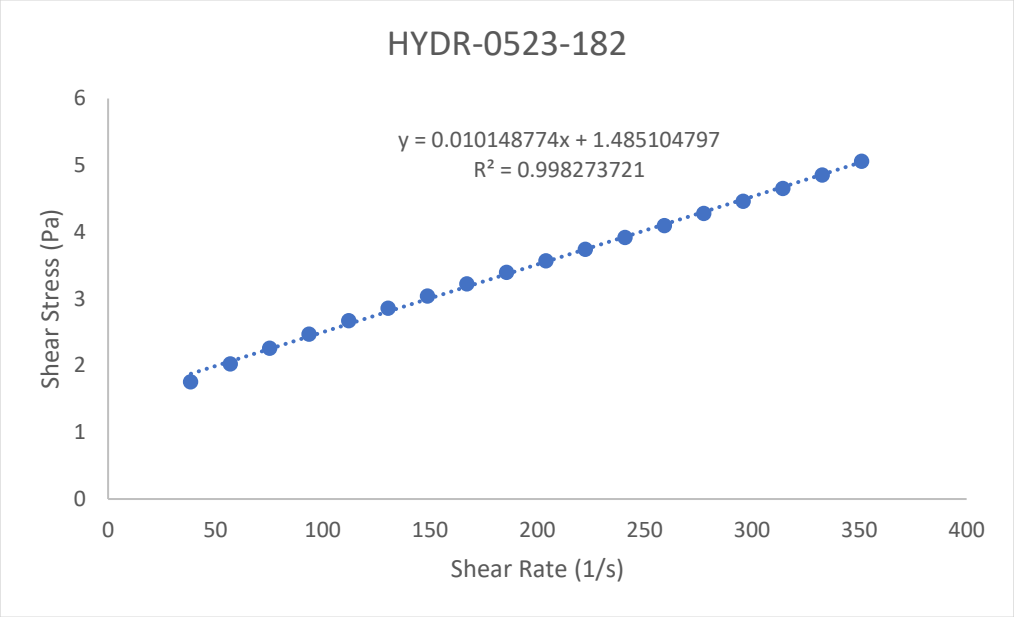
HYDR-0523-182
y = 0.010148774x + 1.485104797
R² = 0.998273721
Shear Stress (Pa)
Shear Rate (1/s)
0
1
2
3
4
5
6
0
50
100
150
200
250
300
350
400

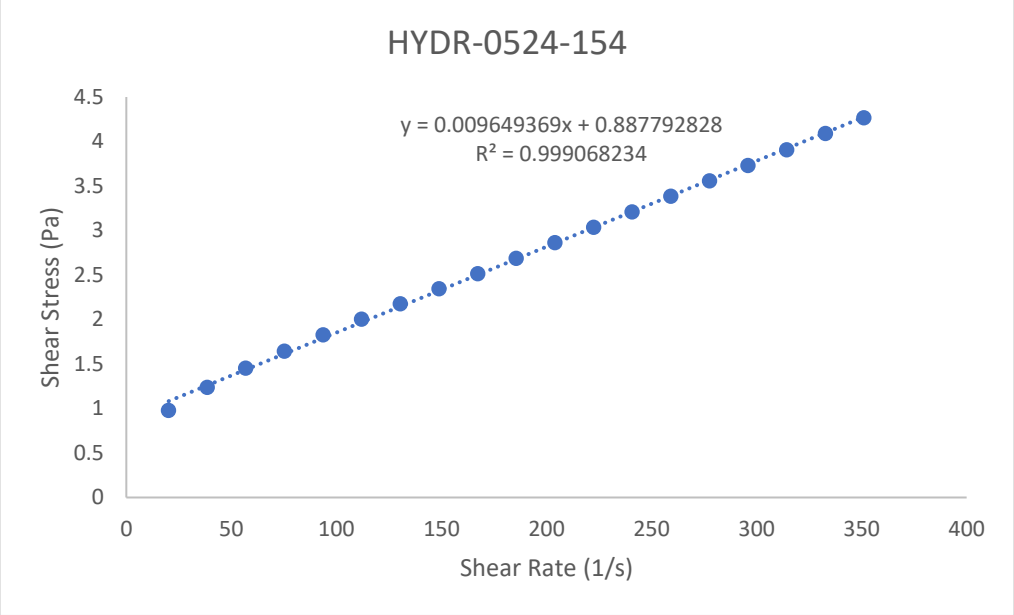
HYDR-0524-154
y = 0.009649369x + 0.887792828
R² = 0.999068234
Shear Stress (Pa)
Shear Rate (1/s)
0
0.5
1
1.5
2
2.5
3
3.5
4
4.5
0
50
100
150
200
250
300
350
400

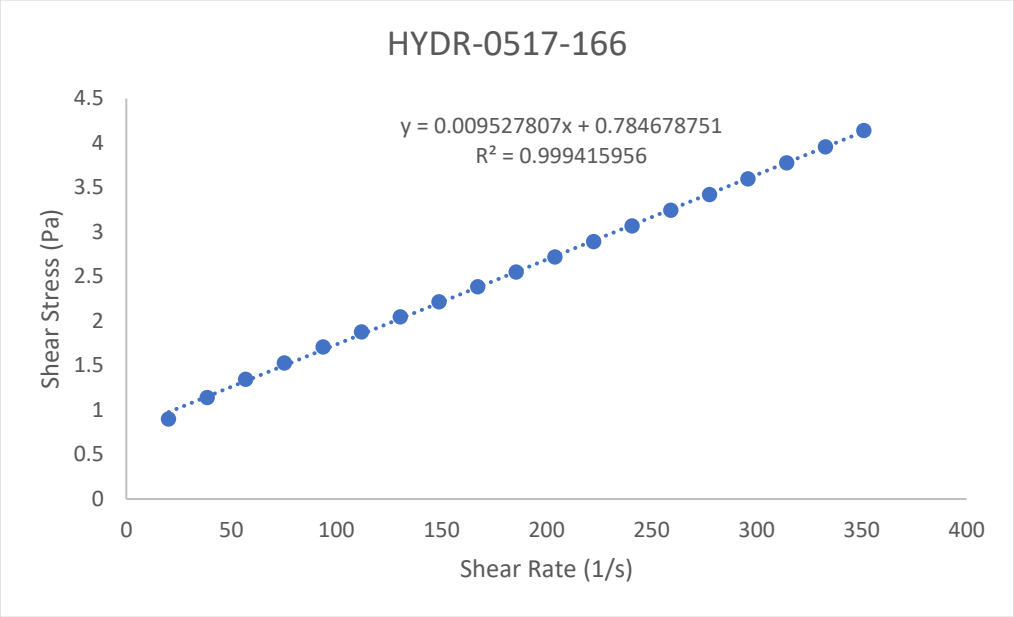
HYDR-0517-166
y = 0.009527807x + 0.784678751
R² = 0.999415956
Shear Stress (Pa)
Shear Rate (1/s)
0
0.5
1
1.5
2
2.5
3
3.5
4
4.5
0
50
100
150
200
250
300
350
400

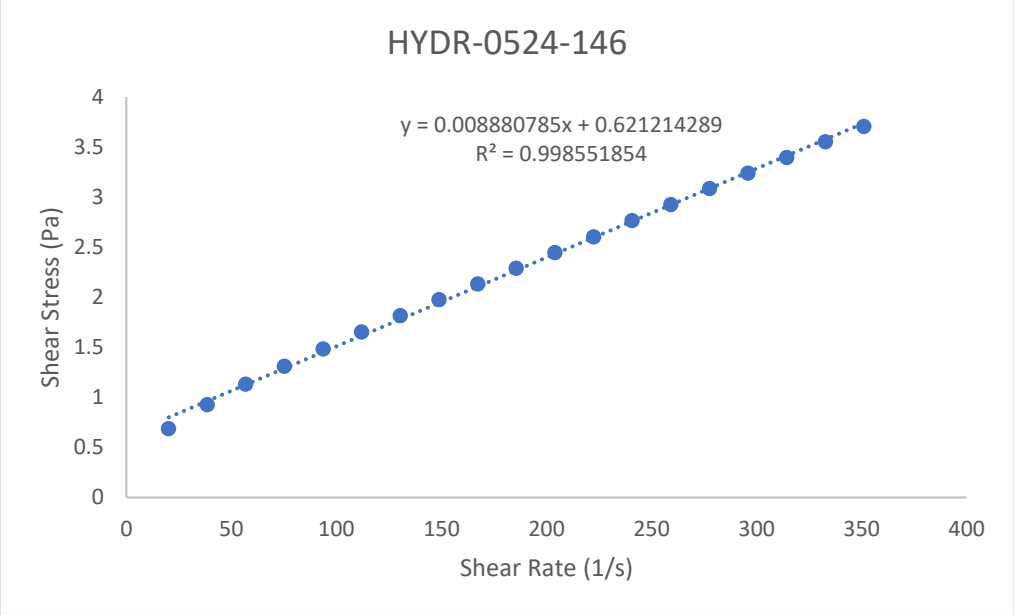
HYDR-0524-146
y = 0.008880785x + 0.621214289
R² = 0.998551854
Shear Stress (Pa)
Shear Rate (1/s)
0
0.5
1
1.5
2
2.5
3
3.5
4
0
50
100
150
200
250
300
350
400

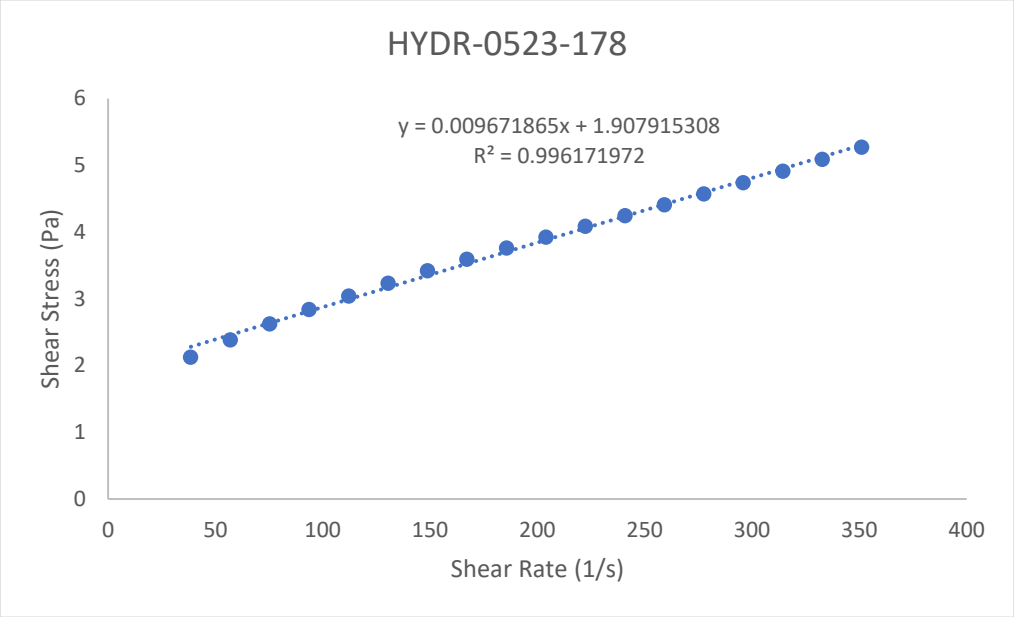
HYDR-0523-178
y = 0.009671865x + 1.907915308
R² = 0.996171972
Shear Stress (Pa)
Shear Rate (1/s)
0
1
2
3
4
5
6
0
50
100
150
200
250
300
350
400

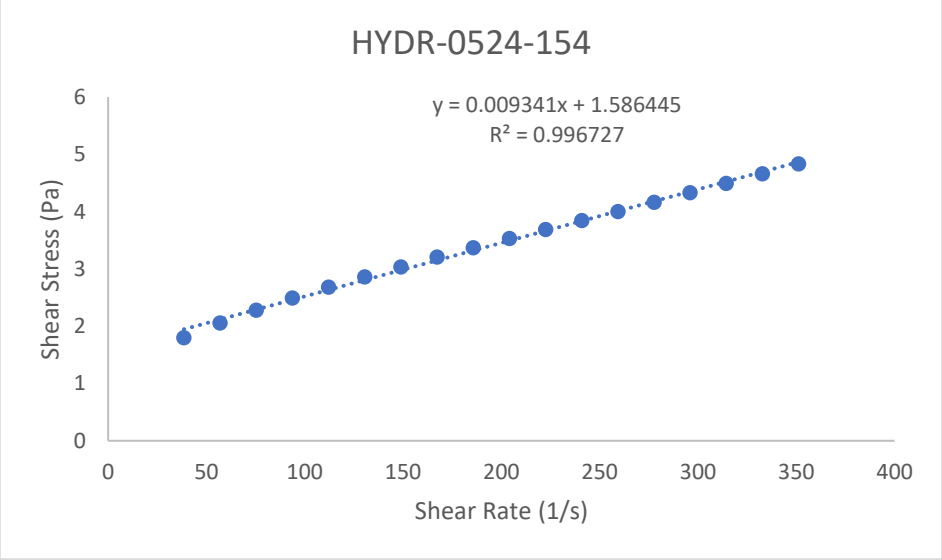
HYDR-0524-154
y = 0.009341x + 1.586445
R² = 0.996727
Shear Stress (Pa)
Shear Rate (1/s)
0
1
2
3
4
5
6
0
50
100
150
200
250
300
350
400

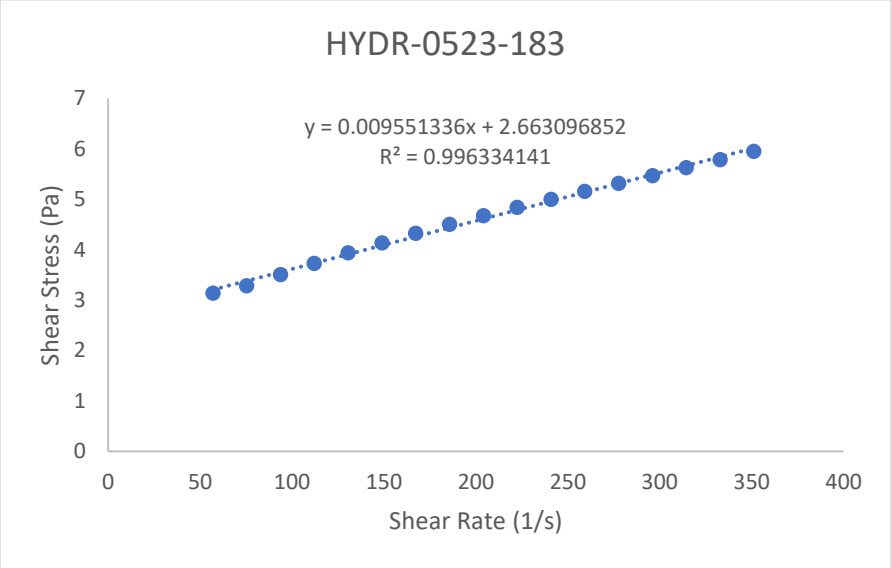
HYDR-0523-183
y = 0.009551336x + 2.663096852
R² = 0.996334141
Shear Stress (Pa)
Shear Rate (1/s)
0
1
2
3
4
5
6
7
0
50
100
150
200
250
300
350
400

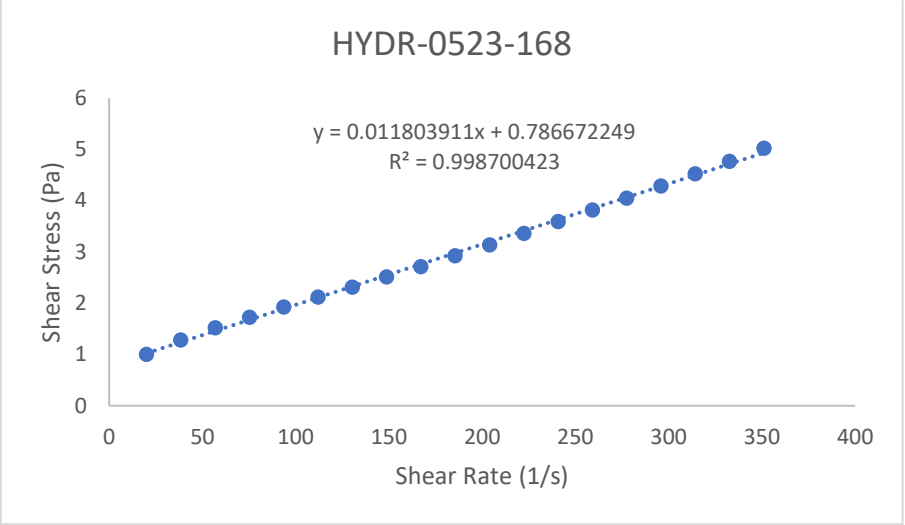
HYDR-0523-168
y = 0.011803911x + 0.786672249
R² = 0.998700423
Shear Stress (Pa)
Shear Rate (1/s)
0
1
2
3
4
5
6
0
50
100
150
200
250
300
350
400

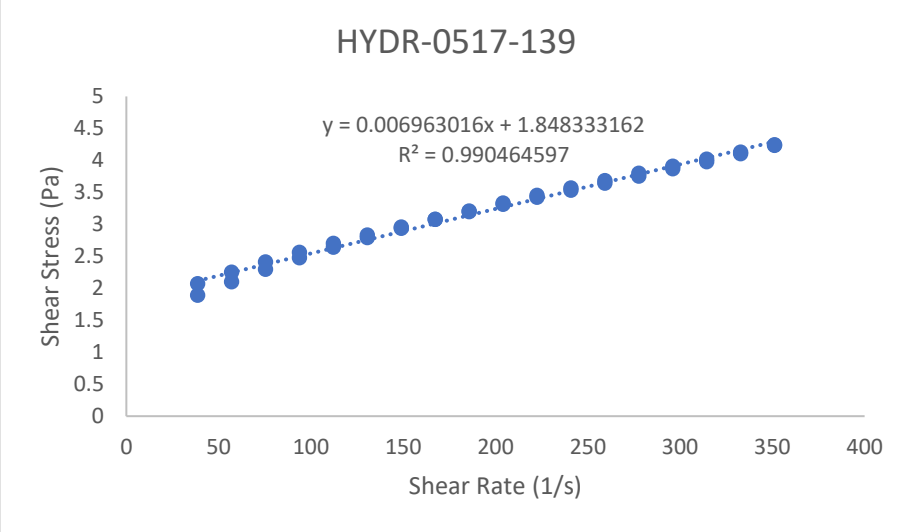
HYDR-0517-139
y = 0.006963016x + 1.848333162
R² = 0.990464597
Shear Stress (Pa)
Shear Rate (1/s)
0
0.5
1
1.5
2
2.5
3
3.5
4
4.5
5
0
50
100
150
200
250
300
350
400

Appendix C

Water Chemistry results

The equation used to determine ionic strength from the water chemistry results is:

$$I = \frac{1}{2} \sum c_i * Z_i^2 \tag{C.1}$$

where I is ionic strength in mol/L, c_i is molar concentration of each ion and Z_i is the ionic charge. The raw data is included on the following pages.

Sample	IS (mol/L)	pH	Al (mg/L)	Ca (mg/L)	K (mg/L)	Li (mg/L)	Mg (mg/L)
PSV Underflow Aug. 1st 20:04	0.0829	8.85	0.0158	21.330	15.12	0.4342	13.270
TOR Underflow Aug. 14th 02:01	0.0692	8.96	0.0176	23.470	14.36	0.3675	11.900
PSV Middlings Aug. 7th 19:30	0.0664	8.98	0.0151	19.330	13.32	0.3216	8.877
TOR Underflow Aug. 20th 05:05	0.0602	8.96	0.0153	9.264	10.42	0.2937	8.134
TOR Underflow Aug. 9th 02:05	0.0771	8.88	0.0149	21.350	13.96	0.3596	11.960
TOR Middlings Aug. 10th 11:19	0.0761	8.98	0.0212	20.990	14.70	0.3741	12.080
PSV Middlings Aug. 10th 13:33	0.0799	8.93	0.0429	29.360	14.92	0.4059	14.870
PSV Middlings Aug. 9th 01:30	0.0700	8.94	0.0182	20.800	13.32	0.3474	11.000
TOR Underflow Aug 6th 17:00	0.0700	8.88	0.0141	7.503	13.42	0.3397	9.406
PSV Underflow Jul. 27th 07:33	0.0678	8.94	0.0135	20.260	14.06	0.3469	9.347
PSV Underflow Aug 7th 01:45	0.0726	9.02	0.0212	22.200	12.98	0.3490	11.340
Tailings Aug. 7th 17:15	0.0518	8.94	0.0130	9.779	11.38	0.5502	8.487
TOR Underflow Jul. 31st 22:59	0.0670	8.99	0.0192	28.090	14.94	0.4014	13.780
TOR Underflow Aug. 16th 11:02	0.0557	8.85	0.0086	7.867	13.82	0.3397	12.810
PSV Middlings Aug. 16th 22:42	0.0742	9.15	0.0225	22.120	12.91	0.3457	9.849
TOR Underflow Aug. 7th 11:05	0.0812	8.92	0.0203	24.070	14.04	0.2034	13.510
PSV Underflow Jul. 30th 22:49	0.0734	8.98	0.0122	7.516	13.93	0.3970	13.140
TOR Underflow Aug. 8th 14:00	0.0752	9.12	0.0097	7.496	13.95	0.3712	13.140
TOR Underflow Aug. 8th 05:01	0.0626	8.91	0.0145	30.270	13.36	0.3275	12.880
PSV Underflow Jul. 29th 16:57	0.0728	8.94	0.0132	19.040	13.49	0.3627	12.830
PSV Middlings Jul. 27th 07:44	0.0568	9.00	0.0123	9.291	11.56	0.3161	7.595
PSV Underflow Aug. 6th 16:31	0.0647	8.95	0.0120	9.184	11.66	0.3262	9.631
TOR Underflow Aug. 7th 17:03	0.0651	8.92	0.0112	21.140	12.45	0.3338	10.270
PSV Middlings Aug. 7th 10:41	0.0772	8.96	0.0121	19.710	11.59	0.3031	9.012

Sample	Na (mg/L)	F (mg/L)	Cl (mg/L)	NO3 (mg/L)	SO4 (mg/L)	Cond. (mS/cm)
PSV Underflow Aug. 1st 20:04	1802	5.50	1100	0.40	1220	9.64
TOR Underflow Aug. 14th 02:01	1602	4.99	945	2.28	879	8.60
PSV Middlings Aug. 7th 19:30	1494	6.41	877	1.00	927	8.24
TOR Underflow Aug. 20th 05:05	1197	5.29	853	2.59	986	8.97
TOR Underflow Aug. 9th 02:05	1671	5.25	1050	1.00	1120	8.93
TOR Middlings Aug. 10th 11:19	1726	6.40	1190	2.26	917	9.25
PSV Middlings Aug. 10th 13:33	1812	5.19	1250	4.16	940	9.65
PSV Middlings Aug. 9th 01:30	1580	4.45	976	2.91	930	8.53
TOR Underflow Aug 6th 17:00	1522	5.11	845	1.00	1120	8.32
PSV Underflow Jul. 27th 07:33	1500	4.59	873	2.45	988	8.35
PSV Underflow Aug 7th 01:45	1614	3.98	858	3.62	1100	8.81
Tailings Aug. 7th 17:15	1138	4.33	693	1.30	749	6.94
TOR Underflow Jul. 31st 22:59	1501	3.81	1020	1.60	812	8.23
TOR Underflow Aug. 16th 11:02	1153	3.38	684	1.00	918	7.05
PSV Middlings Aug. 16th 22:42	1737	5.61	1040	1.00	926	9.12
TOR Underflow Aug. 7th 11:05	1787	4.97	1040	1.00	1190	9.29
PSV Underflow Jul. 30th 22:49	1710	4.74	1070	1.00	917	8.98
TOR Underflow Aug. 8th 14:00	1679	3.43	1010	1.36	1080	8.94
TOR Underflow Aug. 8th 05:01	1326	3.38	809	1.90	930	7.34
PSV Underflow Jul. 29th 16:57	1646	4.13	1030	1.00	960	8.84
PSV Middlings Jul. 27th 07:44	1294	3.83	785	1.00	772	7.50
PSV Underflow Aug. 6th 16:31	1350	3.62	803	1.00	1070	8.11
TOR Underflow Aug. 7th 17:03	1423	3.89	827	1.00	966	7.98
PSV Middlings Aug. 7th 10:41	1578	6.95	1020	1.00	1260	8.91

Appendix D

Viscosity Correlations

Each factor was incorporated with solids concentration to develop a correlation to predict carrier fluid viscosities. The correlations and the respective fits are outlined in the following sections.

D.0.1 CEC

$$\mu_r = 51.16 * C_s + 0.036 * CEC + 1 \tag{D.1}$$

D.0.2 IS

$$\mu_r = 46.43 * C_s + 12.13 * IS + 1 \tag{D.2}$$

D.0.3 pH

$$\mu_r = 54.45 * C_s + 0.22 * pH + 1 \tag{D.3}$$

D.0.4 Al

$$\mu_r = 58.84 * C_s - 9.76 * [Al] + 1 \tag{D.4}$$

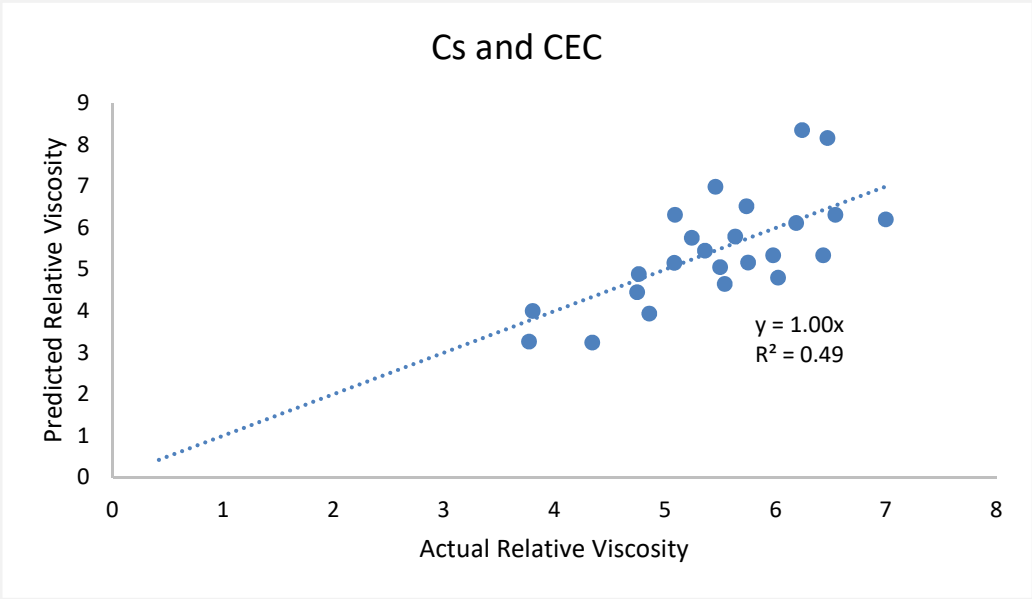

Figure D.1: Predictions for carrier fluid viscosity using solids concentration and CEC

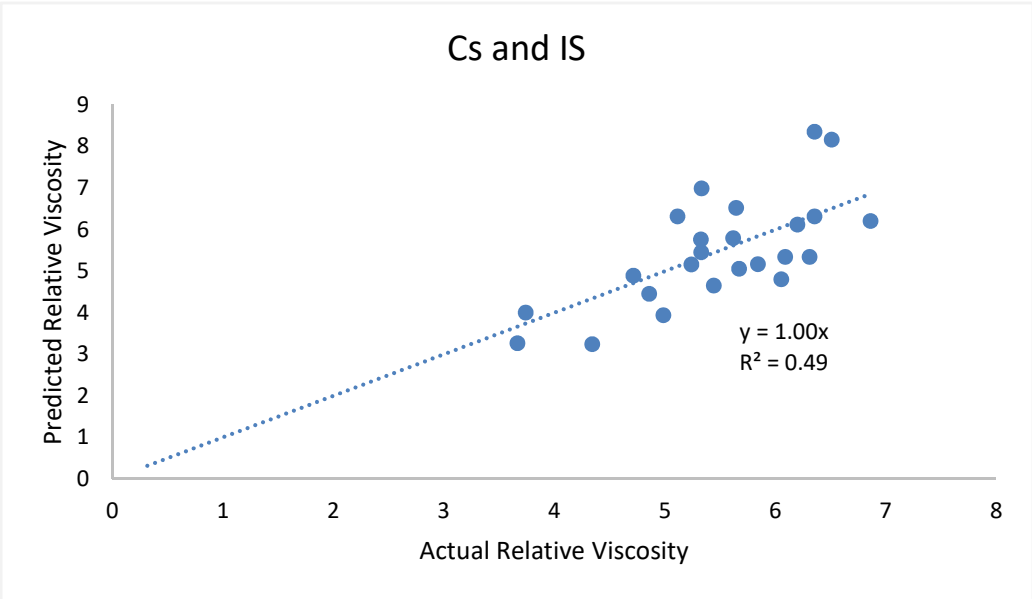

Figure D.2: Predictions for carrier fluid viscosity using solids concentration and IS

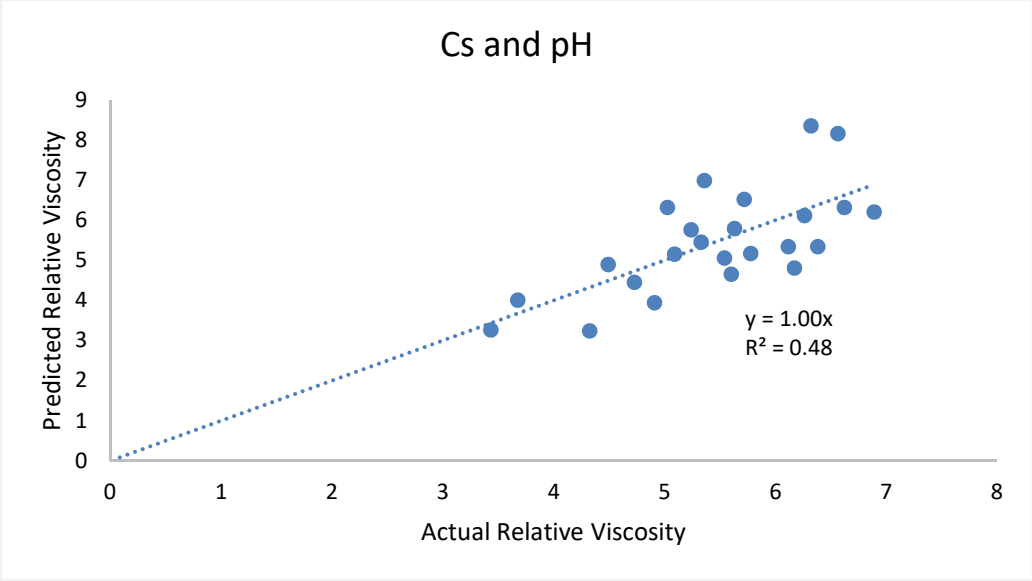

Figure D.3: Predictions for carrier fluid viscosity using solids concentration and pH

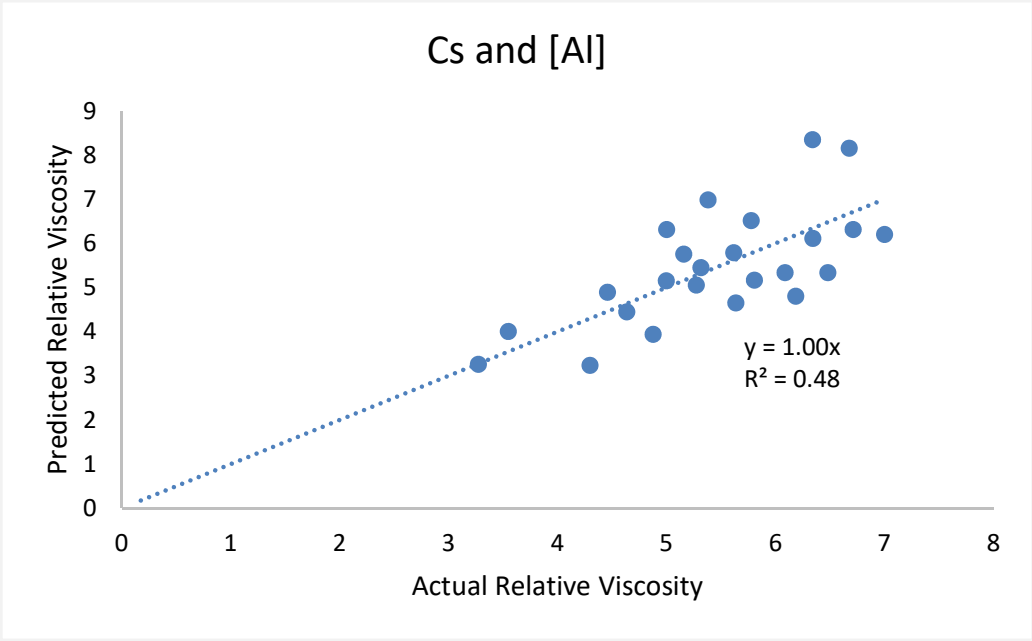

Figure D.4: Predictions for carrier fluid viscosity using solids concentration and concentration of Aluminium ions

D.0.5 Ca

$$\mu_r = 58.39 * C_s - 0.0068 * [Ca] + 1 \tag{D.5}$$

D.0.6 K

$$\mu_r = 61.5 * C_s - 0.0284 * [K] + 1 \tag{D.6}$$

D.0.7 Li

$$\mu_r = 63.6 * C_s - 1.56 * [Li] + 1 \tag{D.7}$$

D.0.8 Mg

$$\mu_r = 61.2 * C_s - 0.031 * [Mg] + 1 \tag{D.8}$$

D.0.9 Na

$$\mu_r = 52.0 * C_s - 0.0003 * [Na] + 1 \tag{D.9}$$

D.0.10 F

$$\mu_r = 47.1 * C_s + 0.166 * [F] + 1 \tag{D.10}$$

D.0.11 Cl

$$\mu_r = 60.13 * C_s - 0.0003 * [Cl] + 1 \tag{D.11}$$

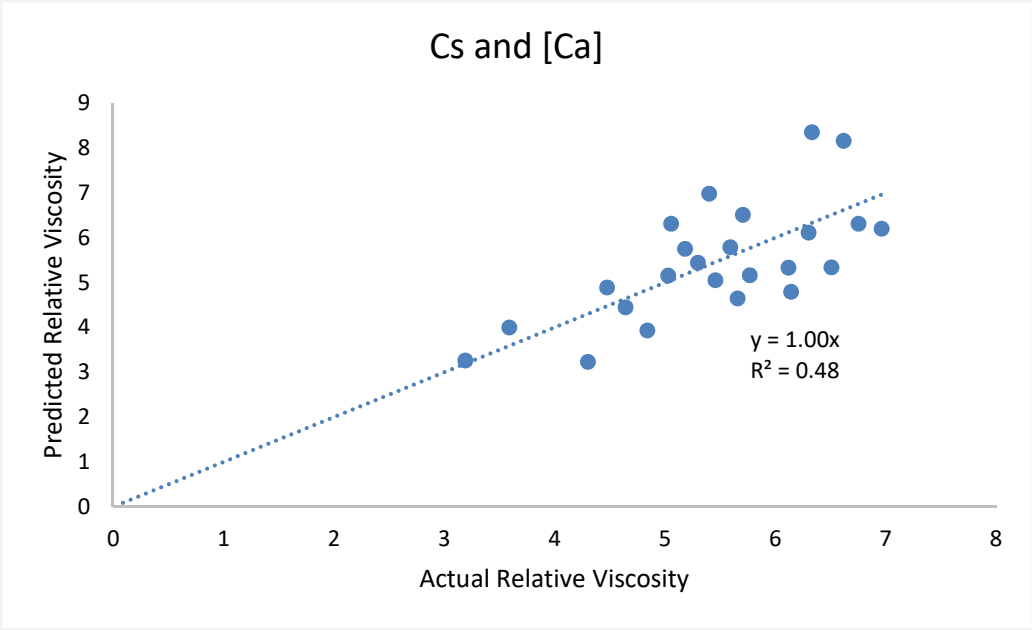

Figure D.5: Predictions for carrier fluid viscosity using solids concentration and concentration of Calcium ions

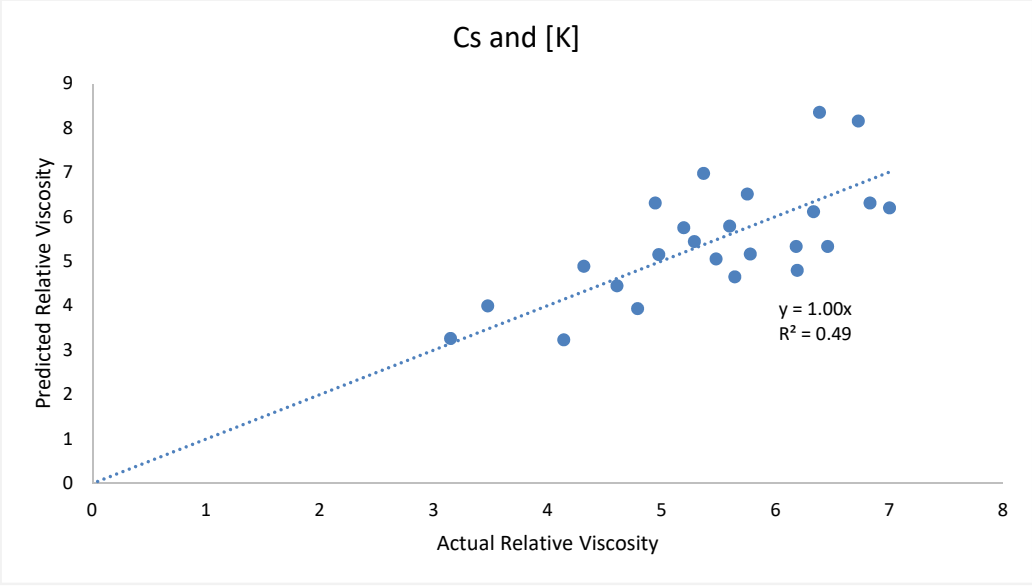

Figure D.6: Predictions for carrier fluid viscosity using solids concentration and concentration of Potassium ions

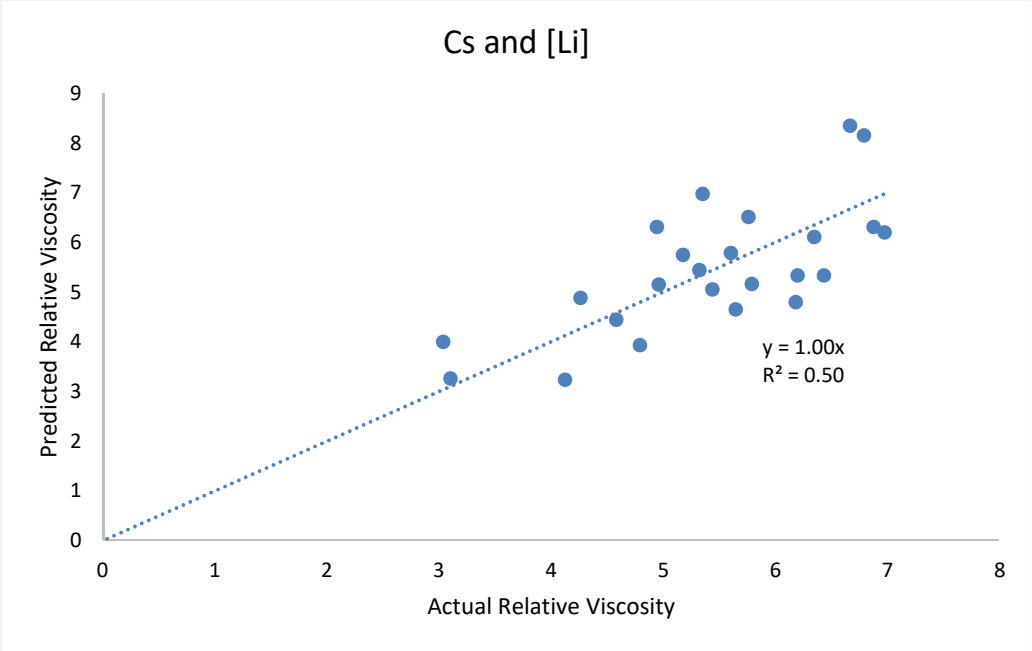

Figure D.7: Predictions for carrier fluid viscosity using solids concentration and concentration of Lithium ions

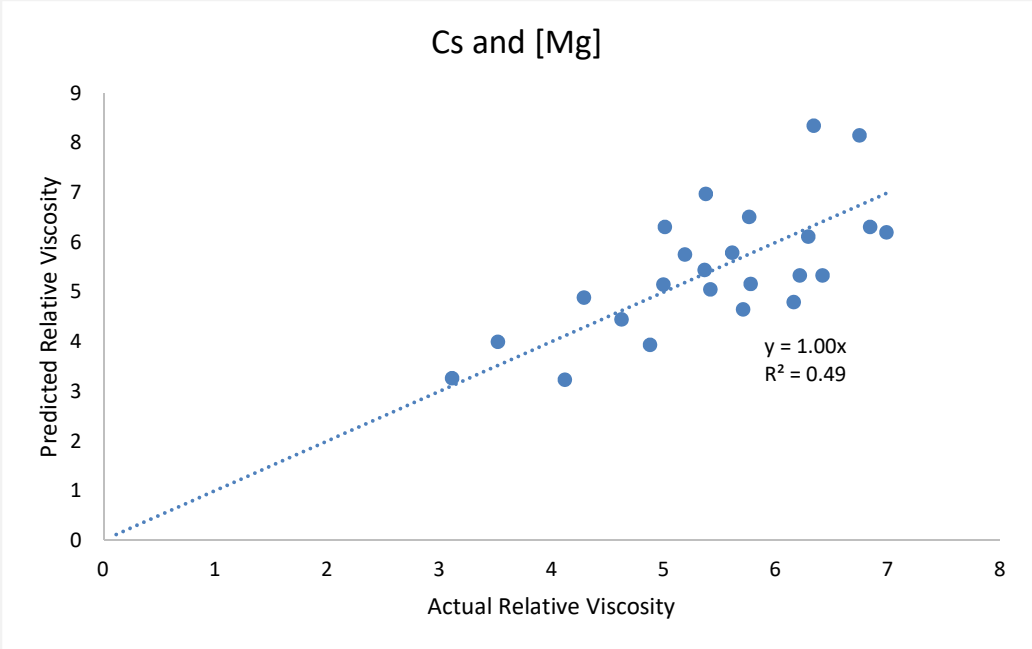

Figure D.8: Predictions for carrier fluid viscosity using solids concentration and concentration of Magnesium ions

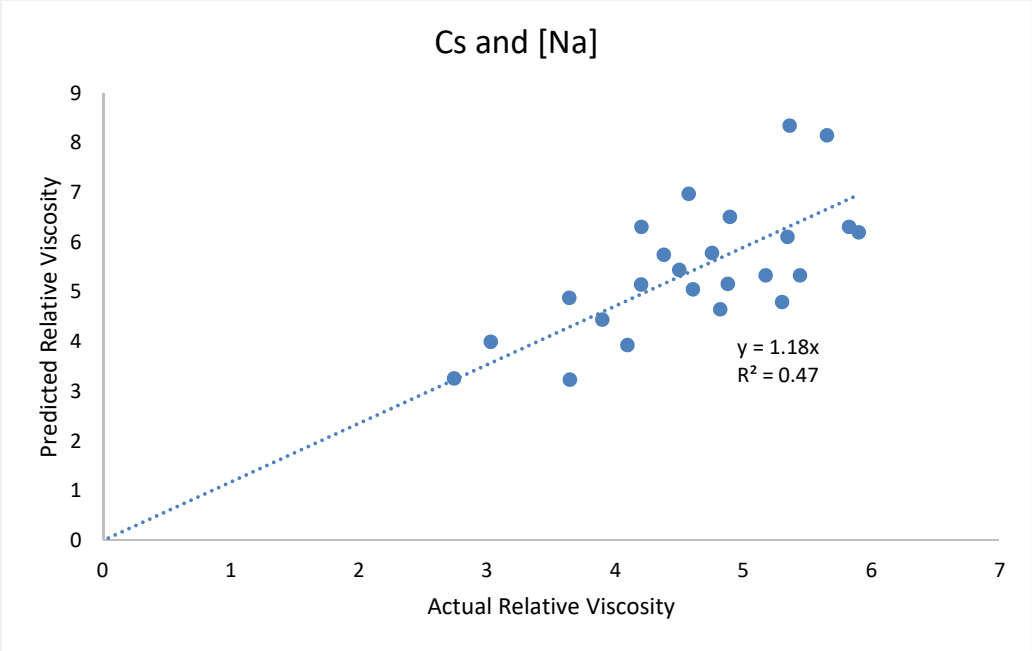

Figure D.9: Predictions for carrier fluid viscosity using solids concentration and concentration of Sodium ions

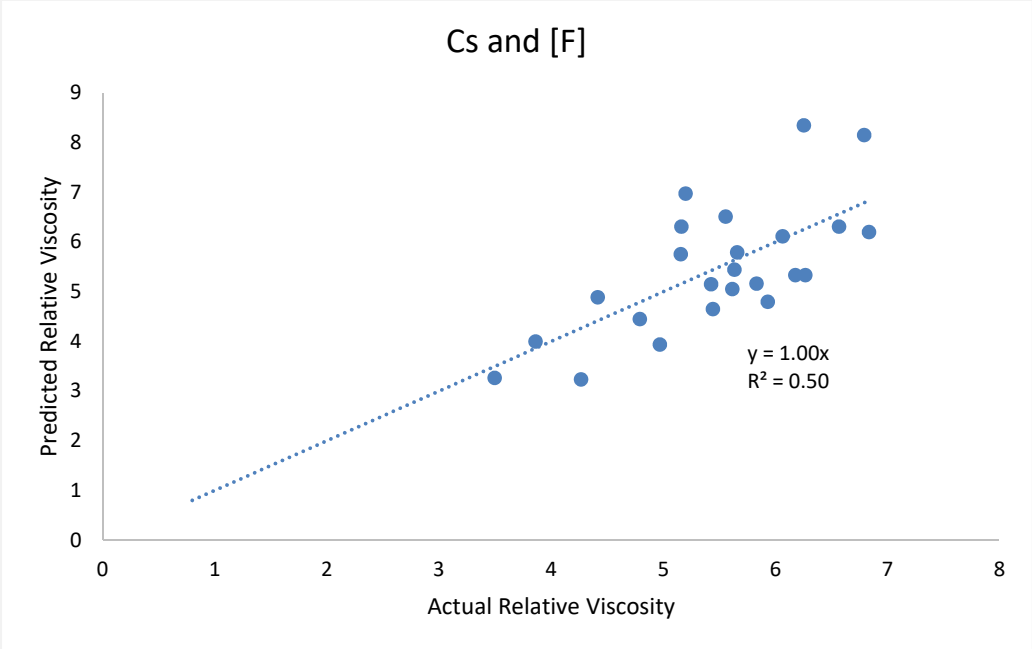

Figure D.10: Predictions for carrier fluid viscosity using solids concentration and concentration of Flouride ions

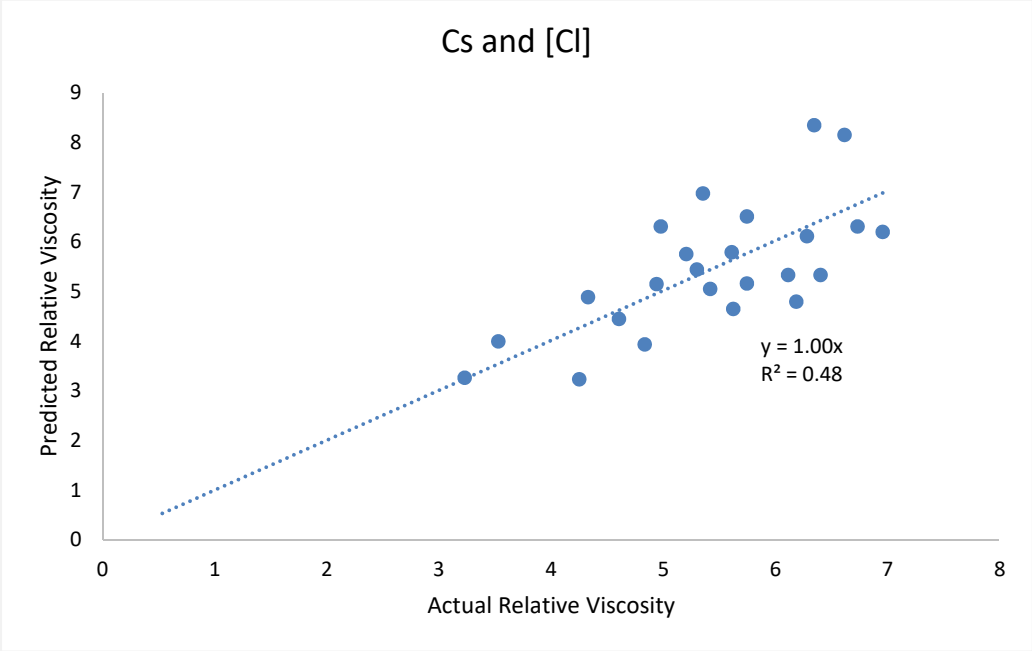

Figure D.11: Predictions for carrier fluid viscosity using solids concentration and concentration of Chloride ions

D.0.12 NO_3

$$\mu_r = 58.43 * C_s - 0.08 * [NO_3] + 1 \tag{D.12}$$

D.0.13 SO_4

$$\mu_r = 33.48 * C_s + 0.0019 * [SO_4] + 1 \tag{D.13}$$

D.0.14 CEC and IS

$$\mu_r = 47.47 * C_s + 0.019 * CEC + 7.44 * IS + 1 \tag{D.14}$$

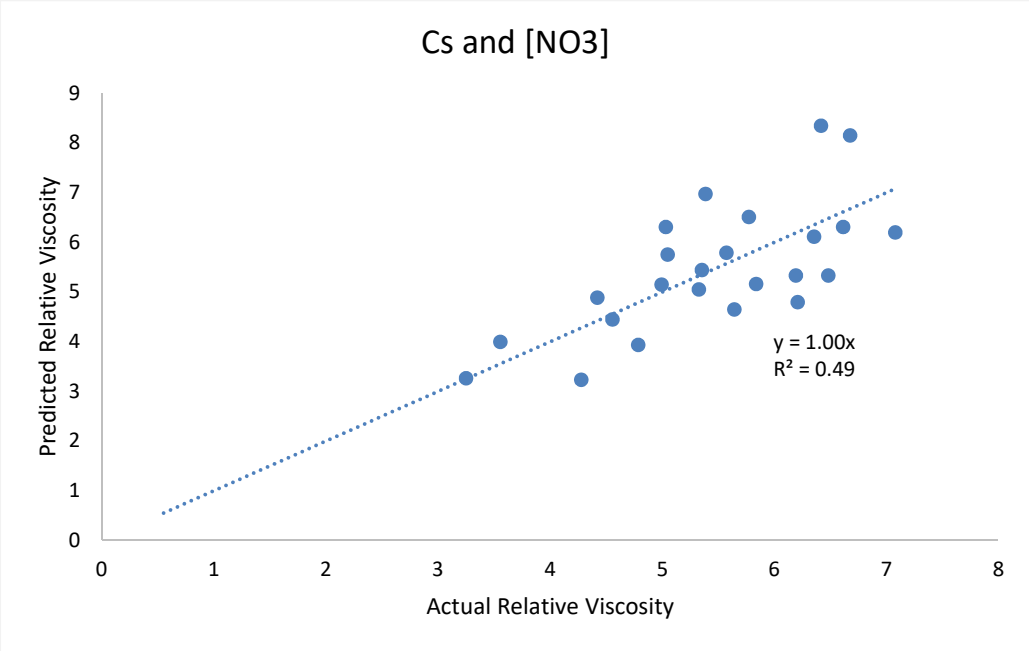

Figure D.12: Predictions for carrier fluid viscosity using solids concentration and concentration of Nitrate ions

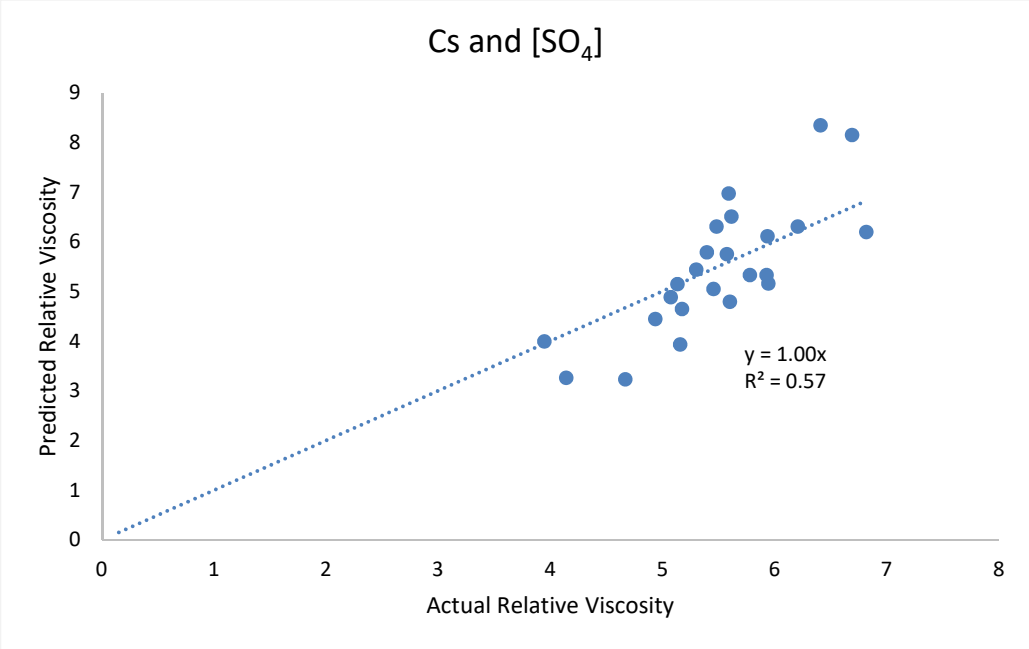

Figure D.13: Predictions for carrier fluid viscosity using solids concentration and concentration of Sulfate ions

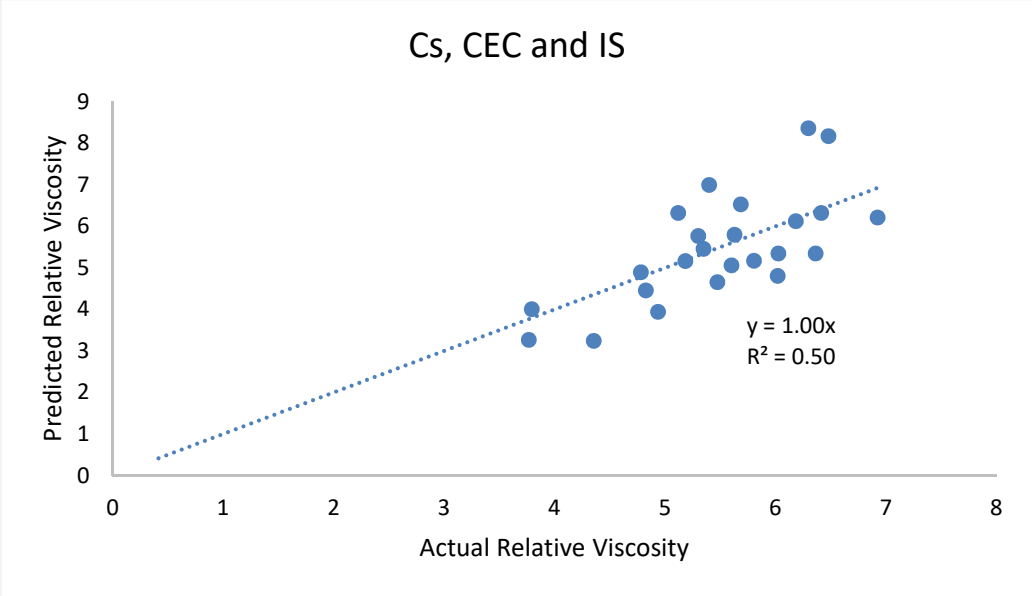

Figure D.14: Predictions for carrier fluid viscosity using solids concentration, CEC and IS

D.0.15 Dilution Curve Coefficients

An attempt was also made to find a relationship between CEC, IS and the coefficients of the dilution curves. The relationship found was:

$$A = 0.57 * CEC - 379.6 * IS + 42.9 \tag{D.15}$$

where

$$\mu_r = exp(A * C_s) \tag{D.16}$$

However, the relationship did not provide reasonable predictions as shown by Figure D.15

D.0.16 Exponential Fit

Similarly, an exponential fit with CEC and IS provided poor predictions of carrier fluid viscosities. The relationship found was:

$$\mu_r = exp(8.93 * CEC * IS * C_s) + 3.51 \tag{D.17}$$

The accuracy of Equation D.17 is shown in Figure D.16.

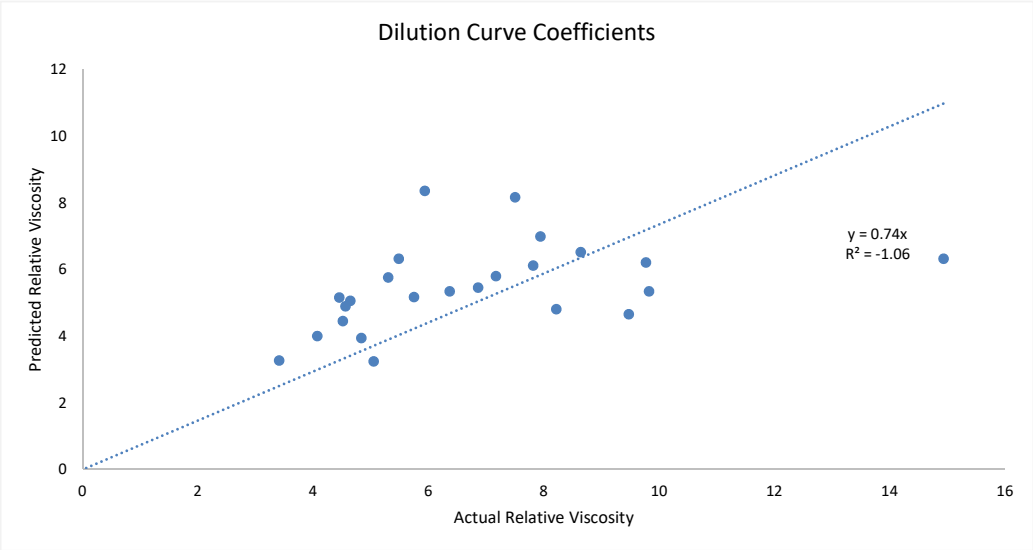

Figure D.15: Predictions for carrier fluid viscosity using dilution curve coefficients

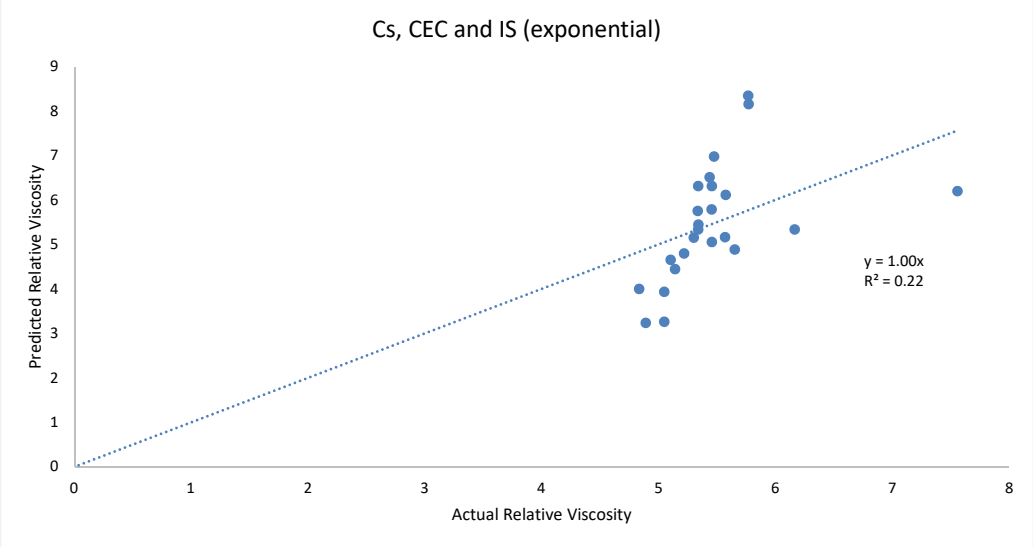

Figure D.16: Predictions for carrier fluid viscosity using an exponential fit for CEC, IS and Cs